

Evaluation of the Interface Mechanical Properties of Craniofacial Implants and Natural Teeth  
Through Development of the Advanced System for Implant Stability Testing (ASIST)

by

Lindsey Westover

A thesis submitted in partial fulfillment of the requirements for the degree of

Doctor of Philosophy

Department of Mechanical Engineering  
University of Alberta

© Lindsey Westover, 2016

# Abstract

Clinical evaluation of the integrity of the bone-implant interface of percutaneous implants is important to prescribe loading, to identify the risk of failure, and to monitor the long-term health of the implant. The same concept of interface integrity can be applied in dentistry where the interface is the periodontal ligament (PDL) connecting the tooth root to the surrounding alveolar bone. Similarly, ongoing clinical evaluation of tooth stability (or mobility) has important applications in dental trauma, orthodontics, and periodontology.

This clinical need has led to the development of several noninvasive methods for stability measurement of both percutaneous implant systems as well as natural teeth. Many of these currently available systems rely on resonance frequency analysis (RFA) or similar analysis of the fundamental frequency of vibration of the system. With these measurement techniques, the details of the system are not taken into account in the interpretation. As a result, there is no clear understanding of how the output values relate to the actual stiffness characteristics at the interface. To have a better understanding of the physical properties at the interface, a coupled experimental-analytical modeling approach has been proposed for percutaneous implants. The approach uses an acceleration measurement during an impact with the abutment and an analytical model is included in the interpretation to isolate the properties at the interface.

This study builds upon previous approaches to develop a measurement system for noninvasive evaluation of interface stiffness that is applicable across a range of applications including bone anchored hearing aid (BAHA) implants and natural teeth. The system is termed the Advanced System for Implant Stability Testing (ASIST) and the interface stability measure is termed the ASIST Stability Coefficient (ASC). The ASIST is developed through *in vitro* laboratory testing

for two commercial BAHA systems. A comparison is presented between the developed ASIST and the commercially available Osstell™ ISQ system for BAHA stability measurement. The ASIST is then used *in vivo* with a longitudinal clinical evaluation for BAHA patients during the first year following surgery. The ASIST technique is also developed for natural teeth and evaluated with longitudinal clinical data during orthodontic treatment.

Through *in vitro* laboratory testing, the ASIST measure was found to be essentially independent of attached components for BAHA implants with variations due to abutment length of approximately 2.9 ASC (less than 10% of the measure). The ASIST was shown to be sensitive enough to detect changes in interface properties between different implant installations. The ASIST showed significant advantages over the commercially available Osstell™ ISQ system for stability measurement of BAHA systems. The Osstell™ ISQ appears to be more sensitive to geometric variations such as abutment length than actual changes in interface properties, while the ASIST was found to be more sensitive to interface changes and essentially independent of abutment length.

Clinical evaluation of BAHA implants showed a wide variety of stability values and healing patterns across patients. The ASIST shows promise to detect differences in implant stability with different surgical techniques or different implant designs. The ASIST was able to provide an indication of longitudinal changes in implant stability for BAHA patients during the first year following surgery.

The ASIST technique was applied to natural teeth to estimate the PDL stiffness. A three degree of freedom analytical model was presented for a single-rooted tooth system. Several geometric approximations were presented and compared. The model prediction of the acceleration was

found to provide a good match with the measured acceleration suggesting that the ASIST technique can be applicable to natural teeth. A longitudinal evaluation was presented showing changes in PDL stiffness properties throughout orthodontic alignment and cuspid retraction. Similar patterns of longitudinal changes were observed for the two maxillary cuspid teeth within individual patients as well as between patients. All patients showed a reduction in PDL stiffness during treatment. This work presented a significant contribution to the experimental-analytical modeling approach for natural teeth, and the work presented here shows promise for future research in this area.

The ASIST has the potential to provide a valuable clinical tool enabling clinicians to quickly and noninvasively evaluate the status of percutaneous implant systems or natural teeth across a variety of applications.

# Preface

This thesis is an original work by Lindsey Westover. The research project received research ethics approval from the University of Alberta Research Ethics Board, Project Name “Nondestructive Mechanical Evaluation of Osseointegrated Implants”, No. Pro00042672, November 13, 2014.

# Acknowledgements

I would like to acknowledge and thank:

My supervisors Don Raboud and Gary Faulkner for your constant support and guidance. It has been a privilege working with you and I am grateful for the opportunity.

Bill Hodgetts for serving on my supervisory committee and for your enthusiasm, encouragement, and guidance throughout this project.

Dr. Jason Carey, Dr. Tom Oxland, and Dr. Chris Dennison. I appreciate you taking the time to serve on my examination committee.

My family for your love and support in my many years of academics. Especially my parents (Bill and Vickie), my brother (Jeff), and my in-laws (Samia, Magdy, and Ramy).

And most of all, my husband Samer. Your love, support, and encouragement are all that I need.

# Table of Contents

<b>Chapter 1: Introduction</b>	<b>1</b>
1.1. Background.....	1
1.2. Literature Review .....	3
1.2.1. Bone Biology.....	3
1.2.2. Osseointegration.....	4
1.2.3. Bone Conduction Hearing Aids.....	6
1.2.4. Dental Biology.....	8
1.2.5. Implant Stability Measurement .....	10
1.2.5.1. Destructive Techniques.....	11
1.2.5.2. Non-Destructive Techniques .....	11
1.2.6. Tooth Mobility (Stability) Measurement.....	14
1.2.7. Development of an Improved Stability Measurement Based on the Periotest®	15
1.3. Objectives.....	17
1.4. Thesis Outline.....	18
<b>Chapter 2: ASIST for Bone Anchored Hearing Aids</b>	<b>21</b>
2.1. Hardware and Measurement.....	21
2.2. Analytical Model .....	23
2.3. Estimating the Interface Properties .....	27
2.3.1. Measured Acceleration Signals – Curve Fit Approximation .....	27
2.3.2. Extracting Information from the Curve Fit .....	28
2.3.3. Matching the Analytical Model to the Measured Acceleration.....	31
2.3.4. Outcome Measure.....	33
2.4. Parametric Sensitivity of Analytical Model .....	33

2.4.1. Modal Analysis.....	34
2.4.2. Analytical Model Frequency Response versus Stiffness Parameters.....	34
2.4.3. Model Solution (ASC and Fit with Measured Data) with Stiffness Parameters $K_I$ and $K_T$ .....	38
2.4.4. Analytical Model Frequency Response versus Geometric and Inertial Parameters 40	
2.4.5. Model Solution (ASC and Fit with Measured Data) with Geometric Parameters $y_A$ and $J_A$ .....	43
2.4.6. Damping Model.....	45
2.5. Detail of the Numerical Analysis .....	46
2.6. Summary.....	47
<b>Chapter 3: ASIST Experimental Development</b>	<b>48</b>
3.1. Application to Oticon Ponto Implant-Abutment System .....	49
3.2. Application to Cochlear Baha® Connect Implant-Abutment System.....	51
3.3. ASIST Development and Experimental Evaluation.....	52
3.3.1. Experimental Testing.....	52
3.3.2. Determining model parameters .....	53
3.3.3. ASIST Evaluation.....	55
3.4. Precision of Experimental Testing .....	55
3.4.1. Laboratory Test Set-up.....	55
3.4.2. Outcome Measures .....	55
3.4.3. Repeatability of Measurement and Effect of Different Handpieces .....	56
3.4.4. Sensitivity to Clinical Variables.....	58
3.4.4.1. Handpiece Distance .....	58
3.4.4.2. Striking Height.....	60

3.4.4.3. Handpiece Angulation .....	61
3.4.5. Intra-User Repeatability .....	63
3.4.6. Inter-User Repeatability .....	67
3.5. Comparison Between ASIST and Osstell™ for BAHA Systems .....	69
3.5.1. Experimental Testing.....	69
3.5.2. Outcome Measures .....	70
<b>Chapter 4: Experimental Results with Bone Anchored Hearing Aid Systems</b>	<b>72</b>
4.1. Application to Oticon Medical Ponto System and Cochlear Baha® Connect System ..	72
4.1.1. Oticon Medical Ponto System .....	72
4.1.2. Cochlear Baha® Connect System .....	75
4.1.3. Application to Additional Abutment (14 mm Oticon Medical) .....	76
4.1.4. Damping Ratio.....	80
4.2. Comparison Between ASIST and Osstell™ for BAHA Systems .....	81
4.3. Summary.....	85
<b>Chapter 5: BAHA Clinical Study</b>	<b>89</b>
5.1. Participants .....	89
5.2. Methods .....	90
5.2.1. Data Collection.....	90
5.2.2. Data Analysis.....	92
5.3. Results .....	93
5.3.1. ASC Results and Model Fit.....	93
5.3.2. Damping Ratio.....	94
5.3.3. Initial Implant Stability.....	96
5.3.4. Longitudinal Changes in Implant Stability.....	99
5.4. Summary.....	105

<b>Chapter 6: Development of the ASIST for Natural Teeth</b>	<b>107</b>
6.1. Analytical Model .....	107
6.2. Geometry and Assumptions .....	110
6.3. ASIST Procedure.....	110
6.3.1. Osseometer to ASIST Transformation .....	110
6.3.2. Curve Fit Approximation and Extracting Information.....	115
6.3.3. Matching the Analytical Model to the Measured Acceleration.....	116
6.3.4. Outcome Measure.....	117
6.4. Parametric Sensitivity of the Tooth Analytical Model.....	118
6.4.1. Center of Resistance .....	118
6.4.2. Modal Analysis.....	119
6.4.3. Analytical Model Frequency Response versus Stiffness Parameters.....	122
6.4.4. Model Solution (ASC and Fit with Measured Data) with Impact Stiffness.....	124
6.4.5. Analytical Model Frequency Response versus Geometric Parameters .....	126
6.4.6. Model Solution (ASC and Fit with Measured Data) with Location of the Center of Mass .....	131
6.4.7. Damping Assumption.....	134
6.5. Clinical Evaluation .....	137
6.5.1. Description of the Data.....	138
6.5.2. Data Analysis – CT Geometry .....	143
6.5.3. Data Analysis – Optimized CT Geometry.....	144
6.5.4. Data Analysis – Approximate Geometry .....	145
6.6. Results .....	147
6.6.1. CT Geometry .....	147
6.6.2. Optimized CT Geometry .....	155

6.6.3. Approximate Geometry .....	159
6.6.4. Comparison with Literature.....	161
6.7. Summary.....	163
<b>Chapter 7: Summary and Conclusions</b>	<b>165</b>
7.1. Summary.....	165
7.2. Conclusions .....	167
7.3. Limitations.....	168
7.4. Future Considerations.....	170
7.4.1. Further Expansion for BAHA Systems .....	170
7.4.2. Evaluation of Implant Designs .....	170
7.4.3. Application to Other Percutaneous Implant Systems .....	170
7.4.4. Further Investigations with Natural Teeth.....	171
<b>References</b>	<b>173</b>
<b>Appendix A: Analytical Model Parameters for BAHA Implant-Abutment Systems</b>	<b>181</b>
<b>Appendix B: Parametric Sensitivity of the Analytical Model for BAHA Implant-Abutment Systems</b>	<b>196</b>
<b>Appendix C: Details of the Numerical Analysis</b>	<b>241</b>
<b>Appendix D: Derivation of the Mass and Stiffness Matrices for Tooth Model</b>	<b>252</b>

# List of Tables

Table 1.1: Relationship between contact time, Periotest value, and tooth mobility (adapted from Lukas and Schulte, 1990).....	15
Table 2.1: Damping proportionality constant ( $\gamma$ ) for Oticon implant-abutment system ( $\text{kg}^{1/2}$ ).....	31
Table 3.1: Oticon BAHA implant sizes .....	49
Table 3.2: Location of the center of mass for Oticon abutments calculated from the simplified geometry .....	50
Table 3.3: Best fit value of Oticon abutment center of mass ( $y_A$ ) for one dataset with each of the FRB-20 implant samples (units of m).....	50
Table 3.4: Mass and geometry properties for Oticon implants and abutments.....	51
Table 3.5: Mass and geometry properties for Cochlear implants and abutments .....	52
Table 3.6: Maximum torsional stiffness values .....	54
Table 3.7: Intra-User Reliability Measures for Oticon Medical Implant Samples (ICC and SEM).....	66
Table 3.8: Inter-User Reliability Measures for Oticon Medical Implant Samples (ICC and SEM).....	68
Table 4.1: Mass and geometry parameters of the Oticon 14 mm abutment .....	77
Table 4.2: Average interface stiffness values (average of 6 mm, 9 mm, and 12 mm abutments) and center of mass values for the 14 mm abutment for the FRB-20 implant specimens.....	77
Table 4.3: ASC values for the FRB-20(1) specimens. Comparison of the average ASC from 6 mm, 9 mm, and 12 mm abutments and the 14 mm abutment. ....	79
Table 5.1: Clinical Study Participant Summary.....	90
Table 5.2: Overview of Clinic Visits .....	92
Table 5.3: Participant Groupings based on Initial Stability (average of first 2 weeks) and Surgeon .....	96
Table 5.4: Participant Groupings based on Initial Stability (average of first 2 weeks) and Gender.....	98
Table 5.5: Participant Groupings based on Initial Stability (average of first 2 weeks) and Implant Type.....	99
Table 6.1: Comparison of ASC and $R^2$ values using different damping assumptions for example datasets from clinical orthodontic patients.....	135
Table 6.2: Mass and Geometry Parameters for Clinical Tooth Data from CT Scans.....	139
Table 6.3: Density of tooth components .....	140

# List of Figures

Figure 1.1:	Osseointegration of a titanium implant surface.....	5
Figure 1.2:	Bone anchored hearing aid (BAHA) device. Left: Illustration showing the attachment to a patient. Right: The individual BAHA components .....	7
Figure 1.3:	Dental notation using the FDI system (from: <a href="http://corinnadental.com.au/">http://corinnadental.com.au/</a> ) .....	9
Figure 1.4:	Tooth schematic showing various materials such as enamel, dentin, pulp, and cementum .....	9
Figure 1.5:	Filtered accelerometer signal used by the Periotest® analysis to calculate the PTV and the raw accelerometer signal extracted from the Periotest® device (adapted from: Swain et al., 2008a; with permission) .....	14
Figure 2.1:	ASIST components including the ASIST unit, the handpiece, a USB dongle, and a computer .....	22
Figure 2.2:	Acceleration signal for a BAHA implant-abutment system. A: The system used by Swain et al. (2008) showing the zero overshoot in the acceleration measurement. B: The ASIST system measurement. ....	23
Figure 2.3:	Schematic of the 4-DOF model of the BAHA implant/abutment system.....	24
Figure 2.4:	Measured accelerometer data (colored) with the curve fit model (red). Vertical dashed line defines the end of the strike.....	28
Figure 2.5:	Damping coefficient relationship for standard (narrow) diameter 4 mm Oticon implant with a 9 mm abutment.....	31
Figure 2.6:	Matched acceleration signal between the model (black) and measured data (colored) with the curve fit (red).....	32
Figure 2.7:	Mode shapes for long/narrow implant (M50128) with 9 mm abutment .....	34
Figure 2.8:	Relationship between the $p_1$ (left) and $p_2$ (right) and the interface stiffness per unit area $k$ for the long/narrow Oticon Medical implant (M50128). The different curves on each plot show the relationship for each abutment length.....	35
Figure 2.9:	Relationship between $p_1$ (left) and $p_2$ (right) and the ASC value for a long/narrow Oticon Medical implant (M50128). The different curves on each plot show the relationship for each abutment length. ....	36
Figure 2.10:	Relationship between $p_1$ (left) and $p_2$ (right) and the impact stiffness $K_I$ for a long/narrow Oticon Medical implant (M50128). The different curves on each plot show the relationship for each abutment length. ....	37
Figure 2.11:	Relationship $p_1$ (left) and $p_2$ (right) and the torsional stiffness $K_T$ for a long/narrow Oticon Medical implant (M50128). The different curves on each plot show the relationship for each abutment length. ....	37

Figure 2.12: Variation in ASC value (blue line) and $R^2$ fit (black line) with changes in impact stiffness ( $K_I$ ) for a long/narrow implant and 9 mm abutment .....	38
Figure 2.13: Variation in ASC value (blue line) and $R^2$ fit (black line) with changes in torsional stiffness ( $K_T$ ) for a long/narrow implant and 9 mm abutment.....	39
Figure 2.14: Relationship between the first and second mode frequency components and the abutment mass .....	41
Figure 2.15: Relationship between the first and second mode frequency components and the abutment length .....	41
Figure 2.16: Relationship between the first and second mode frequency components and the location of the abutment center of mass .....	42
Figure 2.17: Relationship between the first and second mode frequency components and the abutment mass moment of inertia .....	42
Figure 2.18: Variation in ASC value (blue line) and $R^2$ fit (black line) with changes in abutment center of mass ( $y_A$ ) for a long/narrow implant and 9 mm abutment.....	44
Figure 2.19: Variation in ASC value (blue line) and $R^2$ fit (black line) with changes in abutment mass moment of inertia ( $J_A$ ) for a long/narrow implant and 9 mm abutment .....	45
Figure 3.1: Illustrations of the Oticon Medical Ponto (left) and Cochlear Baha® Connect (right) BAHA implant-abutment systems.....	48
Figure 3.2: Laboratory test set-up showing the FRB-20 disc containing the implant with a 9 mm abutment attached. The disc is clamped to a platform for testing and the ASIST handpiece is held in a custom stand. ....	53
Figure 3.3: ASC measurements for a long/wide Oticon Medical implant (M51062 FRB-20(2)) with a 9 mm and 12 mm abutment and three ASIST handpieces. Values are the average of 5 measurements and error bars represent one standard deviation. ....	57
Figure 3.4: ASC measurements for a long/wide Oticon Medical implant (M51062 FRB-20(2)) with a 9 mm and 12 mm abutment and three ASIST handpieces. Values for the color labeled columns are the average of 35 measurements with each handpiece. Values for the “All” columns are the average of all 105 measurements. Error bars represent one standard deviation. ....	57
Figure 3.5: Cochlear implant and abutment geometry showing the chamfer at the top of the abutment .....	59
Figure 3.6: ASC measurements at variations in the handpiece distance from the abutment. Values are the average of five measurements. Error bars represent one standard deviation. Left: Oticon Medical implant (M51062 FRB-20(1)) with 9 mm abutment. Right: Cochlear implant sample (BI300) with 10 mm abutment. ....	60

Figure 3.7:	ASC measurements at variations in the handpiece striking height. Values are the average of five measurements. Error bars represent one standard deviation. Left: Oticon Medical implant (M51062 FRB-20(1)) with 9 mm abutment. Right: Cochlear implant sample (BI300) with 10 mm abutment. ....	61
Figure 3.8:	ASC measurements at variations in the handpiece angulation (angle above the horizontal). Values are the average of five measurements. Error bars represent one standard deviation. Left: Oticon Medical implant (M51062 FRB-20(1)) with 9 mm abutment. Right: Cochlear implant sample (BI300) with 10 mm abutment.....	62
Figure 3.9:	Difference in impact between the Oticon Medical abutment (left) and the Cochlear abutment (right) with a large handpiece angle.....	63
Figure 3.10:	ASC measurements for Oticon Medical implant samples from 14 participants. Values are the average of 10 measurements. Error bars represent one standard deviation. Top: implant samples with a higher stiffness. Bottom: implant samples with a lower stiffness. ....	65
Figure 3.11:	ASC measurements for the Cochlear implant samples for the two participants. Values are the average of 10 measurements. Error bars represent one standard deviation. ....	67
Figure 3.12:	ASIST and Osstell™ measurement methods. Measurements are taken at the level of the abutment or SmartPeg™ and used to indicate the properties at the bone-implant interface.....	70
Figure 4.1:	Representative example for one Oticon implant sample with three abutment lengths .....	73
Figure 4.2:	ASC values for all Oticon samples with three abutment lengths (6 mm, 9 mm, 12 mm).....	74
Figure 4.3:	Representative example for two different samples of one Oticon implant type (4.50 mm diameter, 4 mm length) and 9 mm abutment .....	75
Figure 4.4:	One Cochlear implant sample with four different abutment lengths .....	76
Figure 4.5:	ASC results for FRB-20(1) samples including 14 mm abutment .....	78
Figure 4.6:	Example signals for each implant specimen (FRB-20(1)) with the 14 mm abutment. The colored lines are the measured data (16 strikes) and the black lines are the model response.....	80
Figure 4.7:	ASC and ISQ values for each Oticon Medical implant-abutment combination comparing different abutment lengths for each implant specimen.....	82
Figure 4.8:	ASC and ISQ values for the Cochlear implant specimen comparing the measurements with the four different abutment lengths .....	83
Figure 4.9:	ASC and ISQ values for each implant-abutment combination comparing installations of the same type of implant.....	84
Figure 4.10:	Clinical guidelines for implant stability based on ISQ reading .....	88

Figure 5.1:	Examples of patient data (colored lines) and model fit (black lines) for low, moderate, and high stability values .....	94
Figure 5.2:	Example patient data with low damping ratio (left) and high damping ratio (right).....	95
Figure 5.3:	Mean initial implant stability (average of first 2 weeks) based on surgeon. Average values over all participants. Error bars indicate one standard deviation. * indicates significant difference based on Bonferroni adjusted $t$ -test ( $p < 0.0167$ ).....	97
Figure 5.4:	Initial implant stability as a function of participant age at surgery .....	97
Figure 5.5:	Average ASC values across all patients at each visit. Visit day is averaged for all patients. Error bars represent one standard deviation. ....	99
Figure 5.6:	Set of 15 patients showing a similar trend of longitudinal changes (generally small changes over time, many with a gradual increase in ASC). Initial stability (Low, Moderate, High) and surgeon (S1, S2, S3) are indicated for each patient.....	101
Figure 5.7:	Example patient showing an increase in ASC over time. 6 month results are reported for this patient. 64 year old female with a 4 mm narrow implant (M50128) and 6 mm abutment. (a) Longitudinal mean ASC values. (b) Measured data (colored lines) and model prediction (black line) at each visit with average ASC values and range for repeated measures.....	102
Figure 5.8:	Example patient showing a decrease in ASC over time. 6 month results are reported for this patient. 58 year old male with a 4 mm narrow implant (M50128) and 9 mm abutment. (a) Longitudinal mean ASC values. (b) Measured data (colored lines) and model prediction (black line) at each visit with average ASC values and range for repeated measures.....	103
Figure 5.9:	Example patient showing an initial decrease in ASC followed by an increase in ASC over time. 12 month results are reported for this patient. 67 year old male with a 4 mm narrow implant (M50128) and 9 mm abutment. (a) Longitudinal mean ASC values. (b) Measured data (colored lines) and model prediction (black line) at each visit with average ASC values and range for repeated measures. ....	104
Figure 6.1:	Schematic of the 3-DOF model of the tooth .....	108
Figure 6.2:	Comparison of ASIST and Osseometer data for the same implant sample. The bottom figure shows the difference in the signals ASIST – Osseometer.....	111
Figure 6.3:	Transforming Osseometer data to match ASIST data for an Oticon implant (M50128 with 9 mm abutment in FRB-20). A: The original ASIST data. B: The original Osseometer data showing the function $g(t)$ . C: The transformed Osseometer data overlaid with the original ASIST data. ....	112

Figure 6.4:	Comparison of data collected with the ASIST and the Osseometer for two examples: FRB-20(1) long/narrow (M50128) implant sample with 9 mm abutment (top) and FRB-20(1) long/wide (M51062) implant sample with 12 mm abutment (bottom). ASC values are shown on the figure. ....	113
Figure 6.5:	Comparison of the model fit and ASC value for Osseometer data with a linear transformation (left) and exponential transformation (right) for two example datasets: a long/narrow implant with 9 mm abutment (top) and a long/wide implant with 12 mm abutment (bottom) .....	114
Figure 6.6:	Comparison of original Osseometer data (left) and transformed Osseometer data (right) for an example clinical tooth dataset.....	115
Figure 6.7:	Sample data with curve fit approximation a clinical tooth example .....	115
Figure 6.8:	Free body diagram of a tooth with a horizontal force applied at the center of resistance ( $C_{Res}$ ). The horizontal restraining force is the interface stiffness distributed over the area of the tooth root. ....	118
Figure 6.9:	Mode shapes and undamped acceleration response with varying striking locations: $L_o = 5, 6, 7, 8$ mm from the crown tip. Interface stiffness $k = 0.01 \times 10^{12}$ N/m <sup>3</sup> . ....	121
Figure 6.10:	Relationship between the interface stiffness per unit area ( $k$ ) and the first mode frequency ( $p_1$ ; left) and the second mode frequency ( $p_2$ ; right) for a typical tooth model.....	123
Figure 6.11:	Relationship between the ASC value and the first mode frequency ( $p_1$ ; left) and the second mode frequency ( $p_2$ ; right) for a typical tooth model.....	123
Figure 6.12:	Relationship between the impact stiffness ( $K_I$ ) and the first mode frequency ( $p_1$ ; left) and the second mode frequency ( $p_2$ ; right) for a typical tooth model.....	124
Figure 6.13:	Variation in ASC value (blue line) and $R^2$ fit (black line) with changes in impact stiffness ( $K_I$ ).....	125
Figure 6.14:	Variation in the model fit (black line) with the measured acceleration (colored lines) with changing impact stiffness ( $K_I$ ) for an example dataset (Patient 1; Tooth ID 13). The best match between the model and the measured data as measured by the $R^2$ value is highlighted in red. ....	126
Figure 6.15:	Relationship between the first mode frequency ( $p_1$ ; left) and second mode frequency ( $p_2$ ; right) and the tooth root length ( $L_r$ ).....	127
Figure 6.16:	Relationship between the first mode frequency ( $p_1$ ; left) and second mode frequency ( $p_2$ ; right) and the tooth crown length ( $L_c$ ).....	128
Figure 6.17:	Relationship between the first mode frequency ( $p_1$ ; left) and second mode frequency ( $p_2$ ; right) and the tooth radius ( $R_0$ ).....	128

Figure 6.18: Relationship between the first mode frequency ( $p_1$ ; left) and second mode frequency ( $p_2$ ; right) and the tooth mass ( $m_t$ ) .....	129
Figure 6.19: Relationship between the first mode frequency ( $p_1$ ; left) and second mode frequency ( $p_2$ ; right) and the location of the center of mass ( $y_{CG}$ ).....	129
Figure 6.20: Relationship between the first mode frequency ( $p_1$ ; left) and second mode frequency ( $p_2$ ; right) and mass moment of inertia ( $J_G$ ) .....	129
Figure 6.21: Relationship between the first mode frequency ( $p_1$ ; left) and second mode frequency ( $p_2$ ; right) and the striking height ( $L_o$ ). Note that $L_o$ is measured from the top of the crown, so increasing $L_o$ indicates striking lower on the tooth crown.....	130
Figure 6.22: Variation in ASC value (blue line) and $R^2$ fit (black line) with changes in the location of the center of mass ( $y_{CG}$ ).....	132
Figure 6.23: Variation in the model fit (black line) with the measured acceleration (colored lines) with changing center of mass for an example dataset (Patient 1; Tooth ID 13). The best match between the model and the measured data as measured by the $R^2$ value is highlighted in red.....	133
Figure 6.24: Comparison of model solution (black lines) with viscous damping and proportional damping for orthodontic patient datasets (shown in colored lines) .....	136
Figure 6.25: Comparison of viscous damping and proportional damping for various damping ratios. Second mode damping ratio ( $\zeta_2$ ) and interface damping coefficient ( $c$ ) values are shown on the figures.....	137
Figure 6.26: Separating the tooth into two components (crown and root) to estimate the mass properties with different density values for the two components .....	140
Figure 6.27: Example data (Patient 1; Tooth ID 13) comparing the two density models. Left: mass and center of mass were determined from the uniform density model. Right: mass and center of mass were determined from the two density model. ....	141
Figure 6.28: Change in model fit and ASC values with varying moment of inertia. $J_G$ was varied $\pm 15\%$ . The sample dataset is an example from Patient 1. ....	143
Figure 6.29: Approximate geometric model for a single-rooted tooth .....	146
Figure 6.30: Measured accelerometer data (colored lines) and model predicted response (black line) for Patient 1 (AS) tooth ID 13 using CT geometry. Each plot shows an example of the data and model fit for each clinic visit (visit day indicated on each figure). The ASC values are average $\pm$ SD for repeated measures on each day.....	147
Figure 6.31: Example plot of longitudinal ASC measurements (Patient 1) for tooth ID 13 and 23 using the CT geometry. Reported values are the average of repeated measurements and error bars show one standard deviation. ....	148
Figure 6.32: Longitudinal ASC measurements for Patient 2.....	149

Figure 6.33: Longitudinal ASC measurements for Patient 3.....	149
Figure 6.34: Longitudinal ASC measurements for Patient 4.....	150
Figure 6.35: Longitudinal ASC measurements for Patient 5.....	150
Figure 6.36: Longitudinal ASC measurements for Patient 6.....	151
Figure 6.37: Longitudinal ASC measurements for Patient 7.....	151
Figure 6.38: Longitudinal ASC measurements for Patient 8.....	152
Figure 6.39: Longitudinal ASC measurements for Patient 9.....	152
Figure 6.40: Longitudinal ASC measurements for Patient 10.....	153
Figure 6.41: Longitudinal ASC measurements for Patient 11.....	153
Figure 6.42: Longitudinal ASC measurements for Patient 12.....	154
Figure 6.43: Examples of patient measurements with the highest predicted impact stiffness (left) and the lowest predicted impact stiffness (right).....	155
Figure 6.44: Example of patient data with unusually high damping ratio (0.917). Colored lines are the measured acceleration, red line is the curve fit approximation of the data, and black line is the model prediction.....	155
Figure 6.45: Measured accelerometer data (colored lines) and model predicted response (black line) for Patient 1 (AS) tooth ID 13 using CT geometry with optimized mass and center of mass. Each plot shows an example of the data and model fit for each clinic visit (visit day indicated on each figure). The ASC values are average $\pm$ SD for repeated measures on each day.....	156
Figure 6.46: Measured accelerometer data (colored lines) and model predicted response (black line) for sample data at several visits for Patient 1 (AS) tooth ID 13 comparing the model predicted acceleration response using the original CT geometry (left) and the CT geometry with optimized mass and center of mass (right). For each day (visit day indicated on the figure) the same dataset is shown with the two different model predictions. The ASC values are average $\pm$ SD for repeated measures on each day.....	157
Figure 6.47: Comparison of longitudinal ASC measurements using the original CT geometry and the optimized CT geometry for Patient 1. A: Right maxillary cuspid (Tooth ID 13). B: Left maxillary cuspid (Tooth ID 23). Reported values are the average of repeated measurements and error bars show one standard deviation. ....	158
Figure 6.48: Measured accelerometer data (colored lines) and model predicted response (black line) for Patient 1 tooth ID 13 using approximate geometry. Each plot shows an example of the data and model fit for each clinic visit (visit day indicated on each figure). The ASC values are average $\pm$ SD for repeated measures on each day. ....	159

Figure 6.49: Comparison of longitudinal ASC measurements using the optimized CT geometry and the approximate geometry for Patient 1. A: Right maxillary cuspid (Tooth ID 13). B: Left maxillary cuspid (Tooth ID 23). Reported values are the average of repeated measurements and error bars show one standard deviation. .... 160

Figure 6.50: Change in ASC value between the optimized CT geometry and the approximate geometry ( $ASC_{(CT)} - ASC_{(Approx)}$ ) as a function of the change in root length ( $L_{r(CT)} - L_{r(Approx)}$ ). Reported data is the average change for a particular tooth..... 161

Figure 6.51: Illustration of the difference between the effective stiffness at the tooth interface (A) and the effective stiffness of the entire tooth system with a force applied near the top of the crown (B)..... 162

# Chapter 1: Introduction

## 1.1. Background

Percutaneous implants are used in prosthetic reconstruction of the head and neck to improve function and aesthetics in a variety of applications. Implants can be used to reconstruct dental arches, to install bone anchored hearing aids (BAHA) and prosthetic ears, and to reconstruct craniofacial features after trauma or cancer treatment. The use of implants in such applications can result in a tremendous improvement in the quality of life of patients. The procedure involves installing a screw-shaped titanium implant into the bone. An attached abutment permanently penetrates the skin surface and the device (i.e. the prosthetic tooth or the hearing processor) can then be attached to the abutment for use by the patient.

Percutaneous implants have been used for clinical tooth replacement and for BAHA for decades with great success (Brånemark et al., 1985; Tjellström et al., 1983). The concept of bone anchored implants relies on a structural integration between the implant and the bone, termed osseointegration (Brånemark et al., 1985). The conditions to promote osseointegration of an implant include biocompatibility of the implant material (e.g. titanium), minimal trauma to the bone during the surgical procedure, and an immobile healing phase (Brånemark, 1983; Brånemark et al., 1985). During this healing phase bone is deposited onto the implant surface and remodeling occurs resulting in a bone-implant interface in which the implant is directly connected to the living bone (Brånemark, 1983; Brånemark et al., 1985; Ellingsent and Lyngstadaas, 2003). The success of these implants is dependent on the quality of osseointegration at the bone-implant interface.

While in the long term the success rate is very high, with implant losses typically reported less than 10% for BAHA implants (Dun et al., 2012; Fontaine et al., 2014; House and Kutz, 2007; Nelissen et al., 2014; Tjellström and Granström, 1994), there is uncertainty in the optimal time to begin functional loading of BAHA systems. This is evidenced by a large variation in clinical practices. From the patient perspective, it would be beneficial to begin loading (i.e. begin using the hearing processor) as soon as possible, allowing them to experience significant functional

improvements. At the same time however, proper healing to achieve adequate osseointegration is necessary for long term success of the implant. Traditionally, functional loading of BAHA implants has begun at 3 months post-surgery for adults and 4-6 months for children (Albrektsson et al., 1981; Wazen et al., 2007). However, more recently, loading of BAHA systems has been reported at 6 weeks (Foghsgaard and Caye-Thomasen, 2014; Wazen et al., 2007), 4 weeks (McLarnon et al., 2012), 3 weeks (Faber et al., 2012; Nelissen et al., 2016), and as early as 7-14 days (Hougaard et al., 2015) post-surgery. Due to this uncertainty in appropriate loading times as well as for longer term stability checks, it is important to monitor the integrity of the bone-implant interface during healing and throughout the life of the implant.

Similar concepts of interface integrity can be applied to natural teeth in the clinical fields of dentistry, periodontology, and orthodontics. In this case the interface of interest is the periodontal ligament (PDL) which connects the tooth root to the surrounding alveolar bone (Nishihira et al., 2003). Clinical assessment of the tooth interface has important applications in diagnosing periodontal disease, assessing the condition of the PDL after trauma, understanding the changes that occur in the PDL during and after orthodontic treatment, and assessing outcomes from treatment aimed at improving the integrity of the tooth root or the PDL (Laster et al., 1975; Nakago et al., 1994).

In many clinical situations, particularly with bone anchored implants, the term “stability” is often used to describe the stiffness at the interface and is used as a measure of the integrity of the interface. While stability in an engineering sense has a strict and well-understood definition, clinical stability of both bone-anchored implants and natural teeth may follow a different definition with more variability in the interpretation. In the context of the work presented here, the term stability refers to a clinical stability of the interface and is often used interchangeably with the stiffness at the interface. An implant with a stiffer interface would be considered more stable and would be assumed to have better interface integrity. With this understanding, an unstable interface may show large displacements when subjected to relatively low forces and may be at risk of failure.

This research is focused on the development of a measurement system for non-invasively assessing the interfacial properties in a clinical setting that is applicable across a range of applications including bone anchored implants and natural teeth.

## **1.2. Literature Review**

### **1.2.1. Bone Biology**

Bone anchored implants are anchored into the living bone tissue. In order to understand the osseointegration process and implant healing, it is important to first consider the structure and components of these tissues as well as the mechanisms for growth and remodeling. Bone tissue is composed of approximately 65% minerals such as calcium and phosphate primarily in the form of hydroxyapatite and approximately 35% organic matrix, cells, and water (Cowin, 2001; Nordin and Frankel, 2001). The organic matrix is composed primarily (approximately 90%) of Type I collagen fibers which account for 25 – 30% of the dry weight of bone. The remaining organic matrix is composed of noncollagenous proteins and contains glycosaminoglycans (GAGs) primarily in the form of proteoglycans (PGs) (Cowin, 2001; Nordin and Frakel, 2001). Water is an important component of living bone and comprises approximately 25% of its total weight (Nordin and Frankel, 2001).

There are four major types of bone cells: osteoclasts, osteoblasts, osteocytes, and bone-lining cells. Osteoclasts are bone resorbing cells, while osteoblasts are bone forming cells. During the formation of new bone, osteoblasts synthesize the unmineralized bone matrix. This matrix formation is then followed by mineralization (Cowin, 2001). The most abundant cell type in mature bone is the osteocyte. Osteocytes can sense changes in the magnitude and distribution of strains in the tissue and influence modeling and remodeling behavior (Cowin, 2001). The final cell type is the bone-lining cell. These are formed by osteoblasts that are inactive and are sometimes called resting osteoblasts (Cowin, 2001). Bone-lining cells may also respond to strain within the bone tissue and may be involved in the bone remodeling process (Cowin, 2001; Crockett et al., 2011).

Growth, modeling, and remodeling are processes that control the shape, size, strength, and anatomy of bones and joints (Cowin, 2001). Growth and modeling result in an increase in the amount of bone. Modeling helps to control the development of the bone structure during growth and helps to regulate the bone architecture in response to varying mechanical conditions (Cowin, 2001). Bone remodeling involves the resorption of either old bone or immature woven bone followed by the formation of new lamellar bone (Cowin, 2001). The bone remodeling unit (BRU) passes through six stages: resting, activation, resorption, reversal, formation and mineralization, and subsequent resting. In adults, the majority of the bone surfaces are inactive and are in the resting stage. The initiation of bone remodeling is activation and this phase is believed to occur in response to structural or biomechanical factors (Cowin, 2001). Osteoclasts are recruited in this phase. Resorption occurs when osteoclasts begin to erode the bone surface and this phase can take 1 – 3 weeks (Cowin, 2001). Resorption is followed by a 1 – 2 week period before formation begins referred to as reversal or coupling. Bone formation is then performed which occurs in two stages. The osteoblasts first synthesize the bone matrix followed by a period of mineralization. 70% of the mineralization occurs after approximately 5 – 10 days; however, complete mineralization can take up to 3 – 6 months (Cowin, 2001). Following the formation of new bone, the BRU returns to its resting state. In the context of percutaneous implants, this implies that significant changes in the bone-implant interface can be expected in the first few weeks followed by a gradual improvement.

### **1.2.2. Osseointegration**

Osseointegration of an implant occurs when the living bone grows directly onto the implant surface and the two become integrated together at their interface (Brånemark, 1983; Brånemark et al., 1985; Ellingsent and Lyngstadaas, 2003) (Figure 1.1). Proper surgical techniques must be followed to promote osseointegration. If proper techniques are not followed, for example if there is too much surgical trauma, a soft connective tissue layer may form at the interface (much like a scar tissue) and osseointegration will not be achieved (Brånemark, 1983).

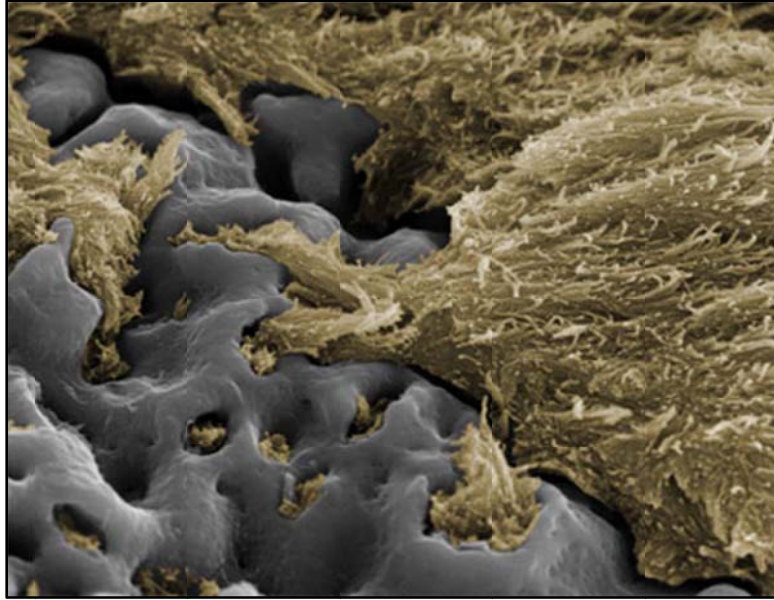


**Figure 1.1: Osseointegration of a titanium implant surface (from: [www.nobelbiocare.com](http://www.nobelbiocare.com))**

The process of osseointegration occurs in three phases (Davies, 2003; Ellingsent and Lyngstadaas, 2003). The first phase involves migration of the osteogenic bone cells to the implant surface. The second phase is *de novo* bone formation, which results in a mineralized matrix similar to the cement line in natural bone. Finally, the third phase involves bone remodeling (Davies, 2003; Ellingsent and Lyngstadaas, 2003) and the end result is a structural integration at the bone-implant interface. The initial inflammatory response occurs within the first 24 hours after implantation and the migration of the bone cells to the implant surface occurs within the first 4 days (Wang et al., 2016). New bone formation occurs on the implant surface around days 5 – 7 and by 4 weeks following implantation the new bone on the implant surface has connected to the host bone (Wang et al., 2016). After 8 – 12 weeks, the bone-implant interface consists of mature lamellar bone in direct contact with the implant surface (Wang et al., 2016).

Loading of bone anchored implants can lead to micromotion at the bone-implant interface. An immobile healing phase of 3-6 months was recommended in the early work with osseointegration by Brånemark et al. (1985) to limit this micromotion during healing. It has been shown that micromotion induced by loading can lead to a fibrous encapsulation at the bone-implant interface instead of direct osseointegration (Cameron et al., 1973; Ducheyne et al., 1977; Schatzker et al., 1975; Szmukler-Moncler et al., 1998; Unthoff, 1973) and the concern with early

loading by some researchers has been that micromotion during healing would not lead to osseointegration (Akagawa et al., 1986; Brunski, 1992; Brunski et al., 1979; Lum et al., 1991; Szmukler-Moncler et al., 1998). However, many reports with early loading, particularly in dental implants, have shown successful osseointegration despite some amount of micromotion during healing (Akagawa et al., 1993; Deporter et al., 1990; Hashimoto et al., 1988; Szmukler-Moncler et al., 1998). It is generally accepted that “excessive” micromotion is what leads to the formation of a fibrous tissue layer and that motion below some threshold can still lead to successful osseointegration (Brunski, 1991; Brunski, 1993; Pilliar, 1991; Szmukler-Moncler et al., 1998). It has been suggested that implant design (such as a screw-type implant) is one factor that can help to achieve adequate primary stability to prevent excessive micromotion and allow for proper osseointegration (Szmukler-Moncler et al., 1998).

### **1.2.3. Bone Conduction Hearing Aids**

Traditional hearing aids transmit sound from a small speaker in the device, placed within the ear canal, through the middle ear to the cochlea (Taghavi, 2014). This type of transmission is known as air conduction (AC). Some patients cannot use traditional AC hearing aids and instead rely on bone conduction (BC) hearing aids to transmit sound through vibrations in the skull directly to the cochlea (Hagr, 2007; Taghavi, 2014). For example, many patients with conductive and mixed hearing loss or single-sided deafness as well as those with chronic middle ear disease or congenital malformations can benefit from BC hearing aids (Taghavi, 2014).

Direct bone conduction hearing aids or bone anchored hearing aids (BAHA) transmit the sound to the skull bones through an osseointegrated implant installed in the mastoid portion of the temporal bone (Tjellström et al., 1983). A skin-penetrating abutment is attached to the implant and the hearing processor is connected via a mechanical coupling from outside the skin (Figure 1.2). Percutaneous BAHA provide a good method for hearing rehabilitation with very good audiological results; however, they have some drawbacks associated with the skin-penetrating abutment including implant loss, skin complications, and aesthetic appearance (Reinfeldt et al., 2015). More recently, transcutaneous BC devices have been developed to overcome some of the drawbacks of percutaneous BAHA.

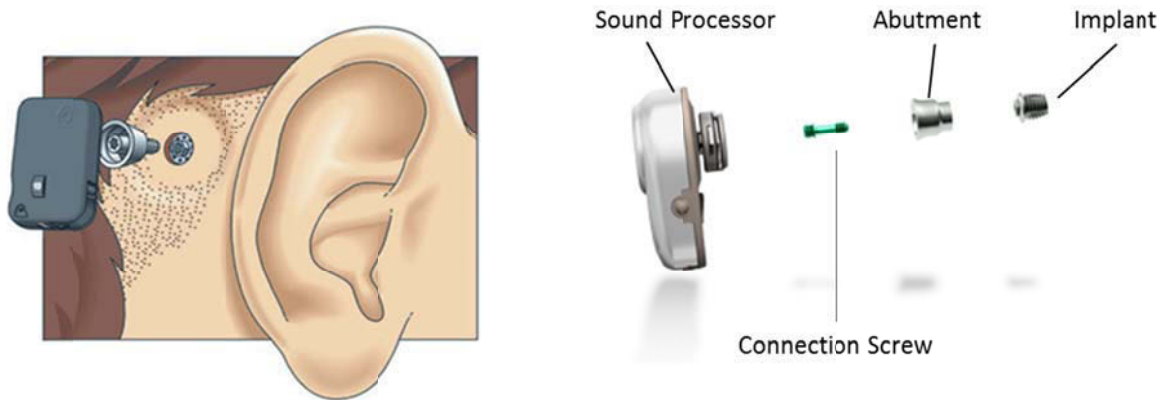


**Figure 1.2: Bone anchored hearing aid (BAHA) device. Left: Illustration showing the attachment to a patient (from: <http://www.silverhairs.co.uk/help28.htm>). Right: The individual BAHA components (from: <http://www.oticonmedical.com/>)**

Transcutaneous BC devices include both passive “skin-drive” devices and active “direct-drive” devices where some portion of the device is implanted under the skin and a sound processor is attached from outside the skin with magnetic retention (Reinfeldt et al., 2015). With passive devices, the transducer is outside the skin and the vibrations from the sound processor are transmitted through the skin (skin-drive). With active devices, the transducer is placed under the skin so the vibrations are transmitted directly to the bone (direct-drive) while only the electromagnetic signal from the sound processor is transmitted through the skin (Reinfeldt et al., 2015). Transcutaneous devices eliminate the need for life-long daily skin care and potential skin complications around the abutment associated with percutaneous BAHA; however, they have their own set of limitations and challenges. The magnetic attachment force must be strong enough to provide a stable long-term fixation; however this must be balanced with the potential for discomfort and skin problems associated with the prolonged skin pressure (Reinfeldt et al., 2015). This is can be particularly problematic for the passive (skin-drive) devices because the attachment force must also be strong enough to provide good transmission of the vibrations through the skin. Another major challenge with transcutaneous devices is providing adequate power to achieve good audiological results (Reinfeldt et al., 2015).

The percutaneous BAHA are still the most powerful BC devices available, providing very good audiological results (Reinfeldt et al., 2015). For these reasons, the percutaneous BAHA are still

the most widely used BC devices available today with over 150,000 patients world-wide (Reinfeldt et al., 2015).

BAHA implants are typically installed with a single-stage surgery where the implant is installed into the bone and the abutment is attached at the time of surgery. The implants are then left for some time before loading to allow for proper osseointegration to occur (Wazen et al., 2007). Functional loading of BAHA implants occurs through fitting and attachment of the sound processor. The load is applied to the abutment during daily attachment and detachment of the processor by the patient and through the weight of the processor (13 – 17 grams) during normal use ([www.cochlear.com](http://www.cochlear.com); [www.oticonmedical.com](http://www.oticonmedical.com)). Various loading times for BAHA implants have been reported ranging from 3 months (4-6 months for children) to 7-14 days post-surgery (Albrektsson et al., 1981; Faber et al., 2012; Foghsgaard and Caye-Thomasen, 2014; Hougaard et al., 2015; McLarnon et al., 2012; Nelissen et al., 2016; Wazen et al., 2007).

#### **1.2.4. Dental Biology**

There are 32 teeth in the adult human mastication system: four incisors, two canines or cuspids, four premolars, and six molars in each of the upper (maxilla) and lower (mandible) jaws (Gray, 1918). There are several notation systems for designating teeth, with the two-digit system of the Fédération Dentaire Internationale (FDI) being one of the most widely used (Türp and Alt, 1995). With the FDI system, the teeth in the upper right jaw are designated with a number 1 and the teeth in the upper left jaw are designated with a number 2. Similarly, the lower left teeth begin with a number 3 and the lower right teeth begin with a number 4 (Figure 1.3).

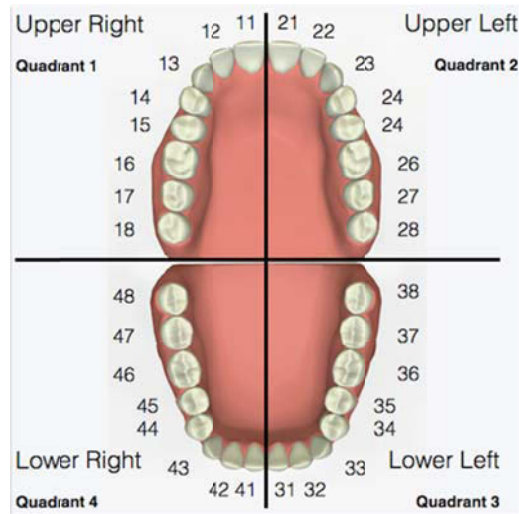


Figure 1.3: Dental notation using the FDI system (from: <http://corinnadental.com.au/>)

Teeth either have a single root or multiple roots. Figure 1.4 shows a schematic of a single-rooted tooth. The central cavity of the tooth is composed of pulp and supplied with vessels and nerves. The pulp cavity is surrounded by dentin which forms the majority of the tooth structure. The exposed portion of the crown is covered with a layer of hard enamel, while the root is surrounded by a thin layer of cementum (Gray, 1918).

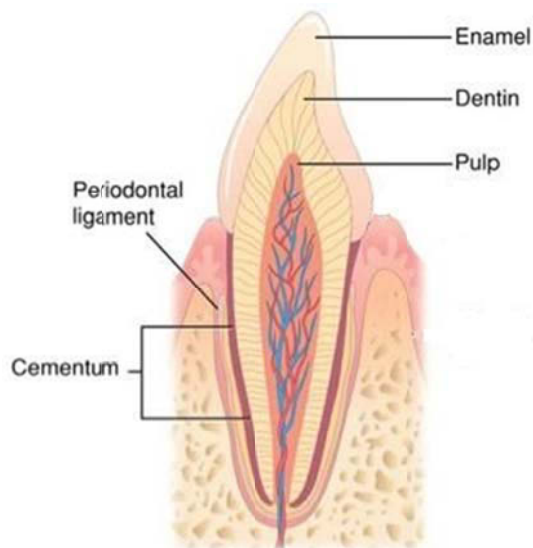


Figure 1.4: Tooth schematic showing various materials such as enamel, dentin, pulp, and cementum (adapted from: <https://s-media-cache-ak0.pinimg.com/736x/cb/d4/ee/cbd4ee49d207fd7ff2460abe5caebdc1.jpg>)

The tooth root is connected to the surrounding alveolar bone by the PDL (Nishihira, 2003). The PDL consists of collagen fibers as well as a ground substance matrix including blood vessels and nerve endings (Carvalho et al., 2006; Romanyk et al., 2013; Toms et al., 2002). The PDL is a viscoelastic tissue that is approximately 0.15 – 0.25 mm in thickness (Carvalho et al., 2006; Romanyk et al., 2013). It stabilizes the tooth root in the bone while allowing for tooth movement in response to applied forces (Fill et al., 2011; Romanyk et al., 2013; Toms et al., 2002). Additionally the PDL provides nutritive, proprioceptive, and reparative functions to the area (Toms et al., 2002). Like many viscoelastic tissues, the PDL behaves elastically under rapid loading such as mastication because the high loading rate does not provide enough time for viscoelastic effects to occur, while it behaves viscoelastically under continuous loading such as orthodontic forces (Romanyk et al., 2013; Toms et al., 2002). The collagen fibers resist tensile forces while the ground substance allows for the viscoelastic response (Carvalho et al., 2006; Fill et al., 2011; Romanyk et al., 2013).

Material properties of the PDL reported in the literature vary widely with reported values for the Young's modulus spanning several orders of magnitude (0.01 – 1750 MPa) and reported values for Poisson's ratio ranging from 0.28 to 0.49 (Fill et al., 2011). This variation is largely due to difficulties in experimental measurement and the wide range of approaches used for measuring or estimating these properties (Fill et al., 2011).

The PDL is an important element in orthodontic tooth movement. Orthodontic forces are applied continuously over an extended period of time. It is generally accepted that orthodontic forces cause bone resorption on the compression side and bone apposition on the tension side of the PDL resulting in tooth motion towards the compression side (Dolce et al., 2002; Fill et al., 2011).

### **1.2.5. Implant Stability Measurement**

Implant stability is thought to occur in two stages: primary and secondary stability (Atsumi et al., 2007; Cehreli et al., 2009). Primary stability is achieved during installation and is the result of mechanical engagement between the threaded implant and the bone (Atsumi et al., 2007; Cehreli et al., 2009). Secondary stability can be referred to as biological stability and is the result of bone remodeling and the osseointegration process (Atsumi et al., 2007; Brånemark, 1983; Brånemark

et al., 1985; Cehreli et al., 2009; Ellingsent and Lyngstadaas, 2003). This secondary stability is important for the lifelong success of the implant. There are many techniques that can be used to estimate implant stability or the integrity of the bone-implant interface (Atsumi, 2007). This section outlines some of the techniques that have been used including both destructive and non-destructive techniques.

#### **1.2.5.1. Destructive Techniques**

There are several invasive or destructive techniques such as histologic analysis and reverse torque or removal torque tests that have been used to assess the integrity of the bone-implant interface. Histologic analysis requires removal of the implant and preparation of the interface specimen and can provide valuable information about osseointegration and the cell structure surrounding the implant (van der Pouw et al., 1998). Removal torque testing measures the torque required to rupture the bone-implant interface and remove the implant from the bone. This method quantifies the torsional strength or a threshold for torsional failure of the implant (Cehreli et al., 2009). Removal torque has been used in animal studies to understand the osseointegration process and longitudinal healing of implants (Johansson and Albrektsson, 1987) and to evaluate different implant designs (Johansson et al., 2015). Because of their destructive nature, these techniques are not suitable for clinical use and have primarily been used in research settings and experimental animal studies (Cehreli et al., 2009).

#### **1.2.5.2. Non-Destructive Techniques**

A clinically useful measure of implant stability should be noninvasive and non-destructive. Conventional imaging techniques such as radiography have been used with the idea that increased radiolucency around the implant indicates failure of osseointegration (Sundén et al., 1995). However, these types of imaging techniques (including radiography, magnetic resonance imaging, and computed tomography) are limited in their ability to monitor the bone-implant interface because the presence of the implant often causes distortion on the image within the area of interest making it difficult to note the subtle changes that may be occurring (Atsumi et al., 2007; Sundén et al., 1995; Swain et al., 2008a).

Several mechanical testing methods have been developed to assess implant stability which rely on the principle that the amount of osseointegration at the interface is related to the stiffness at this interface. A well-integrated implant is believed to be stiffer than a poorly integrated one (Swain et al., 2008a; Swain et al., 2008b). To measure this stiffness, resonance frequency analysis (RFA) uses the idea that the resonance frequency (or natural frequency) of the system comprised of the implant, adjoining superstructure, and supporting bone is dependent on the stiffness at the bone-implant interface. Assuming the other components in the system remain constant, changes in the resonance frequency indicate changes at the interface (Faulkner et al., 1999; Meredith et al., 1996; Meredith, 1997; Swain et al., 2008a; Swain et al., 2008b).

The Osstell<sup>TM</sup> ISQ (Osstell, Göteborg, Sweden) is a commercially available instrument based on the concept of RFA (Sennerby and Meredith, 2008). The Osstell<sup>TM</sup> provides an implant stability quotient (ISQ) between 1 and 100 which indicates the stability of the implant, with higher numbers having greater stability (McLarnon et al., 2012; Sennerby and Meredith, 2008). The Osstell<sup>TM</sup> system is widely used clinically (Faber et al., 2012; Foghsgaard and Caye-Thomasen, 2014; Hougaard, et al., 2015; McLarnon et al., 2012; Nelissen et al., 2015; Nelissen et al., 2016); however it has several limitations. The system makes use of SmartPegs which are metallic pegs that must be attached directly to the system components, either the implant or the abutment. This makes their clinical use inconvenient or limited for several reasons. A specific SmartPeg must be used for each type of implant or abutment. There are over 50 different types of SmartPegs available to accommodate the wide range of implant systems currently used ([www.osstell.com](http://www.osstell.com)). As the SmartPeg must be directly attached to the implant or abutment, the Osstell<sup>TM</sup> system cannot be used with dental implants unless the prosthetic tooth is removed. This is not practical for cemented teeth. In addition, it cannot be used with natural teeth. The other major limitation of the Osstell<sup>TM</sup> is that it does not consider the system components such as the abutment or superstructure in the interpretation of the resonance frequency. Because of this, different results can be obtained for the ISQ value of a given interface depending on the superstructure that is used. It has been recommended that single ISQ values should not be interpreted individually and clinical conclusions should not be based on ISQ values at a particular time (Nelissen et al., 2015). Because of the variation due to the implant and abutment geometry, ISQ values are most meaningful as a trend for an individual patient (Nelissen et al., 2015). This makes it difficult to

compare between patients or between different implant systems and makes it difficult to draw clinical conclusions based on this measure.

The Periotest® (Medizintechnik Gulden, Modautal, Germany) is another commercially available system, originally developed to monitor the mobility and damping of natural teeth, which makes use of an impact technique to assess the interface (Lukas and Schulte, 1990). A handpiece is used to drive a metal rod towards the implant-abutment system. The non-striking end of the rod has an accelerometer attached, which records the acceleration response due to the impact. The impact event comprises approximately half of one cycle at the fundamental frequency of vibration of the system and the time for this half cycle to occur is termed the contact time. The contact time is used to calculate a Periotest value (PTV) between -8 and +50 with lower numbers representing stiffer systems. The equations used to calculate the PTV are as follows (Lukas and Schulte, 1990):

$$\text{For PTV} > 13: \text{PTV} = 10\sqrt{\left(\frac{\text{contact time}}{0.06 \text{ ms}} - 8.493\right)} - 4.17$$

$$\text{For PTV} < 13: \text{PTV} = \frac{\text{contact time}}{0.02 \text{ ms}} - 21.3$$

The idea with the Periotest® is that a shorter contact time indicates a stiffer interface. This system has been applied to implants with limited success mainly due to the fact that the stiffness range for the PDL and natural teeth is considerably larger than for the bone-implant interface of osseointegrated implants (Aparicio et al., 2006; Hobkirk and Wiskott, 2006). The advantage of the Periotest® is that it does not require attachment to the implant system, so it can be used for natural teeth as well as any type of implant-abutment system even with permanently attached superstructures such as prosthetic teeth. Similar to the Osstell™ however, the disadvantage of the Periotest® is that it does not take the system components into account, so it is unclear how the PTV actually relates to the interface properties. Additionally, the Periotest® analysis uses a filtered acceleration signal which removes significant features in the system response (Swain et al., 2008a; Swain et al., 2008b) (Figure 1.5).

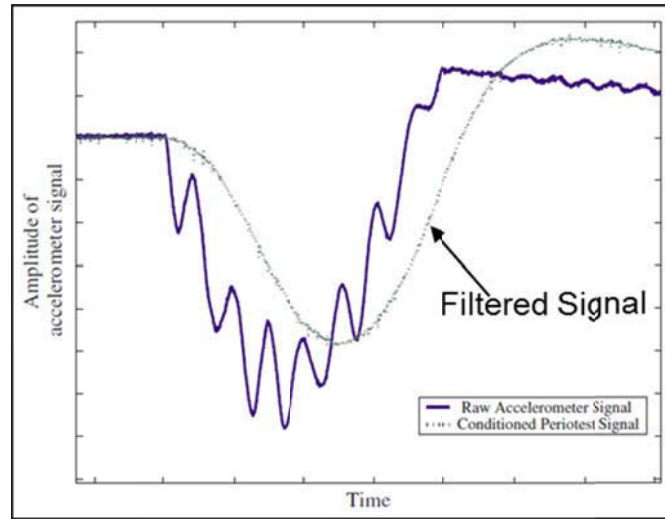


**Figure 1.5: Filtered accelerometer signal used by the Periotest® analysis to calculate the PTV and the raw accelerometer signal extracted from the Periotest® device (adapted from: Swain et al., 2008a; with permission)**

### 1.2.6. Tooth Mobility (Stability) Measurement

Tooth mobility (or the inverse of tooth stability) is an important factor in clinical diagnosis of the integrity of the periodontium (Mühlemann, 1967). Several static measures have been used historically to measure tooth mobility such as the deflection under an applied load (Mühlemann, 1960; Persson and Svensson, 1980). However, these methods require a stable reference frame and good fixation of the measurement device, limiting their clinical use (Castellini et al., 1998; Lukas and Schulte, 1990).

Several dynamic methods have also been proposed to measure tooth mobility. For example the mechanical impedance measuring device (MIMD) uses vibration analysis to measure tooth mobility and estimate the parameters of the periodontal tissue (Nakago et al., 1994; Noyes and Solt, 1973). Additionally, Castellini et al. (1998) proposed a method using a laser Doppler vibrometer to measure the degree of tooth mobility. More recently Yamane et al., (2008) have developed a non-contact vibration device to estimate the stiffness and damping characteristics of the periodontal tissues. This method uses RFA, however a viscoelastic material model of the periodontal tissue is included to allow estimation of the elastic modulus, damping ratio, and coefficient of viscosity from the resonance frequency parameters. This device has been evaluated with *in vitro* studies on simulated tooth models where a cylindrical polyacetal rod (representing the tooth) was embedded in a polyether rubber (representing the PDL) surrounded by plaster

(representing the alveolar bone). This method has also be adapted for dental implants and has been evaluated *in vitro* with a simulated implant model where a cylindrical titanium rod (representing the implant) was embedded in a soft lining material and surrounded by urethane to simulate soft tissue in a bone defect area and the alveolar bone, respectively (Hayashi et al., 2010).

The Periotest® described above is a widely used device for measuring tooth mobility in a clinical setting (Goellner, et al., 2012; Goellner et al., 2013; Jönsson et al., 2007; Tanaka et al., 2005). It uses an impact with the tooth and measures the acceleration response during the time of contact. This contact time is then used to determine the PTV and related to tooth mobility (Lukas and Schulte, 1990) (Table 1.1).

**Table 1.1: Relationship between contact time, Periotest value, and tooth mobility (adapted from Lukas and Schulte, 1990)**

<b>Contact Time (ms)</b>	<b>Periotest Value</b>	<b>Degree of Mobility</b>	
1.21	30	III	Can be moved with labial pressure
0.86	20	II	mobility can be seen
0.65	10	I	mobility can be felt
0.502	4	0	stable anchored
0.426	0		Ankylosis (without periodontium)
0.266	-8		

The limitations of the Periotest® for use with implants have been identified above and similar limitations exist for use with natural teeth. The Periotest® measurement and PTV value calculations are based on a correlation of the signal parameters with clinical tooth mobility as defined by Lukas and Schulte (1990) and are not based on an understanding of the system response under impact loading. Thus it is unclear how the PTV actually relates to the health or stability of the periodontal tissues.

### **1.2.7. Development of an Improved Stability Measurement Based on the Periotest®**

As was described in the sections above, the original Periotest® measure is based on a simple correlation between the contact time and clinical tooth mobility and is not based on an

understanding of the system response or the health of the tissue interface. To better understand the impact response and physical properties at the bone-implant interface, several researchers have coupled the impact technique using the Periotest® handpiece with an analytical model of the implant-abutment system and the surrounding bone at the interface for percutaneous implants.

Giannitsios (2001) developed a two degree of freedom model where the implant-abutment system were considered as a single rigid body and the Periotest® impact rod was modeled as a particle. The bone-implant interface was modeled with horizontal and vertical springs and dampers distributed over the implant length. Giannitsios (2001) used the filtered Periotest® signal showing a single vibration mode in the analysis. The analytical model was reduced to a single degree of freedom system by assuming that the mass of the implant and abutment were negligible compared to the mass of the impact rod. Through *in vitro* testing this work determined that the implant diameter, length of engagement at the bone-implant interface, angulation of the Periotest®, and the striking height along the abutment all affect the output of the Periotest®.

In a follow-up study, Hurst (2002) applied an improved testing protocol to control the testing parameters that had been identified. Additionally, Hurst (2002) was able to extract the unfiltered accelerometer signal from the Periotest® device and used a two degree of freedom model based on the work of Giannitsios (2001). By including the implant and abutment mass, the system was able to return two natural frequencies similar to the measured accelerometer results. The model was compared to a single implant-abutment system using *in vitro* testing, but was met with limited success suggesting that a more complex model was required to adequately represent the experimental system.

Swain et al. (2006; 2008a; 2008b) extended this work and developed a four degree of freedom model considering the implant and abutment as separate rigid bodies. The connections between the impact rod and the abutment and between the implant and abutment were model as linear and torsional springs respectively. Their approach uses the raw acceleration signal and was evaluated for a variety of implant and abutment lengths. The inclusion of the analytical model, allows the measurement to be essentially independent of the details of the implant-abutment system. This approach has been evaluated with *in vitro* experiments for BAHA implants (with a modified

cylindrical abutment) as well as *in vivo* experiments for BAHA patients (Swain, 2006). A similar approach was then extended by Mo (2009) to evaluate dental implants through *in vitro* testing.

While the coupled impact technique and analytical model is a promising method, the previous work has several limitations. The approach relied on the contact time as the only criterion for calculation of the interface stiffness. Further, the raw acceleration measurement extracted from the Periotest® unit suffered from drifting in the reference voltage which directly affected the estimated contact time and did not accurately represent the acceleration response of the system. The previous work also used qualitative matching between the measured accelerometer signal and the analytical model to estimate various parameters and to assess the quality of the model prediction. Additionally, the analytical models are limited in their scope, considering only a BAHA implant with a modified abutment (instead of clinically used abutments) as well as dental implants. To use this technique for BAHA patients, the commercially available abutments must be included in the system. The *in vivo* study by Swain (2006) required removal of the BAHA abutment and attachment of a modified abutment prior to testing, which is not practical for widespread clinical use. Moreover, the previous work included a damping model (proportional damping) that may not adequately represent the physiological system. Finally, these techniques have not been extended beyond the percutaneous implant application; however, the techniques can be applicable to the dental or orthodontic fields by considering natural teeth instead of implant-abutment systems. To use a similar approach in the dental field, an analytical model of a natural tooth must be developed for the system.

### **1.3. Objectives**

The objective of this study is to develop a clinically useful measurement system to noninvasively evaluate the interface stiffness that is applicable across a range of applications and stiffness values including BAHA implants and natural teeth.

The measurement system will be termed the Advanced System for Implant Stability Testing (ASIST) and will consist of three major components. The first is a mechanical handpiece used to obtain experimental accelerometer data from an impact with the superstructure of the system of interest (BAHA abutment, tooth crown, etc.). The second component is an analytical model of

the system of interest. The third component is the correlation between the experimental data and the numerical model to estimate the interface stiffness for the particular application.

The ASIST will be developed through *in vitro* laboratory testing for two commercial BAHA systems: the Oticon Medical Ponto System and the Cochlear Baha® Connect System. A longitudinal clinical study will be conducted in collaboration with the Institute for Reconstructive Sciences in Medicine (iRSM) to evaluate *in vivo* BAHA implant stability during the first year following surgery.

The ASIST technique will be developed for natural teeth and evaluated with *in vivo* clinical data collected over the course of one year for patients undergoing orthodontic treatment.

## 1.4. Thesis Outline

This thesis presents the development and evaluation of a noninvasive measurement system for evaluation of interface stiffness properties for both BAHA implants and natural teeth.

Chapter 1 provides an introduction to the research topic, motivates the clinical significance of the measurement system, and presents a review of relevant literature in the area.

Chapter 2 presents the ASIST for BAHA implant-abutment systems. The hardware and experimental measurement system is presented. The analytical model is developed along with techniques for estimating the interface parameters by matching the analytical model prediction with the measured acceleration response. The results of a parametric sensitivity analysis of the analytical model are presented as well as the details of the numerical analysis and matching procedure.

Chapter 3 presents the *in vitro* experimental development of the ASIST for two commercially available BAHA implant-abutment systems (Oticon Medical Ponto System and Cochlear Baha® Connect System). The experimental methods are presented along with an analysis of the precision and reliability of experimental testing. The ASIST system is compared with the commercially available and widely used Osstell™ ISQ for BAHA implant-abutment systems and the experimental methods of this comparison are presented in this chapter.

Chapter 4 presents the experimental results including the *in vitro* testing for BAHA implant-abutment systems as well as the comparison with the commercially available Osstell™ ISQ system.

Chapter 5 presents the clinical evaluation for BAHA patients with an *in vivo* longitudinal study evaluating implant stability during the first year following surgery.

Chapter 6 presents the development of the ASIST for natural teeth including the analytical model development and numerical analysis procedure. The results of a parametric sensitivity study for the tooth analytical model are presented. An evaluation of the ASIST for natural teeth and results are presented for longitudinal clinical data with orthodontic patients.

Chapter 7 concludes the thesis with a discussion of the major findings as well as limitations and a proposal for future research.

Portions of this thesis have been presented or submitted for publication.

#### **Journal Papers Submitted for Publication:**

1. **L. Westover**, G. Faulkner, W. Hodgetts, D. Raboud. (2016). Advanced System for Implant Stability Testing (ASIST). *Journal of Biomechanics* (Submitted: BM-D-15-01361).
2. **L. Westover**, G. Faulkner, W. Hodgetts, D. Raboud. (2016). Comparison of implant stability measurement devices for bone anchored hearing aid systems. *The Journal of Prosthetic Dentistry* (Submitted: JPD-D-16-00639).

#### **Conference Abstracts Submitted and/or Presented:**

1. **L. Westover**, R. Butz, K. Duke\*, G. Faulkner, W. Hodgetts, D. Raboud. (2016). Noninvasive Evaluation of Periodontal Ligament Stiffness. *22<sup>nd</sup> Congress of the European Society of Biomechanics*, Cité des Congrès de Lyon, France, July 10 – 13, 2016 (Podium).

2. **L. Westover\***, W. Hodgetts, G. Faulkner, D. Raboud. (2015). Advanced System for Implant Stability Testing (ASIST). *OSSEO 2015 5<sup>th</sup> International Congress on Bone Conduction Hearing and Related Technologies*, Fairmont Chateau Lake Louise, Canada, May 20 – 23, 2015 (Podium).
3. G. Faulkner\*, **L. Westover**, B. Hodgetts, D. Raboud. (2015). Comparison of ASIST and Osstell ISQ for Bone-Anchored Hearing Aid Implant Stability. *OSSEO 2015 5<sup>th</sup> International Congress on Bone Conduction Hearing and Related Technologies*, Fairmont Chateau Lake Louise, Canada, May 20 – 23, 2015 (Podium).
4. D. Raboud, M. Athale\*, **L. Westover**, B. Hodgetts, G. Faulkner. (2015). Use of Advanced System for Implant Stability Testing (ASIST) for Assessment of Bone-Anchored Hearing Aid Abutment Screw Loosening. *OSSEO 2015 5<sup>th</sup> International Congress on Bone Conduction Hearing and Related Technologies*, Fairmont Chateau Lake Louise, Canada, May 20 – 23, 2015 (Poster).
5. F. Kamal\*, E. Lou, G. Faulkner, **L. Westover**. (2015). ASIST – A Bluetooth Real-Time Implant/Bone Interface Stability Measurement Device. *OSSEO 2015 5<sup>th</sup> International Congress on Bone Conduction Hearing and Related Technologies*, Fairmont Chateau Lake Louise, Canada, May 20 – 23, 2015 (Poster).
6. **L. Westover\***, D. Raboud, G. Faulkner. (2014). Quantitative assessment of stability of dental implants and natural teeth. *18<sup>th</sup> World Congress on Dental Traumatology*, Istanbul, Turkey, June 19 – 21, 2014 (Poster).
7. **L. Westover\***, D. Raboud, G. Faulkner, W. Hodgetts. (2013). Evaluation of the integrity of implants used for bone conduction hearing. *Spotlight on Research Breakfast & Symposium*, Northlands Expo Centre, Edmonton AB, Canada, October 23, 2013 (Poster).
8. **L. Westover\***, D. Raboud, G. Faulkner, B. Hodgetts. (2013). Non-invasive Assessment of Bone-Anchored Hearing Aid Implant Stability Independent of Structural Components. *OSSEO 2013 4<sup>th</sup> International Symposium on Bone Conduction Hearing – Craniofacial Osseo-integration*, The Sage Gateshead, Newcastle upon Tyne, England, June 6 – 8, 2013 (Podium).

# **Chapter 2: ASIST for Bone Anchored Hearing Aids**

In this chapter, we build on the ideas of the coupled impact technique and analytical model and develop a new Advanced System for Implant Stability Testing (ASIST) which provides a non-invasive, quantitative measure of implant stability that is independent of the system components. This chapter presents the development of the analytical model and a parametric sensitivity analysis. The goals of this chapter are to describe the ASIST for BAHA implant systems including the hardware and measurement system, the analytical model, and the analysis procedures for estimating the interface properties. A parametric sensitivity analysis of the analytical model is presented to understand the behaviour of the model and the sensitivity to various parameters and assumptions. Finally, the details and assumptions of the numerical analyses are investigated and their effects on the ASIST solution are briefly discussed.

## **2.1. Hardware and Measurement**

The previous work described in Section 1.2.7. has shown that the impact technique using the Periotest® handpiece has many practical advantages (Giannitsios, 2001; Hurst, 2002; Mo, 2009; Swain, 2006; Swain et al., 2008a; Swain et al., 2008b). This method provides versatility in the stability measurement system as it can be used with any implant-abutment system as well as with other anatomical systems such as natural teeth as it does not require attachment to the system components. Additionally, the acceleration response provided by the handpiece gives an appropriate level of detail to estimate interface stiffness parameters of the system (Mo, 2009; Swain, 2006; Swain et al., 2008a; Swain et al., 2008b). Because of these advantages, the ASIST continues to use the handpiece of the Periotest® with some modifications to improve the data collection procedure, making it more suitable for regular clinical use. In particular, the electronics to drive the impact rod and collect the acceleration data are redesigned to eliminate the drift in the reference voltage (as discussed below), providing a more accurate representation of the actual acceleration response. The data collection procedure is made wireless using Bluetooth to transfer the acceleration signal to a computer, which greatly improves the clinical utility of the system compared to the wired data acquisition of previous approaches. Finally, the

initial data processing to align the acceleration response of the 16 strikes is made automatic within the data collection software and the resulting acceleration signal is displayed on the computer screen for real-time qualitative evaluation of the response.

The final design of the ASIST consists of a handpiece, the ASIST unit, a USB dongle, and a computer (Figure 2.1). The handpiece is extracted from the Periotest® Classic (Medizintechnik Gulden, Modautal, Germany) and contains the impact rod and accelerometer. The impact rod is a long, cylindrical rod with a diameter of approximately 2 mm. The accelerometer is attached to the non-impacting end of the rod and records the acceleration of the impact rod. The ASIST unit contains the circuitry to initiate the impact, record the accelerometer data, and wirelessly transmit the strike data via Bluetooth to the USB dongle in the computer (Kamal et al., 2015). When the button on the handpiece is pushed, the impact rod is propelled forward. Before the impact rod leaves the end of the handpiece, the propulsion is switched off so that the rod leaves the handpiece at a constant velocity. Similar to the Periotest®, an impact event with the ASIST consists of 16 strikes in 4 seconds, although these parameters are now adjustable. The voltage from the accelerometer is recorded with a sample rate of 294 kHz ( $\Delta t = 3.4 \mu s$ ). The acceleration response is transferred from the ASIST unit to the computer via Bluetooth. The present design uses a USB dongle inserted into the computer to accept the data transfer; however, the dongle can be eliminated if the computer has built-in Bluetooth capabilities.

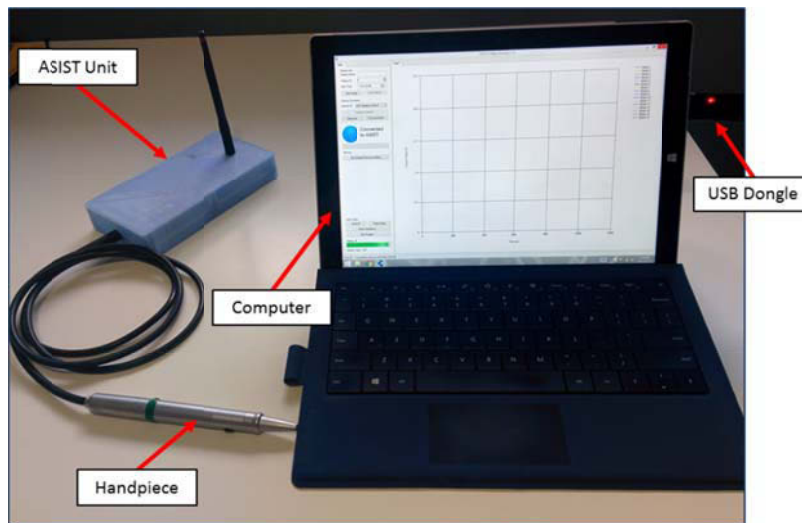


Figure 2.1: ASIST components including the ASIST unit, the handpiece, a USB dongle, and a computer

The previous work by Swain et al. (2006; 2008a; 2008b) extracted the raw accelerometer signal directly from a Periotest® unit. It was found that the acceleration signal at the end of a strike overshoots the zero crossing which was subsequently found to be due to a shift in the reference voltage (Figure 2.2 A). This affected the measurement of the contact time and as a result, directly affected the assessment of the interface stiffness. It should be noted that a positive acceleration for the impact rod is not physically realistic. The custom electronics developed for the ASIST were designed to overcome this problem as shown in Figure 2.2 B.

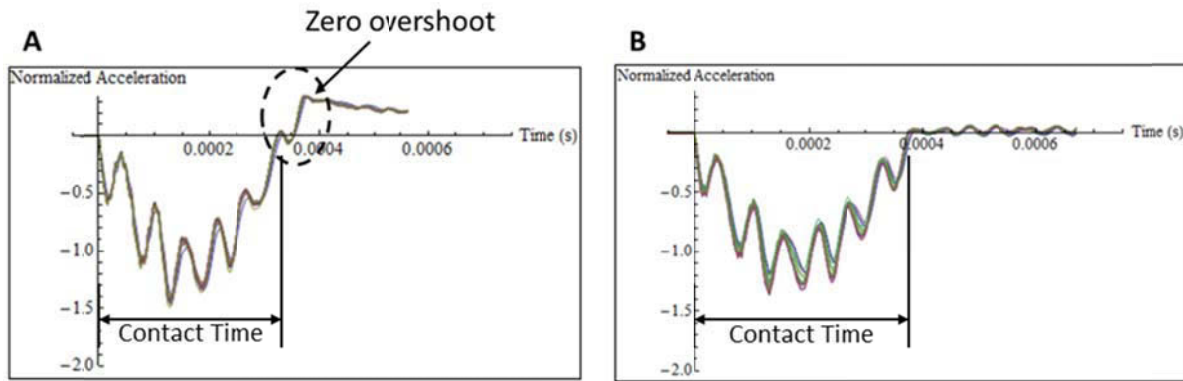


Figure 2.2: Acceleration signal for a BAHA implant-abutment system. A: The system used by Swain et al. (2008) showing the zero overshoot in the acceleration measurement. B: The ASIST system measurement.

The data collection with the ASIST device uses custom software installed on a computer to control the radiofrequency (RF) connection between the ASIST unit and the computer (via the USB dongle). The software displays the acceleration response of the 16 strikes for visual appraisal of the signal during data collection and allows for automatic saving of the raw accelerometer data with convenient file naming including options for patient names and ID numbers.

## 2.2. Analytical Model

The BAHA implant system (Figure 2.3) is modeled as a four degree of freedom (4-DOF) system composed of two rigid bodies (the implant with mass  $m_I$  and moment of inertia  $J_I$ , and the abutment with mass  $m_A$  and moment of inertia  $J_A$ ). The impact rod is modeled as a particle with a mass of 9.4 g (Swain, 2006).

The internal stiffness parameters in the model are a linear spring at the impact site between the impact rod and the abutment ( $K_I$ ) and a linear torsional spring between the implant and the abutment ( $K_T$ ). The bone-implant interface is modeled as a distributed stiffness  $k$  per unit area surrounding the implant. The coordinates used to describe the system are the horizontal displacement of the impact rod ( $x_1$ ), the horizontal displacement of the center of the abutment at the height of impact ( $x_2$ ), the rotation of the abutment ( $\theta_1$ ), and the rotation of the implant ( $\theta_2$ ). With these coordinates,  $\ddot{x}_1$  represents the acceleration of the impact rod which is experimentally measured by the accelerometer.

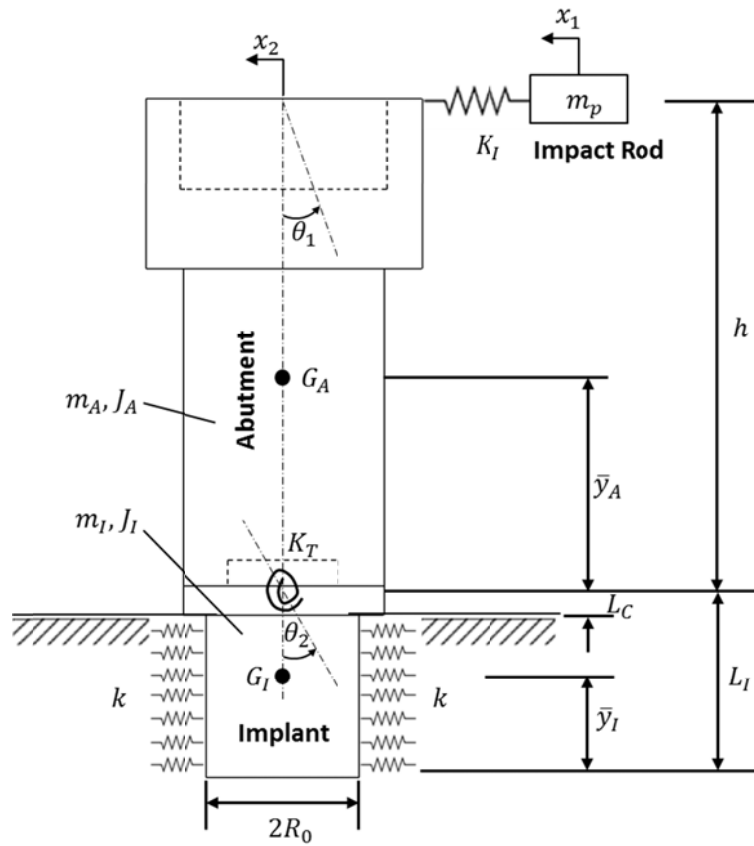


Figure 2.3: Schematic of the 4-DOF model of the BAHA implant/abutment system

The equations of motion for free vibration of the 4-DOF system are given by:

$$[M]\{\ddot{x}\} + [C]\{\dot{x}\} + [K]\{x\} = \{0\}$$

where  $\{x\} = \begin{Bmatrix} x_1 \\ x_2 \\ \theta_1 \\ \theta_2 \end{Bmatrix}$  as illustrated in Figure 2.3.

The impact event is modeled as a free vibration problem during the time of the strike (when the impact rod is in contact with the abutment). The initial conditions for the problem are zero displacement for all coordinates, an initial velocity of the impact rod ( $\dot{x}_1(0) = v_0$ ), and zero velocity for all other coordinates.

The details of the mass  $[M]$ , stiffness  $[K]$ , and damping  $[C]$  matrices can be obtained for this system using the method of influence coefficients (Den Hartog, 1985). The details of these derivations are shown in Appendix A.

The matrix  $[M]$  is given by:

$$[M] = \begin{bmatrix} m_p & 0 & 0 & 0 \\ 0 & m_I + m_A & m_A \bar{y}_A - (m_I + m_A)h & -m_I(L_I - \bar{y}_I) \\ 0 & m_A \bar{y}_A - (m_I + m_A)h & J_A + m_A(h - \bar{y}_A)^2 + m_I h^2 & m_I h(L_I - \bar{y}_I) \\ 0 & -m_I(L_I - \bar{y}_I) & m_I h(L_I - \bar{y}_I) & J_I + m_I(L_I - \bar{y}_I)^2 \end{bmatrix}$$

where:

$L_I$  = length of the implant

$\bar{y}_A$  = distance from the bottom of the abutment to the center of mass

$\bar{y}_I$  = distance from the bottom of the implant to the center of mass

$h$  = distance from the bottom of the abutment to the striking location

The stiffness matrix  $[K]$  is:

$$[K] = \begin{bmatrix} K_I & -K_I & 0 & 0 \\ -K_I & K_I + 4kR_0(L_I - L_C) & -4kR_0(L_I - L_C)h & -2kR_0(L_I^2 - L_C^2) \\ 0 & -4kR_0(L_I - L_C)h & K_T + 4kR_0(L_I - L_C)h^2 & -K_T + 2kR_0(L_I^2 - L_C^2)h \\ 0 & -2kR_0(L_I^2 - L_C^2) & -K_T + 2kR_0(L_I^2 - L_C^2)h & K_T + \frac{4}{3}kR_0(L_I^3 - L_C^3) \end{bmatrix}$$

where  $L_C$  is the portion of the implant that extends above the bone surface i.e. the distributed stiffness at the bone-implant interface  $k$  only acts along the length  $l_i = L_I - L_C$  and  $R_0$  is the radius of the implant.

As with any real system, it is expected that some damping will occur which should be taken into account in the analytical model. One of the major changes to the analytical model compared to the work of Swain et al. (2008a) is the damping assumption that is used. In the present model, we use a general viscous damping model, while Swain et al. used a proportional damping model. In the BAHA implant-abutment system, proportional damping is not believed to be representative of the physiological conditions where higher damping is expected to occur at the bone-implant interface with relatively minimal damping in the rest of the system. As a result, our model assumes that damping is distributed along the bone-implant interface (similar to the interface stiffness) and is negligible elsewhere. In particular (unlike with proportional damping) there is no damping at the spring locations  $K_I$  and  $K_T$ . Moving away from proportional damping to general viscous damping means that a numerical procedure must be used to solve the equations of motion rather than using the analytical approach of modal analysis.

The damping matrix  $[C]$  is given by:

$$[C] = \begin{bmatrix} 0 & 0 & 0 & 0 \\ 0 & 4cR_0(L_I - L_C) & -4cR_0(L_I - L_C)h & -2cR_0(L_I^2 - L_C^2) \\ 0 & -4cR_0(L_I - L_C)h & 4cR_0(L_I - L_C)h^2 & 2cR_0(L_I^2 - L_C^2)h \\ 0 & -2cR_0(L_I^2 - L_C^2) & 2cR_0(L_I^2 - L_C^2)h & \frac{4}{3}cR_0(L_I^3 - L_C^3) \end{bmatrix}$$

where  $c$  is the viscous damping coefficient per unit area surrounding the implant.

## 2.3. Estimating the Interface Properties

A custom Mathematica program (Wolfram Mathematica 10, Champaign, IL, USA) was developed to process the data collected from the ASIST device.

### 2.3.1. Measured Acceleration Signals – Curve Fit Approximation

From the measured accelerometer signals, two dominant frequencies are readily visible (Figure 2.2 B). The time of one strike represents approximately half of one cycle at the first natural frequency.

To correlate the measured signal with the acceleration response of the analytical model, it is necessary to extract relevant information (such as the amplitude and damping content) from the measured signal. This can be done by fitting a curve to the measured data using a least squares minimization procedure. This procedure allows the damping in the measured signal to be estimated and provides a measure of the amplitude of the signal which can be used to normalize the acceleration response as described in Section 2.3.2.

Since the measured accelerometer signals show two prominent modes of vibration, the curve fit model is based on a simplified 2-DOF vibration response:

$$x_1(t) = Ae^{-\zeta_1 p_1 t} \sin(\omega_{d1} t + \phi_1) + Be^{-\zeta_2 p_2 t} \sin(\omega_{d2} t + \phi_2)$$

where  $p_n$  are the natural frequencies of the system and  $\omega_{dn} = \sqrt{1 - \zeta_n^2} p_n$  are the damped natural frequencies.

The form of the acceleration of the impact rod ( $\ddot{x}_1$ ) can then be found by differentiating the displacement response above. An estimate for the unknown parameters in the 2-DOF response ( $A, B, \zeta_1, \zeta_2, p_1, p_2, \phi_1, \phi_2$ ) can be found by determining the value of these parameters that minimizes the difference between the measured accelerometer data and the model equation in a least squares sense. Since only half of a cycle of the first natural frequency is present in the data, the estimate for the first mode damping ratio cannot be accurately determined and is thus not included in the curve fit model ( $\zeta_1 = 0$ ). Additionally, for the curve fit equation to accurately

model the experimental system, the initial condition  $\ddot{x}_1(0) = 0$  should be enforced. To do this, a constraint is placed on the amplitude of the second mode. The parameter  $B$  is not independently varied, but is expressed as a function of the other variables such that  $\ddot{x}_1(0) = 0$ . This curve fit procedure provides a single approximate analytical description of the measured accelerometer data. An example of the measured accelerometer data and the resulting curve fit model are shown in Figure 2.4.

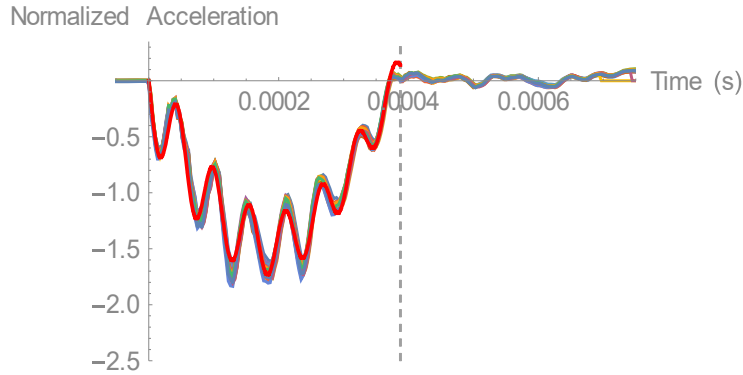


**Figure 2.4: Measured accelerometer data (colored) with the curve fit model (red). Vertical dashed line defines the end of the strike.**

### 2.3.2. Extracting Information from the Curve Fit

The curve fit provides an analytical description of the experimental data which will ultimately be used to determine the best stiffness parameters to match the model predicted acceleration with the experimentally measured data. To ensure proper matching between the measured data and the modeled signal, the modeled acceleration response must be normalized (Swain et al., 2008a). This is because the model simulation has units of acceleration ( $\text{m/s}^2$ ) while the experimental accelerometer data is measured in volts (V).

If we assume that the voltage measured from the accelerometer is linearly proportional to the acceleration of the impact rod, then we can determine the proportionality constant  $V_{amp}$  from the curve fit parameters.

$$\ddot{u}(t) = V_{amp}\ddot{x}(t)$$

where  $\ddot{x}(t)$  is the acceleration of the impact rod ( $\text{m/s}^2$ ) and  $\ddot{u}(t)$  is the normalized acceleration from the accelerometer.  $V_{amp}$  must be determined such that the amplitude of the first mode frequency of the model signal matches that of the measured data. The first mode displacement response of the measured data as represented by the curve fit is simply:

$$x(t) = A \sin(p_1 t + \phi_1)$$

where the parameter  $A$  is determined from the curve fit procedure above.

Now, from the above equations:

$$u(t) = V_{amp} \left[ \frac{\dot{u}(0)}{p_1} \sin(p_1 t + \phi_1) \right]$$

where  $\dot{u}(0)$  is the initial velocity of the impact rod ( $\dot{u}(0) = 0.2 \text{ m/s}$ ) (Swain et al., 2008a).

The amplitude of  $x(t)$  is chosen to match the amplitude of  $u(t)$ . Thus,

$$A = V_{amp} \frac{\dot{u}(0)}{p_1} \quad \Rightarrow \quad V_{amp} = A \frac{p_1}{\dot{u}(0)}$$

where  $\dot{u}(0)$  is known to be 0.2 m/s as indicated above,  $A$  is the amplitude of the first mode and  $p_1$  is the first mode frequency, both taken from the curve fit parameters.

The damping values used in the analytical model can also be determined from the curve fit parameters. In the case of general viscous damping, it is necessary to find the viscous damping coefficient at the bone-implant interface ( $c$ ). This parameter can be estimated based on the curve fit and the mass parameters of the particular system.

For a single degree of freedom system with a single mass, spring, and viscous damper, the damping ratio of the system is given by (Den Hartog, 1985):

$$\zeta = \frac{c}{2\sqrt{mk}} \quad \text{or} \quad c = (2\sqrt{m})\zeta\sqrt{k}$$

So that the damping coefficient is proportional to the damping ratio and the square root of the stiffness (where in the case of a single DOF system the proportionality constant would be  $2\sqrt{m}$ ).

Using an analogous relationship to the 4-DOF system of the BAHA implant-abutment system with damping only at the interface, we assume:

$$c = \gamma \zeta_2 \sqrt{k}$$

where:  $c$  is the damping coefficient at the bone-implant interface per unit area (Ns/m<sup>3</sup>)

$k$  is the stiffness at the bone-implant interface per unit area (N/m<sup>3</sup>)

$\zeta_2$  is the second mode damping ratio determined from the curve fit for a particular set of data

$\gamma$  is the constant of proportionality which must be determined for each implant-abutment system because we can assume that it is related to the mass and other stiffness properties of the system (kg<sup>1/2</sup>)

The value of  $\gamma$  for each implant-abutment combination was determined using the following procedure and the results were included in the Mathematica program for the ASIST model.

For one implant-abutment system (e.g. narrow diameter 4 mm implant with 9 mm abutment) a test grid was defined covering a range of  $k$ -values and a range of  $c$ -values. For each combination of  $k$  and  $c$ , the acceleration response was calculated from the analytical model and a curve was fit to the resulting signal following the curve fit procedure defined previously. The output of interest from the curve fit procedure was the second mode damping ratio  $\zeta_2$ . This produced a set of data where for every  $k$  and  $c$  within the test grid,  $\zeta_2$  predicted from the curve fit is known. The Mathematica function `NonlinearModelFit[]` was used to determine the value of the parameter  $\gamma$  to match the model ( $c = \gamma \zeta_2 \sqrt{k}$ ) with the data. An example of the grid data and the resulting model are shown in Figure 2.5 below, where  $\gamma$  was found to be 181 kg<sup>1/2</sup>.

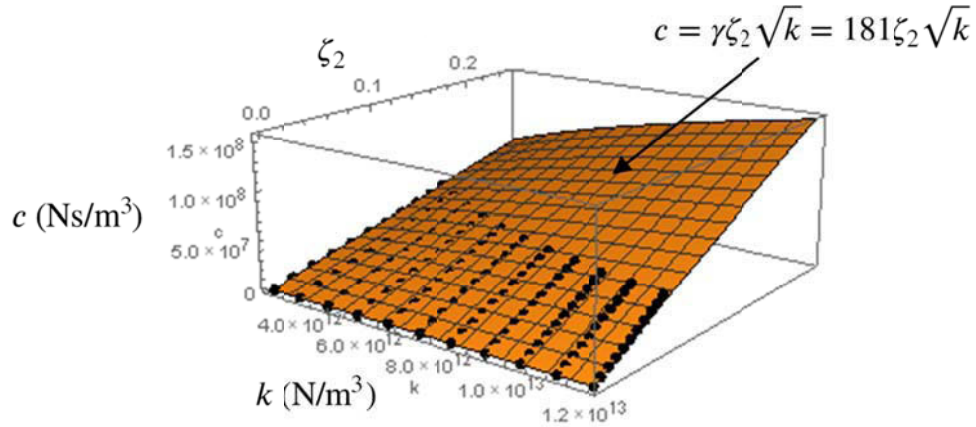


Figure 2.5: Damping coefficient relationship for standard (narrow) diameter 4 mm Oticon implant with a 9 mm abutment

The same procedure was repeated for each of the implant-abutment combinations. The resulting  $\gamma$  values for the Oticon implant system are shown in Table 2.1. (Note that the details of the Oticon implant system are shown later in Section 3.1). As a result, once  $\zeta_2$  is determined from the curve fit, an appropriate  $c$  to use in the 4-DOF analytical model can be determined.

Table 2.1: Damping proportionality constant ( $\gamma$ ) for Oticon implant-abutment system ( $\text{kg}^{1/2}$ )

Implant	6 mm	9 mm	12 mm
M50106	72	173	347
M50128	79	181	352
M51061	107	240	426
M51062	120	252	457

### 2.3.3. Matching the Analytical Model to the Measured Acceleration

The analytical model consists of three stiffness parameters: the interface stiffness per unit area distributed over the integrated portion of the implant ( $k$ ), the torsional stiffness at the connection between the implant and abutment ( $K_T$ ), and the stiffness at the impact site ( $K_I$ ).  $K_T$  and  $K_I$  are determined for the system as described in Section 3.3.2. The interface stiffness is, in general, unknown and is determined as an output of the experimental/numerical procedure by matching the model predicted acceleration with the measured acceleration during an impact.

A numerical procedure was implemented in Mathematica to match the curve fit model from the measured data to the analytical model of the implant-abutment system. The Mathematica function `FindMinimum[]` is used to determine a local minimum for a given objective function. The procedure minimizes the objective function by varying one (or multiple) variables with a specified initial guess for the solution.

The objective function used is the Euclidean norm between the model predicted acceleration and the curve fit approximation of the measured acceleration signal. Both the model predicted acceleration and the curve fit approximation are sampled over the range of the strike at a time-step based on the sampling frequency of the originally recorded data ( $\Delta t = 3.4 \mu\text{s}$ ). The objective function is:

$$\epsilon = \sqrt{\sum_i (f_i - f_{c_i})^2}$$

where:  $f_i$  is the model predicted acceleration of the impact rod (normalized) at the  $i^{\text{th}}$  time point

$f_{c_i}$  is the curve fit approximation of the measured acceleration signal at the  $i^{\text{th}}$  time point

$\epsilon$  is a measure of the distance between the two functions over the entire strike

The algorithm uses the Principal Axis method which is a derivative-free method of multivariable minimization (Wolfram Language & System Documentation Center). Figure 2.6 shows an example of the measured acceleration signal and the resulting matched acceleration response from the analytical model.

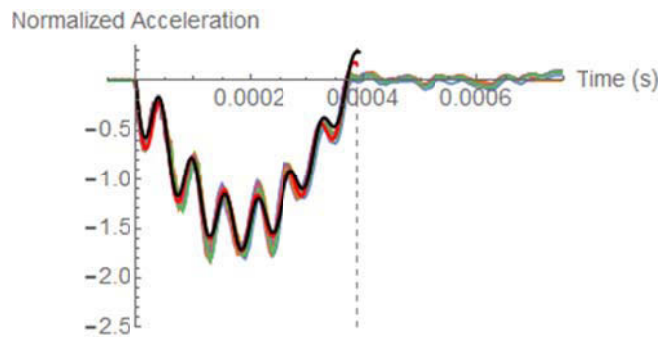


**Figure 2.6: Matched acceleration signal between the model (black) and measured data (colored) with the curve fit (red)**

The developed model allows the matching to be done using multivariable minimization. For example, the combination of  $K_I$  and  $k$  in the analytical model that would result in the best match with the given measured acceleration signal can be determined. This multivariable minimization can be used to determine appropriate values for the model parameters (i.e.  $K_I$  and  $K_T$ ) that are applicable across the range of cases for each BAHA system. Once these appropriate values are determined, they can be fixed in the model leaving the interface stiffness as the only unknown. The interface stiffness from a measurement is then estimated using single-variable minimization to match the analytical model to the given dataset.

### 2.3.4. Outcome Measure

The primary outcome measure is the ASIST Stability Coefficient (ASC) which is a non-dimensional value that is directly related to an effective interface stiffness (over the entire implant area) and normalized to a nominal stiffness at the impact site ( $K_I$ ). The effective stiffness  $K_{eff}$  at the bone-implant interface is given by:

$$K_{eff} = 4kR_0l_i$$

where  $l_i = L_I - L_c$  is the length of the threaded portion of the implant and the interface stiffness per unit area ( $k$ ) is assumed to be constant with a linear relationship between the force and displacement.  $K_{eff}$  represents an effective stiffness of the bone-implant connection with units of N/m. The derivation for the effective stiffness expression is shown in Appendix A. The ASC value relates this effective interface stiffness to a nominal stiffness at the impact site, providing a non-dimensional stiffness ratio:

$$ASC = \frac{K_{eff}}{K_I} = \frac{4kR_0l_i}{K_I} \quad \text{with } K_I = 4 \times 10^6 \text{ N/m}$$

## 2.4. Parametric Sensitivity of Analytical Model

This section presents the results of a theoretical analysis of the analytical model. The details for this analysis are shown in Appendix B. First, the analytical model is examined through modal analysis to provide an understanding of the behavior of the model. Subsequently, an evaluation

of the sensitivity of the model to various stiffness and geometric parameters is presented. Finally, a comparison between two different damping assumptions is presented (proportional damping and general viscous damping).

### 2.4.1. Modal Analysis

The undamped natural frequencies  $p_n$  and mode shapes  $\{\phi\}_n$  of the system can be determined by solving the eigenvalue problem with the matrices  $[K]$  and  $[M]$ . The natural frequencies are given by the square roots of the eigenvalues, and the mode shapes are the corresponding eigenvectors. Figure 2.7 shows a visual representation for an example of the mode shapes for a long/narrow Oticon implant (M50128) and 9 mm abutment. The grey dashed lines represent the initial position of the system, while the solid black lines represent the normalized mode shape. The solid dots represent the location of the center of mass of the impact rod, the center line of the abutment at the height of the strike, the implant-abutment connection, and the bottom of the implant. The natural frequencies of each mode are indicated on the figure.

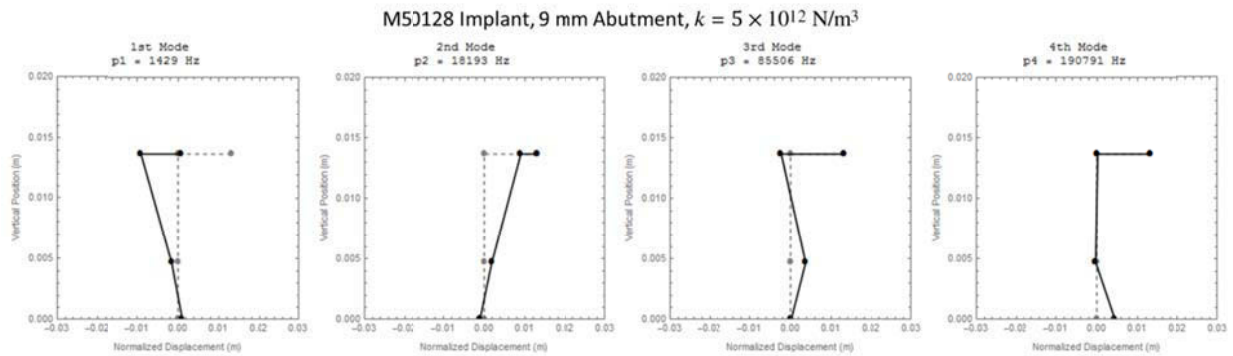


Figure 2.7: Mode shapes for long/narrow implant (M50128) with 9 mm abutment

### 2.4.2. Analytical Model Frequency Response versus Stiffness Parameters

The important stiffness parameters in the analytical model are the impact stiffness ( $K_I$ ) and the torsional stiffness ( $K_T$ ) while the primary variables of interest are the interface stiffness ( $k$ ) and the related ASC value. Using the analytical model, the relationship between the stiffness parameters and the first and second mode frequency components is examined following a similar procedure to the work of Swain (2006). The first and second mode frequencies are readily visible

in the measured acceleration response, while the higher (third and fourth) modes are not visible. Thus the analysis here will only focus on the visible first and second modes as these are the modes that can affect the fit between the model prediction of the acceleration and the measured acceleration response. The frequencies are determined from modal analysis (from the mass and stiffness matrices) without damping considered. This analysis can provide an understanding of the effect of the internal stiffness parameters on the theoretical acceleration response, which will aid in interpreting the measured acceleration signals. Additionally, this analysis will provide an understanding of the sensitivity of the ASIST measure to errors in the estimated parameters such as  $K_I$  and  $K_T$ . Exemplary results are shown here with a full analysis presented in Appendix B.

The relationship between the first mode frequency  $p_1$  and the second mode frequency  $p_2$  and the interface stiffness  $k$  can be seen in Figure 2.8 for an example Oticon Medical implant (long/narrow – M50128) with each abutment length (6 mm, 9 mm, 12 mm, 14 mm). It can be seen that the first mode frequency varies sharply with changing interface stiffness for the low stiffness values and starts to plateau for larger stiffness values.

As expected, the interface stiffness is sensitive to changes in the first mode frequency. In the higher stiffness range, where the curves become flatter, small errors in the frequency measurement can result in large changes in the calculated interface stiffness. These errors should not be clinically important because implants in the high stiffness range would be considered stable. In the lower frequency range, smaller changes in stiffness would result in considerable changes in the first mode frequency and would thus be detected by the ASIST measurement.

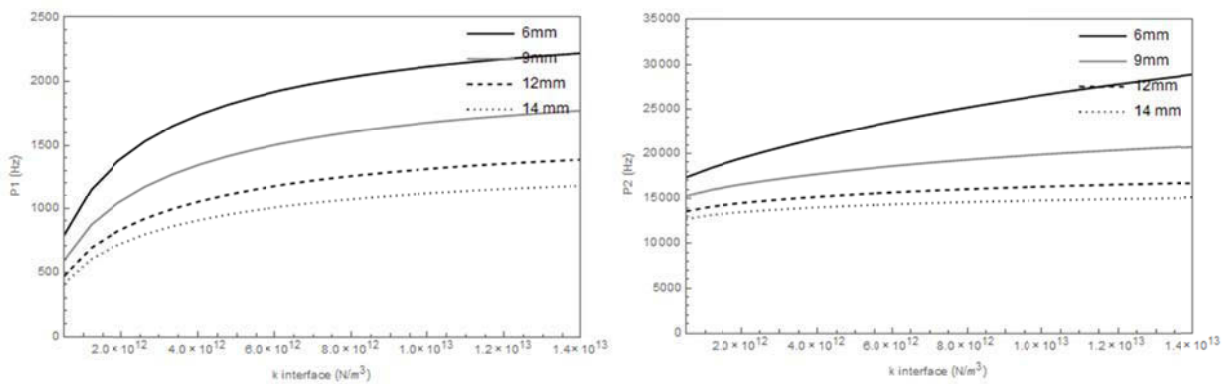


**Figure 2.8: Relationship between the  $p_1$  (left) and  $p_2$  (right) and the interface stiffness per unit area  $k$  for the long/narrow Oticon Medical implant (M50128). The different curves on each plot show the relationship for each abutment length.**

The same relationships are presented in Figure 2.9 using the ASC measure. Consider an implant in the lower stiffness range (ASC of 23 corresponding to an interface stiffness of  $3.07 \times 10^{12}$  N/m<sup>3</sup>). A unit change in ASC from 23 to 24 results in an increase in first mode frequency of 17 Hz (from 1234 – 1251 Hz) or an increase of 1.4%. A doubling of ASC from 15 to 30 results in an increase in first mode frequency of 340 Hz (24% increase). In the high stiffness range (ASC of 75 corresponding to an interface stiffness of  $10 \times 10^{12}$  N/m<sup>3</sup>), a unit change in ASC from 75 to 76 results in an increase in first mode frequency of 4 Hz (0.2% increase).

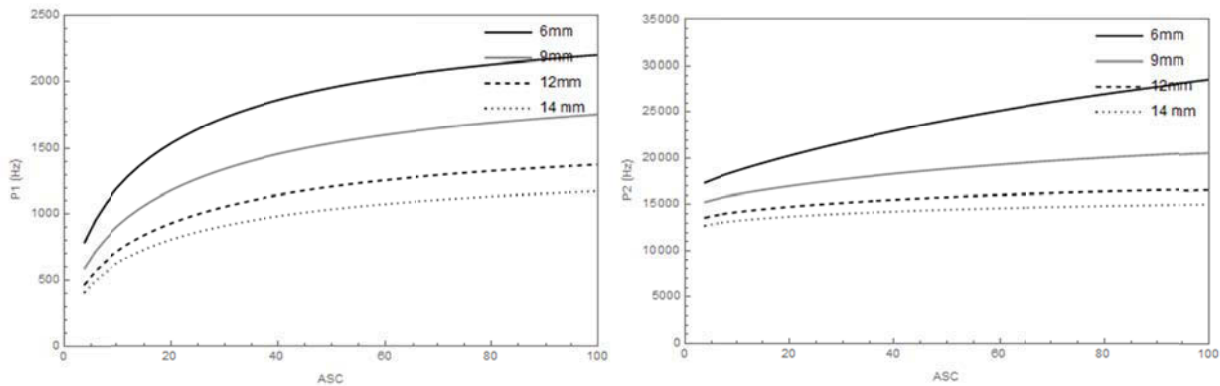


**Figure 2.9: Relationship between  $p_1$  (left) and  $p_2$  (right) and the ASC value for a long/narrow Oticon Medical implant (M50128). The different curves on each plot show the relationship for each abutment length.**

The relationship between the frequency components and the impact stiffness  $K_I$  is shown in Figure 2.10 for the different Oticon Medical implant types and abutment sizes. The first mode frequency is relatively insensitive to changes in the impact stiffness, particularly for the longer abutments. For example, consider a long/narrow implant (M50128) with a 6 mm abutment. A unit change in impact stiffness from  $K_I = 2.9 \times 10^6$  N/m to  $3.9 \times 10^6$  N/m results in an increase in first mode frequency of 110 Hz (from 1835 – 1945 Hz) or a 6% increase. The same change in impact stiffness for a 14 mm abutment results in an increase in first mode frequency of only 15 Hz (from 967 – 982 Hz) or a 1.5% increase. The second mode frequency is more sensitive to changes in the impact stiffness and varies with an approximately linear relationship that is similar across abutment sizes. For the same changes in  $K_I$ , the second mode frequency showed an increase of 2112 Hz (9%) for the 6 mm abutment and 1970 Hz (14%) for the 14 mm abutment.

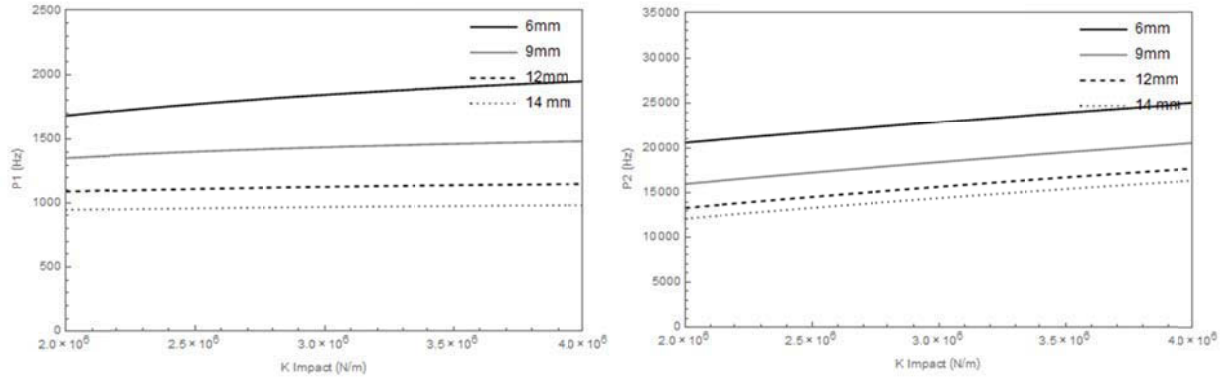


**Figure 2.10: Relationship between  $p_1$  (left) and  $p_2$  (right) and the impact stiffness  $K_I$  for a long/narrow Oticon Medical implant (M50128). The different curves on each plot show the relationship for each abutment length.**

The relationship between the frequency components and the torsional connection stiffness  $K_T$  is shown in Figure 2.11 for the different Oticon Medical implant types and abutment sizes. The first mode frequency is sensitive to changes in the torsional stiffness parameter only in the low stiffness range. Beyond a threshold, both the first and second modes are virtually insensitive to changes in  $K_T$ . In such as situation, the implant-abutment is essentially responding as a rigid body. The sensitivity in the lower  $K_T$  range, suggests that the ASIST measure may be able to detect changes in the implant-abutment connection such as loosening of the abutment screw.

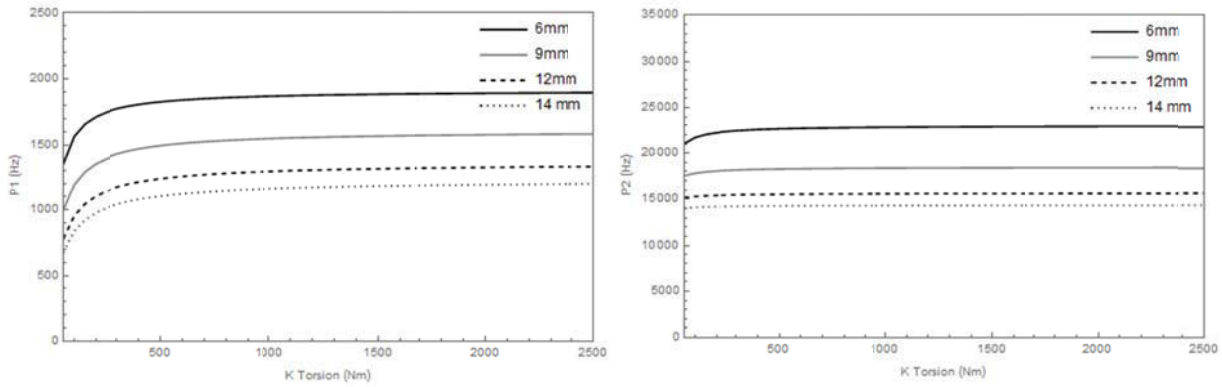


**Figure 2.11: Relationship  $p_1$  (left) and  $p_2$  (right) and the torsional stiffness  $K_T$  for a long/narrow Oticon Medical implant (M50128). The different curves on each plot show the relationship for each abutment length.**

### 2.4.3. Model Solution (ASC and Fit with Measured Data) with Stiffness Parameters $K_I$ and $K_T$

In the analytical model, we have made assumptions for the internal stiffness parameters, namely the impact stiffness ( $K_I$ ) and the torsional stiffness ( $K_T$ ). The sensitivity of the model solution to errors in these parameters was evaluated and the details are shown in Appendix B. As  $K_I$  or  $K_T$  were varied, the calculated interface stiffness and associated ASC value were determined along with the resulting  $R^2$  fit between the model predicted signal and the measured acceleration. For each analysis, a sample dataset was used in order to calculate the ASC and  $R^2$  values.

It was found that variations in the impact stiffness affect the second mode frequency of the model response, which can result in a poor fit between the measured data and model signal. For example, consider a long/narrow implant (M50128) with a 9 mm abutment. The variation in ASC and  $R^2$  with changing impact stiffness  $K_I$  are shown in Figure 2.12. The two plots are overlaid with the scale for the ASC value (blue line) on the left of the figure and the scale for the  $R^2$  value (black line) on the right of the figure.

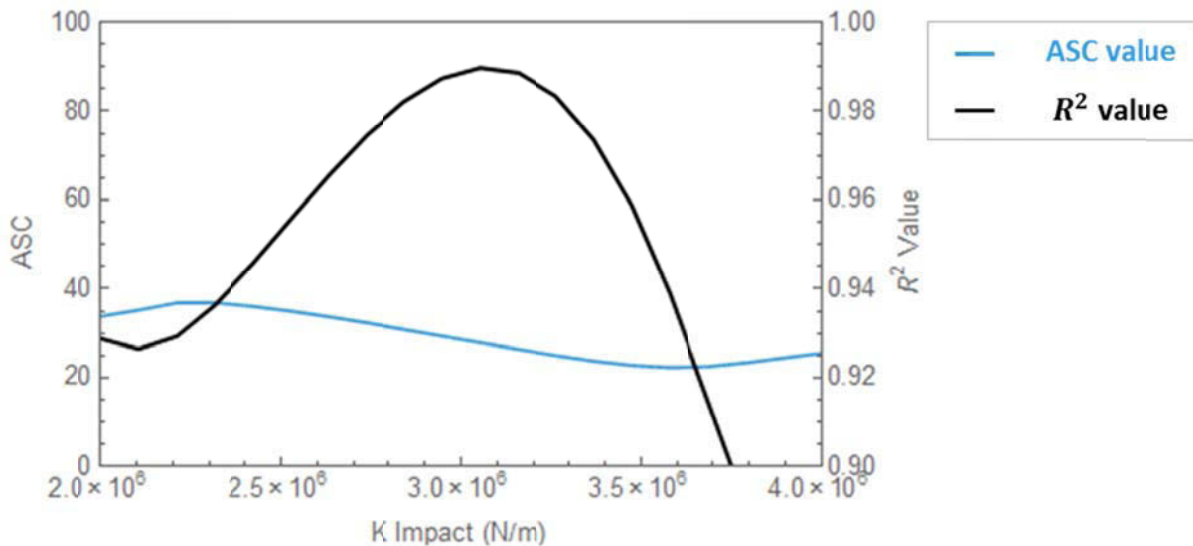


Figure 2.12: Variation in ASC value (blue line) and  $R^2$  fit (black line) with changes in impact stiffness ( $K_I$ ) for a long/narrow implant and 9 mm abutment

As shown in the figure, there is some variation in the ASC value over the range of tested  $K_I$  and a clear peak in the fit between the measured signal and the model prediction as measured by the  $R^2$  value. A unit change in  $K_I$  from  $3 \times 10^6$  N/m to  $4 \times 10^6$  N/m results in a decrease in ASC of 3.1 (11%) and a change in  $R^2$  value from 0.99 to 0.86 (13%) for this example.

For the same sample dataset of a long/narrow implant (M50128) with a 9 mm abutment, the variation in ASC and  $R^2$  with changing torsional stiffness  $K_T$  are shown in Figure 2.13. It can be seen that beyond a threshold of approximately 150 Nm, which corresponds to a torsional stiffness coefficient of 0.13 for a 9 mm abutment, there is only minor variation in both the ASC value and the  $R^2$  fit between the measured data and model prediction and the ASC value determined does not vary substantially. Unlike the impact stiffness curve shown previously, there is no clear peak in the  $R^2$  value curve with a steep drop on either side. In this case there is a steep drop at lower values of  $K_T$  but a very gradual decrease at higher values of  $K_T$ . At higher values of  $K_T$ , the implant-abutment is essentially acting as a single rigid body.

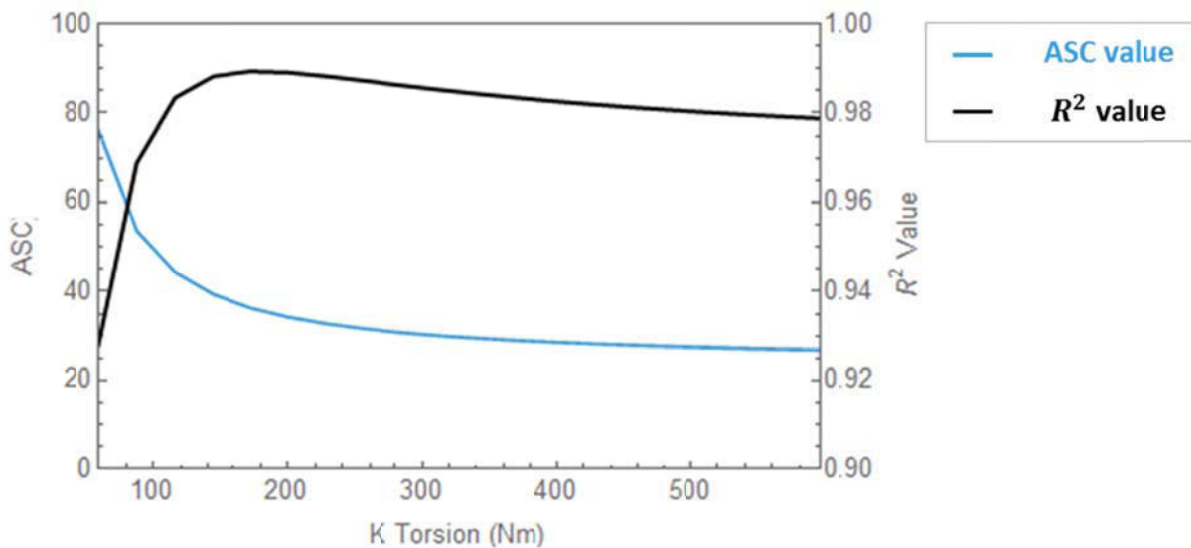


Figure 2.13: Variation in ASC value (blue line) and  $R^2$  fit (black line) with changes in torsional stiffness ( $K_T$ ) for a long/narrow implant and 9 mm abutment

#### 2.4.4. Analytical Model Frequency Response versus Geometric and Inertial Parameters

The important geometric and inertial parameters for the implants in the analytical model are the mass ( $m_I$ ), the length of the threaded portion ( $l_i$ ), the diameter ( $d_i = 2R_0$ ), the location of the center of mass ( $\bar{y}_I$ ), and the mass moment of inertia ( $J_I$ ). Similarly, the important geometric parameters for the abutments in the analytical model are the mass ( $m_A$ ), the length ( $L_A$ ), the location of the center of mass ( $\bar{y}_A$ ), and the mass moment of inertia ( $J_A$ ).  $l_i$ ,  $L_A$ ,  $m_I$ ,  $m_A$ , and  $d_i$  are straightforward to determine and are not subject to appreciable error.

Using the analytical model, the relationships between the geometric parameters and the first and second mode frequency components are examined following the same procedure as the stiffness parameters. This can provide an understanding of the effect of the various geometric parameters on the theoretical acceleration response. Additionally, this analysis will provide an understanding of the sensitivity of the ASIST measure to errors in the estimated parameters such as  $\bar{y}_I, \bar{y}_A, J_I$ , and  $J_A$ . The details of this analysis are shown in Appendix B.

Both the first and second mode frequency components of the model response were found to be virtually insensitive to changes in the implant mass, location of the center of mass, and mass moment of inertia. The center of mass and moment of inertia were estimated for the implants based on simplified geometry. Since the model is fairly insensitive to these parameters, errors in these estimates would not have a large impact on the overall model performance.

The model response is sensitive to changes in implant length and the relationship is nearly linear. The first mode frequency is relatively more sensitive than the second mode frequency. Consider for example an implant with a 9 mm abutment. A change in length from 3 mm to 4 mm (33% increase) results in a change in first mode frequency from 1120 – 1429 Hz, which is an increase of 309 Hz or a 28% increase. The same change in length results in an increase in second mode frequency from 17054 – 18193 Hz, which is an increase of 1139 Hz or a 7% increase. The model response was found to vary slightly with changing implant diameter and again the relationship is nearly linear. Consider again an implant with a 9 mm abutment. A change in diameter from 3.75 mm to 4.50 mm (20% increase) results in an increase of first mode frequency of 69 Hz (5% increase) and a change in second mode frequency of 417 Hz (2% increase).

The relationship between the first mode frequency  $p_1$  and the second mode frequency  $p_2$  and the abutment geometric parameters can be seen in Figure 2.14 - Figure 2.17 for the Oticon Medical implants. The different curves on each figure show the relationships for each implant type: M50106 (short/narrow), M50128 (long/narrow), M51061 (short/wide), M51062 (long/wide). The vertical gridlines in each of the figures show the actual sizes for the different Oticon Medical abutments in the analytical model.

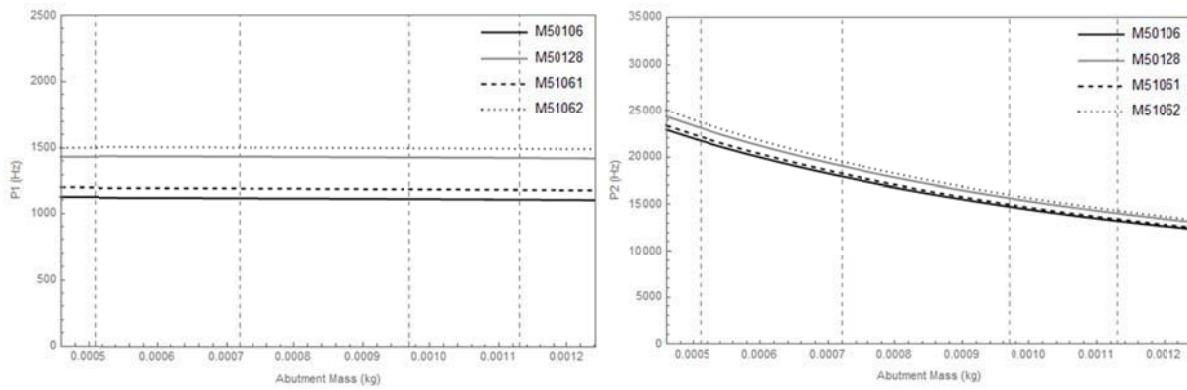


**Figure 2.14: Relationship between the first and second mode frequency components and the abutment mass**

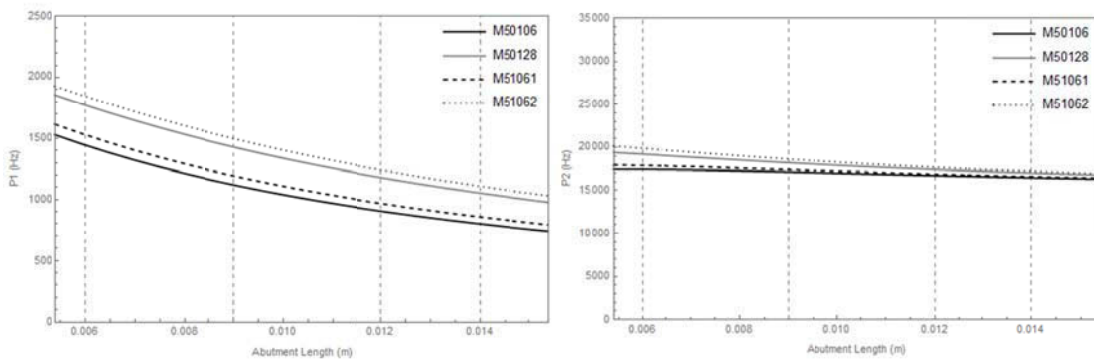


**Figure 2.15: Relationship between the first and second mode frequency components and the abutment length**

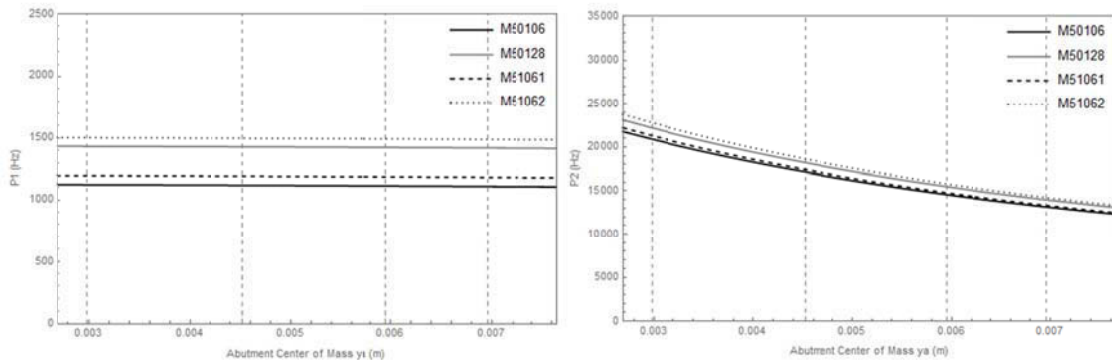


**Figure 2.16: Relationship between the first and second mode frequency components and the location of the abutment center of mass**

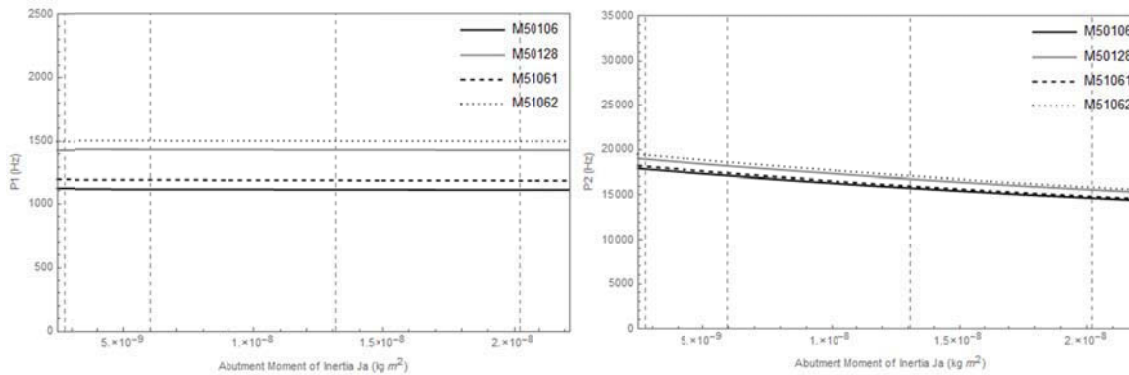


**Figure 2.17: Relationship between the first and second mode frequency components and the abutment mass moment of inertia**

In general, the model response was found to be significantly more sensitive to the abutment geometric parameters compared to the implant parameters, particularly in the second mode frequency. The first mode frequency was found to be insensitive to changes in the abutment mass, while the second mode frequency decreases with increasing abutment mass showing a decreasing slope with increasing mass. Similarly, the first mode frequency was found to be virtually insensitive to changes in the location of the center of mass and the moment of inertia, while the second mode frequency was more sensitive to these parameters. The model response was found to be only slightly sensitive to changes in the abutment moment of inertia.

As expected, the first mode frequency was found to be sensitive to changes in the abutment length, while the second mode frequency was less sensitive. In both cases the frequency was

found to decrease with increasing abutment length. Other measurement methods such as the Periotest® and Osstell™ ISQ that rely on a correlation between the first mode frequency and the interface stiffness without consideration for the abutment length will produce different answers for the stability measurement for varying abutment lengths because of this sensitivity shown here. This is why it is important in the ASIST model to account for the abutment length in the analysis procedure.

#### **2.4.5. Model Solution (ASC and Fit with Measured Data) with Geometric Parameters $\bar{y}_A$ and $J_A$**

In the analytical model, the location of the center of mass and mass moment of inertia of the implant and abutment were estimated based on assumed, simplified geometry. In Section 2.4.4. it was found that the implant parameters including  $\bar{y}_I$  and  $J_I$  have very little effect on the model response, thus errors in these parameters should not have a large effect on the model performance. Conversely, the abutment parameters including  $\bar{y}_A$  and  $J_A$  were found to have more of an effect on the second mode frequency response of the analytical model (particularly  $\bar{y}_A$ ). In this section, we will evaluate the sensitivity of the model solution to errors in these abutment parameters. As  $\bar{y}_A$  or  $J_A$  are varied, the calculated interface stiffness and associated ASC value are determined along with the resulting  $R^2$  fit between the model predicted signal and the measured acceleration. For each analysis, a sample dataset is used in order to calculate the ASC and  $R^2$  values. The details of this analysis are shown in Appendix B while exemplary results are presented here.

Consider for example the long/narrow implant (M50128) with a 9 mm abutment. Figure 2.18 shows the variation in ASC and  $R^2$  value with changing  $\bar{y}_A$ . The two plots are overlaid with the scale for the ASC value (blue line) on the left of the figure and the scale for the  $R^2$  value (black line) on the right of the figure.

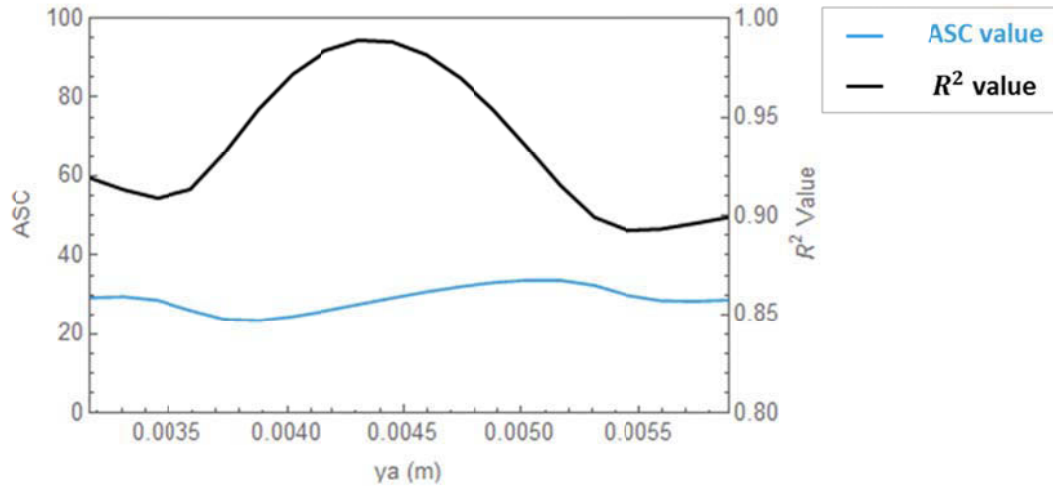


**Figure 2.18: Variation in ASC value (blue line) and  $R^2$  fit (black line) with changes in abutment center of mass ( $\bar{y}_A$ ) for a long/narrow implant and 9 mm abutment**

As shown Figure 2.18, there is some variation in the ASC value over the range of tested  $\bar{y}_A$  and a clear peak in the fit between the measured signal and the model prediction as measured by the  $R^2$  value. A 0.5 mm change in  $\bar{y}_A$  from 4.5 mm to 5.0 mm results in an increase in ASC of 3.9 (13%) and a change in  $R^2$  value from 0.99 to 0.94 (5%) for this example. It was found that variations in the location of the abutment center of mass affect the second mode frequency of the model response, which can result in a poor fit between the measured data and model signal.

Again considering the long/narrow implant with a 9 mm abutment, the variation in ASC and  $R^2$  with changing  $J_A$  is shown in Figure 2.19. It can be seen that there is very little variation in both the ASC value and the  $R^2$  fit with varying abutment moment of inertia. Over the full range tested, there is a change in ASC of 4 (13% change) and all  $R^2$  values are above 0.97 for this sample dataset.

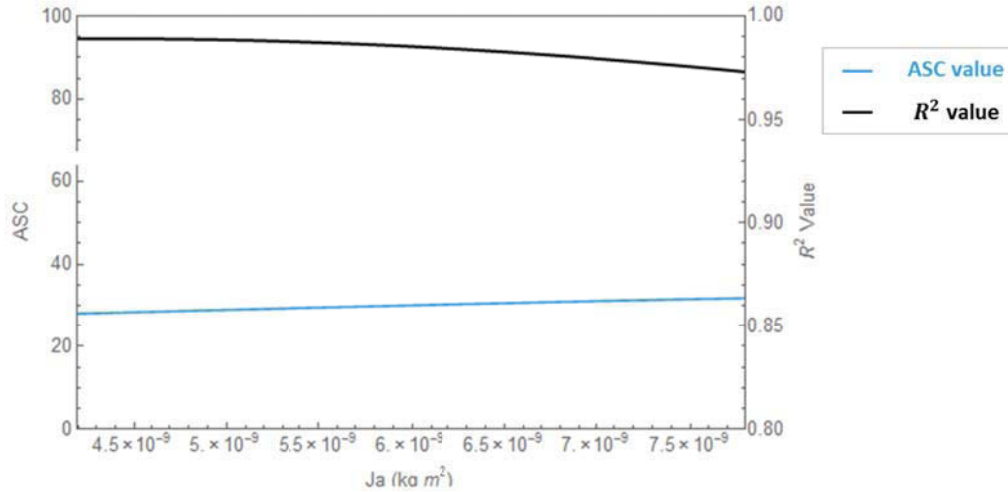


**Figure 2.19: Variation in ASC value (blue line) and  $R^2$  fit (black line) with changes in abutment mass moment of inertia ( $J_A$ ) for a long/narrow implant and 9 mm abutment**

Since the model prediction and  $R^2$  fit are sensitive to the location of the center of mass of the abutment, which is an estimated parameter, this parameter was adjusted for each abutment to find an average value that produced a good fit with each implant type. The procedure for this adjustment is outlined in Section 3.1. Conversely, since the moment of inertia of the abutment was found to have minimal effect on the model outcome, the values estimated based on the simplified geometry were used as the final values in the model with no further adjustment.

#### 2.4.6. Damping Model

The effect of damping can be included in the model in at least two ways: proportional damping and general viscous damping. Using the proportional damping technique, the damping coefficients are assumed to be proportional to the stiffness and/or mass coefficients. This assumption works very well for systems such as buildings and structural systems (Chopra, 2001). However, in the modeled implant-abutment system, this assumption may not be the most appropriate. The site of impact between the impacting rod and the abutment has a relatively large stiffness in the analytical model. However, it is not likely that this location will have a large amount of damping. If proportional damping is used, there is a step change in the acceleration response at  $t = 0$ , which is not observed experimentally. Additionally, the purpose of the ASIST

technique is to estimate the stiffness of the bone-implant interface  $k$  and to identify differences between well-integrated implants and poorly integrated ones. With a poorly integrated implant, the interface stiffness  $k$  may decrease substantially, and with the proportional damping model, the damping in this location would also decrease. However, in the actual system, the bone-implant interface of a poorly integrated implant may have significantly higher damping, for example, due to the formation of scar tissue. For this reason, an alternative damping model was investigated. A comparison is presented to understand the influence of the damping assumption. The details of this comparison are shown in Appendix B.

The ASIST procedure was used to estimate the interface stiffness and calculate the associated ASC value using both the proportional damping assumption and the general viscous damping assumption for a subset of clinical data from 11 BAHA patients. The second mode damping ratio was extracted from the curve fit for each dataset and used in the analysis. The damping content for the BAHA patients is generally very low with an average damping ratio of 0.034 (3.4%) and a range of 0.020 – 0.066 for the sample data. There are very small differences in the results for the two procedures with a maximum difference in the ASC value of 2.2% and differences in the  $R^2$  value below 1%. With such a small damping content, it was found that the choice of damping assumption does not have a large impact on the results. It should be noted that this analysis was done for “good” implants; however, a failing implant may have a different behavior.

## **2.5. Detail of the Numerical Analysis**

There are two major numerical procedures used in the ASIST technique, namely the curve fit approximation to the measured acceleration signals (described in Section 2.3.1. and 2.3.2.) and the optimization procedure for matching the analytical model to the measured acceleration described in Section 2.3.3. We examined some of the assumptions and procedures associated with these numerical techniques in order to determine their effect on the ASIST solution and the details of these analyses are shown in Appendix C. In general, the model solution was found to be insensitive to variations in the numerical analysis parameters. In some cases, variations in the parameters can cause either the curve fit or the optimization procedure to fail to find a solution; however, when a solution is found, it is typically able to find a unique solution within a very small numerical error.

## 2.6. Summary

This chapter presented the ASIST for BAHA implant systems including the hardware and measurement system, the analytical model, and the analysis procedures. The ASIST development built upon previous work in this area (Giannitsios, 2001; Hurst, 2002; Mo, 2009; Swain, 2006; Swain et al., 2008a; Swain et al., 2008b). The contributions of the current author to the final ASIST design include: (1) iterative consultation with collaborators during the development of the hardware (ASIST unit) and data collection software (Kamal et al., 2015), (2) improvements to the analytical model including the use of commercially available BAHA implant-abutment systems (Oticon Medical Ponto and Cochlear Baha® Connect Systems) and the use of a more physiologically appropriate damping model, (3) the analysis procedures including automatic, quantitative, and objective matching between the measured acceleration and the analytical model and evaluation of the quality of fit, which has made the ASIST usable in a clinical situation.

## Chapter 3: ASIST Experimental Development

This chapter presents the experimental development and a laboratory evaluation of the ASIST for the Oticon Medical Ponto System and the Cochlear Baha® Connect System. An *in vitro* laboratory study was conducted with each BAHA implant system to determine the appropriate parameters for the analytical model and to evaluate the performance of the ASIST for both the Oticon and Cochlear systems. Additionally, this chapter presents an analysis of the precision of the experimental testing including the effect of clinical variables such as handpiece positioning along with intra-tester and inter-tester reliability analyses. Finally, this chapter presents the experimental procedure for a comparison between the ASIST and the commercially available Osstell™ ISQ system for stability measurement of BAHA systems in a laboratory setting.

Illustrations of both the Oticon Medical Ponto System and the Cochlear Baha® Connect System are shown in Figure 3.1. Both systems consist of the same components including the implant, the abutment, and a connecting screw. The connecting screw sits in the central shaft of the abutment and threads into the top portion of the implant. All of the components for both systems are made from titanium with portions of the Cochlear implant coated with TiOblast™ and portions of its abutment coated with hydroxyapatite (DermaLock™ Technology) ([www.cochlear.com](http://www.cochlear.com)).

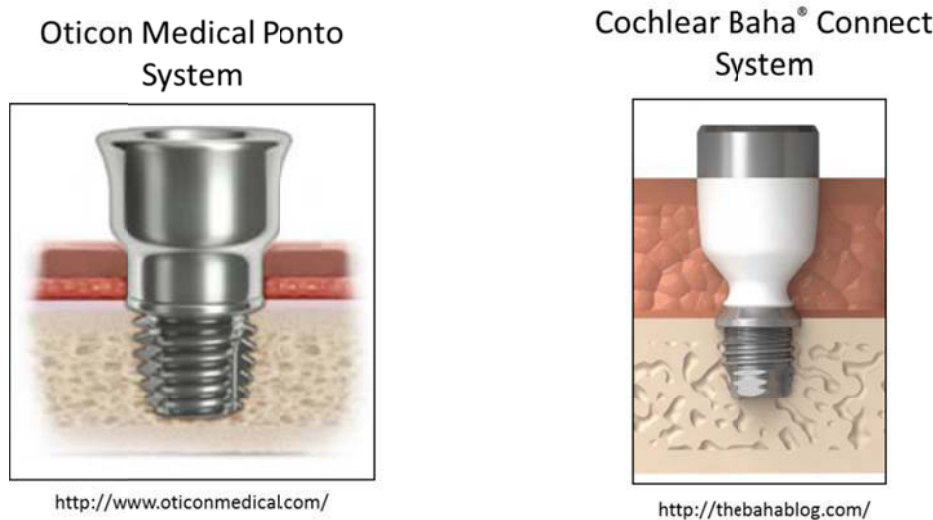


Figure 3.1: Illustrations of the Oticon Medical Ponto (left) and Cochlear Baha® Connect (right) BAHA implant-abutment systems

### 3.1. Application to Oticon Ponto Implant-Abutment System

Four different sizes of Oticon Ponto BAHA implants were obtained from the manufacturer (Ponto System, Oticon Medical). The standard implants developed by Oticon are 4 mm in length and 3.75 mm in diameter. A newer wide version of the implant has also been developed which is 4.50 mm in diameter, increasing the surface area of the bone-implant interface. Both of these implants are also available in a shorter 3 mm length, which are often used in paediatric patients or patients with a thinner mastoid bone. The four types of implants are shown in Table 3.1. Initially, three different lengths of Ponto abutments were obtained: 6 mm, 9 mm, and 12 mm. An additional 14 mm Ponto abutment was added after the initial testing, which will be discussed later in Section 4.1.3. Three samples of each implant and one sample of each abutment were used.

Table 3.1: Oticon BAHA implant sizes

	<b>Short/Narrow M50106</b>	<b>Long/Narrow M50128</b>	<b>Short/Wide M51061</b>	<b>Long/Wide M51062</b>
Diameter (mm)	3.75	3.75	4.50	4.50
Length (mm)	3.0	4.0	3.0	4.0

The location of the center of mass and the mass moment of inertia for the implants and abutments were calculated based on approximate, simplified geometry. Figure 2.3 shows a representative example of the simplified geometry. The schematic is to scale for a long/narrow implant and 12 mm abutment. The nominal diameter and length (Table 3.1) were used for the dimensions of the threaded portion of the implants. For the abutments, it was assumed that the geometry of the upper coupling portion as well as the shaft diameter were constant across abutment sizes. The shaft length was varied such that the total length of each abutment was equal to its nominal length (6 mm, 9 mm 12 mm).

The model response was found to be sensitive to the location of the center of mass of the abutment ( $\bar{y}_A$ ) (Section 2.4). The center of mass of each abutment was adjusted from the calculated value to an average value that best matched sample data from implant specimens

examined in the laboratory setting. The  $\bar{y}_A$  values calculated from the simplified geometry are shown in Table 3.2.

**Table 3.2: Location of the center of mass for Oticon abutments calculated from the simplified geometry**

	$\bar{y}_A$ (base value) (m)
<b>6 mm</b>	0.00284
<b>9 mm</b>	0.00457
<b>12 mm</b>	0.00620

One sample of data from each implant-abutment combination for the eight implant samples was used (Note: the implant samples are described in Section 3.3.1. The eight photoelastic FRB-20 samples were used for this analysis). For each data sample, the location of the center of mass of the abutment was varied  $\pm 10\%$  from the calculated value in a total of 20 discrete values. For each value of  $\bar{y}_A$ , the model was used to estimate the appropriate interface stiffness ( $k$ ) and determine the  $R^2$  value between the model prediction and the data. The value of  $\bar{y}_A$  that produced the best fit between the model and the data as measured by the  $R^2$  value was recorded. For a given abutment, eight values were determined (one from each sample) as shown in Table 3.3. The average of the eight values were calculated for each abutment and used as the fixed values for  $\bar{y}_A$  in the model.

**Table 3.3: Best fit value of Oticon abutment center of mass ( $\bar{y}_A$ ) for one dataset with each of the FRB-20 implant samples (units of m)**

	<b>6 mm</b>	<b>9 mm</b>	<b>12 mm</b>
<b>M50106 FRB-20 (1)</b>	0.00312	0.00445	0.00584
<b>M50106 FRB-20 (2)</b>	0.00255	0.00455	0.00630
<b>M50128 FRB-20 (1)</b>	0.00312	0.00435	0.00577
<b>M50128 FRB-20 (2)</b>	0.00255	0.00455	0.00577
<b>M51061 FRB-20 (1)</b>	0.00312	0.00460	0.00597
<b>M51061 FRB-20 (2)</b>	0.00312	0.00450	0.00597
<b>M51062 FRB-20 (1)</b>	0.00312	0.00474	0.00617
<b>M51062 FRB-20 (2)</b>	0.00312	0.00440	0.00577
<b>Average</b>	<b>0.00298</b>	<b>0.00452</b>	<b>0.00595</b>
<b>SD</b>	<b>0.00026</b>	<b>0.00012</b>	<b>0.00020</b>

The approximated mass and geometry properties for the Oticon implants and abutments are shown in Table 3.4. The mass of the abutment includes the mass of the screw that connects the abutment to the implant. Note that the location of the center of mass is measured from the bottom of the component and the mass moment of inertia is about the center of mass.

Table 3.4: Mass and geometry properties for Oticon implants and abutments

<b>Oticon Implants</b>	<b>Mass (g)</b>	<b>Diameter (mm)</b>	<b>Length (mm)</b>	$\bar{y}_i$ (mm)	$J_I$ (g mm <sup>2</sup> )
<b>M50106</b>	0.126	3.75	3.00	2.19	0.31
<b>M50128</b>	0.157	3.75	4.00	2.71	0.51
<b>M51061</b>	0.173	4.50	3.00	2.04	0.46
<b>M51062</b>	0.222	4.50	4.00	2.54	0.76
<b>Oticon Abutments</b>	<b>Mass (g)</b>	<b>Shaft Diam. (mm)</b>	<b>Length (mm)</b>	$\bar{y}_A$ (mm)	$J_A$ (g mm <sup>2</sup> )
<b>6 mm</b>	0.51	5.00	6.00	2.98	2.72
<b>9 mm</b>	0.72	5.00	9.00	4.52	5.99
<b>12 mm</b>	0.97	5.00	12.00	5.95	13.07

### 3.2. Application to Cochlear Baha® Connect Implant-Abutment System

One type of Cochlear Baha® Connect implant (BI300) was obtained from the manufacturer (Cochlear Bone Anchored Solutions, Göteborg, Sweden). The implant diameter is approximately 4.45 mm and the nominal length is 4 mm. Four different lengths of the BA400 abutment were obtained (nominal lengths: 6 mm, 8 mm, 10 mm, 12 mm). One sample of the implant and one sample of each abutment were used.

The general components of the Cochlear system are the same as for the Oticon system, thus the developed analytical model is applicable for both systems. To use the analytical model for the Cochlear Baha® Connect system, the mass and geometry properties must be modified. The values determined for the Cochlear system are shown in Table 3.5.

Table 3.5: Mass and geometry properties for Cochlear implants and abutments

<b>Cochlear Implant</b>	<b>Mass (g)</b>	<b>Diameter (mm)</b>	<b>Length (mm)</b>	$\bar{y}_i$ (mm)	$J_I$ (g mm <sup>2</sup> )
<b>BI300</b>	0.22	4.45	4.00	2.66	0.78
<b>Cochlear Abutments</b>	<b>Mass (g)</b>		<b>Length (mm)</b>	$\bar{y}_A$ (mm)	$J_A$ (g mm <sup>2</sup> )
<b>6 mm</b>	0.50	N/A	4.67	2.15	2.68
<b>8 mm</b>	0.70	N/A	6.67	3.85	4.42
<b>10 mm</b>	1.03	N/A	8.67	4.93	8.22
<b>12 mm</b>	1.40	N/A	10.67	6.01	14.39

### 3.3. ASIST Development and Experimental Evaluation

#### 3.3.1. Experimental Testing

Each implant was installed into a disc of either photoelastic FRB-20 (Measurements Group Inc., Raleigh, NC) or a 3D printed PLA (Cubify, 3D Systems Inc.) to simulate a well-integrated implant in bone. Two samples of each Oticon implant type were installed in FRB-20 and one sample was installed in PLA. For each implant sample, a pilot hole that is slightly smaller than the implant diameter was drilled through the material. The implant, which is self-tapping, was screwed into the hole by hand to create the threads and then removed. The threaded portion of the hole was coated with 5-minute epoxy (for the FRB-20 samples) or standard super glue (for the PLA samples) and the implant was then re-installed. The adhesive was used to ensure a more uniform interface between the implant and the material and to simulate osseointegration in bone. The different materials and different adhesives were used to simulate a range of interface stiffness values (i.e. the FRB-20 samples were expected to be stiffer than the PLA samples). Each of the Oticon Medical implant samples were tested with each of the three corresponding abutments (6 mm, 9 mm, 12 mm).

One implant sample was prepared for the Cochlear Baha® Connect System. The BI300 implant was installed in a disc of FRB-20 and secured with super glue and tested with each of the four Cochlear BA400 abutments (6 mm, 8 mm, 10 mm, 12 mm).

The disc containing the implant was clamped to a platform and an abutment was attached with 25 Ncm of torque as per manufacturer instructions (Figure 3.2). The ASIST handpiece was held in a custom built adjustable stand (Swain, 2006; Swain et al., 2008a) to minimize variations in the handpiece position. Five ASIST measurements were taken with each implant-abutment combination.

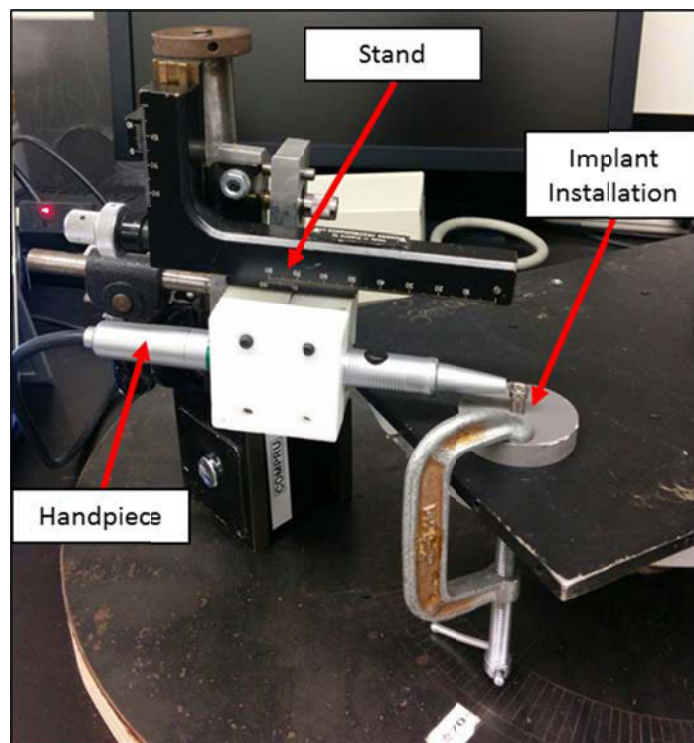


Figure 3.2: Laboratory test set-up showing the FRB-20 disc containing the implant with a 9 mm abutment attached. The disc is clamped to a platform for testing and the ASIST handpiece is held in a custom stand.

### 3.3.2. Determining model parameters

In order to objectively determine the interface stiffness  $k$ , all other parameters in the system should be known. Thus, we must determine appropriate values for the stiffness parameters  $K_T$  and  $K_I$ .

The maximum torsional stiffness for a given system  $K_{T(max)}$  is determined similar to the work of Swain (2006; 2008a). The details for this approximation are shown in Appendix A. It can be shown that  $K_{T(max)}$  is dependent on the abutment length. The  $K_{T(max)}$  values for all abutments are shown in Table 3.6.

Table 3.6: Maximum torsional stiffness values

Oticon System		Cochlear System	
Abutment Length (mm)	$K_{T(max)}$ (Nm)	Abutment Length (mm)	$K_{T(max)}$ (Nm)
		6 mm	2963
6 mm	2183	8 mm	1732
9 mm	1191	10 mm	1404
12 mm	856	12 mm	1125

It is assumed that the actual torsional stiffness is less than the maximum value because the screw connection between the implant and abutment will not provide a rigid fixed connection. Thus, the actual value of  $K_T$  was assumed to be some fraction of the maximum value:

$$K_T = \alpha K_{T(max)}$$

The torsional stiffness coefficient ( $\alpha$ ) is assumed to be constant within each BAHA system.

The impact stiffness  $K_I$  represents the local deformation of the impact rod and the abutment at the location of the strike. The value of  $K_I$  is similarly assumed to be constant across abutments from the same system.

Appropriate average values for  $K_I$  and  $\alpha$  were determined for the Oticon system using the numerical model. Multivariable minimization was used to first determine an appropriate value for  $\alpha$  which was found to be 0.26. The data was processed again using multivariable minimization (keeping  $\alpha$  fixed) to determine  $K_I$ . The final value for the impact stiffness for the Oticon system was found to be  $K_I = 2.90 \times 10^6$  N/m. The appropriate values for the Cochlear system were determined in a similar manner and found to be  $\alpha = 0.50$  and  $K_I = 4.74 \times 10^6$  N/m.

### **3.3.3. ASIST Evaluation**

The measured data was analyzed with the model parameters chosen as described above. For each measurement, an appropriate interface stiffness was determined. The ASC values were determined for each individual measurement.

## **3.4. Precision of Experimental Testing**

This section presents an evaluation of the repeatability and sensitivity of measurements with the ASIST in a laboratory setting with BAHA implant-abutment systems.

### **3.4.1. Laboratory Test Set-up**

Each test specimen was created by installing a BAHA implant into a disc of FRB-20 material and securing the implant with an adhesive (either epoxy or super glue) as outlined in Section 3.3.1. Both Oticon Ponto and Cochlear Baha® Connect implant-abutment systems were used in this study. The specific implant-abutment combinations that were used for each test are outlined in the sections below. The repeatability of measurement, sensitivity to handpieces, and sensitivity to clinical variables were tested using an apparatus to hold the handpiece to accurately control the positioning. The intra-user and inter-user repeatability was examined holding the device by hand, to better represent the clinical situation.

### **3.4.2. Outcome Measures**

The primary outcome measure of the ASIST is the ASIST Stability Coefficient (ASC). All repeatability and sensitivity measures were analyzed using the ASC value. The intra-user and inter-user reliability were assessed using the intraclass correlation coefficient (ICC) and the standard error of measurement (SEM) calculated using SPSS (IBM SPSS Statistics 23, Armonk, NY, USA). An ICC of 1.0 indicates perfect agreement, while an ICC of zero indicates only random agreement (Hallgren, 2012). The commonly cited ranges for the ICC rate the quality of reliability as poor ( $<0.40$ ), fair ( $0.40 - 0.59$ ), good ( $0.60 - 0.74$ ), and excellent ( $0.75 - 1.0$ ) (Hallgren, 2012). The SEM provides an indication of the precision of the measurement

(expressed in the units of the measurement i.e. ASC in this case) and is based on the distribution of the measurement error (Shultz et al., 2006).

### **3.4.3. Repeatability of Measurement and Effect of Different Handpieces**

The repeatability of measurement was examined using a long/wide Oticon Medical implant (M51062 FRB-20(2)) with both 9 mm and 12 mm Oticon Medical abutments. The ASIST device was positioned using the custom apparatus to strike the upper rim of the abutment. The handpiece was placed at an angle of 5 degrees above the horizontal and the tip of the handpiece was held 1.0 mm away from the lip of the abutment. The handpiece was positioned so the middle of the impact rod would strike the lip of the abutment. The ASIST was designed with a removable handpiece, so multiple handpieces can be used with the same device. This allows the front portion of the handpiece to be removed and cleaned or sterilized during clinical use. Three handpieces were tested (labeled with a colored sticker “Green”, “Orange”, and “Gray”) to evaluate any additional variability caused by exchanging multiple handpieces. For each handpiece, seven sets of five consecutive measurements were taken. The ASIST was repositioned between each set of five measurements for a total of 35 measurements with one handpiece. These 35 measurements were then repeated with each of the three handpieces for a total of 105 measurements for each implant-abutment combination (210 measurements in total).

The ASC results for each handpiece are shown in Figure 3.3. The subfigures show the measurements for each handpiece. The measurements shown are the average of the five consecutive measurements and the error bars represent one standard deviation. The averages of all 35 measurements with each handpiece are shown in Figure 3.4 along with the average of all 105 measurements for each implant-abutment combination. For the 9 mm abutment the mean ASC value is 33.7 and the standard deviation of all measurements is 1.5. For this sample, the maximum difference in the average measurement between the three handpieces is 3.0 ASC. For the 12 mm abutment the mean ASC value is 34.4 and the standard deviation of all measurements is 1.4. For this sample, the maximum difference in the average measurement between the three handpieces is 2.1 ASC.

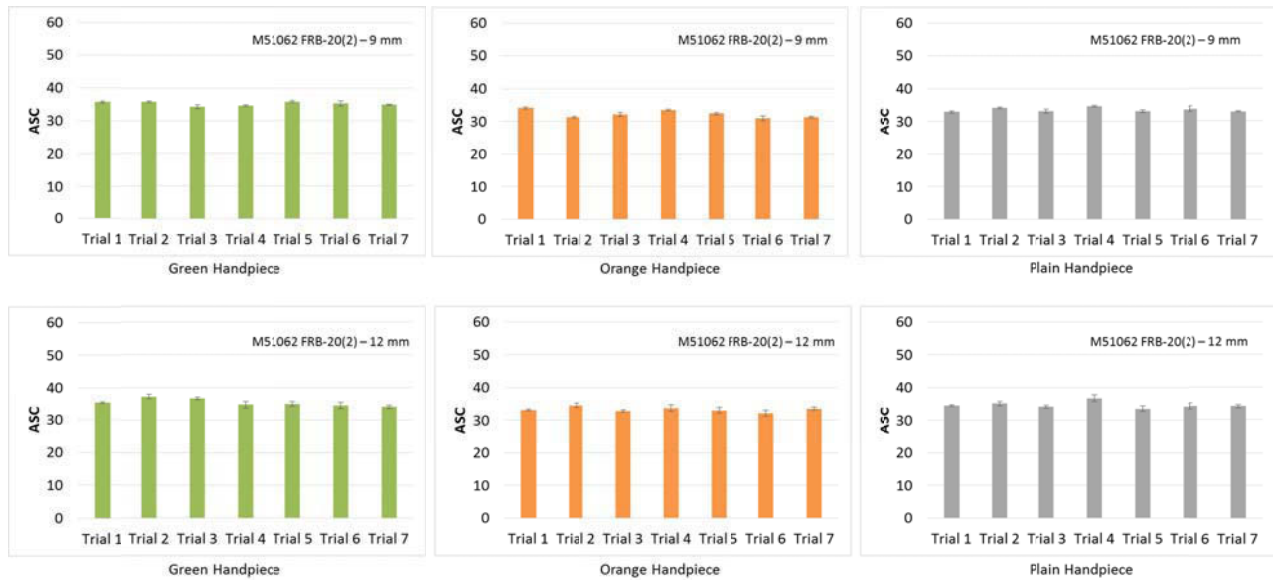


**Figure 3.3: ASC measurements for a long/wide Oticon Medical implant (M51062 FRB-20(2)) with a 9 mm and 12 mm abutment and three ASIST handpieces. Values are the average of 5 measurements and error bars represent one standard deviation.**

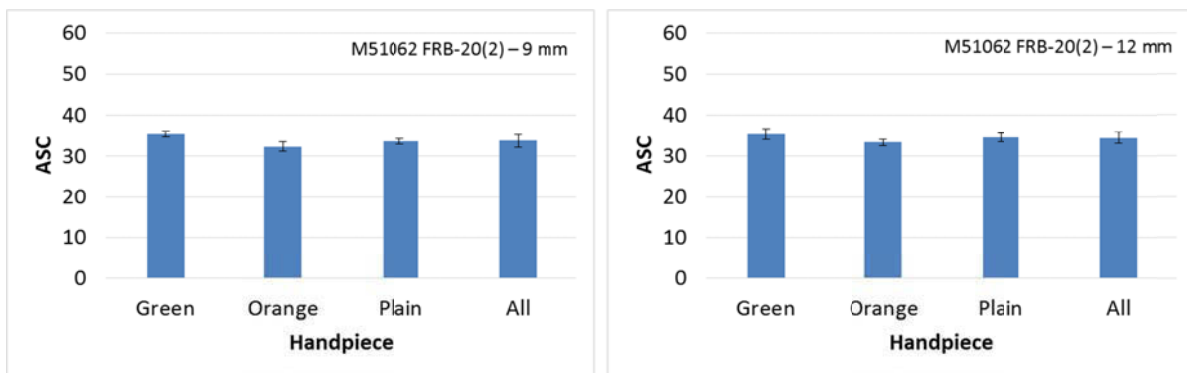


**Figure 3.4: ASC measurements for a long/wide Oticon Medical implant (M51062 FRB-20(2)) with a 9 mm and 12 mm abutment and three ASIST handpieces. Values for the color labeled columns are the average of 35 measurements with each handpiece. Values for the “All” columns are the average of all 105 measurements. Error bars represent one standard deviation.**

The results presented in Figure 3.3 and Figure 3.4 represent only one implant sample with an interface stiffness in the higher range where the interface stiffness and ASC are more sensitive to small differences in acceleration measurement. To understand the average variation in measurement, the repeatability was also assessed using the full range of Oticon Medical implant types spanning a range of interface stiffness conditions. The 12 implant samples and three

abutments (6 mm, 9 mm, 12 mm) described in Section 3.3.1. were tested with one handpiece. The apparatus was used to control the handpiece position and five measurements were recorded with each implant-abutment combination. The results of these measurements are reported in Section 4.1.1. and here we can further analyze this data to determine the repeatability of measurement when the handpiece position is controlled using the apparatus. Each of the 36 implant-abutment combinations was treated as a separate condition and the ICC and SEM for intra-tester repeatability were calculated. The ICC was found to be 0.998, indicating excellent reliability (Hallgren, 2012) and the SEM was 0.96 ASC.

### **3.4.4. Sensitivity to Clinical Variables**

The previous section evaluated the repeatability of the ASIST when the handpiece position is controlled using an apparatus. The sensitivity to clinical variables such as handpiece distance from abutment, striking height, and handpiece angulation were examined to understand the effect of variations in the handpiece position on the outcome measure. For this analysis, the analytical model was not changed (the nominal values were used) and ASC was determined to understand the effect of variations in handpiece positioning. A long/wide Oticon implant sample (M51062 FRB-20(1)) was tested with the 9 mm Oticon abutment and the Cochlear implant sample BI300 was tested with the 10 mm BA400 Cochlear abutment. For both tests the green handpiece was used. In all cases, the custom apparatus was used to control the position of the handpiece and five consecutive measurements were recorded without repositioning.

#### **3.4.4.1. Handpiece Distance**

To examine the effect of the handpiece distance from the abutment, the handpiece was positioned at an angle of 5 degrees from the horizontal with the middle of the striking rod at the lip of the Oticon abutment. Five consecutive measurements were recorded at each of the following distances from the abutment: 1.0 mm, 1.5 mm, 2.0 mm, 2.5 mm, and 3.0 mm.

Since there is no lip on the Cochlear abutment, the handpiece was positioned with the striking rod at the bottom of the abutment chamfer (Figure 3.5). Five consecutive measurements were recorded at 1.0 mm, 1.5 mm, 2.0 mm, and 2.5 mm.



Cochlear Implant-Abutment  
<http://www.cochlear.com/>

**Figure 3.5: Cochlear implant and abutment geometry showing the chamfer at the top of the abutment**

The results for these analyses are shown in Figure 3.6. For the Oticon Medical implant sample, the average ASC value was 42.3 (range: 40.6 – 43.2). There is very little difference in ASC with varying handpiece distance and a standard deviation of all the measurements of 1.1. For the Cochlear implant sample, the average ASC value was 32.3 (range: 31.8 – 32.7). Again, there is very little difference in ASC with varying handpiece distance and a standard deviation of all the measurements of 0.4.

These results suggest that there is very little variation in the results with varying handpiece distance between approximately 1.0 mm and 2.5 or 3.0 mm. At distances larger than approximately 3.0 mm, the impact rod does not extend far enough to achieve a good contact with the abutment. At distances less than approximately 1.0 mm, the ASIST is not able to record a proper signal for the 16 strikes. This may be due to the time required to prepare the propulsion of the impact rod and data collection between strikes.

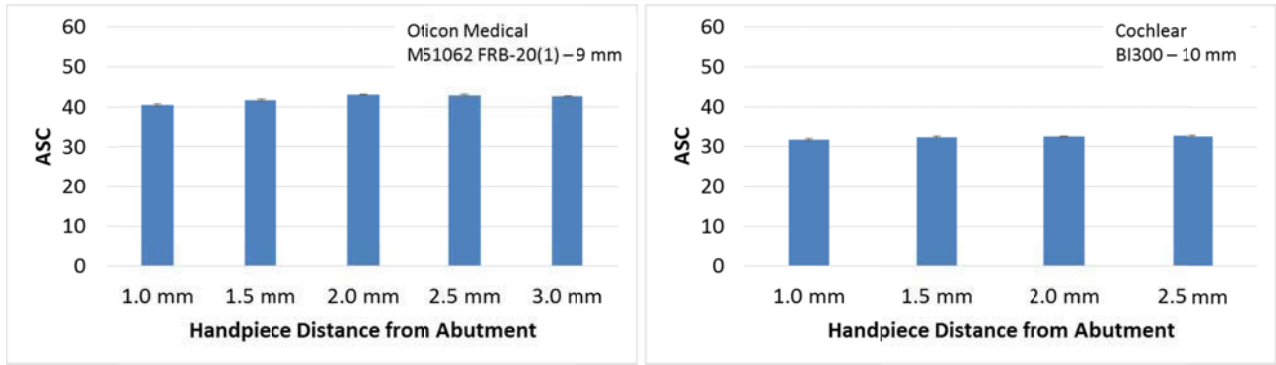


**Figure 3.6:** ASC measurements at variations in the handpiece distance from the abutment. Values are the average of five measurements. Error bars represent one standard deviation. Left: Oticon Medical implant (M51062 FRB-20(1)) with 9 mm abutment. Right: Cochlear implant sample (BI300) with 10 mm abutment.

### 3.4.4.2. Striking Height

To examine the effect of the striking height, the handpiece was positioned at an angle of 5 degrees from the horizontal at a distance of 1.5 mm from the abutment. The Oticon abutment is designed with a lip at the top and it is not practical to strike anywhere below the lip. Thus the striking heights tested only span the range where the striking rod can contact the abutment lip. A striking height of zero corresponds to the case where the bottom of the rod is in contact with the lip of the abutment and a positive height represents the distance below the abutment lip to the bottom of the striking rod. The maximum value for the striking height represents the case where the top of the striking rod is in contact with the abutment lip. Five consecutive measurements were recorded at each of the following heights: 0 mm, 0.5 mm, and 1.0 mm. For the Cochlear system, the abutment is designed with straight edges and a small chamfer at the top of the abutment (Figure 3.5). Thus it is possible to strike the Cochlear abutment at any location along the straight portion. In this case, a striking height of zero represents the case where the top of the striking rod is just at the bottom of the chamfer and positive heights indicate the distance below the lower edge of the chamfer. Five consecutive measurements were recorded at striking heights of 0 mm, 0.5 mm, 1.0 mm, 1.5 mm, 2.0 mm, and 2.5 mm.

The results for these analyses are shown in Figure 3.7. For the Oticon Medical implant sample, the average ASC value was 38.9 (range: 36.4 – 40.6) and the standard deviation of all measurements was 1.9. There is only a small variation in the ASC value with changing striking height for the Oticon implants. The lip of the Oticon abutment design helps to ensure that the

strike is always within the lip region. Thus only small variations in the striking height are possible for this implant-abutment system.

For the Cochlear implant sample, the average ASC value was 32.3 (range: 28.8 – 35.7) and the standard deviation of all measurements was 2.6. With the exception of the first measurement, there is a tendency of increasing ASC with increasing striking height (i.e. moving down from the top of the abutment). The first measurement at 0.0 mm is just below the chamfer on the abutment, which may add extra variability to the measure. Intuitively it is expected that the ASC would increase as the handpiece is moved lower on the abutment because the first mode frequency would tend to increase while the analytical model assumes that the strike occurs at the top of the abutment.

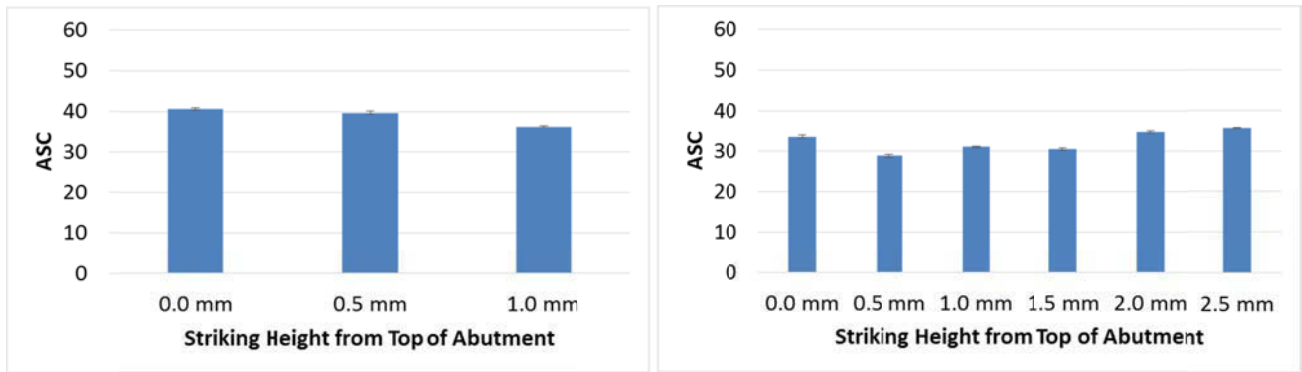


**Figure 3.7: ASC measurements at variations in the handpiece striking height. Values are the average of five measurements. Error bars represent one standard deviation. Left: Oticon Medical implant (M51062 FRB-20(1)) with 9 mm abutment. Right: Cochlear implant sample (BI300) with 10 mm abutment.**

### 3.4.4.3. Handpiece Angulation

To examine the effect of the angulation of the handpiece (angle above the horizontal) the ASIST was positioned at a distance of 1.5 mm from the abutment with the middle of the striking rod at the lip of the Oticon abutment and with the top of the striking rod at the bottom of the chamfer for the Cochlear abutment. Five consecutive measurements were recorded at angles of 0 degrees, 2.5 degrees, 5 degrees, 10 degrees, and 15 degrees. It should be noted that the distance from the abutment was adjusted to 2.0 mm for the Cochlear system at an angle of 15 degrees to ensure a proper recording.

The results of these analyses are shown in Figure 3.8. For the Oticon Medical implant, the average ASC value was 43.1 (range: 39.3 – 51.6) and the standard deviation of all measurements was 4.8. With a handpiece angle between 0 and 5 degrees, there is very little variation in the ASC value. However, with a handpiece angle of 10 to 15 degrees, there is a substantial increase in the ASC value with a change in ASC from 5 degrees to 15 degrees of 11.7 ASC. As the handpiece angle is increased, more of the impact load is applied axially on the top of the abutment lip which causes an increase in the first mode frequency (measured in the direction of the impact load). To maintain consistent results, the handpiece should be held approximately 0 – 5 degrees above the horizontal during clinical use.

For the Cochlear implant sample, the average ASC value was 30.1 (range: 27.8 – 32.1) with a standard deviation of all measurements of 1.7. There is some variation in ASC due to changing handpiece angulation; however, there is no clear pattern as was seen with the Oticon implants. This is due to the difference in abutment design. With the Cochlear abutments, the impact was applied on the straight portion of the abutment just below the chamfer. As the handpiece angle is increased, there is no large increase in the axial load applied to the abutment because the handpiece is still striking along the side of the abutment as opposed to the top of the abutment. This difference is illustrated in Figure 3.9.

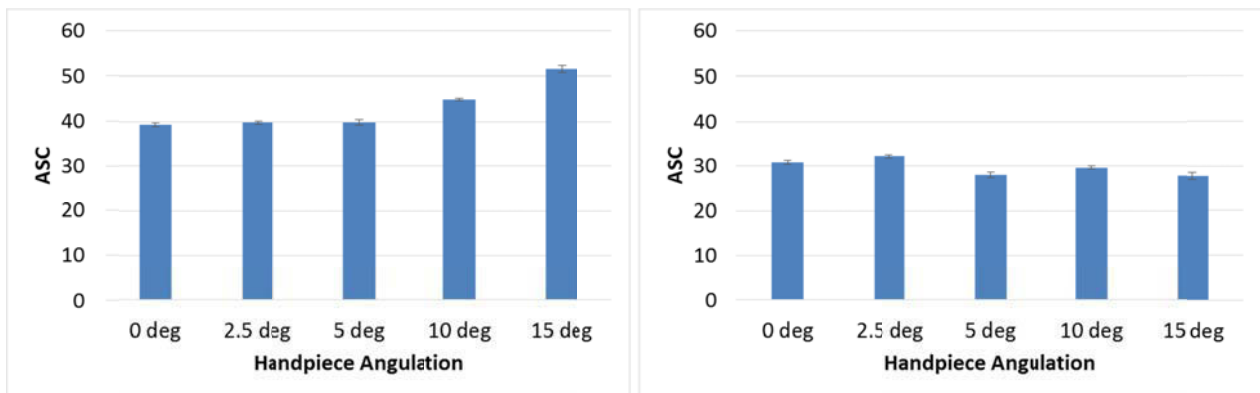


**Figure 3.8: ASC measurements at variations in the handpiece angulation (angle above the horizontal). Values are the average of five measurements. Error bars represent one standard deviation. Left: Oticon Medical implant (M51062 FRB-20(1)) with 9 mm abutment. Right: Cochlear implant sample (BI300) with 10 mm abutment.**

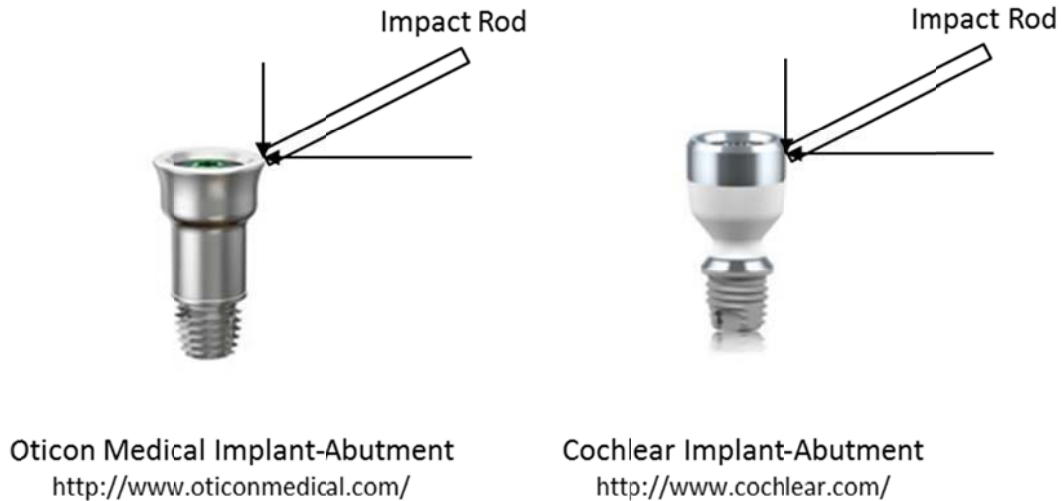


**Figure 3.9: Difference in impact between the Oticon Medical abutment (left) and the Cochlear abutment (right) with a large handpiece angle**

### 3.4.5. Intra-User Repeatability

Intra-user repeatability was assessed for the Oticon Medical implant-abutment system with multiple testers including clinicians familiar with using the Periotest® for stability assessment of BAHA patients, the primary author and a research assistant who are familiar with using the ASIST for stability assessment in the laboratory setting and with BAHA patients, and graduate students with no prior knowledge of BAHA implant systems. 14 testers participated over two days. All measurements were done with the green handpiece. Seven participants tested two samples of the long/wide implant (M51062 FRB-20) with the 9 mm and 12 mm abutments (6 clinical assistants from iRSM and the primary author). These samples represented implants in the higher stiffness range with ASC values greater than 30. Participants were given verbal instructions regarding handpiece positioning. Since the participants were familiar with the Periotest® device (which uses a similar handpiece and measurement protocol) minimal instructions or training were given.

Seven participants tested two additional samples representing implants in the lower stiffness range with ASC values less than 15. The tested samples were the long/narrow implant (M50128 PLA) with the 6 mm abutment and the short/wide implant (M51061 PLA) with the 9 mm abutment. The participants included the primary author, a research assistant, and five graduate

students in Civil Engineering at the University of Alberta. Since, this second set of participants were not familiar with the measurement system, they were given verbal instructions and a demonstration of the proper handpiece positioning. These participants were also given a chance to practice a few measurements before testing began.

Intra-user repeatability was also assessed for the Cochlear BI300 implant with the 10 mm abutment with two testers (primary author and research assistant).

For all tests, the handpiece was held by hand as would be done clinically. The handpiece was positioned between 0-5 degrees from the horizontal at a distance of 1-2 mm away from the abutment as per the instructions given to the participants. For the Oticon system the striking rod was positioned at the lip of the abutment and for the Cochlear system the striking rod was positioned at the bottom of the abutment chamfer. Ten consecutive measurements were recorded with each implant-abutment combination for each participant.

For the Oticon implants, the ICC and SEM were calculated for each tester and the intra-user repeatability is reported as the average ICC and average SEM over the range of testers. For the Cochlear implant, the ICC could not be calculated because only one sample was tested. The repeatability is assessed through the standard deviation of the measurements.

Figure 3.10 shows the average ASC measurements for the Oticon Medical implant samples for each of the 14 participants. The average values for 10 measurements are shown for each tester along with error bars representing one standard deviation. The ASC values for the higher stiffness implant samples were  $37.4 \pm 4.3$  and  $34.3 \pm 3.7$  (mean  $\pm$  SD) for the M51062 FRB-20(1) 9 mm and M51062 FRB-20(2) 12 mm samples, respectively. The ASC values for the lower stiffness implant samples were  $8.0 \pm 0.4$  and  $14.2 \pm 1.0$  for the M50128 PLA 6 mm and M51061 PLA 9 mm samples, respectively. For the higher stiffness samples, the maximum standard deviation for the measurements from an individual tester was 5.7 while the lowest was 0.8. It should be noted that some outlier measurements existed for the higher implant samples. For Tester 1, one high ASC measurement was recorded (48.6 versus the mean value of 34.4 for this tester) for the 9 mm abutment specimen. This was the first measurement recorded from this tester and the high value is due to an increased angle in the handpiece position. The position was corrected for the remaining measurements from this participant. For Tester 2, there are four

outlier measurements with the 12 mm implant sample. In this case, the clamp holding the implant disc to the table was obstructing the most comfortable position for this participant to hold the handpiece. These four outlier measurements were caused by incorrect handpiece positioning while the participant was becoming comfortable with the setup. Excluding these outlier measurements, the largest standard deviation for measurements from an individual tester with the high stiffness implant samples was 3.1. For the low stiffness samples, the maximum standard deviation for the measurements from an individual tester was 0.7 while the lowest was 0.1.

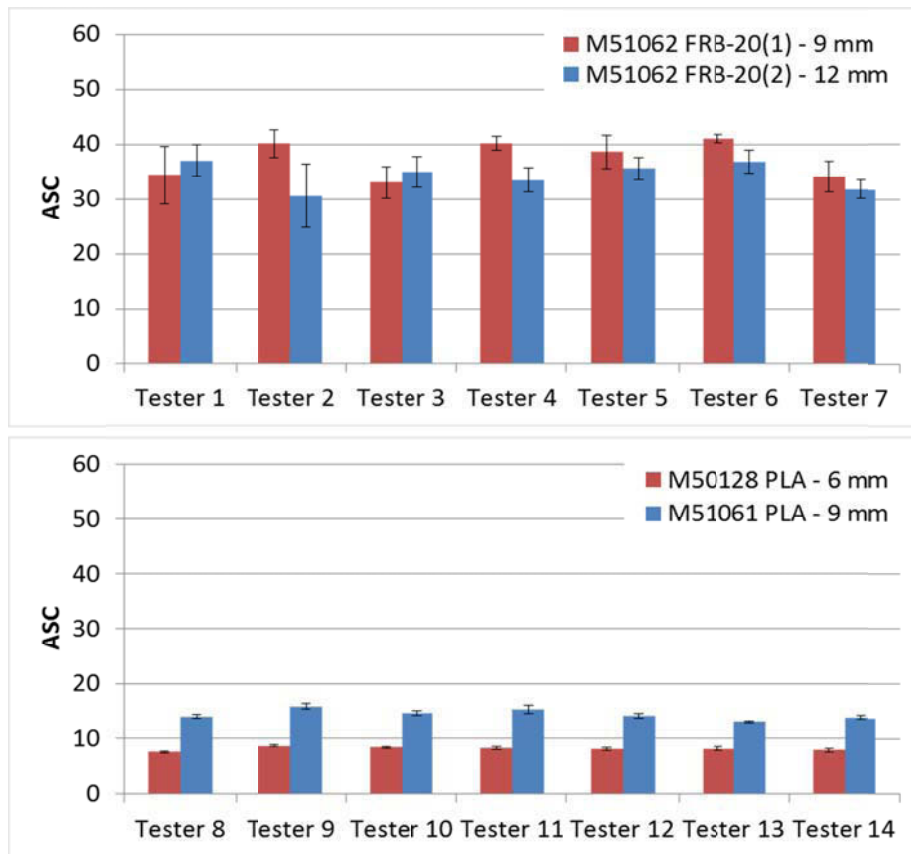


**Figure 3.10: ASC measurements for Oticon Medical implant samples from 14 participants. Values are the average of 10 measurements. Error bars represent one standard deviation. Top: implant samples with a higher stiffness. Bottom: implant samples with a lower stiffness.**

The ICC and SEM values for each tester are shown in Table 3.7. The average ICC for the high stiffness implant samples is 0.533 (fair reliability) and the average SEM after removing outliers is 1.86. The choice of having two implant samples with very similar stiffness properties is

contributing to the low ICC for this set. The average ICC for the low stiffness implant samples is 0.994 (excellent reliability) and the average SEM is 0.33. Considering all of the data, ICC was found to be 0.941 (excellent reliability) and the SEM was 1.52 (or 0.97 excluding outliers) for intra-user reliability. These values indicate only slightly higher variability than the values reported for the full range of ASC values using the stand to control handpiece position (Section 3.4.3.).

**Table 3.7: Intra-User Reliability Measures for Oticon Medical Implant Samples (ICC and SEM)**

	<b>Tester</b>	<b>ICC</b>	<b>SEM</b>
<b>High stiffness ASC &gt;30</b>	Tester 1	0.074	4.50
	Tester 2	0.686	5.09
	Tester 3	0.153	1.82
	Tester 4	0.876	1.59
	Tester 5	0.364	2.58
	Tester 6	0.776	1.40
	Tester 7	0.307	1.94
	<b>Average Average (removing outliers)</b>	<b>0.533</b>	<b>2.70</b> <b>1.86</b>
<b>Low Stiffness ASC &lt;15</b>	Tester 8	0.997	0.20
	Tester 9	0.995	0.36
	Tester 10	0.994	0.36
	Tester 11	0.989	0.48
	Tester 12	0.992	0.38
	Tester 13	0.994	0.26
	Tester 14	0.994	0.27
	<b>Average</b>	<b>0.994</b>	<b>0.33</b>
<b>All Data</b>	<b>Average Average (removing outliers)</b>	<b>0.941</b>	<b>1.52</b> <b>0.97</b>

The ASC measurements for the Cochlear implant sample were  $30.2 \pm 0.8$  and  $37.1 \pm 1.2$  (average  $\pm$  SD) for testers 1 and 2, respectively (Figure 3.11). For this sample, within tester variability is low with a maximum standard deviation of 1.2. The high inter-user variability in this case is likely due to a difference in handpiece position, for example Tester 2 may have struck slightly lower on the abutment than Tester 1.

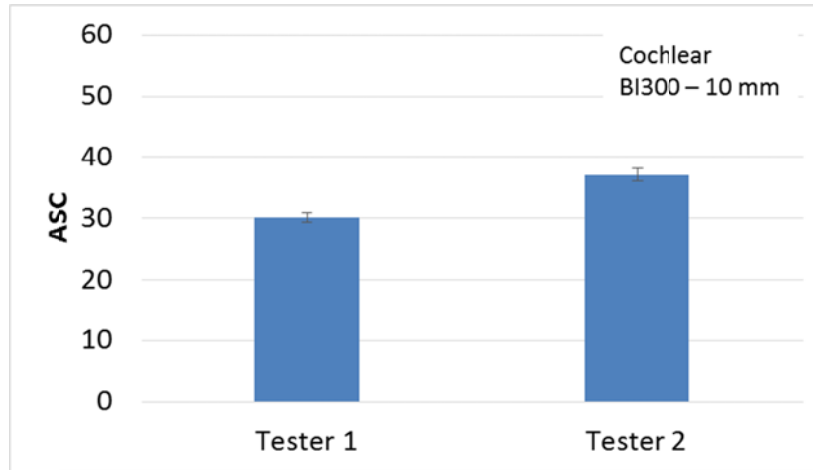


**Figure 3.11: ASC measurements for the Cochlear implant samples for the two participants. Values are the average of 10 measurements. Error bars represent one standard deviation.**

### **3.4.6. Inter-User Repeatability**

Inter-user repeatability was assessed following the same protocol as the intra-user repeatability outlined in the previous section. For the Oticon implants, the ICC and SEM were calculated comparing the same trial across participants and the inter-user repeatability is reported as the average ICC and average SEM over the trials (Table 3.8). Again, for the Cochlear implant the ICC was not calculated because only one sample was tested.

**Table 3.8: Inter-User Reliability Measures for Oticon Medical Implant Samples (ICC and SEM)**

	<b>Trial</b>	<b>ICC</b>	<b>SEM</b>		<b>Trial</b>	<b>ICC</b>	<b>SEM</b>
<b>High stiffness ASC &gt;30</b>	Trial 1	0.28	4.10	<b>All Data</b>	Trial 1	0.976	2.62
	Trial 2	0.159	3.14		Trial 2	0.975	2.27
	Trial 3	-0.17	3.83		Trial 3	0.974	2.55
	Trial 4	0.029	3.44		Trial 4	0.966	2.61
	Trial 5	0.052	2.57		Trial 5	0.966	2.40
	Trial 6	0.163	7.80		Trial 6	0.909	4.83
	Trial 7	0.179	3.58		Trial 7	0.966	2.71
	Trial 8	0.019	3.85		Trial 8	0.965	2.77
	Trial 9	0.253	3.45		Trial 9	0.969	2.50
	Trial 10	0.264	4.49		Trial 10	0.941	3.71
	<b>Average</b>	<b>0.124</b>	<b>4.02</b>		<b>Average</b>	<b>0.964</b>	<b>2.90</b>
<b>Low Stiffness ASC &lt;15</b>	Trial 1	0.962	0.74	<b>All Data (removing outliers)</b>	Trial 1	0.976	2.62
	Trial 2	0.973	0.63		Trial 2	0.975	2.27
	Trial 3	0.968	0.64		Trial 3	0.974	2.55
	Trial 4	0.955	0.88		Trial 4	0.966	2.61
	Trial 5	0.961	0.64		Trial 5	0.966	2.40
	Trial 6	0.952	0.77		Trial 6	0.952	3.19
	Trial 7	0.977	0.35		Trial 7	0.979	2.24
	Trial 8	0.973	0.63		Trial 8	0.965	2.77
	Trial 9	0.982	0.39		Trial 9	0.976	2.32
	Trial 10	0.973	0.58		Trial 10	0.973	0.58
	<b>Average</b>	<b>0.969</b>	<b>0.63</b>		<b>Average</b>	<b>0.971</b>	<b>2.36</b>

The ASC measurements for the Cochlear implant sample were reported in the previous section (Figure 3.11). Between testers there is a difference in the mean ASC value of 6.9 and a standard deviation of all measurements of 5.1. With this limited sample, the results suggest that hand testing with the Cochlear implant-abutment system introduces more variability compared to the Oticon implant-abutment system, particularly between testers. This is likely due to the difference in abutment design between the two systems. The lip on the Oticon abutments makes it much easier to consistently strike the same location compared to the chamfer and straight edge design of the Cochlear abutments. More samples of the Cochlear implant-abutment system should be tested with more participants to get a better idea of the intra-user and inter-user reliability across the range of conditions. A more specific clinical protocol or instructions and training may be required for testing with the Cochlear abutments.

## **3.5. Comparison Between ASIST and Osstell™ for BAHA Systems**

This section presents a comparison of the ASIST and Osstell™ ISQ for BAHA implant stability measurement in a laboratory setting. The two techniques are compared in terms of the ability to assess interface properties independent of system components and sensitivity to changes in interface properties for a BAHA implant-abutment system.

### **3.5.1. Experimental Testing**

The 12 Oticon Medical implant specimens described in Section 3.3.1. were used in this analysis. Four types of Oticon Medical implants were tested. Two samples of each type were installed in FRB-20 and one sample of each type was installed in PLA. Each of the 12 implant specimens were tested with three different sizes of Oticon Medical Ponto abutments (6 mm, 9 mm, 12 mm) for a total of 36 implant-abutment combinations. One Cochlear Baha® Connect implant sample (BI300) installed in the FRB-20 material was tested with four sizes of BA400 abutments (6 mm, 8 mm, 10 mm, 12 mm).

The following test protocol was performed for each implant specimen. The disc containing the implant was clamped to a platform. Five measurements with the Osstell™ were recorded at the level of the implant, removing and reattaching the SmartPeg™ (type 9) between measurements. An abutment was attached with 25 Ncm of torque and five measurements with the Osstell™ were recorded, removing and reattaching the SmartPeg™ (type 55) between measurements. The Osstell™ system was tested in one orientation and kept constant throughout testing. In the few cases where two measurements were reported by the Osstell™, the lower number was recorded as a more conservative estimate of the implant stability. The abutment was removed and another abutment was attached. The process was repeated for each implant-abutment combination. For the Cochlear implant specimen, Osstell™ measurements were not recorded at the level of the implant because the appropriate SmartPeg™ (type 30) was not available at the time of testing and thus measurements were taken only with each of the four abutments.

A similar test protocol was followed for the ASIST measurements as described in Section 3.3.1. The disc containing the implant sample was clamped to a platform and an abutment was attached with 25 Ncm of torque. The ASIST handpiece was held in a custom stand to control the measurement position (Swain et al. 2008a) and five measurements with the ASIST were recorded. The abutment was removed and another abutment was attached. This procedure was repeated for each implant-abutment combination.

### 3.5.2. Outcome Measures

The outcome measure for the ASIST is the ASC value and the outcome measure for the Osstell™ is the ISQ, which are both non-dimensional values with a higher value indicating a stiffer interface. With both systems, the measurement is taken at some distance away from the implant-support interface (i.e. on the abutment or on the SmartPeg™ attached to the implant or abutment) (Figure 3.12). Thus it is important to understand how the measurement is related to the properties at the interface.

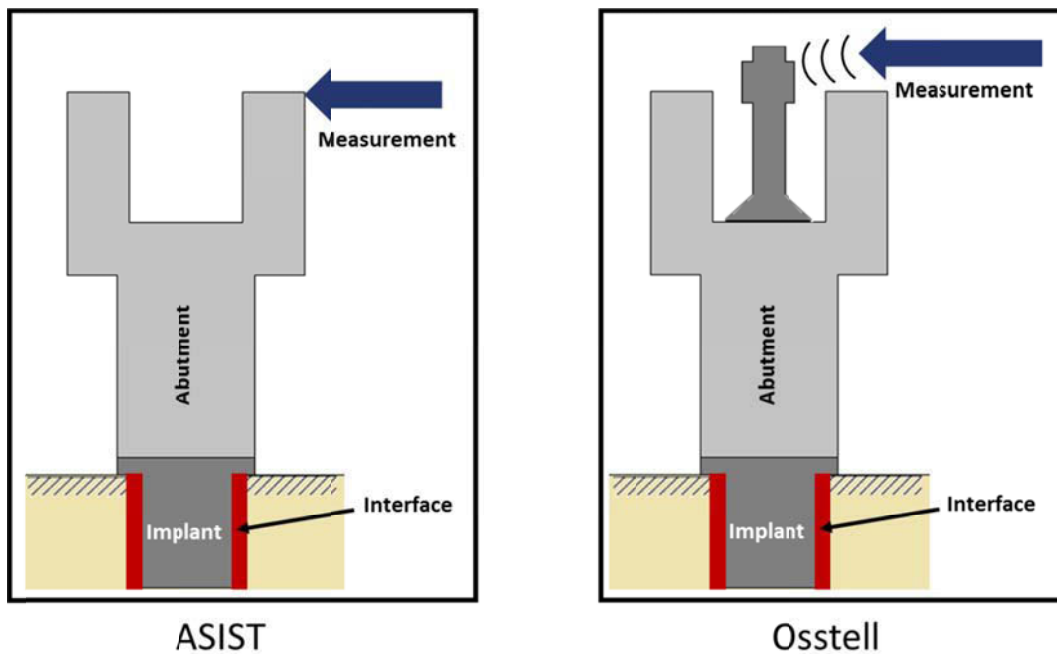


Figure 3.12: ASIST and Osstell™ measurement methods. Measurements are taken at the level of the abutment or SmartPeg™ and used to indicate the properties at the bone-implant interface.

The Osstell™ system uses RFA which is based on the idea that changes in the resonance frequency (or natural frequency) of the system indicate changes at the bone-implant interface, assuming there are no other changes in the system (Meredith et al., 1996).

The aim of this section is to compare the ASIST and Osstell™ for stability measurement of BAHA implants in terms of their ability to assess the interface stability independent of the abutment length and their sensitivity to changes in the support conditions. The effect of abutment length is assessed by examining each implant specimen with the different sized abutments attached. Since the interface does not change when the different abutments are used, the stability assessment should ideally remain constant for a given implant specimen. Additionally, the sensitivity to differences in support conditions is assessed for the Oticon Medical system by examining the differences in the stability measurement (ASC or ISQ) for the different installations of the same implant type.

# **Chapter 4: Experimental Results with Bone Anchored Hearing Aid Systems**

This chapter presents the results of the laboratory evaluation of the ASIST for BAHA systems. The experimental procedures for application of the ASIST to the Oticon Medical Ponto System and the Cochlear Baha® Connect System were described in Chapter 3 above and the goal of this chapter is to present the results of those analyses. Additionally, the experimental procedures for a laboratory comparison between the ASIST and the commercially available Osstell™ ISQ for BAHA implant systems was presented in Chapter 3 and the results of that comparison are presented and discussed in this chapter.

## **4.1. Application to Oticon Medical Ponto System and Cochlear Baha® Connect System**

### **4.1.1. Oticon Medical Ponto System**

The results from a representative Oticon Medical implant sample (4.50 mm diameter, 4 mm length) with three abutment lengths are shown in Figure 4.1. The differences in the acceleration signal with each abutment are clearly visible in the figure. These differences are expected and illustrate that changing the abutment changes the system and thus changes the measured acceleration. It can be observed that the shorter abutments (e.g. 6 mm) result in a higher fundamental frequency than the longer abutments (e.g. 12 mm). There is a good fit between the measured acceleration signal and the analytical model prediction in all cases with average  $R^2$  values between 0.97 and 0.98 (averaged over repeated measurements for each implant-abutment combination). Additionally, as shown in the figure, despite the significant change in the measured response, the calculated ASC values are within 4.0 points (range: 37.9-41.9) for this example.

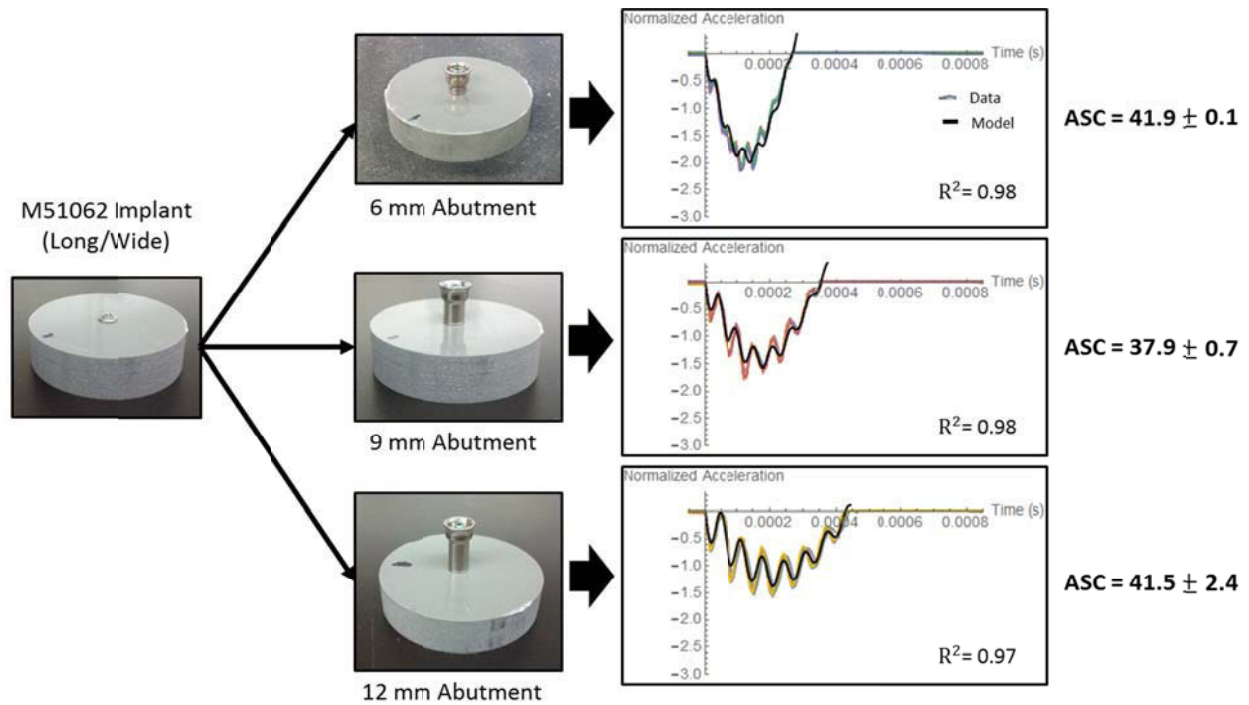


Figure 4.1: Representative example for one Oticon implant sample with three abutment lengths

The average ASC values for each Oticon Medical implant-abutment combination are shown in Figure 4.2. For the Oticon Medical system, the average ASC values ranged from 7.6-78.1 (average over repeated measurements). Considering each group of bars in Figure 4.2 (each implant sample with the three abutments), the effect of abutment length on the ASC value was found to be small as the average difference in ASC value due to changes in abutment length is 2.9 or 8.0% of the ASC value. It can be seen from Figure 4.2 that, in general, samples with higher ASC values have a slightly larger variation due to changing abutment length. At higher values of the interface stiffness and higher natural frequencies, small changes in the frequency response can result in larger changes in the ASC value. The sensitivity of the ASC value in the higher frequency range should not be clinically important because implants with higher ASC values would be considered stable and would not be of clinical concern.

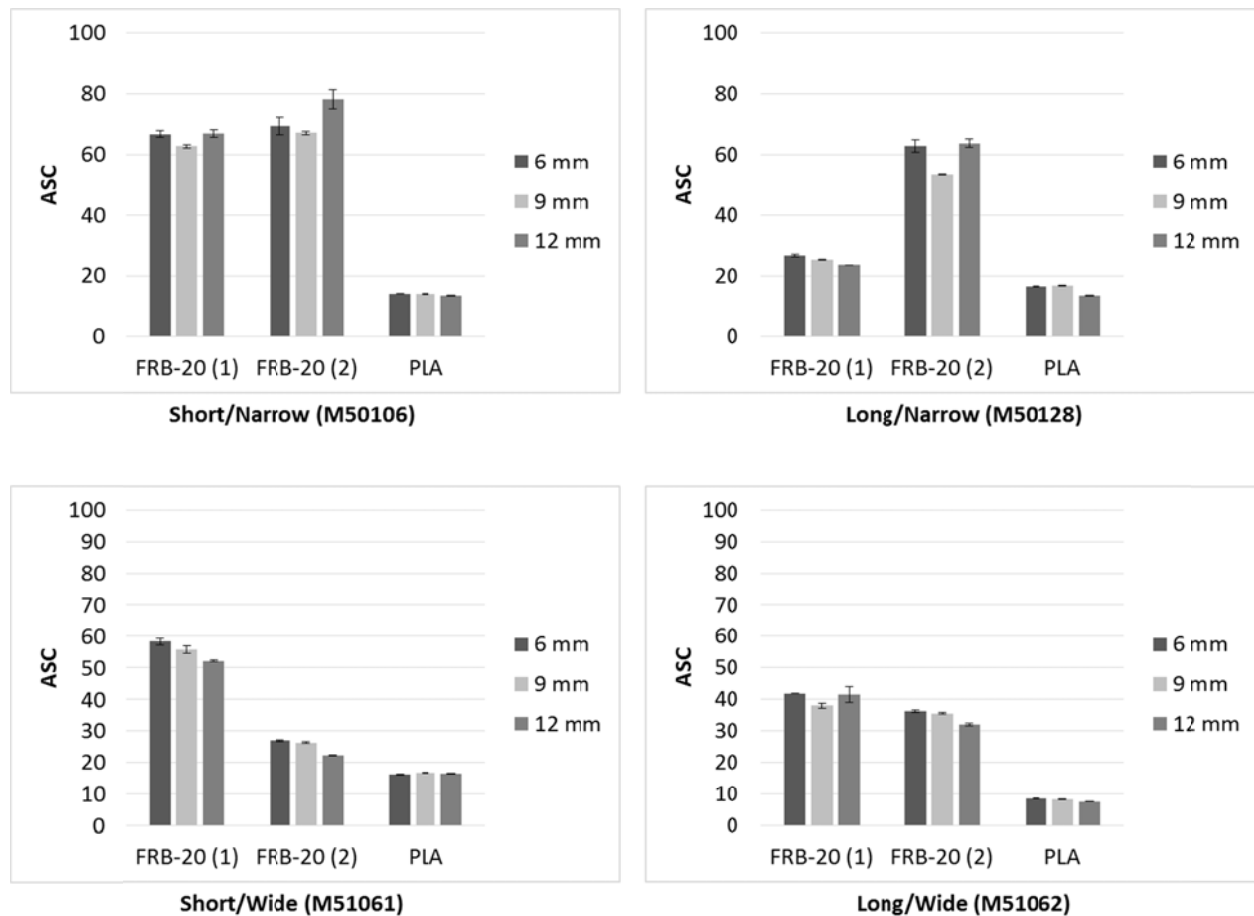


Figure 4.2: ASC values for all Oticon samples with three abutment lengths (6 mm, 9 mm, 12 mm)

Comparing the different groups of bars in each subfigure in Figure 4.2, there are clear differences in the ASC values determined for each implant sample, suggesting that the measure is sensitive to changes in the support conditions. Figure 4.3 shows a representative example for two different samples of the same Oticon Medical implant type (4.50 mm diameter, 4 mm length). The first sample is installed in FRB-20 (same sample shown in Figure 4.1) and the second sample is installed in PLA. Both samples shown in Figure 4.3 have a 9 mm abutment attached. There are clear differences in the measured acceleration response with the PLA sample having a lower fundamental frequency than the FRB-20 sample. In this case, this results in a 78% difference in the ASC value (ASC = 37.9 for FRB-20, ASC = 8.3 for PLA). In both cases there is a good fit between the measured acceleration signal and the analytical model prediction with  $R^2$  values of 0.98 and 0.95 for the stiffer and softer samples respectively.

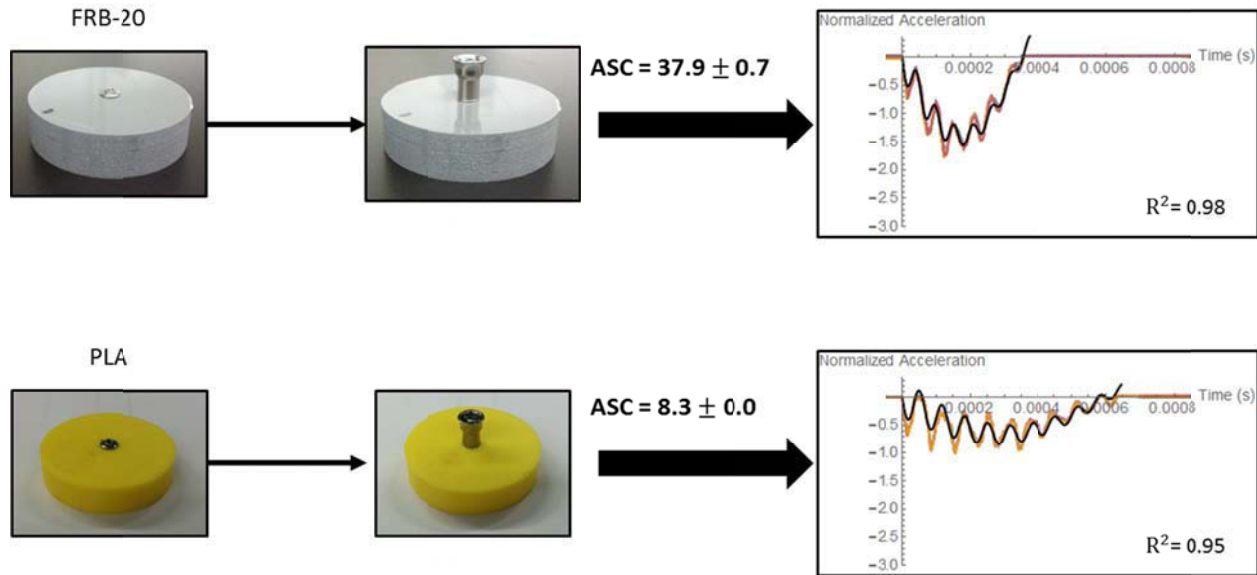


Figure 4.3: Representative example for two different samples of one Oticon implant type (4.50 mm diameter, 4 mm length) and 9 mm abutment

#### 4.1.2. Cochlear Baha® Connect System

Figure 4.4 shows the results for the Cochlear implant sample with four different abutments. There is a reasonably good fit between the measured acceleration signal and the analytical model prediction in all cases with  $R^2$  values between 0.94 and 0.98. The difference in ASC values due to changing abutment length with the Cochlear implant system is 2.8 or 9.5% of the ASC value. The range of ASC values for the four different abutments is 26.6 – 31.8.

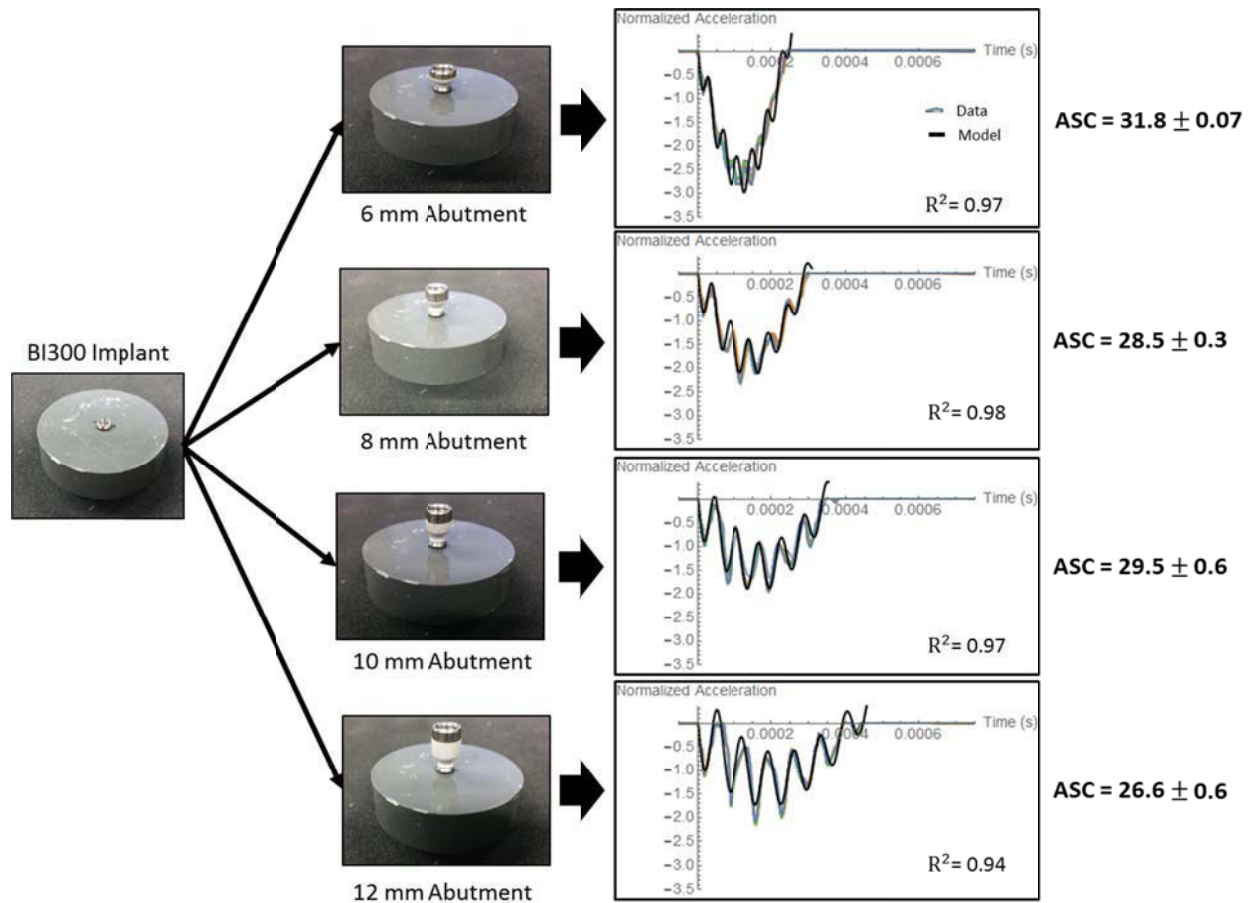


Figure 4.4: One Cochlear implant sample with four different abutment lengths

#### 4.1.3. Application to Additional Abutment (14 mm Oticon Medical)

An additional Oticon Medical abutment of 14 mm in length became available from the manufacturer after the other abutments had been assessed. A sample was obtained to verify the applicability of the ASIST procedure for this additional abutment size. The impact stiffness and torsional stiffness coefficient were the same as those used for the other Oticon abutments ( $K_I = 2.9 \times 10^6$  N/m;  $\alpha = 0.26$ ). The mass and geometry parameters of the 14 mm abutment were included in the model as shown in Table 4.1. Nominal values were used for the diameter and length while the mass moment of inertia was estimated based on a simplified geometric model, similar to the other Oticon Medical abutments. The location of the center of mass was also obtained in a similar manner to the other Oticon Medical abutments. The center of mass was first estimated based on the simplified geometric model (0.00726 mm) and then adjusted to an

average value that best matched sample data from the FRB-20 implant specimens. One sample of data from 7 of the 8 FRB-20 implant samples was used (Note: the short wide implant M51061 FRB-20(2) was not used because the implant had come loose from the FRB-20 material prior to testing). For each data sample, the location of the center of mass of the abutment was varied  $\pm 10\%$  from the calculated value in a total of 20 discrete values. For each value of  $\bar{y}_A$ , the model was used to determine the  $R^2$  value between the model prediction and the measured data. The interface stiffness ( $k$ ) was fixed to the average value obtained using the 6 mm, 9 mm, and 12 mm abutments with the particular implant specimen. The value of  $\bar{y}_A$  that resulted in the best fit between the model and the data as measured by the  $R^2$  value was recorded and the average of all 7 values was used as the value of  $\bar{y}_A$  in the model. The values determined for the 7 implant samples are shown in Table 4.2 along with the average value.

**Table 4.1: Mass and geometry parameters of the Oticon 14 mm abutment**

<b>Oticon Medical Abutment</b>	<b>Mass (g)</b>	<b>Shaft Diam. (mm)</b>	<b>Length (mm)</b>	<b><math>\bar{y}_A</math> (mm)</b>	<b><math>J_A</math> (g mm<sup>2</sup>)</b>
<b>14 mm</b>	1.13	5.00	14.00	6.96	20.16

**Table 4.2: Average interface stiffness values (average of 6 mm, 9 mm, and 12 mm abutments) and center of mass values for the 14 mm abutment for the FRB-20 implant specimens**

	<b>Average <math>k</math> (<math>\times 10^{12}</math> N/m<sup>3</sup>)</b>	<b><math>\bar{y}_A</math> 14 mm (m)</b>
<b>M50106 FRB-20 (1)</b>	11.64	0.00691
<b>M50106 FRB-20 (2)</b>	12.72	0.00676
<b>M50128 FRB-20 (1)</b>	3.36	0.00699
<b>M50128 FRB-20 (2)</b>	7.99	0.00668
<b>M51061 FRB-20 (1)</b>	8.21	0.00706
<b>M51061 FRB-20 (2)</b>		
<b>M51062 FRB-20 (1)</b>	4.49	0.00714
<b>M51062 FRB-20 (2)</b>	3.84	0.00714
<b>Average</b>		<b>0.00696</b>
<b>SD</b>		<b>0.00018</b>

The 14 mm abutment was tested with one FRB-20 specimen of each type of implant following the same protocol that was used for the other abutments.

The results are shown in Figure 4.5 (average ASC values with error bars representing one standard deviation for the five measurements with each implant-abutment specimen). The results are presented along with the ASC values for the same implant specimens with the other abutment sizes (6 mm, 9 mm, 12 mm).

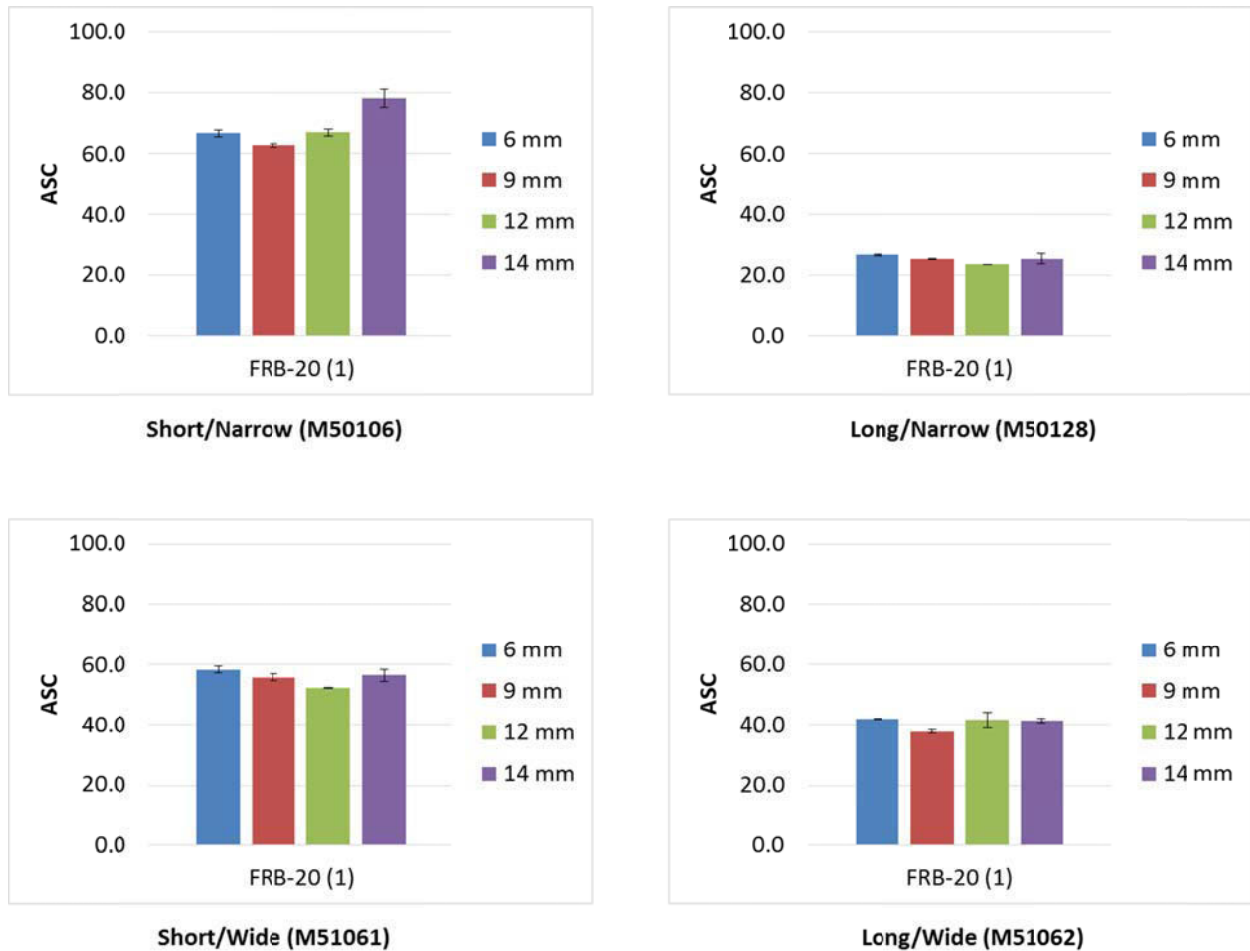


Figure 4.5: ASC results for FRB-20(1) samples including 14 mm abutment

For the long/narrow (M50128), short/wide (M51061), and long/wide (M51062) specimens, the ASC calculated for the 14 mm abutment (average over 5 strikes with a given specimen) are within 1.0 ASC of the average ASC value with the 6 mm, 9 mm, and 12 mm abutments for the given specimen as shown in Table 4.3. For the short/narrow (M50106) specimen, the 14 mm abutment resulted in an ASC value of 78.1 while the average of the 6 mm, 9 mm, and 12 mm abutments was 65.5. This is a difference of 12.7 ASC values. There is a larger difference for this

specimen is likely due to the fact that is in the higher ASC range where the results are sensitive to small changes in the measured frequency (see sensitivity results in Section 2.4.2.). In a clinical situation, an implant with an ASC of this range would be considered stable regardless of the high difference in the ASC value between abutments.

**Table 4.3: ASC values for the FRB-20(1) specimens. Comparison of the average ASC from 6 mm, 9 mm, and 12 mm abutments and the 14 mm abutment.**

	<b>Average ASC (6 mm, 9 mm, 12 mm abutments)</b>	<b>ASC (14 mm abutment)</b>	<b>Difference</b>
<b>M50106 FRB-20(1)</b>	65.5	78.1	12.7
<b>M50128 FRB-20(1)</b>	25.2	25.4	0.2
<b>M51061 FRB-20(1)</b>	55.4	56.4	1.0
<b>M51062 FRB-20(1)</b>	40.5	41.4	0.9

Example signals from each of the implant types with the 14 mm abutment are shown in Figure 4.6. The measured data and model response are shown for each sample. The  $R^2$  values are the average of the five strikes for each sample. The average and standard deviation of the ASC values are also shown for each sample.

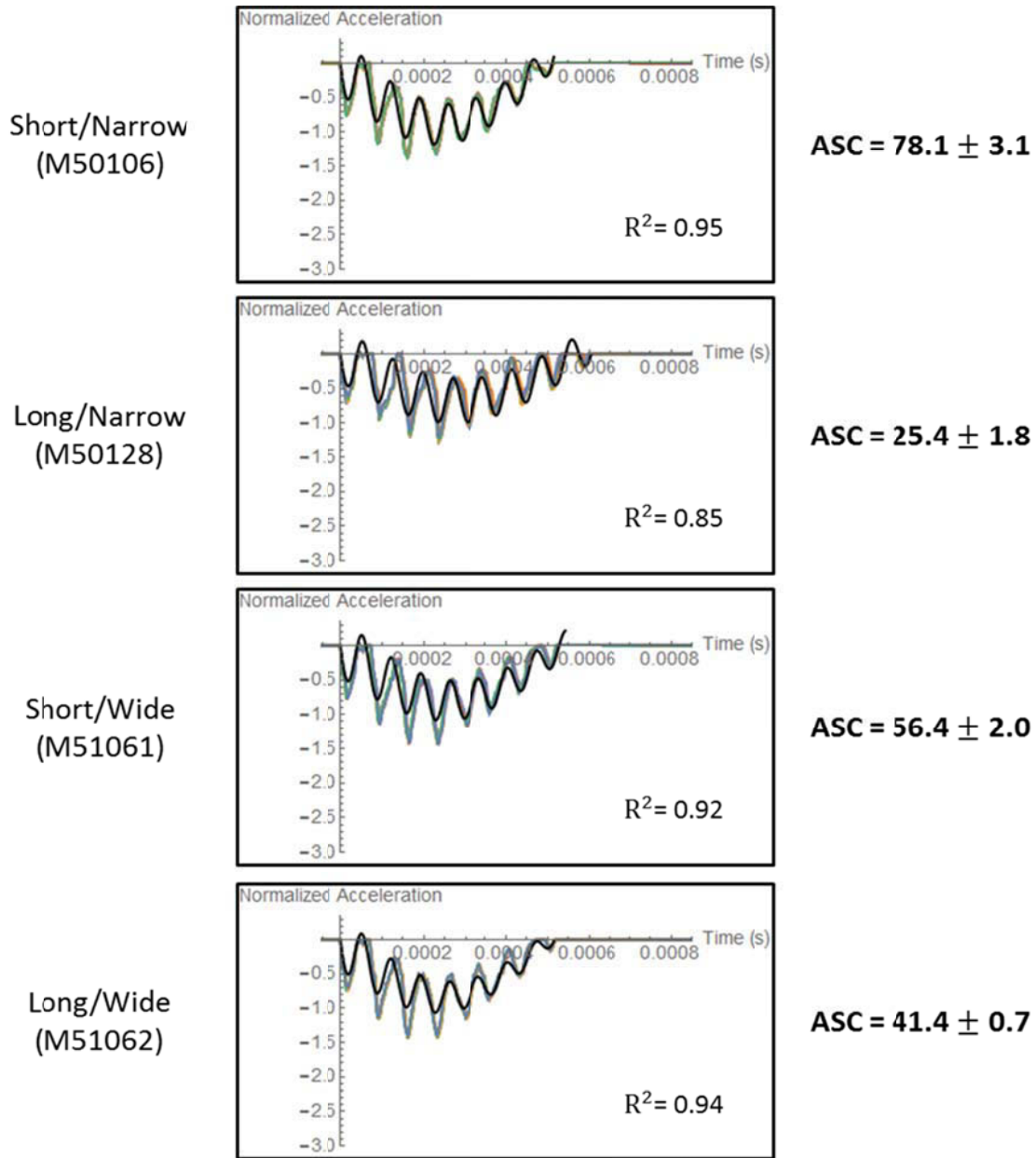


Figure 4.6: Example signals for each implant specimen (FRB-20(1)) with the 14 mm abutment. The colored lines are the measured data (16 strikes) and the black lines are the model response.

#### 4.1.4. Damping Ratio

The damping ratio of the higher frequency component of the measured acceleration was estimated from the curve fit approximate ( $\zeta_2$ ) for all cases. A *t*-test was used to test for differences in the damping ratio between groups (significance  $p < 0.05$ ). Grouping all of the Oticon implant samples together, the damping ratio was  $0.026 \pm 0.017$  (average  $\pm$  SD) with a

range of 0.005 – 0.081. The Oticon FRB-20 samples had a significantly lower damping ratio ( $0.021 \pm 0.010$ ) than the Oticon PLA samples ( $0.037 \pm 0.023$ ) with  $p = 1.6 \times 10^{-9}$ . The Oticon implant samples were found to have a significantly higher damping ratio than the Cochlear samples, which had a damping ratio of  $0.015 \pm 0.006$  ( $p = 0.003$  using all Oticon samples and  $p = 0.005$  using only FRB-20 Oticon samples). It should be noted that there was only one Cochlear sample, so this group consists of only 20 measurements (5 trials with each of 4 abutments on the single implant sample) while the Oticon group consists of 180 measurements (5 trials with 36 implant-abutment combinations). In general, it was found that the BAHA implant samples had relatively low damping with average damping ratios less than 4% across groups.

## 4.2. Comparison Between ASIST and Osstell™ for BAHA Systems

The ASC and ISQ measurements for each Oticon Medical implant-abutment combination are shown in Figure 4.7. Each sub-figure shows one implant specimen. The different colored bars represent the different abutment lengths and, for the ISQ, the implant level measurement is also shown. In this case, bars that are at the same height are considered “better” since they are meant to indicate the underlying interface condition, which are the same for each group of bars. It can be seen that abutment length has only a small effect on the measured ASC value. The difference in ASC due to changing abutment length was found to be  $2.9 \pm 3.0$  (average  $\pm$  SD) or 8.0% of the ASC value on average as discussed earlier. Conversely there are large variations in ISQ value with varying abutment lengths with a clear relationship of decreasing ISQ with increasing abutment length as has been noted previously by many researchers (Nelissen et al., 2015). For example, consider the long/narrow implant (M50128) FRB-20(2) installation. The ISQ values range from 53.0 – 90.6 (average over repeated measures). According to the clinical guidelines cited by Osstell ([www.osstell.com/clinical-guidelines/](http://www.osstell.com/clinical-guidelines/)), an implant with ISQ greater than 70 is considered to have high stability and is eligible for immediate loading while an implant with ISQ less than 60 is at risk and should be monitored. According to these guidelines, this example implant could be classified having low stability, medium stability, or high stability depending on the abutment that is used or if the measurement is taken at the implant level resulting in vastly different clinical recommendations.

It can be noted that the ISQ difference is most pronounced when stepping from the implant level to the 6 mm abutment measurement with a decrease in ISQ of  $25 \pm 4.2$  (average  $\pm$  SD) or a 29% decrease on average. For both the ASIST and Osstell™ systems, we can consider the maximum variation in stability measurement between the three abutment lengths for each implant specimen. Averaged over the 12 Oticon Medical implant specimens, the maximum variation in ASC was found to be  $4.4 \pm 3.4$  or 12% of the ASC value, while the maximum variation in ISQ was found to be  $17 \pm 3.2$  or 34% of the ISQ value.

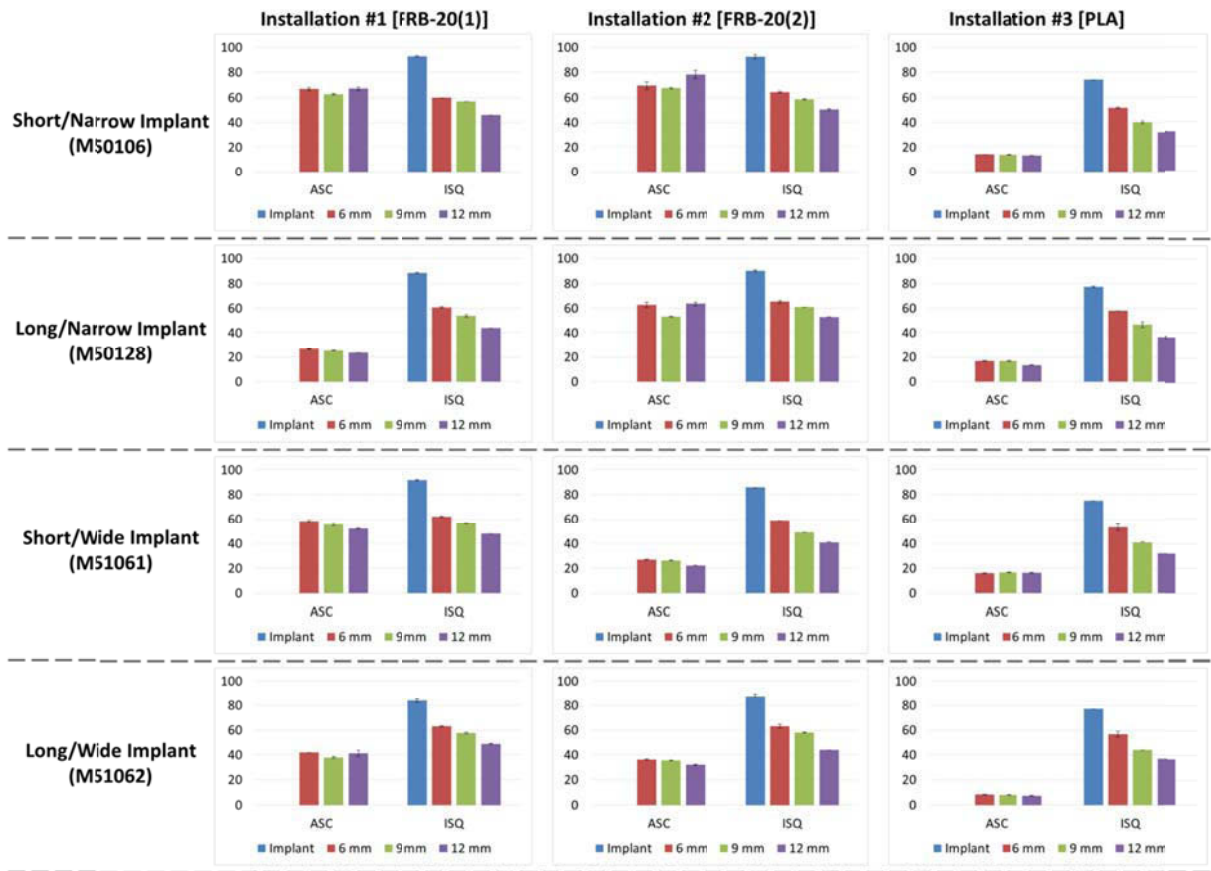
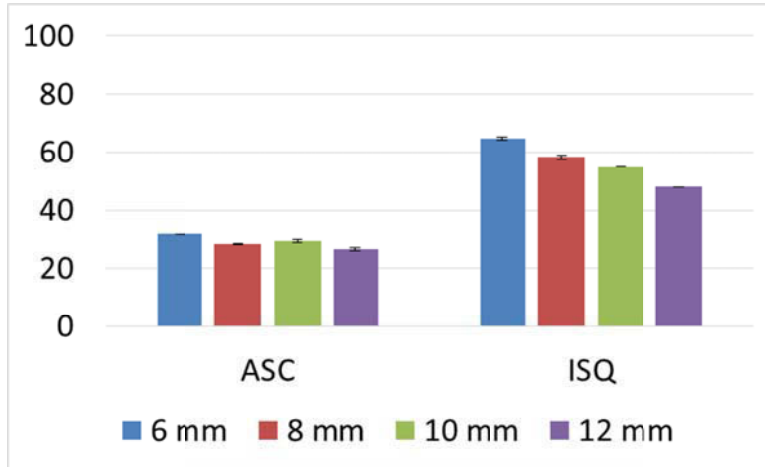


Figure 4.7: ASC and ISQ values for each Oticon Medical implant-abutment combination comparing different abutment lengths for each implant specimen

The ASC and ISQ measurements for each Cochlear implant-abutment combination are shown in Figure 4.8. Again, there is a small variation in the ASC value due to the abutment length ( $2.8 \pm 1.4$  or 9.5% of the ASC value on average). Similar to the Oticon Medical results, there is a larger variation in ISQ due to abutment length with a clear relationship of decreasing ISQ with

increasing abutment length. The maximum variation in ASC between the four abutment lengths was 5.2 or 18% of the ASC value, while the maximum variation in ISQ was 16.8 or 30% of the ISQ value.



**Figure 4.8: ASC and ISQ values for the Cochlear implant specimen comparing the measurements with the four different abutment lengths**

The ASC and ISQ measurements for the Oticon Medical implants are again shown in Figure 4.9 highlighting the variations in measurement between the three different support conditions (FRB-20(1), FRB-20(2), and PLA) with the same type of implant. Each sub-figure in Figure 4.9 shows one type of implant with a particular abutment (or no abutment) attached. The different colored bars represent the different support conditions and the two groups of bars separate the ASC and ISQ values. Here the purpose is to investigate differences in the underlying support conditions; thus the height of the bars within a group need not be the same. In this case, larger differences within each group of bars indicate higher sensitivity. The first column of figures shows the results for the implant only tests (without an abutment attached). In these cases, only the ISQ values are shown because it is not possible to measure the implant stability using the ASIST without an abutment attached.

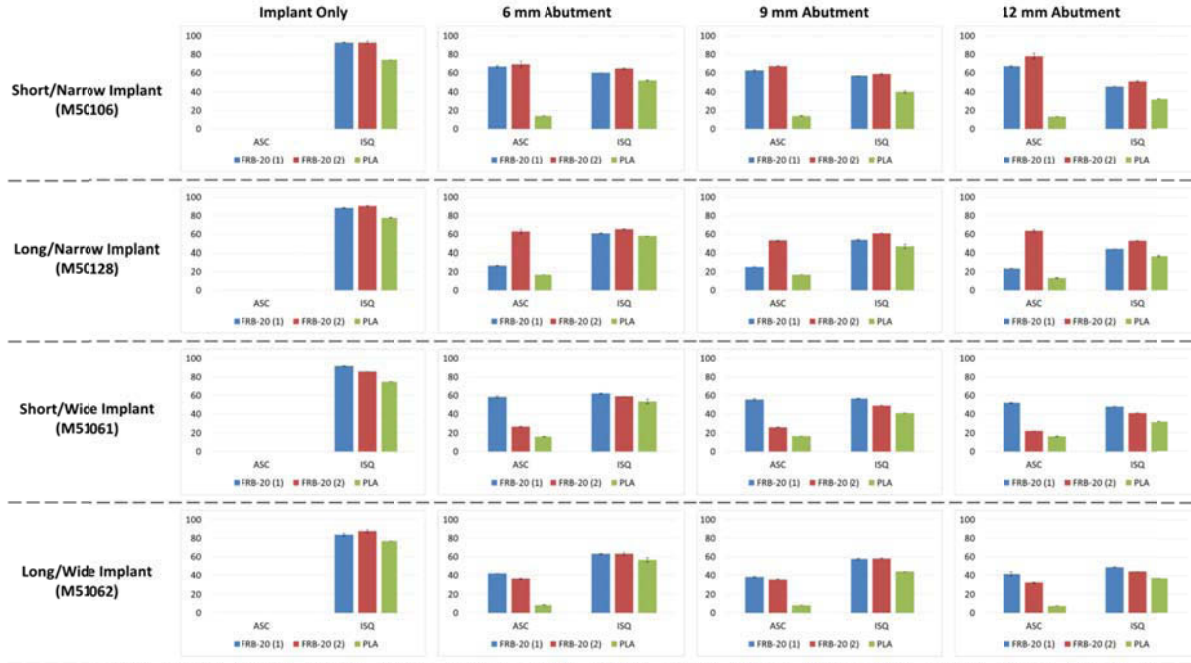


Figure 4.9: ASC and ISQ values for each implant-abutment combination comparing installations of the same type of implant

The two specimens of each Oticon Medical implant type installed in FRB-20 broadly followed the same installation procedure. Variations in the stability values between the two similar specimens were noted in some cases. Since the same disc material and the same adhesive were used for the two specimens, these variations are most likely attributed to uncontrolled differences in the installation technique. The implants were installed by hand, so many variables may contribute to differences in the implant stability. Even a small unintended lateral motion while drilling could have affected the fit between the implant and the base material. Other factors which may contribute to differences include the installation torque (which was not controlled), different amounts of epoxy, or slight angulation in the implant. While similar comments apply to the PLA material, it should be noted that the PLA samples were intentionally created to provide lower stability compared to the FRB-20 samples.

The three specimen types (FRB-20(1), FRB-20(2), and PLA) represent three different interface conditions for the same type of implant. Both the ASIST and the Osstell™ were able to detect differences in the stability between the three installations and both systems were in agreement in

terms of the relative ranking of the three specimens in each case. The ASIST was found to be more sensitive to differences in implant stability than the Osstell™ (including both differences in installation technique and differences in the support material) by showing a much larger variation in the stability measurements between the different specimens. For example, we can consider the FRB-20 specimens of the long/narrow implant type (M50128). Both the ASIST and Osstell™ show a difference in the stability measurement between these two specimens; however the ASIST shows a much greater difference than the Osstell™. If we consider for example the 12 mm abutment, the increase in ASC from the FRB-20(1) specimen to FRB-20(2) is 40.3 (from 23.5 to 63.8; 172% increase) while the increase in ISQ is 9.0 (from 44 to 53; 21% increase). Similarly, we can consider the change in implant stability from the FRB-20(1) specimen to the PLA specimen for the long/wide implant type (M51062) with the 12 mm abutment. The decrease in ASC is 34.0 (from 41.5 to 7.5; 82% decrease) while the decrease in ISQ is 12 (from 49 to 37; 24% decrease).

### **4.3. Summary**

For the ASIST system, there is a good fit between the measured acceleration signal and the analytical model in all cases, indicating that the analytical model is a good representation of the systems analyzed. It was shown that there is minimal effect due to abutment length on the ASC value, indicating that the method is able to isolate the interface properties from the overall system and the measurement is independent of the attached components. In clinical use, the abutment is only changed in rare cases, so one may argue that having the measure independent of the abutment length is not important when looking at relative changes over time. However, this aspect of the ASIST gives us confidence that the measurement is representative of the interface properties and would allow for consistent comparisons across clinical situations. It also allows comparison over time for the few patients where the abutment must be changed. Additionally, it may allow comparisons between patients or development of a suggested range of ASC values that indicate normal or healthy implants. Independence from the system components simplifies the interpretation of the results for the clinician because the interpretation of the ASC is the same regardless of the abutment length for the particular patient.

The ASIST measurement was found to be sensitive to changes in interface stiffness which is of primary importance. Ultimately this system will be used clinically to detect changes over time so it must be sensitive enough to detect meaningful changes.

This chapter also presented a laboratory comparison between the ASIST and Osstell™ ISQ for the stability measurement of the Oticon Medical Ponto and Cochlear Baha® Connect implant-abutment systems. The implant installations used in this study were used to simulate BAHA implants installed in bone. The range of ISQ values reported in this study (32.0 – 65.4 for installations with an abutment) are similar to values for clinical ISQ measurements reported in the literature (44 – 76) for a variety of BAHA implant-abutment systems (Faber et al., 2012; Foghsgaard and Caye-Thomasen, 2014; McLarnon et al., 2012). This suggests that the results presented here should be representative of typical clinical situations.

Because of the use of an analytical model, the ASIST was better able to isolate the actual support conditions than the Osstell™. This is evident from Figure 4.7 and Figure 4.8 which illustrate the much lower variation in stability values with changing abutments on an individual implant installation (maximum difference of 12%) compared to the ISQ measurements (maximum difference of 34%). The large variation in ISQ with the same implant installation would make it more difficult to establish clinical guidelines because the abutment length must be included in the interpretation. Because of the comparatively low variation with different attachments to the implant, the ASC has the potential to establish guidelines for clinical assessment independent of the specific details of the components connected to the implant.

The ASC and ISQ values for different installations of the same type of implant were examined (Figure 4.9). For all implant-abutment combinations, the ASC and ISQ values were in agreement in terms of the ranking of stiffness for the three installations of each type of implant. The relative changes in stability values were larger for the ASIST than the Osstell™ ISQ. The ASIST had a maximum variation in ASC of 64.7 (83% decrease), while the Osstell™ ISQ showed a maximum variation of 19 (37% decrease). In both cases, this maximum difference occurred between the FRB-20 (2) and the PLA samples of the short/narrow implant (M50106). In general, the variation in ISQ due to abutment length was found to be larger than the variation due to differences in interface stiffness between installations. This suggests that the Osstell™ appears to be more

sensitive to geometric changes (i.e. changing abutment length) than actual changes in the interface properties. Conversely, the ASIST is more sensitive to the interface stiffness and would thus be better able to detect small variations in interface properties compared to the Osstell™ ISQ.

The Osstell™ company (Osstell, Göteborg, Sweden) provides clinical guidelines indicating low, medium, and high implant stability based on the ISQ value (Figure 4.10) where  $ASC < 60$  indicates low stability,  $ASC$  between 60 – 65 and between 65 – 70 indicate varying levels of medium stability, and  $ASC > 70$  indicates high stability. The clinical guidelines do not account for the length of the abutment in their interpretation. However, we have shown that the abutment length has a significant impact on the resulting ISQ value. For example all of the installations for the Oticon implant system examined here have ISQ values that span the entire range indicated in the clinical guidelines (from less than 60 to greater than 70) depending on the abutment length that is used or if the measurement is taken at the implant level (Figure 4.7). Thus with the ISQ measurement, a clinician may interpret the same implant installation as having very low stability, medium stability, or high stability depending on the abutment that is used for testing. Additionally, we found that even implants with very high stability (for example the short/narrow M50106 or long/narrow M50128 FRB-20(2) installations) can have ISQ values below 60 when a 12 mm abutment is used (Figure 4.7). This suggests that patients with long abutments such as the 12 mm or 14 mm abutment may never register an ISQ reading above the “low stability” level simply because of the length of their abutment. These clinical interpretations make it essential to have the ability to isolate the actual interface properties from the implant-abutment system and present the stability measurement independent of the attached components. The results for the Osstell™ ISQ presented here agree with findings by Nelissen et al. (2015) as well as their recommendations that the implant and abutment type and length should be specified when presenting ISQ values because these parameters influence the ISQ value. Additionally, Nelissen et al., (2015) recommended that in clinical use conclusions should not be based on individual ISQ measurements at a certain time, but that ISQ measurements are most meaningful as a trend in an individual patient or population over time. From the comparison presented here, the ASIST shows tremendous potential to provide more meaningful stability measurements in a clinical setting compared to the ISQ.

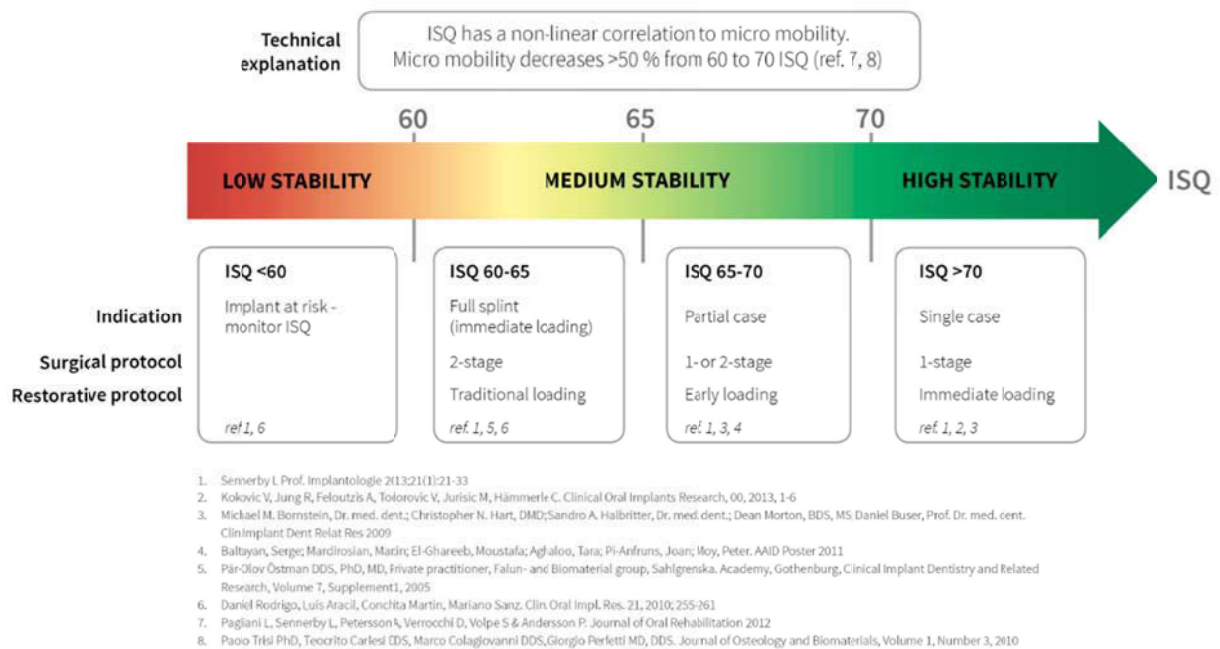


**Figure 4.10: Clinical guidelines for implant stability based on ISQ reading (from: <http://www.osstell.com/clinical-guidelines/>)**

This chapter has presented a quantitative comparison between the Osstell™ ISQ and the ASIST for implant stability measurement. Both systems are able to provide an indication of variations in stiffness at the bone-implant interface. It was found that the ASIST is more sensitive to changes in the implant stability and shows much less variation due to changes in abutment length compared to the Osstell™ ISQ.

# Chapter 5: BAHA Clinical Study

This chapter describes a clinical evaluation of BAHA implant stability using the ASIST. The longitudinal observational study was carried out in collaboration with the Institute for Reconstructive Sciences in Medicine (iRSM) located at the Misericordia Community Hospital in Edmonton Alberta. The aim of the study was to evaluate longitudinal changes in interface stability for BAHA patients from the time of surgery to one year post-operative. As per the usual clinical protocol at iRSM, the patients received their hearing processor at three months post-surgery. Approval was obtained from the University of Alberta Health Research Ethics Board and all patients signed informed consent prior to participation in the study. ASIST measurements were collected at the time of surgery and at the regular clinical follow up appointments over approximately one year.

## 5.1. Participants

The patient study group is summarized in Table 5.1. Patients who were selected to receive a bone anchored hearing aid at iRSM as part of their rehabilitation for hearing loss were considered for this study. There were 39 participants enrolled with an average age at the time of surgery of 50.1 (range: 17 – 79 years). One third of the participants (n = 13) were male and two-thirds (n = 26) were female. All participants had a one-stage surgery to install a bone anchored implant and abutment and all participants had a single implant installed (i.e. no bilateral patients). Implants were installed with 40 Ncm of torque, and abutments were attached with 25 Ncm of torque. Participants from three different surgeons were included in the study. All participants had the Oticon Ponto implant-abutment system. Thirty-one (79%) of the patients had the 4 mm narrow platform (3.75 mm diameter) implant. Later in the study, seven patients (17.9%) had the 4 mm wide platform (4.50 mm diameter) BHX implant which was the newer design from Oticon and 6 of those 7 patients had the Minimally Invasive Ponto Surgery (MIPS) surgical technique which is designed to reduce disruption to the surrounding soft tissue. For these 7 patients, the implants and abutments were preassembled in the package and installed in one step. One patient (2.6%) had a 3 mm narrow platform implant due to a reduced bone thickness. For each patient, the abutment size was chosen by the surgeon at the time of surgery. Four patients (10.3%) had a 6

mm abutment, 25 patients (64.1%) had a 9 mm abutment, and 10 patients (25.6%) had a 12 mm abutment. It should be noted that one of the patients with a 12 mm abutment (Patient 4) had his abutment changed for clinical reasons to a 14 mm abutment approximately 8 months after surgery.

**Table 5.1: Clinical Study Participant Summary**

<b>Total Participants</b>	39	
<b>Age at Surgery (yr)</b>	50.1 (range: 17 - 79)	
<b>Gender (n(%))</b>		
<b>Male</b>	13 (33.3%)	
<b>Female</b>	26 (66.7%)	
<b>Surgeon (n(%))</b>		
<b>Surgeon 1</b>	15 (38.5%)	
<b>Surgeon 2</b>	15 (38.5%)	
<b>Surgeon 3</b>	9 (23.1%)	
<b>Implant (n(%))</b>		
<b>Oticon 4 mm/Narrow</b>	31 (79.5%)	
<b>Oticon 4 mm/Wide (BHX)</b>	7 (17.9%)	<b>6 MIPS</b>
<b>Oticon 3 mm/Narrow</b>	1 (2.6%)	
<b>Abutment (n(%))</b>		
<b>Oticon 6 mm</b>	4 (10.3%)	
<b>Oticon 9 mm</b>	25 (64.1%)	
<b>Oticon 12 mm</b>	10 (25.6%)	

## 5.2. Methods

### 5.2.1. Data Collection

ASIST measurements were collected at the time of surgery and at each of the clinical follow up visits for the first year following surgery. A total of 7 visits were planned at the following approximate time points: surgery, 3 days, 2 weeks, 1 month, 3 months, 6 months, and 12 months. The measurements were completed at the patients' regularly scheduled visits to minimize additional time commitments for the patients participating in the study. The surgical measurement was taken inside the operating room while the patient was lying down. The 2 week measurement was taken at the surgeon's office (patient seated) and all other measurements were taken in the clinical operatory rooms at iRSM with the patients in a seated position. The majority

of the measurements at surgery were taken by the operating surgeon, while a few were taken by the primary author. The majority of the follow up measurements were taken by the primary author; however, some measurements were taken by a research assistant or a clinical assistant at iRSM as scheduling required.

At each visit a target of 2 ASIST measurements were recorded. Typically, 1 – 3 ASIST measurements were recorded with the majority of visits having 2 measurements. During testing, the measured accelerometer signal is displayed on the computer screen. A third measurement was recorded in cases when the accelerometer signal from one of the earlier measurements appeared to be different or a clean signal was not obtained. A third measurement was also recorded in the event that there was a poor contact between the impact rod and the abutment with one of the measurements due to either poor handpiece control or movement from the patient. Several measurements were discarded based on a subjective analysis of the accelerometer measurement or the testing conditions. These cases sometimes resulted in only 1 usable measurement for a clinic visit. It is worth noting that a single measurement consists of 16 strikes with the abutment as described in Section 2.1.

It should be noted that over a period of five months from Feb 27, 2015 – July 29, 2015 the electronic unit of the ASIST device had problems with connectivity which resulted in some poor measurements for the clinical study during that time frame. In many instances, the ASIST was unable to maintain a connection to the computer and was unable to download the recorded data. Several visits during this time period resulted in no usable measurements.

There were a total of patient 228 visits completed. Eight patients were followed for 1 year, 19 additional patients were followed for 6 months, 11 patients were followed for 1 – 3 months, and 1 patient was lost to follow up after the 2 week visit. Of the completed visits, 185 (81.8%) have resulted in good ASIST measurements, while 16 measurements (7.0%) were missed due to problems with the ASIST device or measurement error. Additionally, 27 visits (11.8%) have been missed for various reasons including patient no shows, visits not scheduled by the clinicians, or changes in schedule causing the researcher to miss the visit.

An overview of the timing of clinic visits is shown in Table 5.2 where  $n$  indicates the number of good measurements available to date. It should be noted that four of the patients who had the

MIPS surgical technique (Patient 1D: 36-39) had their two-week visit scheduled at 6 weeks post-surgery. This change in protocol was decided by the operating surgeon and was primarily due to the lack of sutures used in the surgical procedure (for prior patients the sutures were typically removed at the two-week visit).

**Table 5.2: Overview of Clinic Visits**

<b>Visit</b>	<b>Days after Surgery Mean (Range)</b>	<b><i>n</i></b>
Surgery	0	28
3 Days	3.2 (2 - 4)	33
2 Weeks	18.5 (10 - 41)	34
1 Month	33.8 (26 - 60)	31
3 Months	101.2 (83 - 148)	30
6 Months	196.5 (153 - 287)	22
1 Year	374.0 (363 - 397)	7

### **5.2.2. Data Analysis**

The ASC values were determined for each of the ASIST measurements. For each visit, the mean ASC value is reported in the case of multiple measurements. Longitudinal changes over time were reported for each patient. The damping ratio of the higher frequency component of the measured acceleration was estimated from the curve fit approximation ( $\zeta_2$ ). The mean value was reported for each visit and a *t*-test ( $p < 0.05$ ) was used to investigate differences between the damping ratio of the clinical data and the laboratory data with BAHA implants reported in Chapter 4.

The ASC values can be categorized into “Low” ( $ASC < 20$ ), “Moderate” ( $20 \leq ASC < 40$ ), and “High” ( $ASC \geq 40$ ) values. A value of 20 was chosen as the cutoff to define low stability based on the laboratory experimental work presented in Chapter 2. The PLA implant installations were designed to have a lower stability than the FRB-20 installations. All of the PLA implants reported an ASC value of less than 20; thus 20 was chosen as a cutoff for this category. It should be noted that this does not indicate that patients showing ASC values in the low stability range are at risk of implant failure. This categorization is simply used to aid in the interpretation of some of the data presented here. Further clinical evaluation will need to be conducted to draw

conclusions about the risk of implant failure. At the upper limit, an ASC of 40 was chosen to define the high stability range based on the parametric sensitivity analysis presented in Chapter 3. From Figure 2.9 it can be seen that for ASC values above approximately 40 for all implant-abutment combinations, the curve representing the relationship between the first mode frequency and the ASC value begins to plateau. Beyond this region, small differences in the measured acceleration signal can cause larger variations in the ASC measurement. Conversely, large increases in the interface stiffness or ASC value in this region do not have a large impact on the acceleration response of the system. Considering the analytical model, this indicates that in the high stability range, further increases in the interface stiffness do not have a large effect on the system response. The ASIST is less precise in this region, but since the implant is stable this may be of less importance.

Correlations were investigated between ASC values and several parameters including operating surgeon, age at surgery, gender, and implant type. Differences in implant stability between groups were investigated using a *t*-test ( $p < 0.05$ ) with a Bonferroni adjustment for multiple comparisons where appropriate. As a preliminary analysis simple correlations were conducted to assess the effect of individual parameters; however, the problem is multifactorial in nature. A larger sample size would allow for a multiple regression analysis to account for the effects of multiple confounding variables. This may be of interest and should be investigated in a larger study. The analyses presented here can provide preliminary insight into the effect of various parameters for the sample of patients included in this study.

## **5.3. Results**

### **5.3.1. ASC Results and Model Fit**

The ASC values for the patient data ranged from 11.9 to 74.5 (average  $\pm$  SD:  $30.5 \pm 16.2$ ). This is similar to the range of ASC values for the laboratory data reported in Chapter 4, suggesting that the laboratory results can provide an appropriate simulation of the clinical situation. Additionally, this wide range suggests that there is a large variability in implant stability across patients.

Of the completed visits, there have been 57 (31%) low stability measurements, 82 (44%) moderate stability measurements, and 46 (25%) high stability measurements. Figure 5.1 shows examples of clinically measured acceleration signals along with the resulting model prediction and ASC values in the low, moderate, and high stability ranges. All patients in this example had the 4 mm narrow platform implant and a 9 mm abutment and the measurements shown are from the first post-operative visit at three days following surgery. The differences in the acceleration measurement between the three examples can be seen in the figure with the lower ASC values have a lower fundamental frequency than the higher ASC values. It was also observed that the amplitude of the higher frequency component decreases with higher ASC values. These features are consistent with model predictions as the interface stiffness increases. Additionally, it can be seen that there is a good fit between the measured data and the analytical model in all cases.

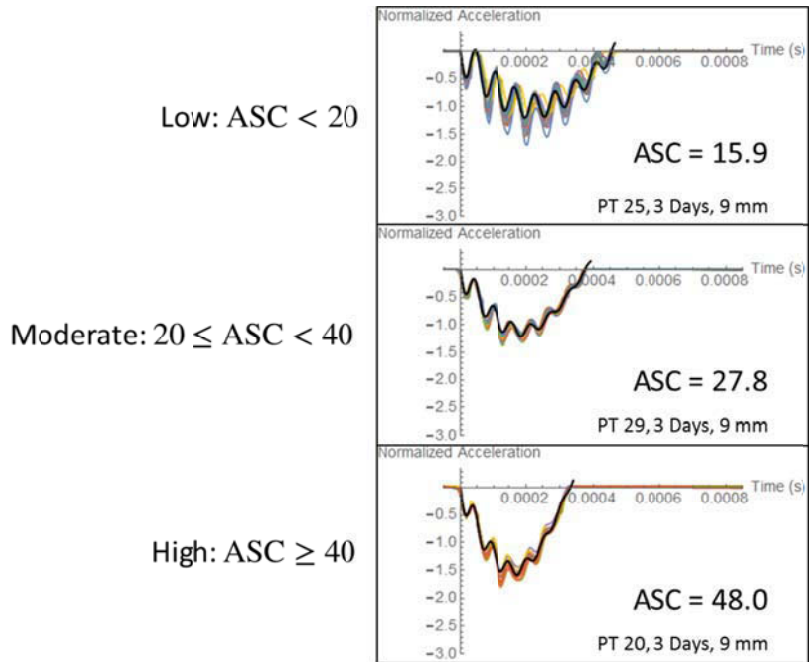
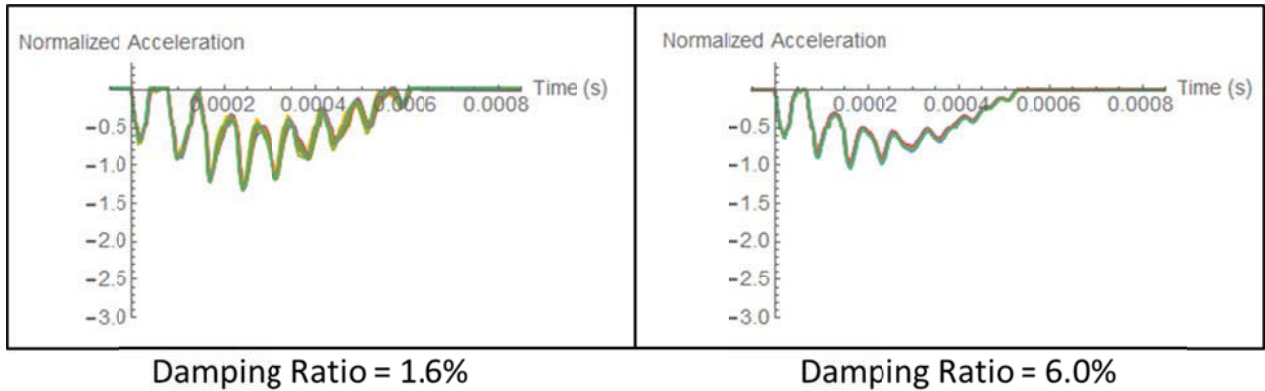


Figure 5.1: Examples of patient data (colored lines) and model fit (black lines) for low, moderate, and high stability values

### 5.3.2. Damping Ratio

The damping ratio for the patient data (as estimated from the curve fit approximation) was  $0.039 \pm 0.017$  (average  $\pm$  SD) with a range of 0.0002 – 0.105. This was similar to the damping ratio reported for the Oticon PLA samples from the laboratory data, which had a damping ratio of

$0.037 \pm 0.023$  and no significant differences were found between these two groups ( $p = 0.42$ ). Conversely, the BAHA patient data had a significantly higher damping ratio than the Oticon FRB-20 samples, which had a damping ratio of  $0.021 \pm 0.010$  ( $p = 1.1 \times 10^{-22}$ ). Figure 5.2 shows examples of measured accelerometer data from two patients: the left image is an example of a patient with a low damping ratio (1.6%) and the right image is an example of a patient with a high damping ratio (6.0%). The differences in the damping of the high frequency component can be seen in the figures.



**Figure 5.2: Example patient data with low damping ratio (left) and high damping ratio (right)**

The damping ratio of the data from patients who had the MIPS surgical technique ( $0.048 \pm 0.014$ ) appears to be higher than that of the patients who had the incision technique ( $0.038 \pm 0.017$ ) with  $p = 0.006$ . However, it should be noted that there were only a small sample of patients with the MIPS technique. This difference may be attributed to the greater soft tissue preservation associated with the MIPS technique and can be further explored with a larger sample size.

In general, the damping in the BAHA implant patient data was found to be small with an average damping ratio less than 4% and a maximum damping ratio of approximately 10%.

### 5.3.3. Initial Implant Stability

All participants had at least one good measurement in the first two weeks following implantation. The average measurement in the first two weeks following surgery was used as an indication of the initial stability of the implant. It was found that 10 participants had high initial stability with  $ASC \geq 40$ , 18 participants had moderate initial stability with  $20 \leq ASC < 40$ , and 11 participants had low initial stability with  $ASC < 20$  (Table 5.3).

There appears to be differences in initial implant stability level between surgeons (Table 5.3), suggesting that surgical technique can play a role in initial implant stability. Differences between surgeons can be further explored by considering the mean initial ASC value for the three surgical groups (Figure 5.3). Significance was investigated using a Bonferroni adjusted *t*-test with three comparisons (comparisons between each surgeon) ( $p < 0.0167$ ). The average initial ASC value for the patients of Surgeon 2 ( $ASC = 21.0 \pm 10.6$ ; mean  $\pm$  SD) was found to be significantly lower than those of Surgeon 1 ( $ASC = 39.1 \pm 16.2$ ;  $p = 0.0012$ ) and Surgeon 3 ( $ASC = 35.0 \pm 10.7$ ;  $p = 0.0049$ ). No significant differences were found between the initial ASC value for the patients of Surgeons 1 and 3 ( $p = 0.51$ ).

**Table 5.3: Participant Groupings based on Initial Stability (average of first 2 weeks) and Surgeon**

	<b>Low</b>	<b>Moderate</b>	<b>High</b>	<b>Total</b>
<b>Surgeon 1</b>	2	7	6	15
<b>Surgeon 2</b>	9	5	1	15
<b>Surgeon 3</b>	0	6	3	9
<b>Total</b>	11	18	10	39

Low:  $ASC < 20$ ; Moderate:  $20 \leq ASC < 40$ ; High:  $ASC \geq 40$

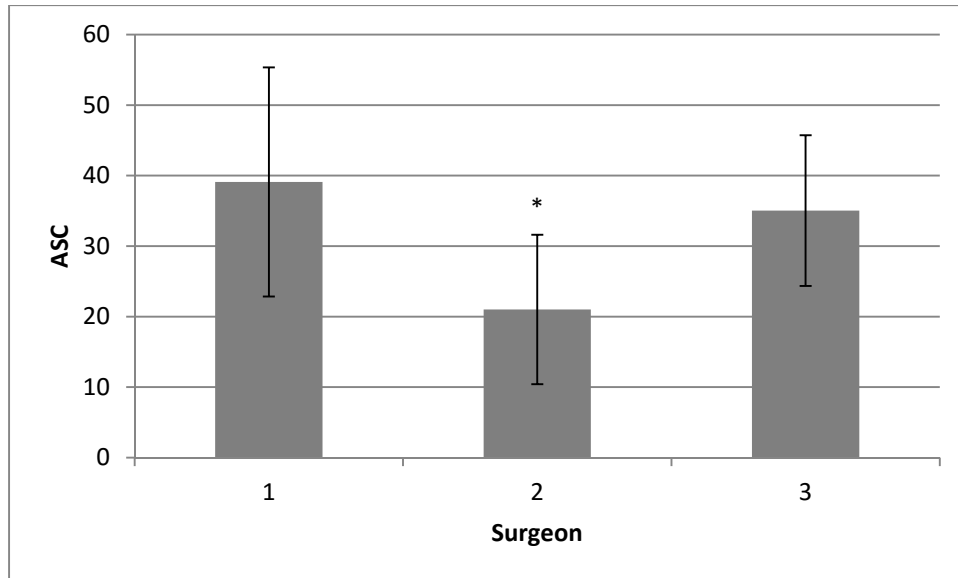


**Figure 5.3: Mean initial implant stability (average of first 2 weeks) based on surgeon. Average values over all participants. Error bars indicate one standard deviation. \* indicates significant difference based on Bonferroni adjusted  $t$ -test ( $p < 0.0167$ ).**

There appears to be no correlation between initial implant stability and age at surgery across the participants (Figure 5.4).

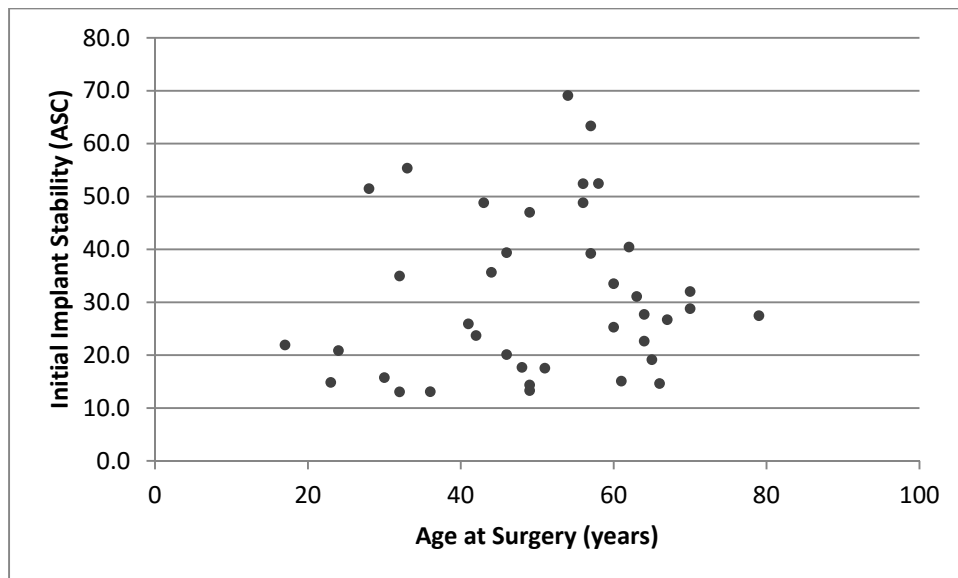


**Figure 5.4: Initial implant stability as a function of participant age at surgery**

Table 5.4 shows the initial stability groupings separated by gender. The majority of the male participants (8/13; 62%) had moderate initial stability while the female participants were split almost equally across the three categories. There were no significant differences in the mean initial stability between the two groups ( $p = 0.71$ ) with males having an initial ASC of  $32.5 \pm 15.1$  and females having an initial ASC of  $30.5 \pm 15.6$ .

**Table 5.4: Participant Groupings based on Initial Stability (average of first 2 weeks) and Gender**

	<b>Low</b>	<b>Moderate</b>	<b>High</b>	<b>Total</b>
<b>Male</b>	2	8	3	13
<b>Female</b>	9	10	7	26
<b>Total</b>	11	18	10	39

Low: ASC < 20; Moderate:  $20 \leq$  ASC < 40; High: ASC  $\geq$  40

Table 5.5 shows the initial stability groupings separated by implant type including the 4 mm narrow platform implant (M50128), the 4 mm wide platform BHX implant, and the 3 mm narrow platform implant (M50106). It should be noted that six out of the seven BHX implants also used the MIPS surgical technique while the remaining implants were installed using an incision technique with the implant placed in the incision line. It should also be noted that all BHX implants as well as the shorter 3 mm implant were installed by the same surgeon (Surgeon 1). Approximately half of the 4 mm narrow implants had moderate initial stability (16/31; 52%) with the others split between low (9/31; 29%) and high (6/31; 19%). For the BHX implant, 4/7 had high initial stability (57%), including the patient with the BHX implant and the incision surgical technique, while 2/7 (29%) had low and 1/7 (14%) had moderate initial stability. Although there was a small sample size of BHX implants tested, the initial stability of these implants seems to be significantly higher than the 4 mm narrow platform ( $p = 0.03$ ) based on a  $t$ -test between the two groups. The initial ASC of the M50128 implants was  $28.4 \pm 13.1$  while the initial ASC of the BHX implants was  $42.0 \pm 20.7$ . This is a preliminary result that should be explored further with increased sample sizes and accounting for possible differences between surgeons or other confounding variables.

**Table 5.5: Participant Groupings based on Initial Stability (average of first 2 weeks) and Implant Type**

	Low	Moderate	High	Total
<b>M50128</b>	9	16	6	31
<b>BHX</b>	2	1	4	7
<b>M50106</b>	0	1	0	1
<b>Total</b>	11	18	10	39

Low:  $ASC < 20$ ; Moderate:  $20 \leq ASC < 40$ ; High:  $ASC \geq 40$

### 5.3.4. Longitudinal Changes in Implant Stability

Many studies investigating longitudinal changes in implant stability (as measured by the ISQ) group the patients together and present average and SD values or box and whisker plots across the study period (Dun et al., 2011; Faber et al., 2012; Foghsgaard and Caye-Thomasen, 2014; Marsella et al., 2012; Nelissen et al., 2016). The large variability in the data across patients often makes the longitudinal changes difficult to interpret from this kind of presentation. In the present study, grouping all of the patients together, we see only small changes in the average ASC values throughout the study period (Figure 5.5). There appears to be a slight decrease in the ASC up to approximately three months post-surgery followed by a slight increase. However, like stability measurements reported in the literature, there is a large amount of variability in the data as shown by the large error bars (one standard deviation) which makes it difficult to draw conclusions on average trends for the group as a whole.

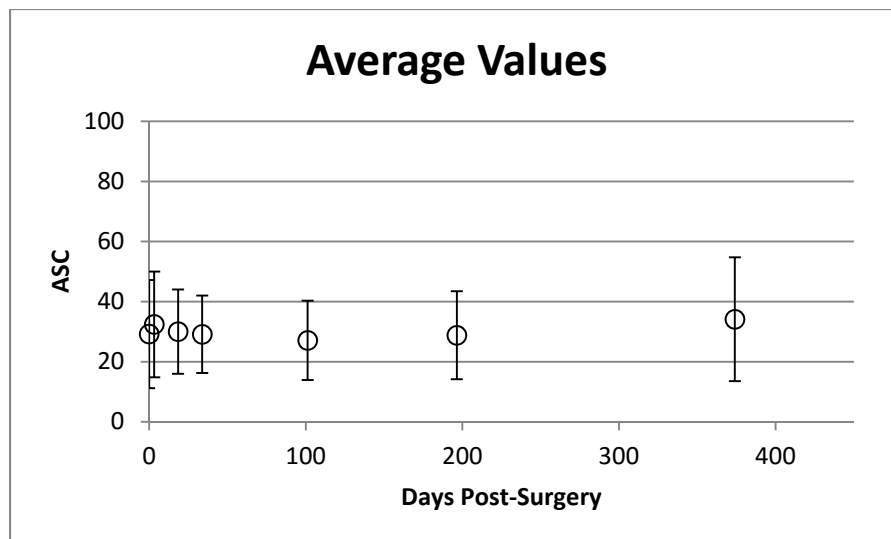


**Figure 5.5: Average ASC values across all patients at each visit. Visit day is averaged for all patients. Error bars represent one standard deviation.**

We can instead focus on longitudinal changes for individual patients. In general, there was a large variability in the patterns of longitudinal changes across patients. However, there were 15 patients who showed a similar trend with generally small changes in ASC over time and many within this group showing a gradual increase in ASC (Figure 5.6). All 11 of the patients that were classified as having low initial stability were found to have this trend of longitudinal changes as well as 4 patients with moderate initial stability. The patients with moderate initial stability had ASC values in the lower end of the moderate range with initial stability values between 22.0 and 28.8. However, it should be noted that there were many patients with moderate initial stability within this range that did not follow this same trend of longitudinal changes. For this set of 15 patients, two were operated on by Surgeon 1 using the MIPS surgical technique, 10 were seen by Surgeon 2, and 3 were seen by Surgeon 3.

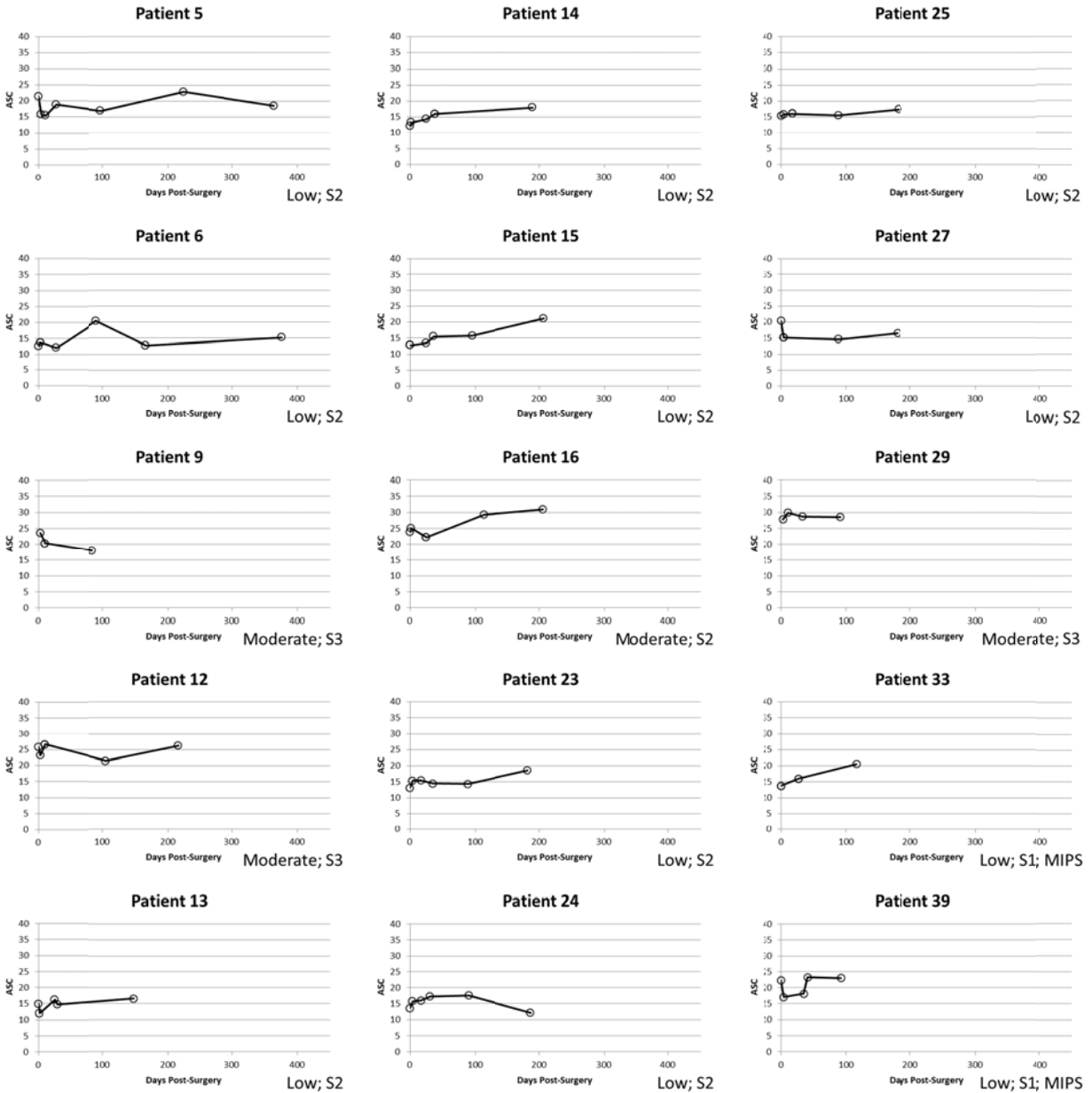
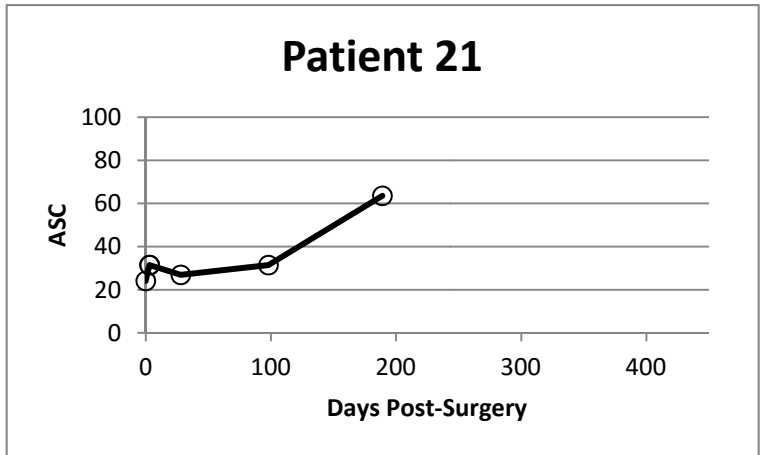
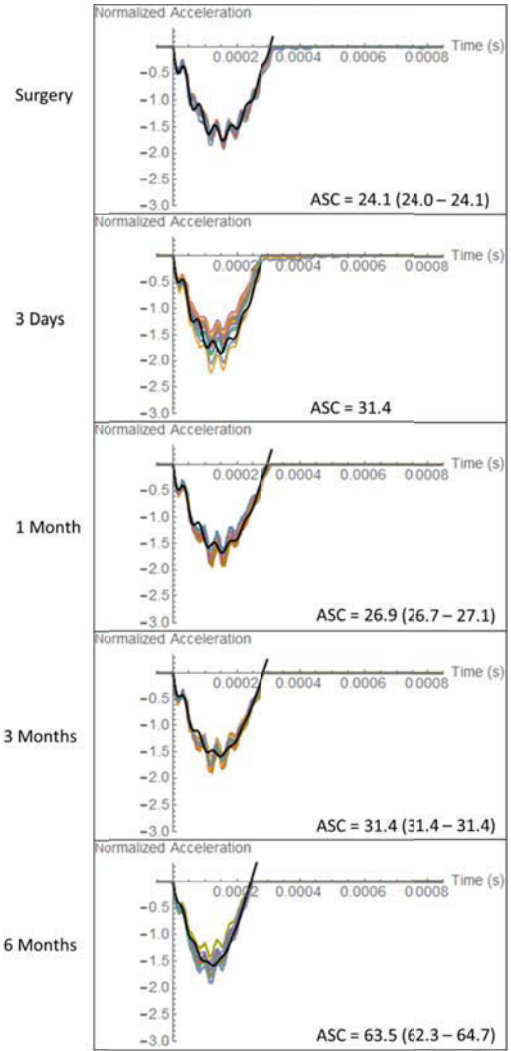


**Figure 5.6: Set of 15 patients showing a similar trend of longitudinal changes (generally small changes over time, many with a gradual increase in ASC). Initial stability (Low, Moderate, High) and surgeon (S1, S2, S3) are indicated for each patient.**

Some patients showed a substantial increase in stability over time (for example, Patient 21 shown in Figure 5.7) while others showed a substantial decrease in stability over time (for example, Patient 20 shown in Figure 5.8). Some patients also showed both increasing and decreasing variations in ASC over time. For Example Patient 3 showed an initial decrease after surgery, followed by an increase to the one year visit (Figure 5.9).

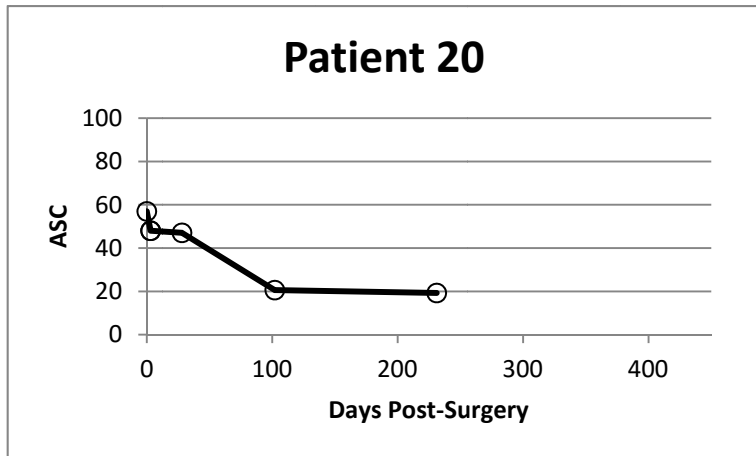


(a)

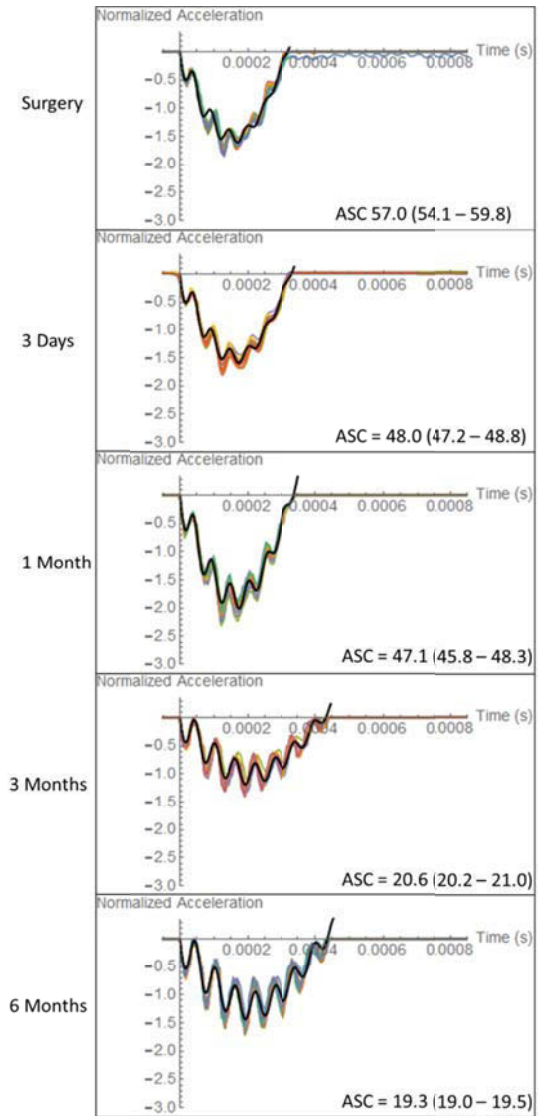


(b)

Figure 5.7: Example patient showing an increase in ASC over time. 6 month results are reported for this patient. 64 year old female with a 4 mm narrow implant (M50128) and 6 mm abutment. (a) Longitudinal mean ASC values. (b) Measured data (colored lines) and model prediction (black line) at each visit with average ASC values and range for repeated measures.

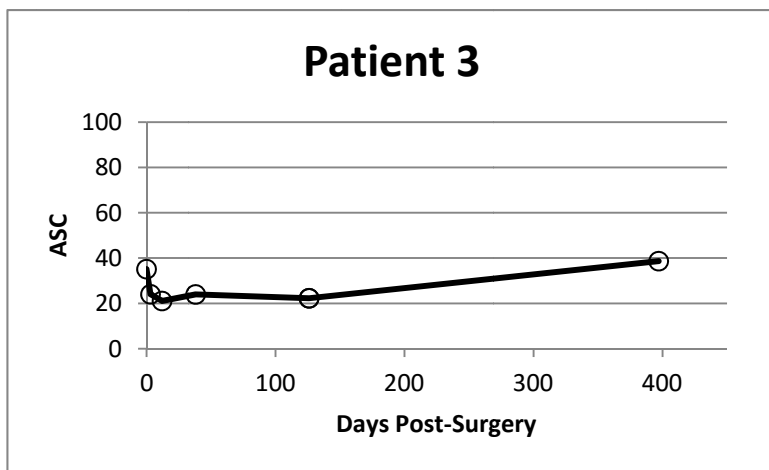


(a)

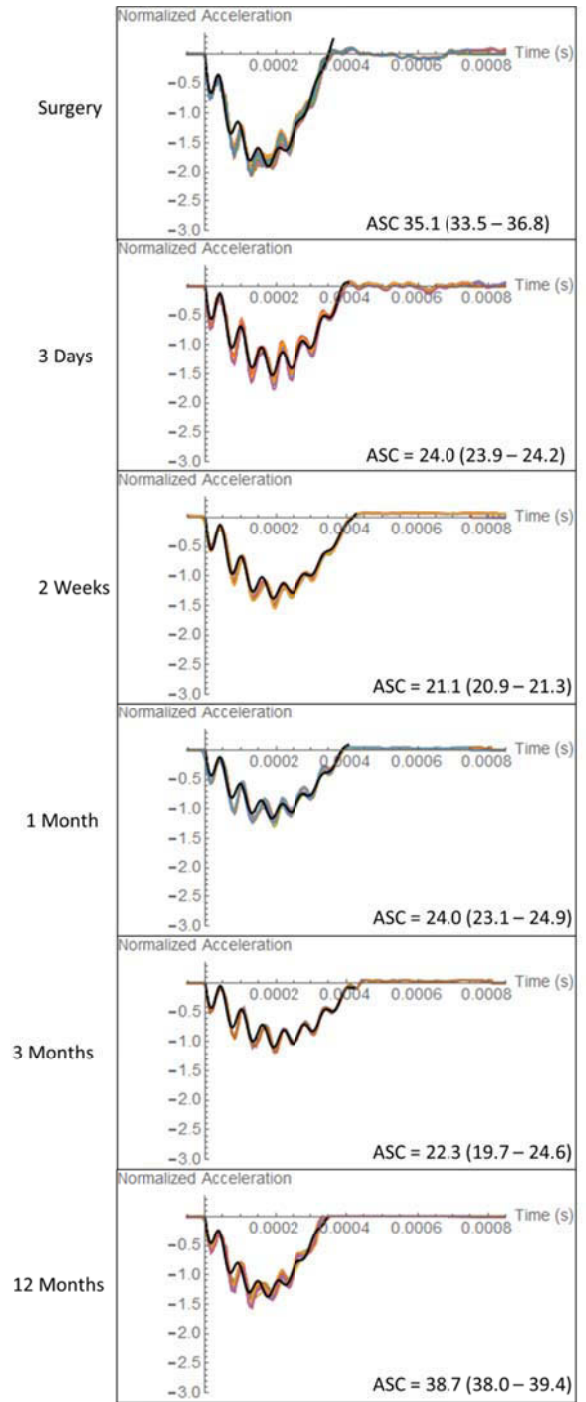


(b)

**Figure 5.8: Example patient showing a decrease in ASC over time. 6 month results are reported for this patient. 58 year old male with a 4 mm narrow implant (M50128) and 9 mm abutment. (a) Longitudinal mean ASC values. (b) Measured data (colored lines) and model prediction (black line) at each visit with average ASC values and range for repeated measures.**



(a)



(b)

**Figure 5.9: Example patient showing an initial decrease in ASC followed by an increase in ASC over time. 12 month results are reported for this patient. 67 year old male with a 4 mm narrow implant (M50128) and 9 mm abutment. (a) Longitudinal mean ASC values. (b) Measured data (colored lines) and model prediction (black line) at each visit with average ASC values and range for repeated measures.**

## 5.4. Summary

This chapter presents a clinical evaluation of the longitudinal changes in implant stability for BAHA patients during the first year following surgery. The acceleration measurements from the patient data matched closely with those from the laboratory data presented in Chapter 4 and the range of ASC values from the clinical data was very similar to the range that was found for the laboratory data suggesting that the laboratory results should provide a good representation of the clinical situation. Additionally, the ASIST technique was found to provide a good fit between the model response and the measured acceleration indicating that the analytical model is able to provide a good approximation of the physiological system.

Using the ASC measure, we were able to detect differences in the initial stability of BAHA implants between different surgeons. Additionally, we have shown that there is potential to detect differences in ASC values between different implant types by comparing a small sample of BHX wide diameter implants from Oticon Medical with the standard narrow platform implants from the same manufacturer. These are important results and suggest that the ASIST may be used to detect differences between surgical techniques, implant designs, or other variables of clinical interest.

The pattern of longitudinal changes in implant stability as measured by the ASC value was found to vary across the 39 patients that were included in this study. There was a large group (15 patients) with generally low initial stability who showed similar longitudinal trends with ASC values that were relatively constant or gradually increasing over time. Many of the remaining patients showed large increases or decreases in ASC values between visits. This suggests that healing patterns can vary substantially across patients, at least in the early stages following surgery. There are many studies in the literature investigating longitudinal changes in BAHA implant stability for various situations using the ISQ measure (Dun et al., 2011; Faber et al., 2013; Foghsgaard and Caye-Thomasen 2014; Nelissen et al., 2016). These studies tend to report a large variability in the ISQ values across patients (even when abutment height is controlled), which is consistent with the implant stability results presented here. Additionally, the finding that the patients with generally low initial stability showed similar longitudinal changes suggests that the initial implant stability can influence the subsequent implant healing patterns. This is

consistent with the idea that adequate primary (mechanical) stability is required for successful secondary stability and osseointegration (Atsumi et al., 2007).

It should be emphasized that “low stability” in this analysis is not meant to indicate a problem with the implant integration as none of the implants in this study failed. With further study it may be possible to establish ASC levels that would indicate implants at risk of failure; however we are not at that stage with this preliminary study. The ASIST appears to be sensitive enough that the goal of establishing such a criterion appears to be feasible.

We have shown promising results using the ASIST in a clinical setting with the clinical evaluation presented here. The ASIST has the potential to provide a better understanding of the changes that occur at the bone-implant interface during healing and throughout the life of the implant.

# Chapter 6: Development of the ASIST for Natural Teeth

This chapter presents the development and evaluation of the ASIST for the application to natural teeth. In this case, the interface stability is related to the mechanical properties of the periodontal ligament (PDL) which connects the tooth root to the surrounding alveolar bone (Nishihira et al., 2003). This chapter presents the analytical model and ASIST procedure for the tooth application, a parametric sensitivity study from the analytical model, and a clinical application of the ASIST for patients undergoing orthodontic treatment.

## 6.1. Analytical Model

To adapt the ASIST technique for any other application such as natural teeth, an appropriate analytical model must be developed. The analytical model (Figure 6.1) is similar to that developed for the BAHA implant-abutment systems presented in Section 2.2. Here, a single-rooted tooth is modeled as a 3-DOF system composed of a rigid body (the tooth with mass  $m_t$  and moment of inertia  $J_G$ ) as well as the impacting rod which is again modeled as a particle with a mass of  $m_p = 9.4$  g.

The internal stiffness parameter  $K_I$  is a spring at the impact site between the impact rod and the tooth at a height  $h$  above the center of mass of the tooth (Figure 6.1). The periodontal ligament is modeled as a distributed stiffness  $k$  and viscous damping  $c$  per unit area surrounding the tooth root. The PDL stiffness is oriented perpendicular to the root surface (Carvalho et al., 2006). The coordinates used to describe the system are the horizontal displacement of the impact rod ( $x_1$ ), the horizontal displacement of the center of the tooth at the height of impact ( $x_2$ ), and the rotation of the tooth ( $\theta$ ). With these coordinates,  $\ddot{x}_1$  represents the acceleration of the impact rod which is experimentally measured by the accelerometer.

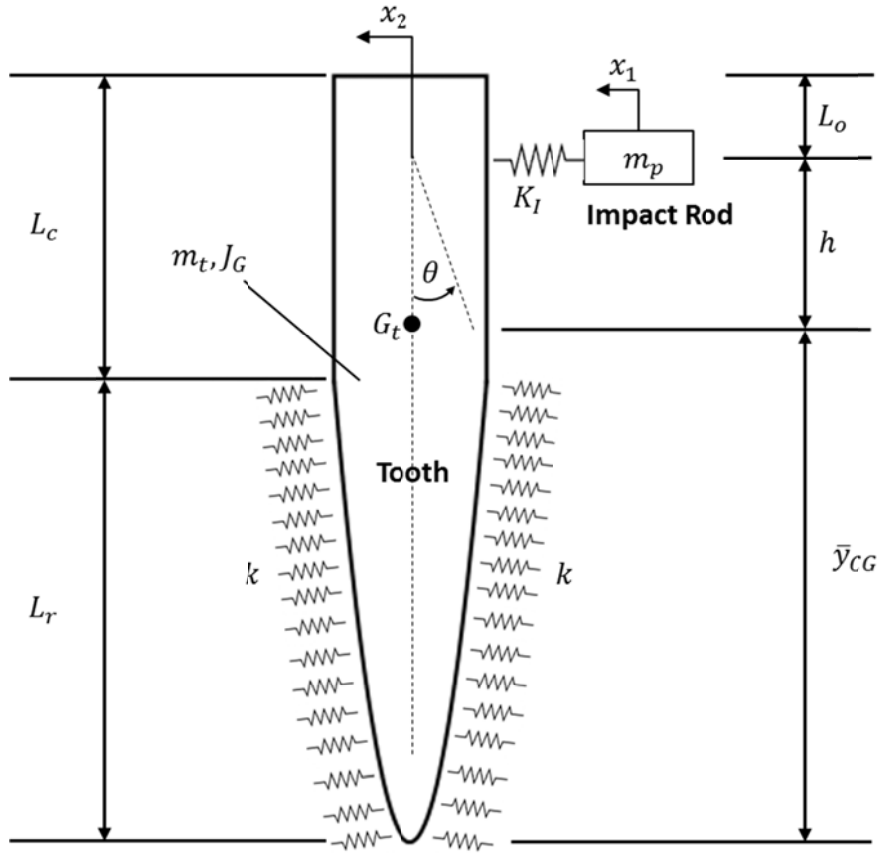


Figure 6.1: Schematic of the 3-DOF model of the tooth

The equations of motion for free vibration of the 3-DOF system are given by the following:

$$[M]\{\ddot{x}\} + [C]\{\dot{x}\} + [K]\{x\} = \{0\}$$

Where the coordinates for  $\{x\} = \begin{Bmatrix} x_1 \\ x_2 \\ \theta \end{Bmatrix}$  are shown in Figure 6.1.

The mass  $[M]$ , stiffness  $[K]$ , and damping  $[C]$  matrices can be obtained for this system using the method of influence coefficients (Den Hartog, 1985). The details for these derivations are shown in Appendix D.

The mass matrix  $[M]$  is given by:

$$[M] = \begin{bmatrix} m_p & 0 & 0 \\ 0 & m_t & -m_t h \\ 0 & -m_t h & J_G + m_t h^2 \end{bmatrix}$$

The stiffness matrix  $[K]$  is given by:

$$[K] = \begin{bmatrix} K_I & -K_I & 0 \\ -K_I & K_I + 4 \int_0^{L_r} kr \cos^2 \alpha dy & -4 \int_0^{L_r} kr \cos^2 \alpha (L - L_o - y) dy \\ 0 & -4 \int_0^{L_r} kr \cos^2 \alpha (L - L_o - y) dy & 4 \int_0^{L_r} kr \cos^2 \alpha (L - L_o - y)^2 dy \end{bmatrix}$$

Where:

$k$  is the stiffness per unit area surrounding the tooth root

$r$  is the radius of the tooth root as a function of the height  $y$  ( $y = 0$  at the bottom of the root)

$\alpha$  is the angle between a line perpendicular to the tooth root and the horizontal axis as a function of the height  $y$

$L_r$  is the total length of the tooth root

$L$  is the total length of the tooth

$L_o$  is the distance from the top of the tooth (crown tip) to the location of the strike

The damping matrix  $[C]$  is given by:

$$[C] = \begin{bmatrix} 0 & 0 & 0 \\ 0 & 4 \int_0^{L_r} cr \cos^2 \alpha dy & -4 \int_0^{L_r} cr \cos^2 \alpha (L - L_o - y) dy \\ 0 & -4 \int_0^{L_r} cr \cos^2 \alpha (L - L_o - y) dy & 4 \int_0^{L_r} cr \cos^2 \alpha (L - L_o - y)^2 dy \end{bmatrix}$$

Where  $c$  is the damping coefficient per unit area surrounding the tooth root. Viscous damping was assumed only at the interface with negligible damping in the rest of the system, following the same assumptions used for the BAHA model described in Section 2.2.

## 6.2. Geometry and Assumptions

The geometry of the tooth must be approximated in the model for two reasons. The first is to define the root profile since the effective interface stiffness is dependent on the root shape, and the second is to define the mass and geometry parameters of the tooth. As shown in the stiffness (and damping) matrices above, the radius and angle of the tooth root as a function of the height must be estimated. In the analytical model, the tooth root is modeled as a paraboloid. This shape has been used previously to model the tooth root shape (Provatidis, 2001). The tooth crown is modeled as a simple cylinder with a radius equal to the radius of the root at the crown-root junction. The detail of the tooth crown is only required in the model to determine its contribution to the mass, the position of the center of mass, and the moment of inertia of the tooth.

The following geometric parameters are needed in the model: the length of the root ( $L_r$ ), the length of the crown ( $L_c$ ), the radius of the tooth at the crown-root junction ( $R_0$ ), the tooth mass ( $m_t$ ), the location of the center of mass ( $\bar{y}_{CG}$ ) measured from the root tip, and the mass moment of inertia measured about the center of mass ( $J_G$ ). These parameters can be estimated for a particular tooth from computed tomography (CT) scans; however, when not available, an approximate shape can be used to estimate the parameters as will be discussed later.

## 6.3. ASIST Procedure

### 6.3.1. Osseometer to ASIST Transformation

A large amount of useful accelerometer data for the tooth application exists from previous studies, particularly the clinical data that will be discussed in Section 6.5. This data was collected with a previous version of the ASIST unit termed the Osseometer. As described in Section 2.1, the acceleration measurement was collected by extracting the raw accelerometer signal from a commercial Periotest® unit. This acceleration measurement suffered from the zero-overshoot in the signal as shown previously in Figure 2.2. Prior to analyzing the existing data with the ASIST procedure, it is important to transform the data to compensate for the zero-overshoot.

Both the Osseometer and the ASIST were used to collect data from the same set of samples (FRB-20 samples of Oticon implants) so the difference between the two acceleration signals can be analyzed (Figure 6.2).

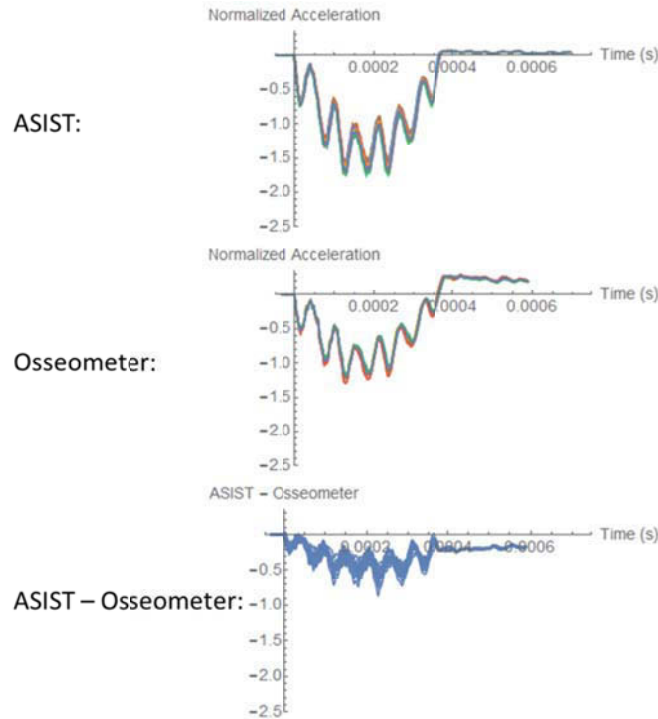


**Figure 6.2: Comparison of ASIST and Osseometer data for the same implant sample. The bottom figure shows the difference in the signals ASIST – Osseometer.**

A simple linear function was used to transform the original Osseometer signal to match the ASIST signal (Figure 6.3).

$$TO = O - g(t)$$

Where:

$TO$  is the transformed Osseometer data

$O$  is the original Osseometer data

$g(t) = \frac{\Delta}{T}t$  as shown in Figure 6.3

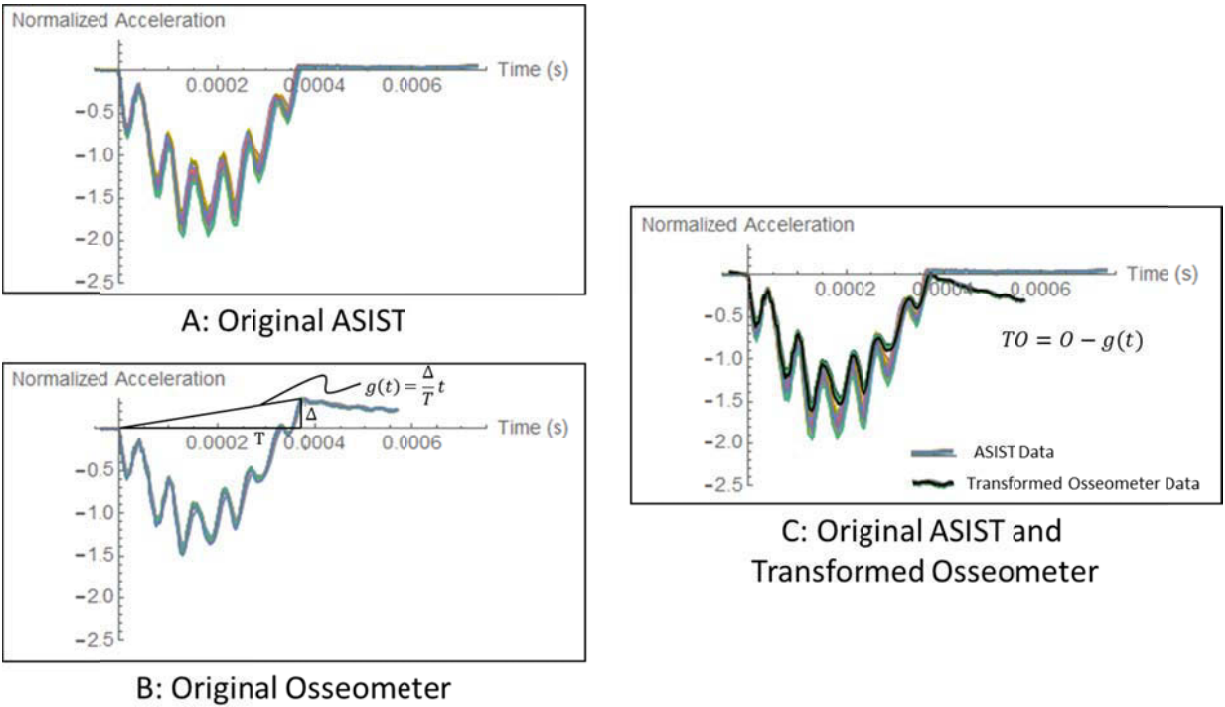


**Figure 6.3: Transforming Osseometer data to match ASIST data for an Oticon implant (M50128 with 9 mm abutment in FRB-20). A: The original ASIST data. B: The original Osseometer data showing the function  $g(t)$ . C: The transformed Osseometer data overlaid with the original ASIST data.**

Figure 6.4 shows a comparison of data collected with the ASIST and the Osseometer for two example datasets of FRB-20 implant samples. The first is the the long/narrow (M50128) implant with a 9 mm abutment and the second is the long/wide (M51062) implant with a 12 mm abutment. The Osseometer data shown in the figure is after the linear transformation was applied. It should be noted that the ASIST and Osseometer datasets were collected during two different sessions so there may be some additional variations in the experimental measurement (such as clamping the disc to the platform and attaching the abutment); however, the results are expected to be similar between the two cases because the same implant installation was used. There were small differences in the calculated ASC value between the ASIST data and the transformed Osseometer data with differences in the ASC value of 2.0 (6.6%) and 3.7 (10.2%) for the 9 mm and 12 mm examples, respectively.

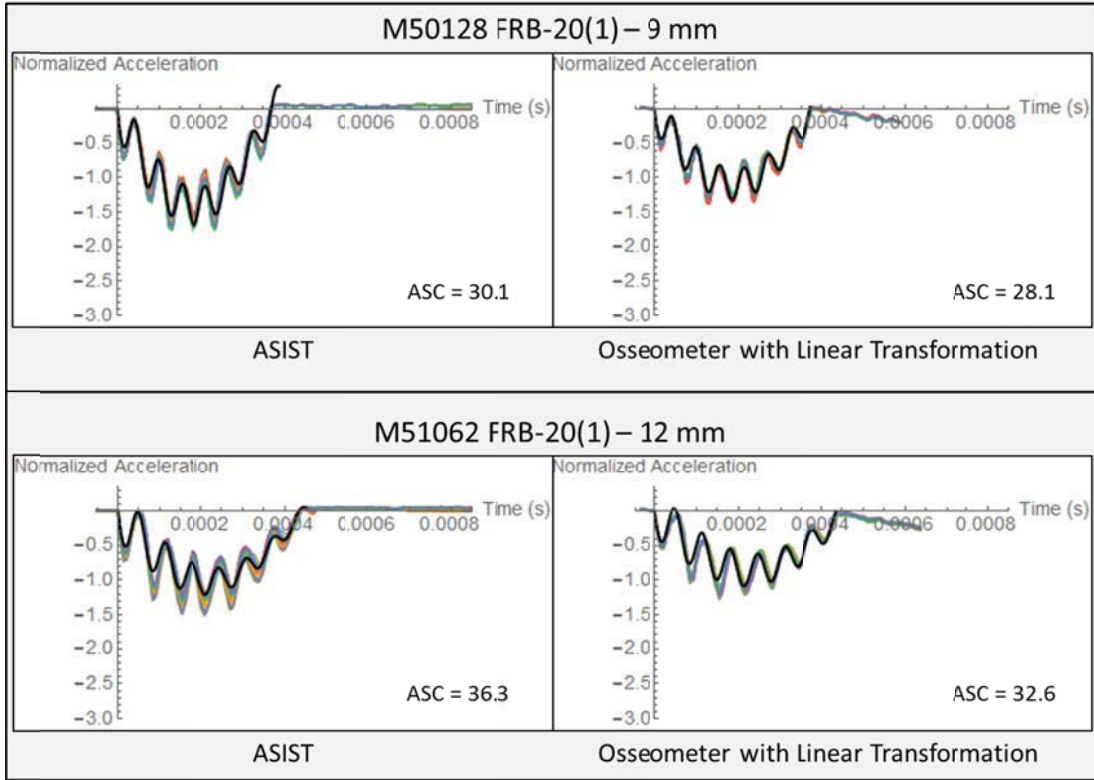


**Figure 6.4: Comparison of data collected with the ASIST and the Osseometer for two examples: FRB-20(1) long/narrow (M50128) implant sample with 9 mm abutment (top) and FRB-20(1) long/wide (M51062) implant sample with 12 mm abutment (bottom). ASC values are shown on the figure.**

An exponential function was also examined to understand the influence of the transformation function on the resulting acceleration signal. In this case the function was of the form:

$$g_1(t) = A(e^{-\lambda t} - 1)$$

where,  $A$  and  $\lambda$  are constants.

Figure 6.5 shows the model fit and calculated ASC value using both the linear transformation and the exponential transformation for two example datasets collected with the Osseometer. For the long/narrow implant with 9 mm abutment example there is no difference in the calculated ASC value and for the long/wide implant with 12 mm abutment there is a difference in the ASC value of 1.8 (5.5%).

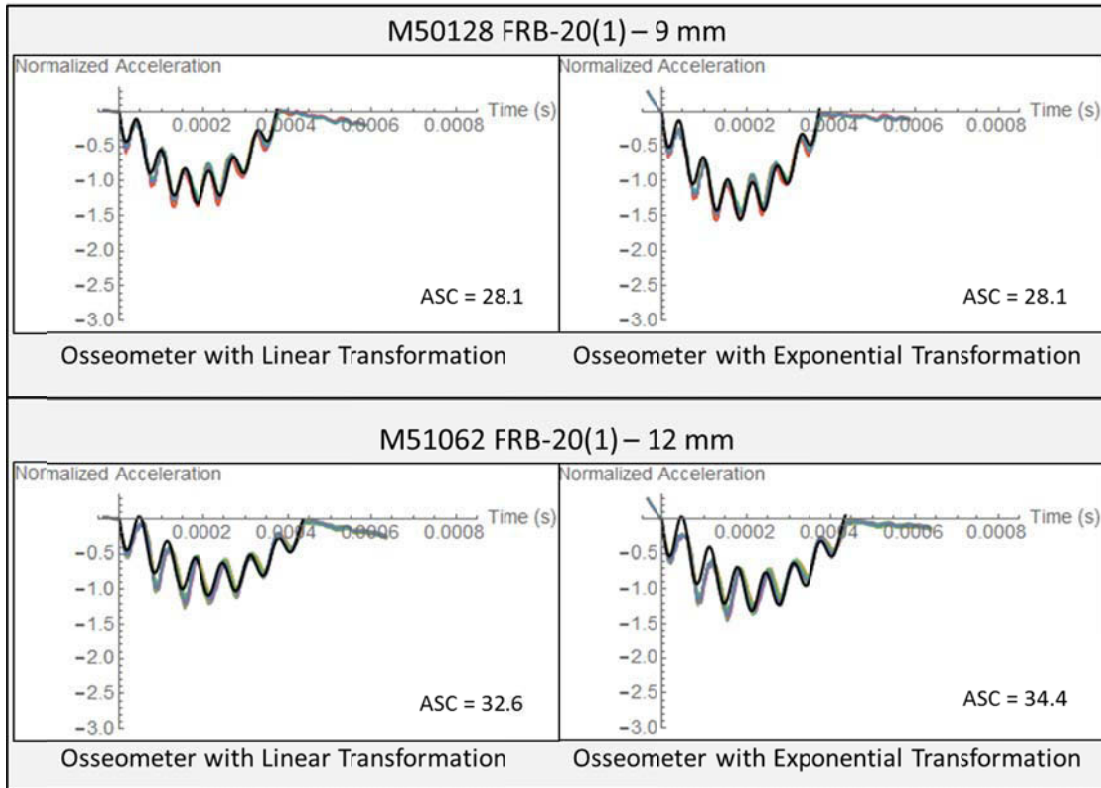


**Figure 6.5: Comparison of the model fit and ASC value for Osseometer data with a linear transformation (left) and exponential transformation (right) for two example datasets: a long/narrow implant with 9 mm abutment (top) and a long/wide implant with 12 mm abutment (bottom)**

From these examples, the choice of transformation function does not appear to have much effect on the resulting signal and subsequent ASC value. Qualitatively, the model fit appears to be slightly better with the linear transformation function for these examples. The linear transformation described above was used for subsequent analyses with the previously collected Osseometer data.

Examples of tooth data where both the Osseometer and ASIST were used to collect the acceleration measurement were not available for this study, thus it was not possible to make a direct comparison for this application. However, the clinical tooth data collected with the Osseometer shows a similar zero-overshoot compared to the BAHA implant data discussed above. Thus it is expected that the same transformation procedure would be applicable for the tooth data. Figure 6.6 shows an example dataset from a tooth collected with the Osseometer in a

clinical setting. The figure shows the original Osseometer data (left) and the transformed data using the linear transformation function (right).

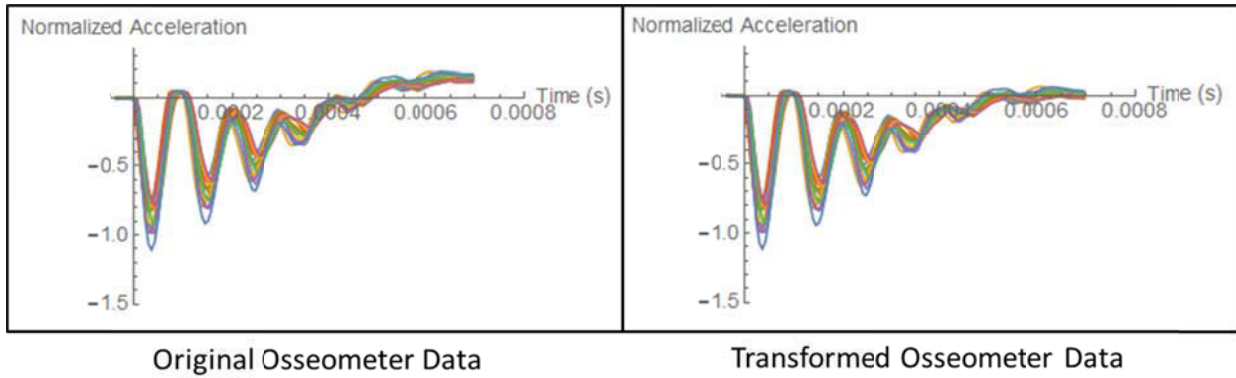


Figure 6.6: Comparison of original Osseometer data (left) and transformed Osseometer data (right) for an example clinical tooth dataset

### 6.3.2. Curve Fit Approximation and Extracting Information

The same curve fit procedure described in Section 2.3.1. was used for the tooth application. Figure 6.7 shows the curve fit approximation for a sample of tooth data from clinical testing with a maxillary cuspid tooth from an adolescent female undergoing orthodontic treatment. As seen in the figure, the curve fit procedure results in a good approximation of the data.

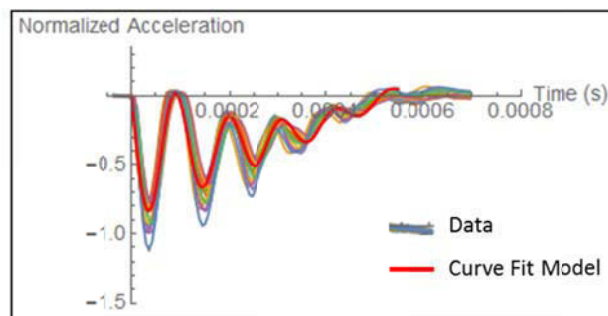


Figure 6.7: Sample data with curve fit approximation a clinical tooth example

The curve fit approximation provides a single analytical description of the data and allows two important pieces of information to be extracted from the data: the amplitude and the damping.

The amplitude is normalized following the procedure outlined in Section 2.3.2. where the normalization factor  $V_{amp}$  is determined from the curve fit model.

The damping coefficient  $c$  in the analytical model can be estimated from the curve fit model following a similar procedure to that outlined in Section 2.3.2. The second mode damping ratio  $\zeta_2$  from the curve fit model is related to the damping coefficient  $c$  through the mass and stiffness matrices. For the BAHA implants described in Section 2.3.2, there were a discrete set of cases to be considered (i.e. each implant-abutment combination) and a proportionality constant was determined for each case. In the case of natural teeth, the mass and geometry parameters vary between teeth. The same procedure could be applied here; however it would have to be customized for each individual tooth. This is not practical for widespread use of the ASIST procedure with teeth, thus a slightly different procedure was adopted. The mass of the tooth ( $m_t$ ) was explicitly expressed in the relationship:

$$c = \gamma \sqrt{m_t} \sqrt{k} \zeta_2$$

This expression is analogous to that presented in Section 2.3.2; however, in this case the mass appears directly in the expression and the proportionality constant  $\gamma$  would be equal to 2 for a single degree of freedom system. An approximate value for the proportionality constant  $\gamma$  was estimated based on visual appraisal of the resulting model fit for the full set of clinical tooth data that was available.

### **6.3.3. Matching the Analytical Model to the Measured Acceleration**

Once the mass and geometry parameters of the particular tooth are estimated, there are three unknown variables left in the analytical model: the striking location ( $L_o$ ), the impact stiffness ( $K_I$ ), and the interface stiffness surrounding the tooth root ( $k$ ) which is the primary variable of interest. The striking location should be estimated when conducting the acceleration measurement test and input into the ASIST model. It should be noted however that much of the data analyzed in this study had been collected previously thus an accurate striking height was not known for this data. For the clinical data, the striking height was estimated based on visual

appraisal of the resulting model fit for several samples and was fixed in the model for all analyses with all patients.

The unknown stiffness parameters in the model were determined by matching the model predicted acceleration to the measured data following the procedure outlined in Section 2.3.3. where the Mathematica function `FindMinimum[]` is used to minimize the Euclidean norm between the analytical model acceleration response and the curve fit approximation of the data. For the tooth application, multivariable minimization is used to find both the impact stiffness ( $K_I$ ) and the interface stiffness per unit area ( $k$ ) that minimize the specified norm. In this case, contrary to the BAHA implant application, the impact stiffness was allowed to vary in the model. This is because there may be some variability in this stiffness and in the striking conditions between teeth. Additionally, since much of the data had been previously collected prior to this study, the exact striking conditions were unknown.

### 6.3.4. Outcome Measure

The primary outcome measure for this application is again the ASIST Stability Coefficient (ASC). Similar to the BAHA implant application, the ASC is a non-dimensional quantity that is directly related to the effective interface stiffness surrounding the tooth root and normalized to a nominal stiffness value.

The effective interface stiffness is:

$$K_{eff} = 4 \int_0^{L_r} kr \cos^2 \alpha dy$$

Using the paraboloid model, the radius and angle of the tooth root are:

$$r = R_0 \sqrt{\frac{y}{L_r}}$$

$$\alpha = \tan^{-1} \left( \frac{r}{2y} \right)$$

where  $R_0$  is the radius of the tooth at the crown-root junction, and  $L_r$  is the length of the root.  $K_{eff}$  represents the total effective stiffness of the tooth root interface in the direction of loading with units of N/m. The ASC relates this effective interface stiffness to a nominal stiffness value:

$$ASC = \frac{K_{eff}}{K_N} \text{ with } K_N = 4 \times 10^6 \text{ N/m}$$

The nominal stiffness value  $K_N$  was chosen to be the same as that used for the ASC value calculated for the BAHA implant systems (Section 2.3.4.).

## 6.4. Parametric Sensitivity of the Tooth Analytical Model

### 6.4.1. Center of Resistance

The center of resistance ( $C_{Res}$ ) of a tooth is an important parameter in orthodontic biomechanics.  $C_{Res}$  is defined as the point on the tooth where an applied force would produce only translation without any rotation of the body (Marcotte, 1990). The location of the center of resistance was determined for the analytical tooth model. A free body diagram (FBD) for the system is shown in Figure 6.8 with a horizontal force applied through the center of resistance. Only the restraining forces in the direction of motion were considered (horizontal component) for this applied loading configuration. This horizontal restraining force is applied through the interface stiffness distributed over the area of the tooth root.

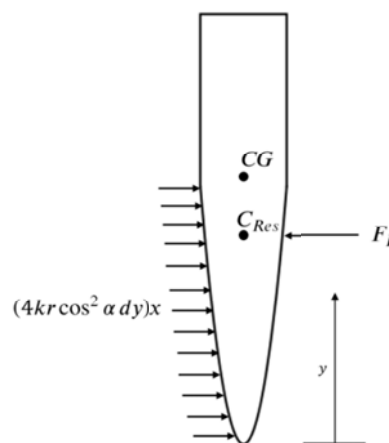


Figure 6.8: Free body diagram of a tooth with a horizontal force applied at the center of resistance ( $C_{Res}$ ). The horizontal restraining force is the interface stiffness distributed over the area of the tooth root.

With a static force applied through  $C_{Res}$ , the deformed shape of the system will have the tooth remaining in a vertical position (i.e. the deformed shape will be a simple horizontal translation without rotation) by definition. The equilibrium equations for the system are then:

$$\sum F_x = 0 \rightarrow 4 \left( \int_0^{L_r} kr \cos^2 \alpha dy \right) x - F_I = 0 \rightarrow F_I = 4 \left( \int_0^{L_r} kr \cos^2 \alpha dy \right) x$$

$$\sum M_{CG} = 0 \rightarrow 4 \left( \int_0^{L_r} kr \cos^2 \alpha (\bar{y}_{CG} - y) dy \right) x - F_I (\bar{y}_{CG} - y_{CR}) = 0$$

Where  $x$  is the horizontal translation of the tooth. Solving these equations for the location of the center of resistance, we find:

$$y_{CR} = \bar{y}_{CG} - \left( \frac{\int_0^{L_r} kr \cos^2 \alpha (\bar{y}_{CG} - y) dy}{\int_0^{L_r} kr \cos^2 \alpha dy} \right)$$

Where  $r$ ,  $\alpha$ , and  $\bar{y}_{CG}$  are defined by the shape and mass distribution of the tooth. For example, consider a tooth with a root length of  $L_r = 13$  mm, a crown length of 10 mm, and a radius of  $R_0 = 3.5$  mm. Consider also, a tooth shape with a paraboloid for the root, a cylinder for the crown, and a uniform mass distribution. For such a tooth model, the center of mass is located at  $\bar{y}_{CG} = 14.32$  mm from the tip of the root. The center of resistance is located 6.19 mm below the center of mass at a distance of 8.13 mm from the bottom of the root. For comparison, Marcotte (1990) cites that the center of resistance is located approximately  $2/5H$  from the top of the root, where  $H$  is the amount of root that is covered by bone (i.e. the root length in the present model). With this approximation, the center of resistance would be located 7.8 mm from the bottom of the root, which is a difference of only 4% from the location calculated here.

#### 6.4.2. Modal Analysis

The undamped natural frequencies  $p_n$  and mode shapes  $\{\phi\}_n$  of the system were determined for the tooth model by solving the eigenvalue problem with the matrices  $[K]$  and  $[M]$ .

The natural frequencies and mode shapes are dependent on the system parameters. The analysis was completed for a tooth with root length  $L_r = 13.03$  mm, crown length  $L_c = 10.28$  mm, and

radius  $R_0 = 3.84$  mm. The mass, the location of the center of mass, and the moment of inertia were assumed to be constant at  $m_t = 1.17$  g,  $\bar{y}_{CG} = 13.95$  mm and  $J_G = 38.01$  gmm<sup>2</sup>, respectively. These parameters correspond to measurements from a maxillary cuspid tooth used for the clinical evaluation that will be presented in Section 6.5. The impact stiffness was fixed at  $K_I = 2.9 \times 10^6$  N/m for all analyses. The effect of the striking height, the root shape, and the interface stiffness on the resulting mode shapes and undamped acceleration response were examined.

The striking location on the tooth will have an effect on the system response. This was investigated by varying the striking height from  $L_o = 5$  mm to  $L_o = 8$  mm from the crown tip. Figure 6.9 show examples of the mode shapes and undamped acceleration response for various striking height locations. The grey dashed lines represent the initial position of the system, while the solid black lines represent the normalized mode shapes. The solid dots represent the location of the center of mass of the impact rod, the center line of the tooth at the height of the strike, and the bottom of the tooth root.

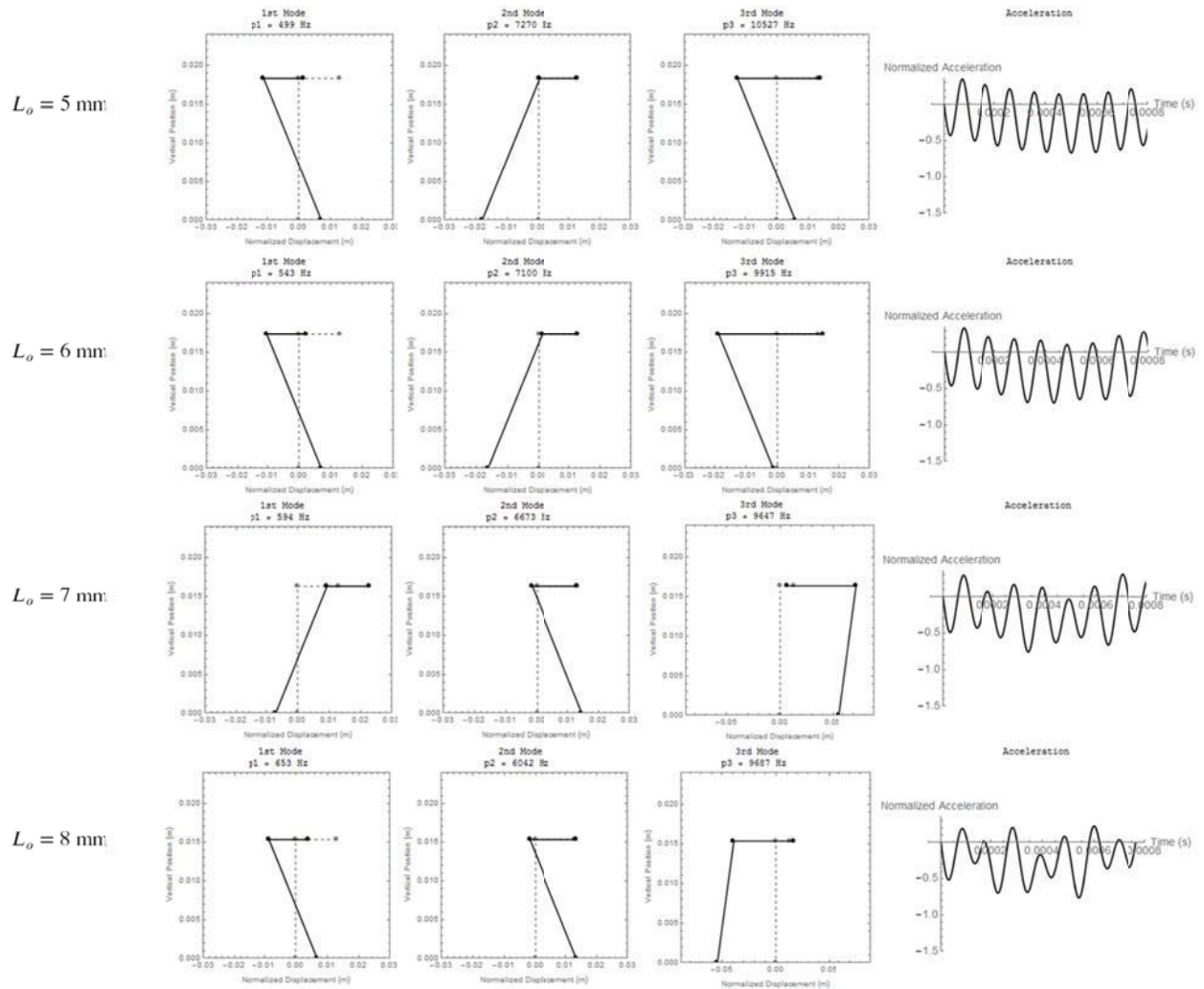


**Figure 6.9: Mode shapes and undamped acceleration response with varying striking locations:  $L_o = 5, 6, 7, 8$  mm from the crown tip. Interface stiffness  $k = 0.01 \times 10^{12} \text{ N/m}^3$ .**

When the strike is near the top of the tooth (e.g.  $L_o = 5$  mm), the modal participation factor of the second mode is approximately one order of magnitude less than the third mode indicating that the second mode contributes very little to the acceleration response in this case. As the strike is moved lower on the tooth, the frequency of the second and third modes become closer together and the modal participation of the second mode increases compared to the third mode. In this case, the three modal frequencies can be observed in the undamped acceleration signal (for example, the last case in Figure 6.9). Additionally, as the strike is moved lower on the tooth, the third mode shape tends to have a larger contribution of horizontal translation. This may be due to

the fact that the strike is moving closer to the center of resistance of the tooth. It should be noted that the horizontal scale in Figure 6.9 has been adjusted for the third mode shape with  $L_o = 7$  mm and  $L_o = 8$  mm to accommodate the large relative horizontal displacement within the frame of the figure.

### 6.4.3. Analytical Model Frequency Response versus Stiffness Parameters

The important stiffness parameter in the analytical tooth model is the impact stiffness ( $K_I$ ) while the primary variables of interest are the interface stiffness ( $k$ ) and the related ASC value. Using the analytical model, the relationship between the stiffness parameters and the first and second mode frequency components was examined. This provides an understanding of the effect of the internal stiffness parameters on the theoretical acceleration response, which will aid in interpreting the measured acceleration signals.

The relationship between the undamped first and second mode frequencies ( $p_1$  and  $p_2$ ) and the interface stiffness  $k$  can be seen in Figure 6.10 for a maxillary canine tooth. The first mode frequency is sensitive to changes in the interface stiffness showing an increase in  $p_1$  with increasing stiffness. The slope of the curve tends to decrease at the higher stiffness values. The second mode frequency is relatively less sensitive to changes in interface stiffness particularly at the moderate or high stiffness values where the curve begins to plateau. It can be seen from the figures that these relationships become nearly linear at higher interface stiffness values. A unit change in interface stiffness from  $k = 1 \times 10^{10}$  N/m<sup>3</sup> to  $k = 2 \times 10^{10}$  N/m<sup>3</sup> results in an increase in the first mode frequency of 126 Hz (27% increase) while a unit change in interface stiffness from  $k = 4 \times 10^{10}$  N/m<sup>3</sup> to  $k = 5 \times 10^{10}$  N/m<sup>3</sup> results in an increase in the first mode frequency of 74 Hz (9.6% increase). The same changes in interface stiffness result in increases in the second mode frequency of 1101 Hz (15% increase) and 154 Hz (1.7% increase) for the lower and higher stiffness ranges, respectively.

Interface Stiffness Per Unit Area ( $k$ )

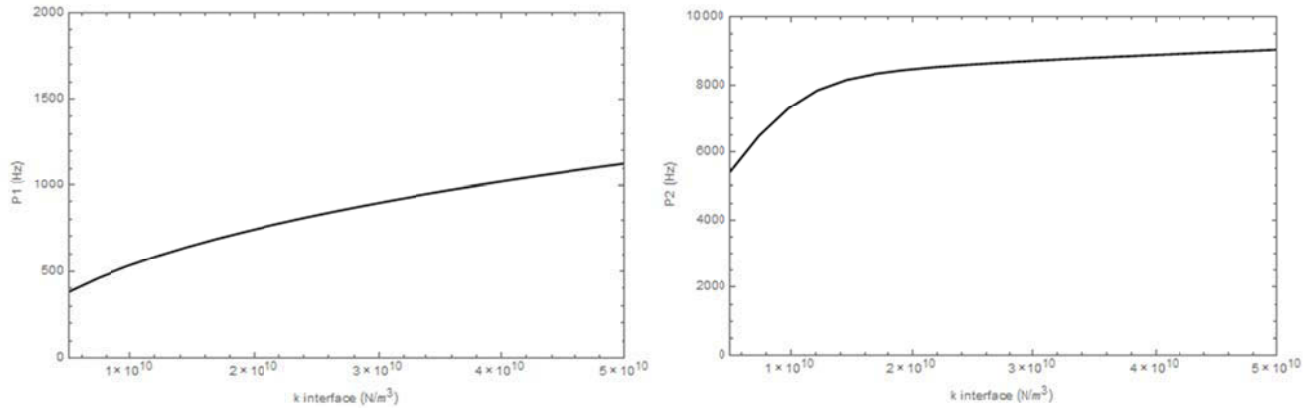


**Figure 6.10: Relationship between the interface stiffness per unit area ( $k$ ) and the first mode frequency ( $p_1$ ; left) and the second mode frequency ( $p_2$ ; right) for a typical tooth model**

The same relationships are presented in Figure 6.11 using the ASC measure.

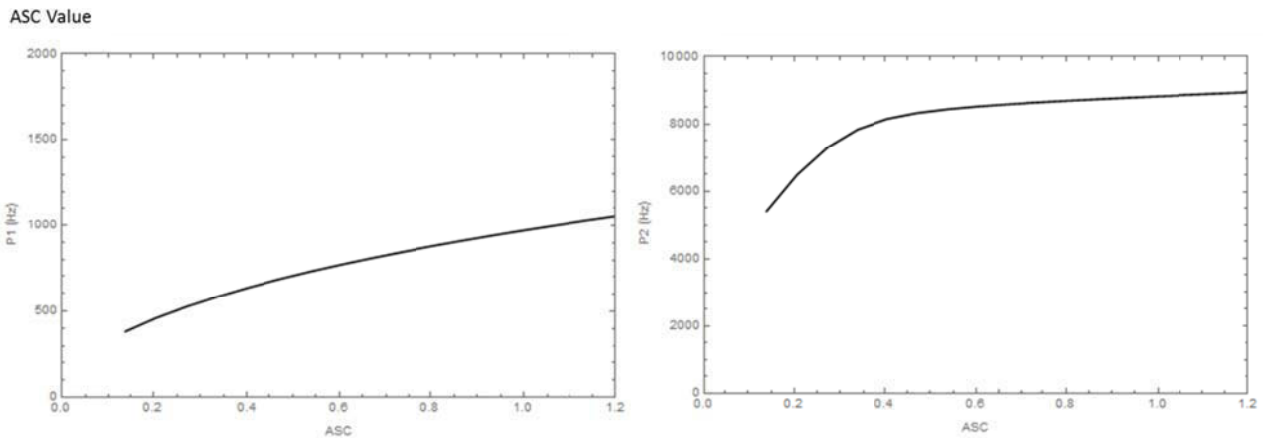


**Figure 6.11: Relationship between the ASC value and the first mode frequency ( $p_1$ ; left) and the second mode frequency ( $p_2$ ; right) for a typical tooth model**

The relationship between the frequency components and the impact stiffness ( $K_I$ ) are shown in Figure 6.12. The first mode frequency is essentially insensitive to changes in the impact stiffness while the second mode frequency shows much more sensitivity showing increasing frequency with increasing impact stiffness. For example, doubling the impact stiffness from

$K_I = 2 \times 10^6$  N/m to  $K_I = 4 \times 10^6$  N/m results in an increase in the first mode frequency of 11 Hz (1.8% increase) and an increase in the second mode frequency of 1830 Hz (26% increase).

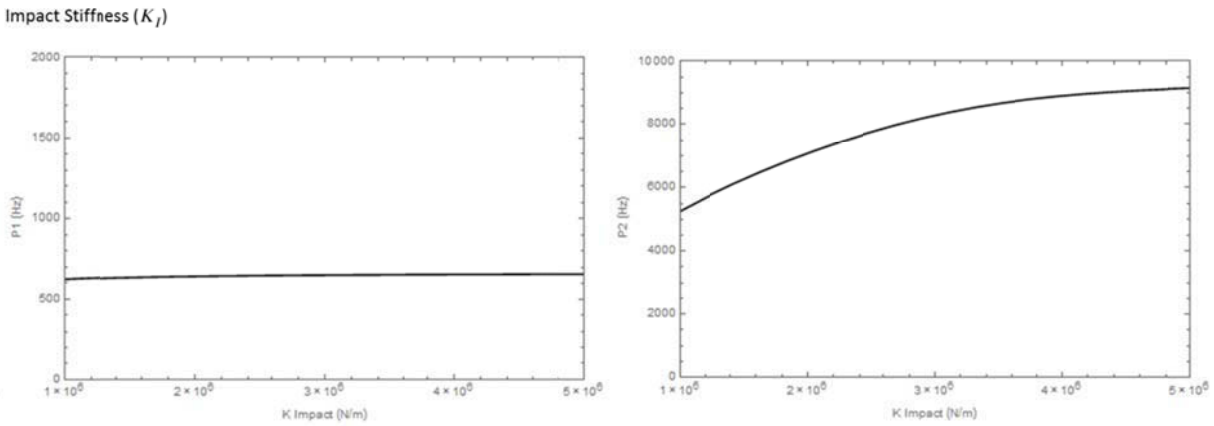


Figure 6.12: Relationship between the impact stiffness ( $K_I$ ) and the first mode frequency ( $p_1$ ; left) and the second mode frequency ( $p_2$ ; right) for a typical tooth model

#### 6.4.4. Model Solution (ASC and Fit with Measured Data) with Impact Stiffness

In this section, we evaluate the sensitivity of the model solution to changes in the impact stiffness. As  $K_I$  is varied, the calculated interface stiffness and associated ASC value are determined along with the resulting  $R^2$  fit between the model predicted signal and the measured acceleration. For each analysis, a sample dataset from a maxillary canine tooth from the available clinical data is used in order to calculate the ASC and  $R^2$  values.

Figure 6.13 shows the variation in the ASC and  $R^2$  values with changing  $K_I$ . The two plots are overlaid with the scale for the ASC value (blue line) on the left of the figure and the scale for the  $R^2$  value (black line) on the right of the figure.

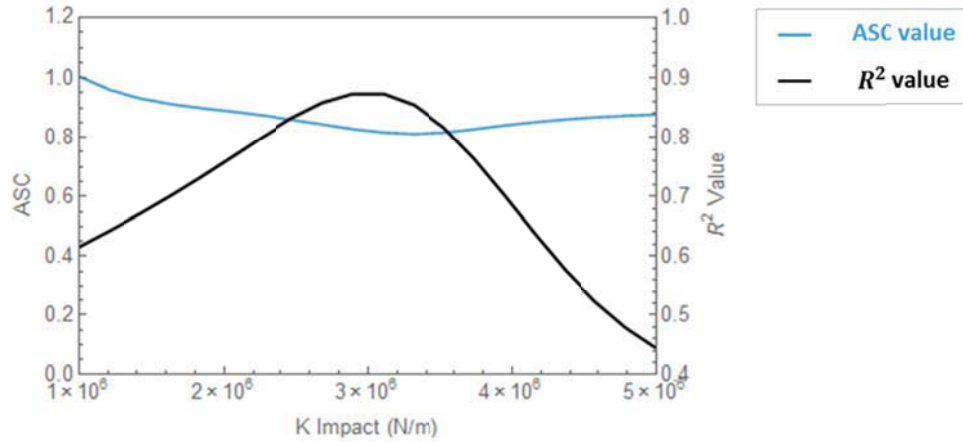


Figure 6.13: Variation in ASC value (blue line) and  $R^2$  fit (black line) with changes in impact stiffness ( $K_I$ )

As shown in the figure, there is some variation in the ASC value over the range of tested  $K_I$  and a clear peak in the fit between the measured signal and the model prediction as measured by the  $R^2$  value. Over the full range, the ASC values range from 0.811 – 1.00, with the ASC value corresponding to the best fit with the data of 0.828 at an impact stiffness of  $2.89 \times 10^6$  N/m. Figure 6.14 shows the variation in the signals as  $K_I$  is varied. The measured data is shown in the colored lines (the same for all subfigures) and the model predicted signal is shown in black. The subfigure that is highlighted with a red outline corresponds to the best match between the measured signal and the model response ( $K_I = 2.89 \times 10^6$  N/m, ASC = 0.828 for this sample dataset). It is clear from the figures that variations in the impact stiffness affect the second mode frequency of the model response, which can result in a poor fit between the measured data and model signal.

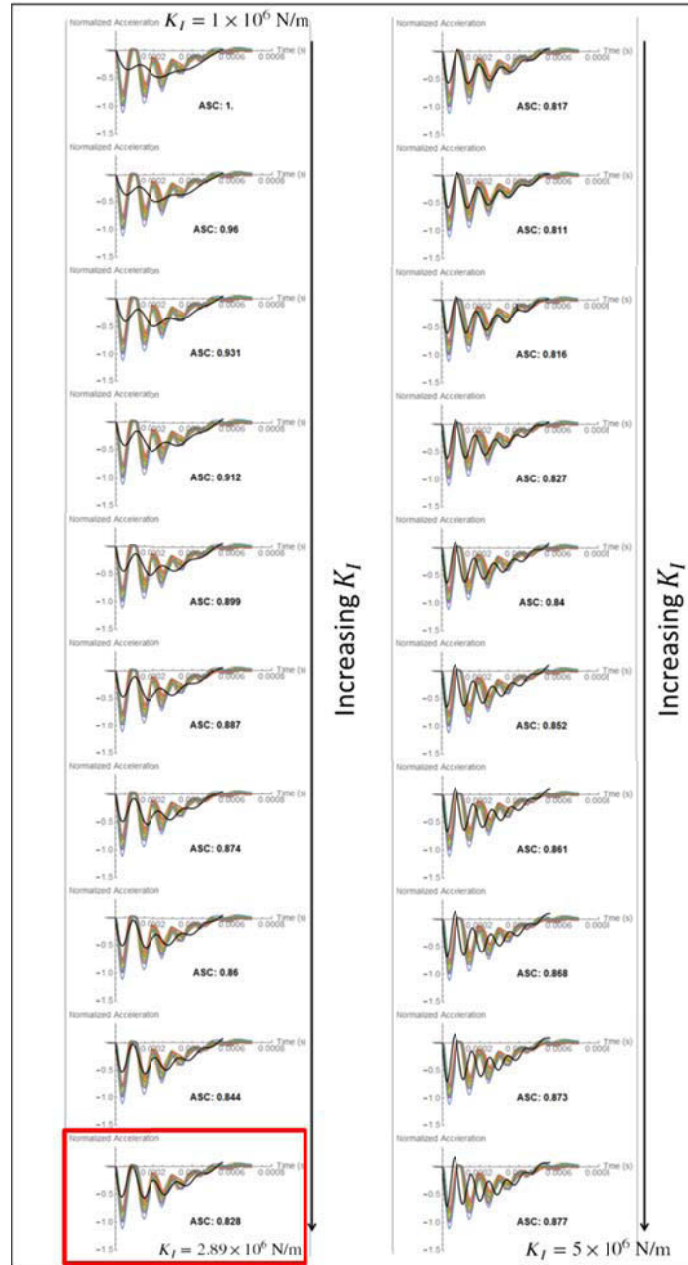


Figure 6.14: Variation in the model fit (black line) with the measured acceleration (colored lines) with changing impact stiffness ( $K_I$ ) for an example dataset (Patient 1; Tooth ID 13). The best match between the model and the measured data as measured by the  $R^2$  value is highlighted in red.

### 6.4.5. Analytical Model Frequency Response versus Geometric Parameters

The important geometric parameters in the analytical tooth model are the lengths of the tooth root ( $L_r$ ) and crown ( $L_c$ ), the radius at the crown-root junction ( $R_0$ ), the mass of the tooth ( $m_t$ ),

the location of the center of mass ( $\bar{y}_{CG}$ ), the mass moment of inertia ( $J_G$ ), and the striking height ( $L_o$ ).

Using the analytical model, the relationships between the geometric parameters and the first and second mode frequency components were examined following the same procedure as the stiffness parameters. This can provide an understanding of the effect of the various geometric parameters on the theoretical acceleration response. Additionally, this analysis will provide an understanding of the sensitivity of the ASIST measure to errors in the estimated parameters. For each parameter, the value was varied over a range of values and all other parameters were kept fixed in the model. It should be noted that when the root length and crown length were varied, the mass, location of the center of mass, and moment of inertia were adjusted as a function of the given lengths. An impact stiffness of  $K_I = 2.9 \times 10^6$  N/m and an interface stiffness of  $k = 1.5 \times 10^{10}$  N/m<sup>3</sup> (corresponding to an ASC value of approximately 0.4) was used for all analyses.

The relationship between the first mode frequency  $p_1$  and the second mode frequency  $p_2$  and the tooth geometric parameters can be seen in Figure 6.15 – Figure 6.21.

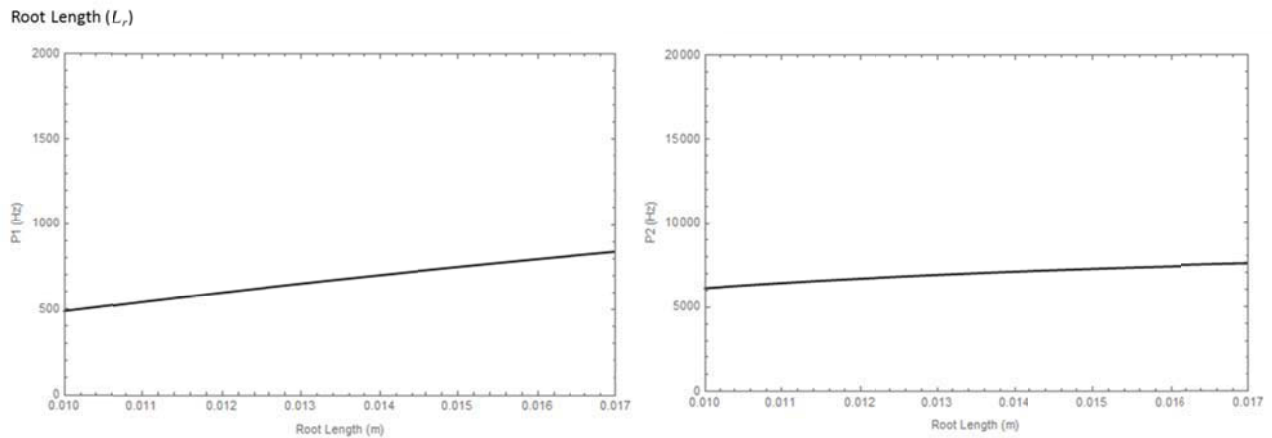


**Figure 6.15: Relationship between the first mode frequency ( $p_1$ ; left) and second mode frequency ( $p_2$ ; right) and the tooth root length ( $L_r$ )**

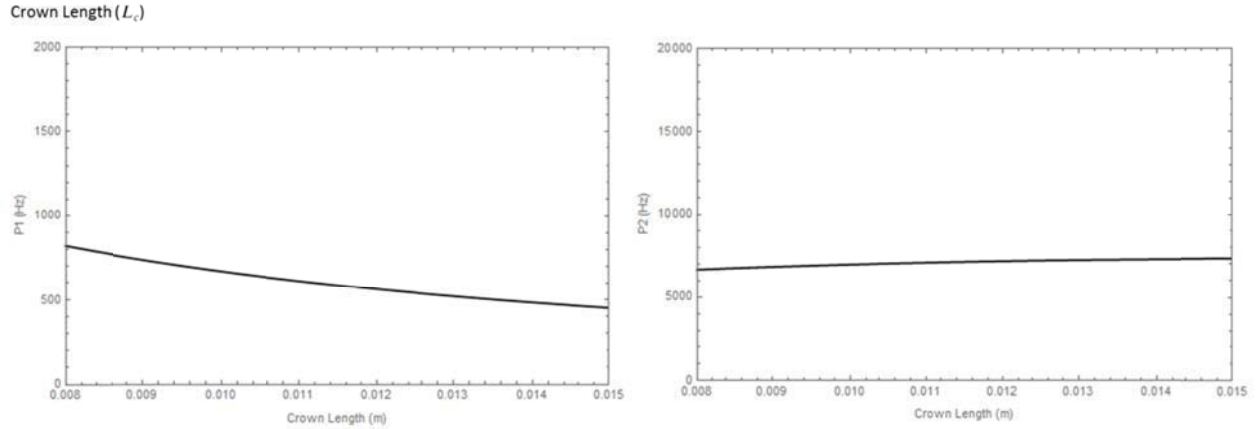


**Figure 6.16: Relationship between the first mode frequency ( $p_1$ ; left) and second mode frequency ( $p_2$ ; right) and the tooth crown length ( $L_c$ )**

The first mode frequency of the model response is sensitive to changes in both tooth root length and crown length and the relationships are nearly linear. The first mode frequency was found to increase with increasing root length while it was found to decrease with increasing crown length. In both cases, the first mode frequency is more sensitive than the second mode frequency. For example, a change in root length from 12.6 mm to 14.8 mm (18% increase) results in an increase in first mode frequency of 111 Hz (17% increase). The same change in root length results in an increase in the second mode frequency of 417 Hz (6.1% increase). Similarly, a change in crown length from 10.6 mm to 12.8 mm (21% increase) results in a decrease in the first mode frequency of 107 Hz (17% decrease) and an increase in the second mode frequency of 192 Hz (2.7% increase). It should be noted that the striking height was kept at a fixed distance from the top of the crown for these analyses.

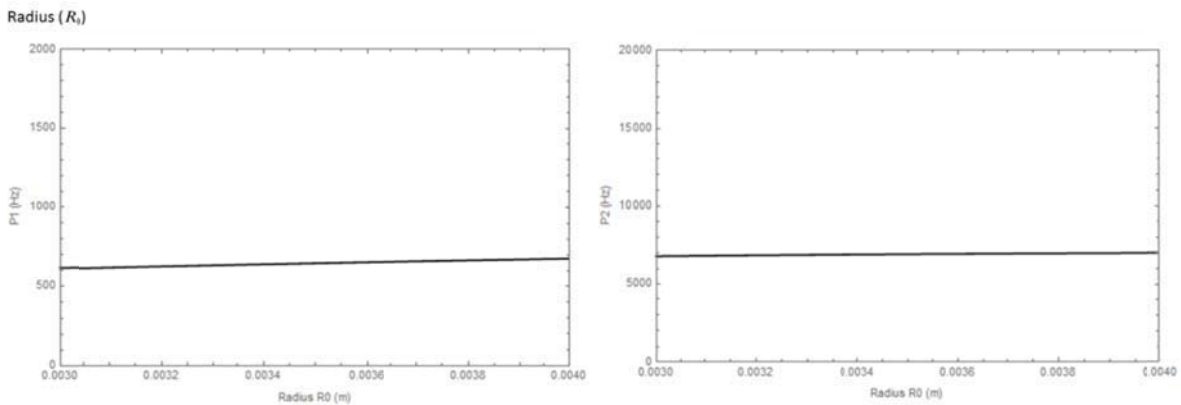


**Figure 6.17: Relationship between the first mode frequency ( $p_1$ ; left) and second mode frequency ( $p_2$ ; right) and the tooth radius ( $R_0$ )**

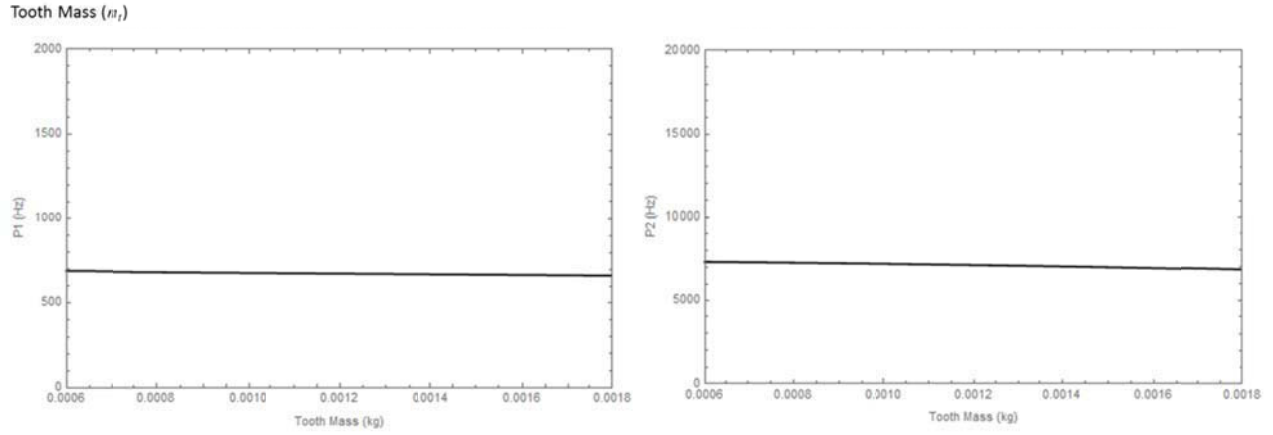


Figure 6.18: Relationship between the first mode frequency ( $p_1$ ; left) and second mode frequency ( $p_2$ ; right) and the tooth mass ( $m_t$ )

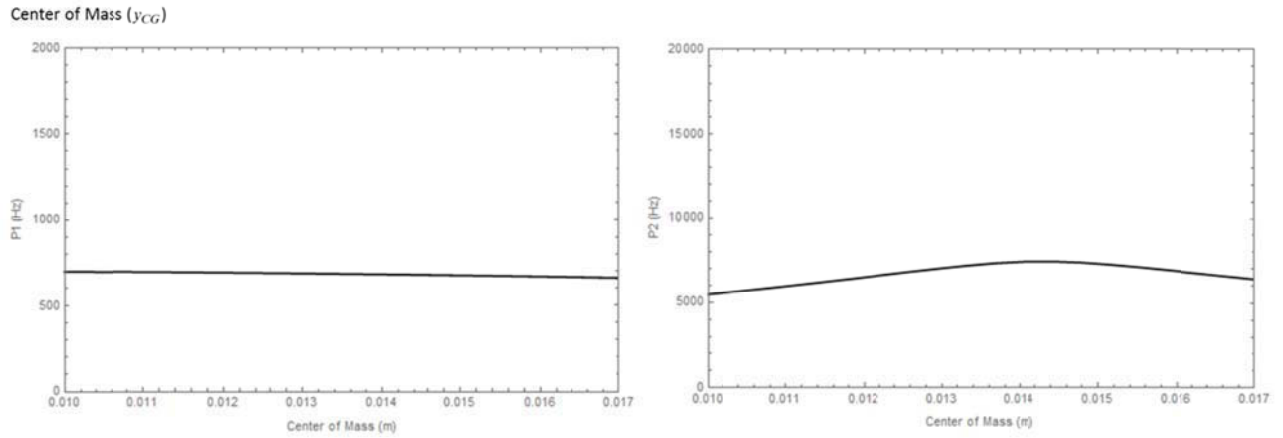


Figure 6.19: Relationship between the first mode frequency ( $p_1$ ; left) and second mode frequency ( $p_2$ ; right) and the location of the center of mass ( $\bar{y}_{CG}$ )

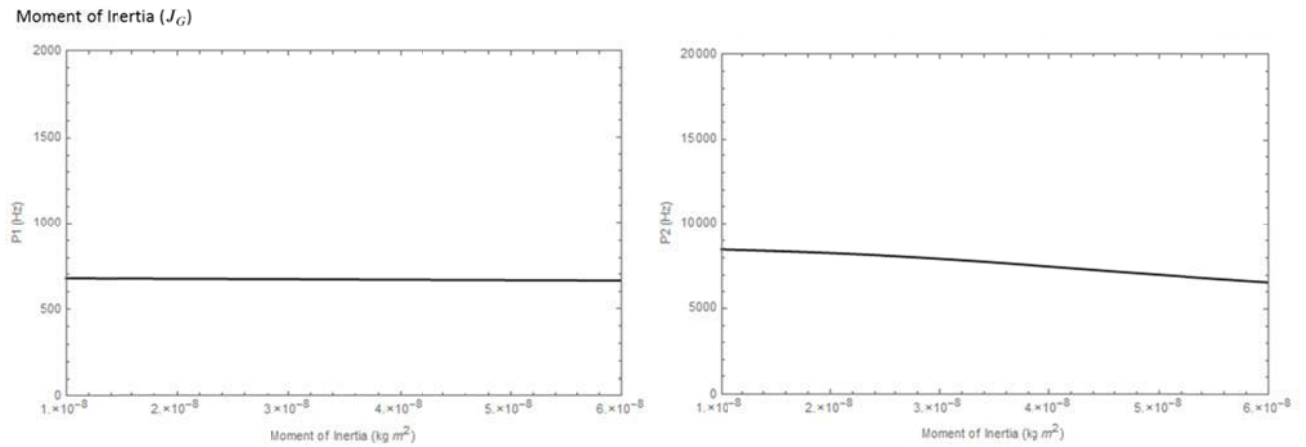
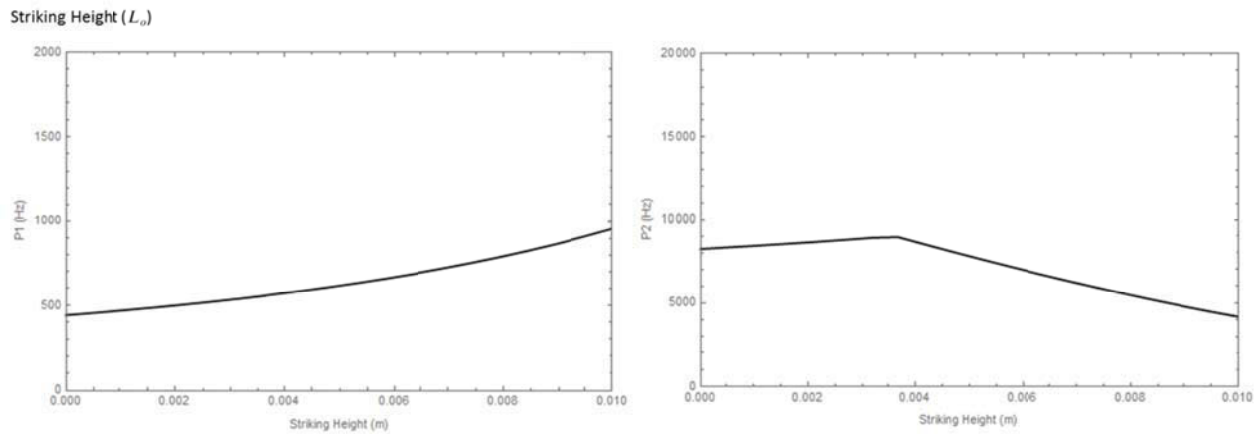


Figure 6.20: Relationship between the first mode frequency ( $p_1$ ; left) and second mode frequency ( $p_2$ ; right) and mass moment of inertia ( $J_G$ )

The first mode frequency was found to be relatively insensitive to changes in both the location of the center of mass and the mass moment of inertia, while the second mode frequency showed some sensitivity to these parameters. For lower values of the center of mass, the second mode frequency increased with increasing  $\bar{y}_{CG}$ ; however, beyond a threshold of approximately 14 mm for the given tooth example, the second mode frequency begins to decrease with increasing  $\bar{y}_{CG}$ . For example, a change in  $\bar{y}_{CG}$  from 10.0 mm to 12.2 mm (22% increase) results in an increase in the second mode frequency of 1146 Hz (21% increase) while a change in  $\bar{y}_{CG}$  from 15.2 mm to 17.0 mm (12% increase) results in a decrease in the second mode frequency of 858 Hz (12% decrease). Additionally, the second mode frequency was found to decrease slightly with increasing moment of inertia. For example, a change in  $J_G$  from 20.5 kgm<sup>2</sup> to 41.6 kgm<sup>2</sup> (approximately double) results in a decrease in the second mode frequency of 856 Hz (10% decrease).



**Figure 6.21: Relationship between the first mode frequency ( $p_1$ ; left) and second mode frequency ( $p_2$ ; right) and the striking height ( $L_o$ ). Note that  $L_o$  is measured from the top of the crown, so increasing  $L_o$  indicates striking lower on the tooth crown.**

Both the first and second mode frequency components were found to be sensitive to changes in the striking location. Since both the impact rod and the tooth are included in the analytical system, adjusting the location of the strike changes the physical system that is modeled. It was found that the first mode frequency increased with increasing  $L_o$ . Recall that since  $L_o$  is measured from the top of the crown, increasing  $L_o$  indicates that the striking location is moving downwards away from the top of the crown. The slope of the curve was found to increase with

larger values of  $L_o$ . For example, a change in  $L_o$  from 1.05 mm to 2.10 mm results in an increase in the first mode frequency of 33 Hz (6.9% increase) while a similar change in  $L_o$  from 6.84 mm to 7.90 mm results in an increase in the first mode frequency of 69 Hz (9.6%). It can be seen from Figure 6.21 that the second mode frequency is relatively insensitive to changes in  $L_o$  for low values with only a slight increase. Beyond a threshold of approximately 4 mm for this tooth model, the second mode frequency decreases quite substantially with increasing  $L_o$ . For example, the same changes in  $L_o$  result in changes in the second mode frequency of 223 Hz (2.6% increase) and -785 Hz (12% decrease) for the lower and higher  $L_o$  ranges respectively.

Unlike the other geometric and inertia parameters, the model response was found to be relatively insensitive to changes in both the radius at the crown-root junction and the tooth mass.

#### **6.4.6. Model Solution (ASC and Fit with Measured Data) with Location of the Center of Mass**

The location of the center of mass of the tooth was found to have an effect on the second mode frequency response of the analytical model. In this section, we will evaluate the sensitivity of the model solution to variations in this parameter. As  $\bar{y}_{CG}$  is varied, the calculated interface stiffness and associated ASC value are determined along with the resulting  $R^2$  fit between the model predicted signal and the measured acceleration for a sample dataset (maxillary canine from the available clinical data). The location of the center of mass was varied across a range of values in 20 discrete steps. The model was used to determine the ASC value and  $R^2$  fit for each variation in  $\bar{y}_{CG}$ .

Figure 6.22 shows the variation in ASC and  $R^2$  value with changing  $\bar{y}_{CG}$ . The two plots are overlaid with the scale for the ASC value (blue line) on the left of the figure and the scale for the  $R^2$  value (black line) on the right of the figure.

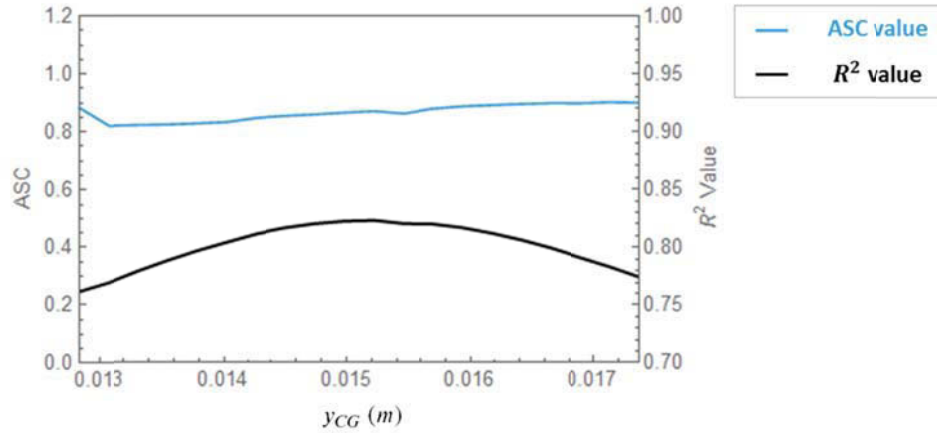


**Figure 6.22: Variation in ASC value (blue line) and  $R^2$  fit (black line) with changes in the location of the center of mass ( $\bar{y}_{CG}$ )**

As shown in the figure, there is a small variation in the ASC value over the range of tested  $\bar{y}_{CG}$  values and a peak in the fit between the measured signal and the model prediction as measured by the  $R^2$  value. Over the full range, the ASC values range from 0.820 – 0.901, with the ASC value corresponding to the best fit with the data of 0.871 with  $\bar{y}_{CG} = 15.2$  mm.

Figure 6.23 shows the variation in the shape of the signals as  $\bar{y}_{CG}$  is varied. The measured data is shown in the colored lines (the same for all subfigures) and the model predicted signal is shown in black. The subfigure that is highlighted with a red outline corresponds to the best match between the measured signal and the model response ( $\bar{y}_{CG} = 15.2$  mm, ASC = 0.871 for this sample dataset). It can be seen from the figures that variations in the center of mass affect the amplitude of second mode frequency response, particularly in matching the first cycle of the second mode. It should be noted that the impact stiffness was allowed to vary for each analysis. As was shown in Section 6.4.4, the impact stiffness has an effect on the frequency of the second mode; thus allowing this parameter to vary in the model allows the optimization procedure to determine an appropriate value of  $K_I$  to produce a good match for the second mode frequency. Conversely,  $K_I$  was found to have very little effect on the first mode frequency. If we instead kept this parameter fixed in the model, it would primarily affect the fit between the model and the measured data; however, it would not have a large effect on the resulting ASC. It can also be noted from Figure 6.23 that changing  $\bar{y}_{CG}$  affects the damping in the second mode. For these analyses, the damping coefficient  $\gamma$  was kept fixed in the model. However, the damping coefficient is dependent on both the mass and stiffness matrices. Thus, changing important

geometric parameters such as  $\bar{y}_{CG}$  affects the damping in the model. This effect should be taken into account when determining the damping coefficients in future applications of the ASIST technique for natural teeth.

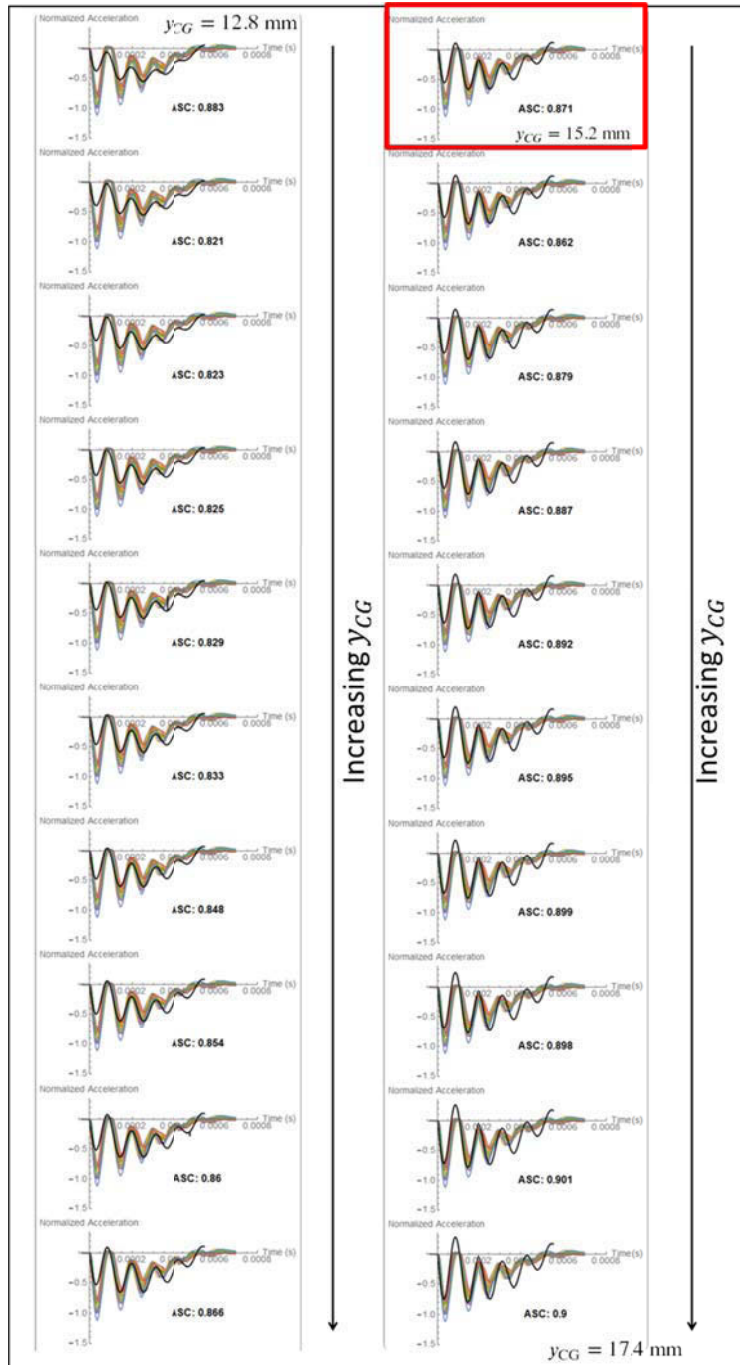


Figure 6.23: Variation in the model fit (black line) with the measured acceleration (colored lines) with changing center of mass for an example dataset (Patient 1; Tooth ID 13). The best match between the model and the measured data as measured by the  $R^2$  value is highlighted in red.

### 6.4.7. Damping Assumption

The damping in the analytical model can be included in a variety of ways and two methods were investigated in this study: proportional damping and general viscous damping at the interface. The details of these different methods are described for the BAHA implant-abutment system in Appendix B and the same assumptions can be applied for teeth. These two damping methods were evaluated on a subset of clinical data (11 samples) from patients undergoing orthodontic treatment. The ASIST procedure was used to estimate the interface stiffness and calculate the associated ASC value using both the proportional damping assumption and the general viscous damping assumption. The second mode damping ratio was extracted from the curve fit approximation for each dataset and used in the analysis.

The average damping ratio for this sample data is 0.092 (9.2%) with a range of 0.038 – 0.172. The ASC values and  $R^2$  values using both damping methods are presented in Table 6.1. The average difference in ASC value between the two methods is 5.6% with a maximum difference of 14.7%. The  $R^2$  fit is better for the viscous damping than the proportional damping in all cases with an average difference in  $R^2$  of 18.9%.

**Table 6.1: Comparison of ASC and  $R^2$  values using different damping assumptions for example datasets from clinical orthodontic patients**

Dataset	Damping Ratio (Curve Fit)	ASC Viscous	ASC Proportional	% Diff ASC	$R^2$ Viscous	$R^2$ Proportional	% Diff $R^2$
1	0.076	0.52	0.52	0.6	0.84	0.69	18.7
2	0.095	0.78	0.84	7.2	0.91	0.78	14.4
3	0.078	0.41	0.41	1.3	0.89	0.70	21.1
4	0.081	0.35	0.33	5.4	0.74	0.45	39.4
5	0.172	1.39	1.59	14.7	0.96	0.78	18.7
6	0.038	0.85	0.82	3.4	0.69	0.53	22.0
7	0.119	0.41	0.45	10.3	0.91	0.80	12.0
8	0.110	0.74	0.84	13.8	0.95	0.85	10.1
9	0.066	0.50	0.50	0.1	0.84	0.70	16.4
10	0.094	0.83	0.86	3.4	0.91	0.76	16.9
11	0.088	0.79	0.78	1.2	0.84	0.69	18.3

Figure 6.24 shows the data with the model response using viscous damping and using proportional damping. The difference between the two damping assumptions can be clearly seen from the figures with the viscous damping showing a better fit with the measured acceleration in general. This is evident by visual appraisal of the figures and is further supported by the higher  $R^2$  values with viscous damping in Table 6.1.

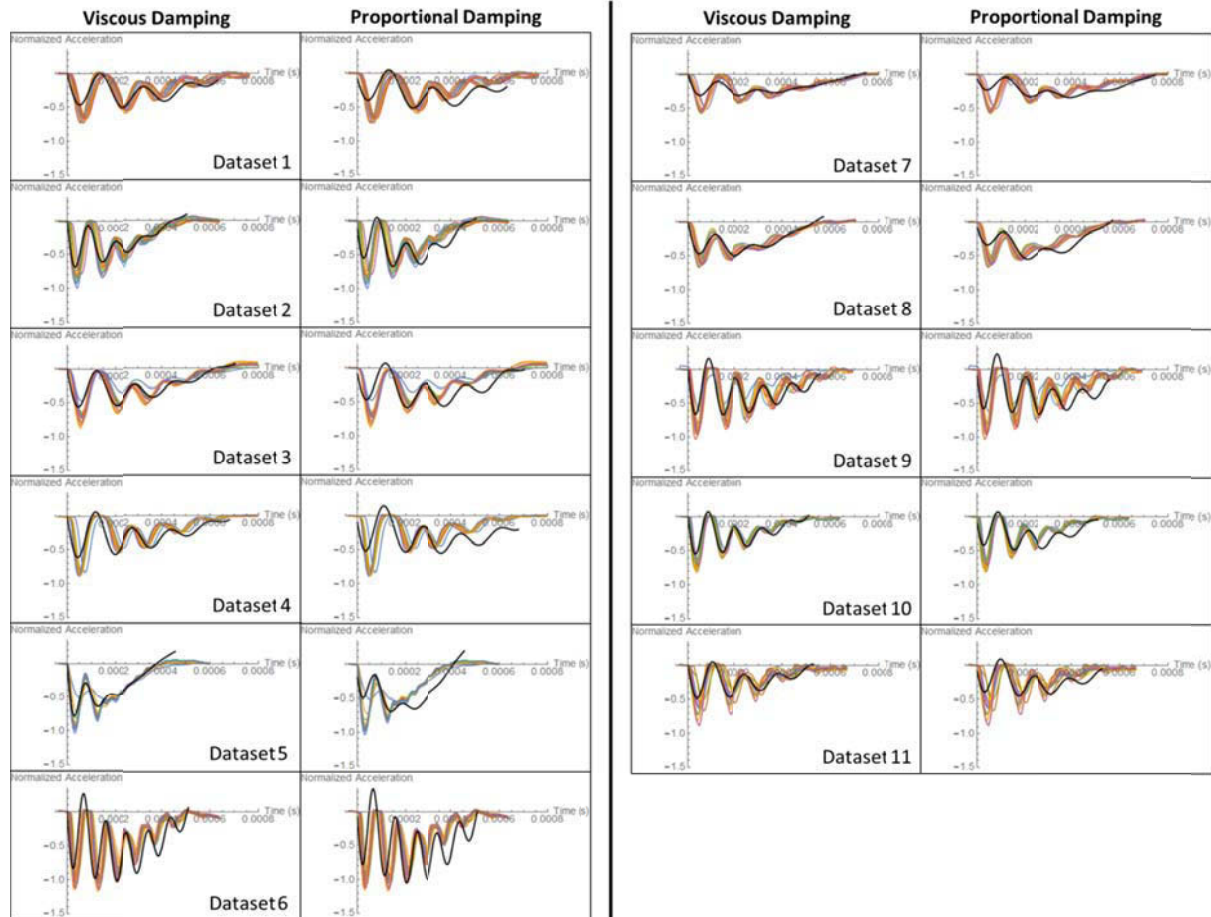


**Figure 6.24: Comparison of model solution (black lines) with viscous damping and proportional damping for orthodontic patient datasets (shown in colored lines)**

The acceleration response can be determined for any combination of interface stiffness and damping ratio using both the viscous damping and proportional damping assumptions. Figure 6.25 shows a comparison between the acceleration response for each damping model for a tooth with dimensions matching one of the patients from the clinical study (Patient 2; Tooth ID 13) with  $k = 0.19 \times 10^{12} \text{ N/m}^3$  (ASC 0.73). The figure shows the comparison for damping ratios of  $\zeta_2 = 0, 0.01, 0.05, 0.08, 0.1,$  and  $0.15$ . The corresponding interface damping coefficient values ( $c$ ) are shown on the subfigures. At higher damping ratios, the difference in the acceleration response of the two models becomes much more evident as expected.

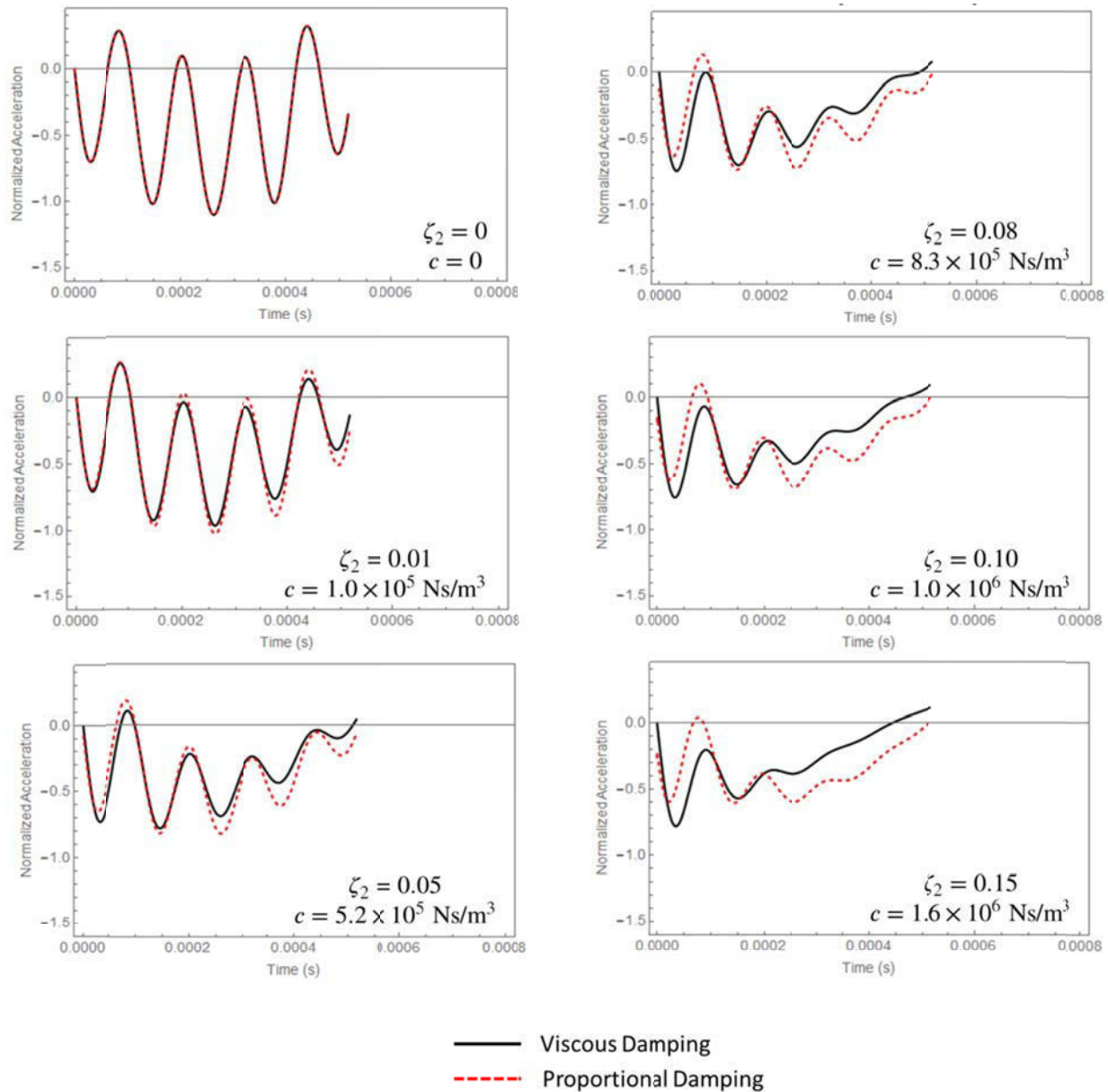


Figure 6.25: Comparison of viscous damping and proportional damping for various damping ratios. Second mode damping ratio ( $\zeta_2$ ) and interface damping coefficient ( $c$ ) values are shown on the figures.

## 6.5. Clinical Evaluation

The ASIST technique was developed and evaluated for a set of clinical tooth data. This section describes the available data, which was collected while the patients were undergoing orthodontic treatment as part of a previous study, along with the ASIST application and results.

### **6.5.1. Description of the Data**

Acceleration measurements were collected for 12 adolescent female participants (12-15 years) during orthodontic treatment as part of a previous study. Participants were recruited from the pool of patients seeking orthodontic treatment at the University of Alberta Graduate Orthodontic Clinic. All participants in the study required extraction of the first maxillary premolars for overjet reduction. For each patient, stability measurements were recorded for the two maxillary cuspid teeth (teeth ID 13 and 23) at approximately 12 visits over a 1 year span (range: 11 – 14 visits). At each visit, three acceleration measurements were typically collected for each tooth (range: 1 – 5 measurements). In some cases, no usable measurements were collected at a particular visit, which may have been due to an error in the data collection. In total, 6 visits were excluded for this reason.

At the initial visit, the first maxillary premolars were extracted and full fixed orthodontic appliances (Ormco Orthos, Orange CA, USA) were placed. The participants attended several check-up visits during the initial alignment and leveling phase. Following this, an osseointegrated palatal implant (Straumann, Basel, Switzerland) was installed to provide posterior anchorage for the retraction phase. Cuspid retraction was achieved through specialized hooks and shape memory alloy springs. Forces were applied to the cuspids such that the force on one side was half the force on the other side and these force levels were randomly assigned to each side (left and right) for all participants. Maxillary impressions were taken at the initial activation of the retraction phase and spring adjustments were made at subsequent follow-up visits to achieve the desired force levels. Following the retraction phase, the palatal implant was removed and participants attended a final check-up visit to conclude the study. After cuspid retraction, the participants continued with any remaining orthodontic treatment that was required.

CT volumetric scans were obtained for both maxillary cuspid teeth for each participant during treatment (NewTom, Verona, Italy). The mass and geometry parameters were estimated from the 3D reconstructed models from the CT data (Table 6.2).

Table 6.2: Mass and Geometry Parameters for Clinical Tooth Data from CT Scans

Patient ID	Tooth ID (Maxillary Cuspids)	Tooth Length (mm)	Root Length (mm)	Crown Length (mm)	Radius (mm)	$\bar{y}_{CG}$ (mm)	Mass (g)	$J_G$ (g mm <sup>2</sup> )
1	23	23.74	12.90	10.84	3.92	14.27	1.19	38.27
1	13	23.32	13.03	10.28	3.84	13.95	1.17	38.01
2	23	25.51	15.78	9.73	3.84	14.62	1.17	47.59
2	13	26.34	16.77	9.57	3.83	15.51	1.15	47.13
3	23	26.10	14.06	12.03	3.58	15.29	1.18	43.85
3	13	25.89	15.06	10.83	3.65	15.66	1.11	37.59
4	23	25.23	14.55	10.68	3.24	15.03	1.22	40.19
4	13	25.69	15.05	10.65	3.49	15.07	1.20	38.77
5	23	22.71	12.33	10.38	3.68	12.96	1.27	34.35
5	13	21.83	11.44	10.38	3.61	12.27	1.19	31.56
6	23	20.81	11.34	9.47	3.73	11.17	0.96	25.57
6	13	23.62	13.87	9.75	3.62	13.81	0.88	25.99
7	23	23.61	13.68	9.93	3.37	13.70	1.26	35.95
7	13	25.39	15.03	10.36	3.59	15.16	1.21	37.80
8	23	25.53	15.16	10.37	3.48	14.74	1.14	37.88
8	13	22.69	12.87	9.82	3.41	13.24	1.11	34.44
9	23	26.01	15.97	10.04	3.85	15.68	1.36	50.48
9	13	24.25	13.64	10.61	3.93	13.61	1.33	46.28
10	23	21.40	11.97	9.43	3.75	12.38	1.07	26.68
10	13	21.81	12.15	9.66	3.62	12.63	0.99	23.85
11	23	26.89	16.48	10.41	3.61	16.44	1.13	44.20
11	13	25.24	14.98	10.26	3.47	15.01	1.02	40.49
12	23	22.51	11.87	10.64	3.47	12.87	1.04	33.30
12	13	22.84	12.71	10.13	3.57	13.00	1.05	33.99

Initially, the mass, the location of the center of mass, and the moment of inertia were estimated assuming the tooth volume has a uniform density (results reported in Table 6.2). For each tooth the average density was estimated from the Hounsfield units (HU) determined from the grayscale pixels over the CT scan. The density was calculated from the average HU using the regression equation reported by Lagravère et al. (2006) for a NewTom QR-DVT 9000 cone-beam CT unit:

$$\rho = 0.002H - 0.381$$

Where  $\rho$  is the density in g/cm<sup>3</sup> and  $H$  is the Hounsfield Units (HU). The average density over all of the teeth with this method is  $\rho = 1192 \text{ kg/m}^3$ .

The density of a natural tooth, however, is not uniform. The tooth consists of several components whose densities can vary quite substantially (Ghorayeb et al., 1998). The tooth is composed of enamel, dentin, pulp, and a thin layer of cementum (Figure 1.4). The approximate density of these components as reported in Ghorayeb et al. (1998) and Vafaeian et al. (2015) are shown in Table 6.3.

**Table 6.3: Density of tooth components**

	Density (kg/m <sup>3</sup> )
<b>Enamel</b>	2950
<b>Dentin</b>	2000
<b>Pulp</b>	1000
<b>Cementum</b>	2030

\*Ghorayeb et al., 1998; Vafaeian et al., 2015

If we assume that the tooth crown is composed of enamel, dentin, and some pulp, we can estimate the average density to be  $\rho_c = 2500 \text{ kg/m}^3$ . Similarly, if we assume that the tooth root is composed of primarily pulp and dentin with some cementum, we can estimate the average density to be  $\rho_r = 1500 \text{ kg/m}^3$ . We can then use an alternative method to estimate the mass, location of center of mass, and moment of inertia of the tooth by separating the tooth into two components (the crown and the root) and assigning different density values to each component (Figure 6.26).

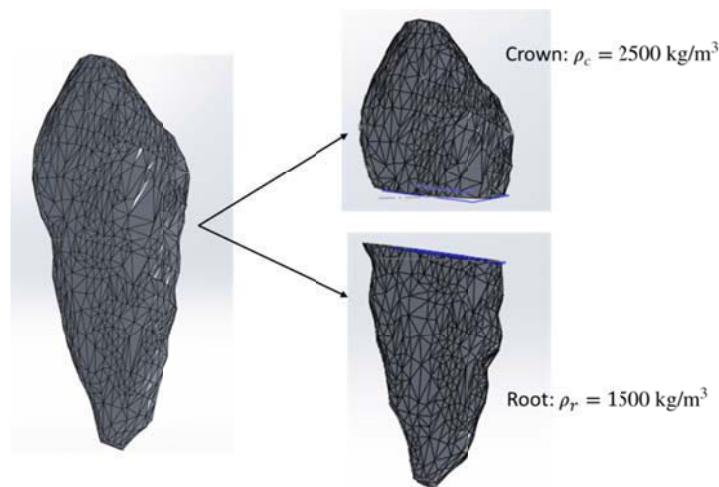


**Figure 6.26: Separating the tooth into two components (crown and root) to estimate the mass properties with different density values for the two components**

The 3D reconstructed model for each tooth was separated into two components using Solidworks (Solidworks 2015, Dassault Systèmes Solidworks Corp., Waltham MA, USA). This resulted in a difference in the calculated mass of  $0.07 \pm 0.04$  g (6.6%) with the predicted mass increasing for 71% of the teeth and decreasing for 29%. There was a difference in the calculated  $\bar{y}_{CG}$  of  $1.13 \pm 0.09$  mm (8.1%) with the predicted  $\bar{y}_{CG}$  moving up (towards the crown tip) in 100% of the cases. There was a difference in the calculated  $J_G$  of  $1.39 \pm 1.19$  gmm<sup>2</sup> (3.8%) with the predicted  $J_G$  increasing for 79% of the teeth and decreasing for 21%.

Figure 6.27 shows an example of the model fit with the measured acceleration for one measurement from the clinical data (Patient 1; Tooth ID 13). The same data is used in both cases. The image on the left shows the model fit using the mass, center of mass, and moment of inertia determined from the uniform density model. The image on the right shows the model fit using the mass and center of mass from the two density model. The two density model appears to provide a better fit with the measured acceleration, particularly in matching the first cycle of the second mode frequency. There is a very small change in the predicted ASC value between these two cases as shown in the figure. Since an improved fit can be achieved with the two density model, the values from this model were used in the analysis of the clinical data.

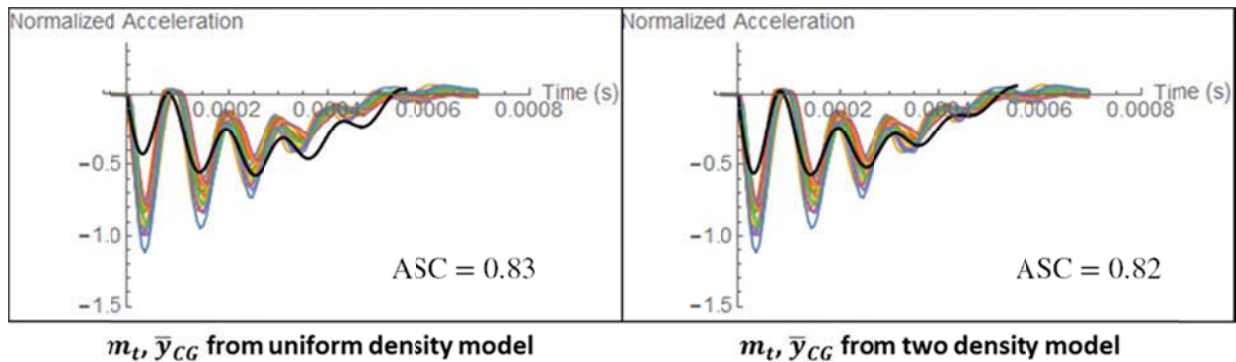


Figure 6.27: Example data (Patient 1; Tooth ID 13) comparing the two density models. Left: mass and center of mass were determined from the uniform density model. Right: mass and center of mass were determined from the two density model.

As reported above, the two density model had a minor effect on the calculated mass moment of inertia of the tooth with an average difference in  $J_G$  of 3.8% (range: 0.2 – 10.5%). It can also be shown that the ASC value and the model fit are relatively insensitive to changes in  $J_G$  within this

range. To demonstrate this, the moment of inertia was varied  $\pm 15\%$  for three example datasets with original  $J_G$  values of approximately 47  $\text{gmm}^2$  (high), 38  $\text{gmm}^2$  (mid-range), and 24  $\text{gmm}^2$  (low). An example for the mid-range  $J_G$  is shown in Figure 6.28. It can be seen from the figure that there is virtually no change in the model fit across the range. The maximum changes in the  $R^2$  values were 0.01, 0.01, and 0.02 for the high, mid-range, and low  $J_G$  examples, respectively. The maximum changes in ASC values were 0.006 (0.9%), 0.012 (1.4%), and 0.004 (0.4%) for the high, mid-range, and low  $J_G$  examples, respectively. This indicates that varying  $J_G$  has very little effect on both the ASC value and the fit between the model and the measured acceleration. For this reason, the original moment of inertia values determined from the uniform density model were used in subsequent analyses of the clinical data.

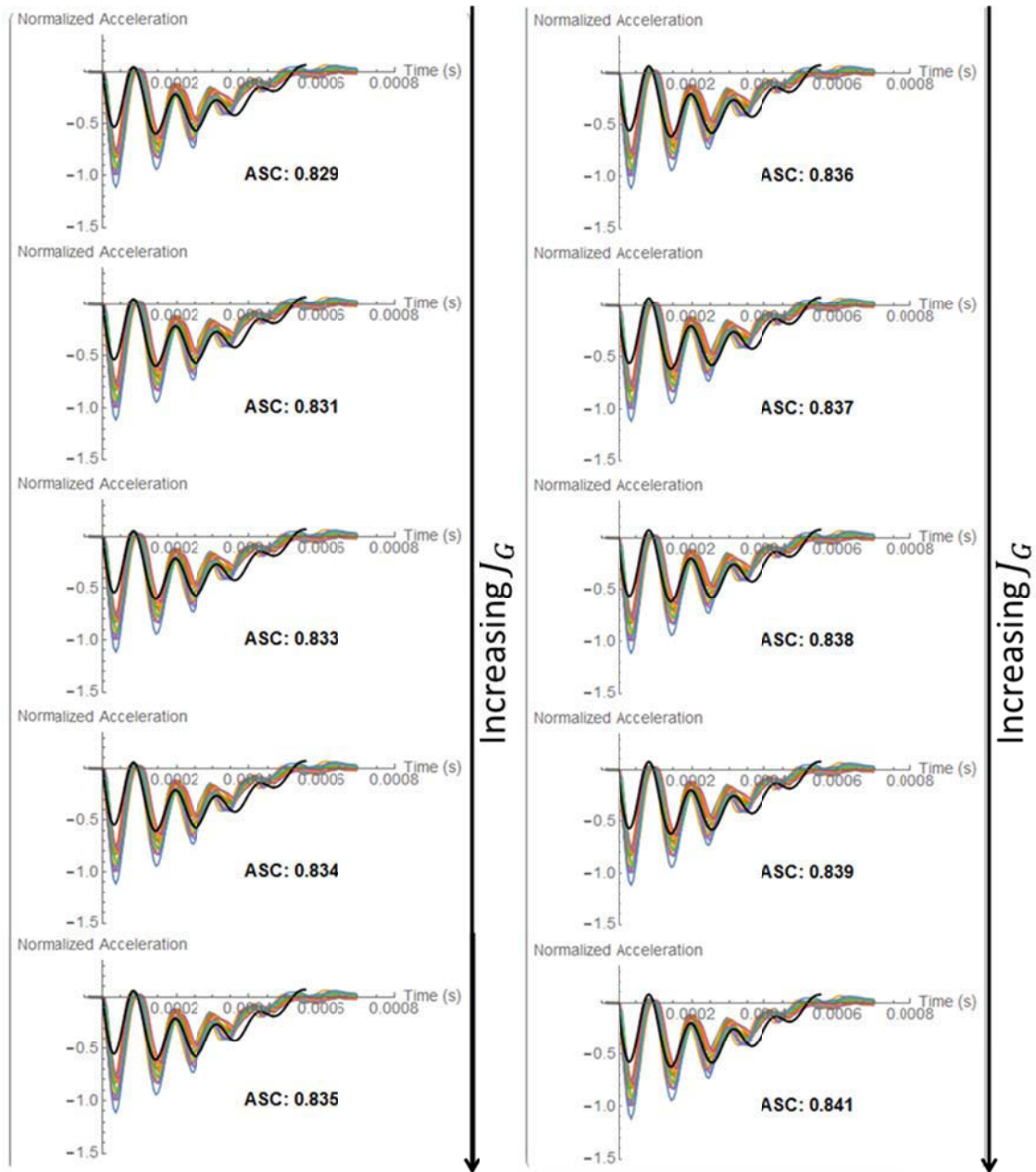


Figure 6.28: Change in model fit and ASC values with varying moment of inertia.  $J_G$  was varied  $\pm 15\%$ . The sample dataset is an example from Patient 1.

### 6.5.2. Data Analysis – CT Geometry

The ASIST procedure was used to analyze the clinical data to determine the ASC values for each visit throughout orthodontic treatment for the given set of patients. The primary outcome measures were (1) the fit between the model response and the measured acceleration signal to

understand the effectiveness of the ASIST for applications to natural teeth and (2) the longitudinal changes in ASC for individual patients to provide some understanding of the changes in the PDL throughout orthodontic treatment.

Since the CT scan data was available for both teeth for all patients, the data was first analyzed using the geometric parameters from the CT scans as described above. The tooth mass, root length, crown length, radius at the crown-root junction, location of center of mass, and mass moment of inertia were input individually into the Mathematica model. The exact striking height during data collection was unknown, so this value was estimated and fixed in the model. It was found that a striking height of  $L_o = 0.006$  m below the tooth tip produced an appropriate model response for this data. The proportionality constant for the damping coefficient was estimated to be  $\gamma = 1000$  and fixed for all analyses.

Appropriate values were chosen as initial guesses for the impact stiffness and the interface stiffness per unit area, and the ASIST optimization procedure was used to determine the final values for these parameters, along with the ASC value, for each set of data.

### **6.5.3. Data Analysis – Optimized CT Geometry**

It was shown above that the mass of the tooth and the location of the center of mass can affect the fit between the model prediction and the measured acceleration (Figure 6.27). Additionally, the values for these parameters calculated from the solid models are simple approximations that may not accurately reflect the physiological values. For these reasons, a second analysis was performed with the clinical data using adjusted mass and center of mass values. For each tooth, the mass was increased by 15%. This value was chosen because it was able to provide some improvement in the fit between the model prediction and the measured data while maintaining a reasonable deviation from the originally calculated mass. Additionally, the location of the center of mass was increased (moved towards the crown tip) by 15% in 10 increments for each tooth. A sample dataset was analyzed with the ASIST procedure at each variation of  $\bar{y}_{CG}$  to determine the ASC value and the fit between the model and the measured acceleration. The value of  $\bar{y}_{CG}$  that produced the best fit as measured by the  $R^2$  value was chosen as the “optimized” center of mass

for each tooth. Across all datasets, it was found that the optimized center of mass was  $9.6 \pm 1.9\%$  higher than the original center of mass (average  $\pm$  SD).

The second analysis with the clinical data used the original length, diameter, and moment of inertia parameters from the CT data along with these adjusted values for the mass and center of mass which were deemed the optimized values. The increase in the center of mass of the teeth altered the mass and stiffness matrices, which in turn altered the damping in the model. In this case the proportionality constant for the damping coefficient was estimated to be  $\gamma = 2000$  and was fixed in the model for all analyses. The results using the optimized CT geometry were compared with the original CT geometry for each patient.

#### **6.5.4. Data Analysis – Approximate Geometry**

In a general application of the ASIST for natural teeth, it is unlikely that CT scans will be available for the tested tooth. In this case, the mass and geometry parameters can be approximated using some parameters that would be readily available in a clinical setting. An approximate geometric model of the tooth was developed with the assumption that the radius of the tooth and one length parameter could be easily approximated. In the ASIST procedure presented here, the user is required to input the total length of the tooth and the radius at the crown-root junction and all other mass and geometry parameters are calculated according to the approximate model (Figure 6.29).

The tooth root shape was approximated as a paraboloid and the crown shape was approximated as a cylinder. The length of the root was assumed to be 57% of the total tooth length while the crown was assumed to be 43% of the total tooth length. These values were determined as the average values from the 24 teeth available from the clinical data. The density of the root was estimated to be  $\rho_r = 1500 \text{ kg/m}^3$  based on the assumption that the root is composed of a combination of pulp and dentin as described for the two density model in Section 6.5.1. The crown was assumed to be composed of both enamel and dentin with the enamel making up the top 30% of the crown and dentin making up the lower 70% as shown in Figure 6.29. This distribution was chosen because it resulted in mass and center of mass values that were relatively close to the optimized values and the resulting model prediction produced a good match with the

measured data. It should be noted that the mass moment of inertia values determined from the approximate geometry model were  $34 \pm 18\%$  higher (average  $\pm$  SD) than those determined from the original CT geometry; however, it was shown previously that the ASC and model fit results are relatively insensitive to variations in  $J_G$ .

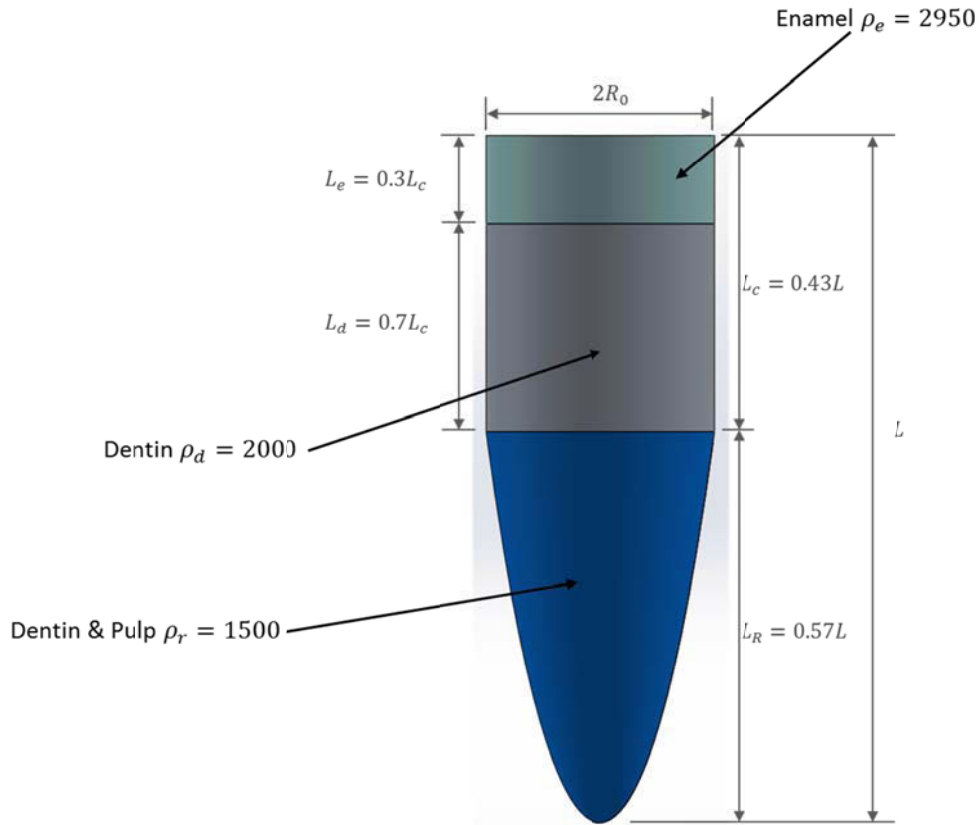


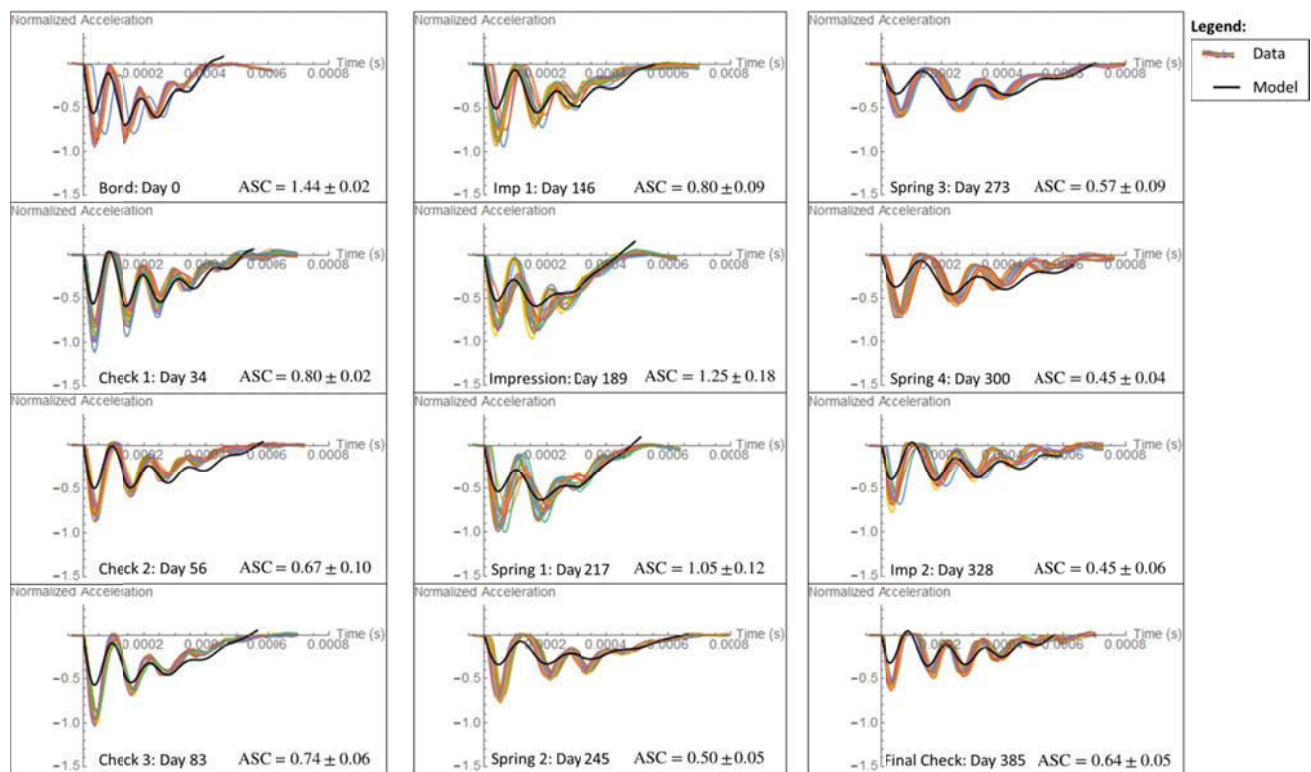
**Figure 6.29: Approximate geometric model for a single-rooted tooth**

The clinical data for all orthodontic patients was analyzed again using this approximate geometry where the tooth length and radius at the crown-root junction are input into the model. The subsequent ASIST procedure is the same as described previously. The striking height was fixed at  $L_o = 0.006$  m and the ASIST optimization procedure was used to determine the impact stiffness and interface stiffness per unit area along with the corresponding ASC for each set of data. The results using the approximate geometry were compared to those using the optimized CT geometry for each patient.

## 6.6. Results

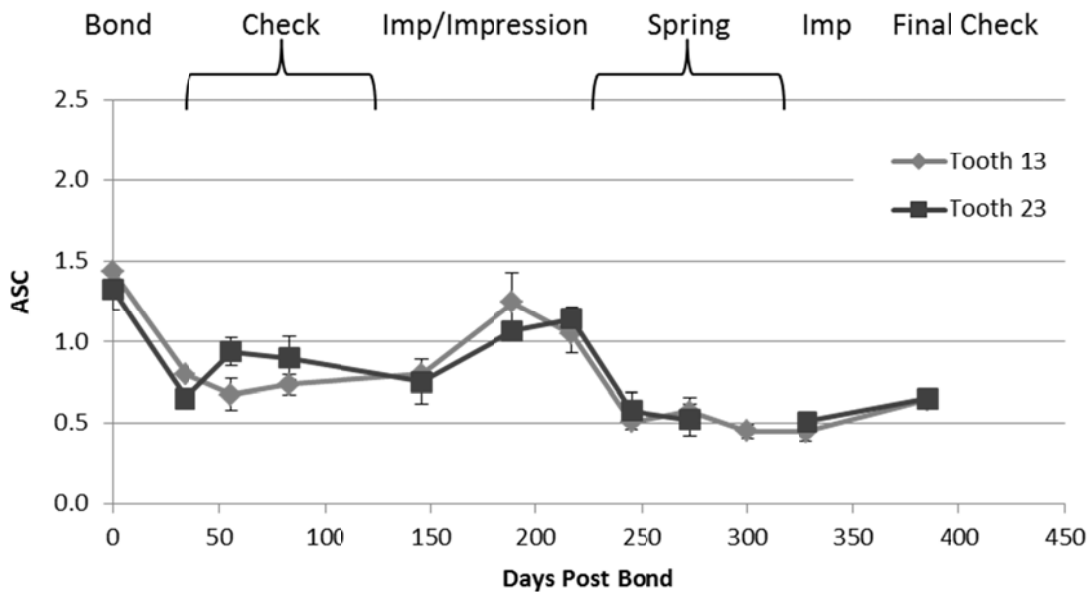
### 6.6.1. CT Geometry

Figure 6.30 shows the measured accelerometer data and resulting model prediction for each visit for one example patient (Patient 1; tooth ID 13). The model prediction is obtained using the full CT geometry and it can be seen from the figure that there is a relatively good fit between the model and the measured data for each case. The figures show one example from each visit (visit day is reported on the figure). The ASC values are also shown on the figures and are reported as the average  $\pm$  SD for repeated measures at each visit. It can be noted that the ASC values for the tooth application were found to be approximately two orders of magnitude lower than those reported for the BAHA implant systems.



**Figure 6.30: Measured accelerometer data (colored lines) and model predicted response (black line) for Patient 1 (AS) tooth ID 13 using CT geometry. Each plot shows an example of the data and model fit for each clinic visit (visit day indicated on each figure). The ASC values are average  $\pm$  SD for repeated measures on each day.**

Figure 6.31 shows an exemplary plot of the longitudinal changes in ASC throughout the course of orthodontic treatment (Patient 1). The reported values are the average of repeated measures at each visit and the error bars show one standard deviation. The results are reported for both maxillary cuspid teeth. It can be seen from the figure that both teeth show a similar pattern of longitudinal changes in ASC for this patient. It can also be seen from the figure that there is an initial decrease in ASC following the initial (Bond) visit with a subsequent increase at the implant visit. There is a substantial decrease during the retraction phase (spring visits) which can also be identified by examining the accelerometer signals shown in Figure 6.30 where clear differences in the signals are observed compared to the initial visits. Finally, there is a slight increase in ASC at the final check-up appointment. It can be noted that there is a gap in the data for the left cuspid (ID 23) for this patient at the third to last visit. This is due to an error in the collected accelerometer data as described in Section 6.5.1.



**Figure 6.31: Example plot of longitudinal ASC measurements (Patient 1) for tooth ID 13 and 23 using the CT geometry. Reported values are the average of repeated measurements and error bars show one standard deviation.**

Figure 6.32 through Figure 6.42 show the longitudinal changes in ASC value for the remaining patients. The values were determined using the CT geometry.

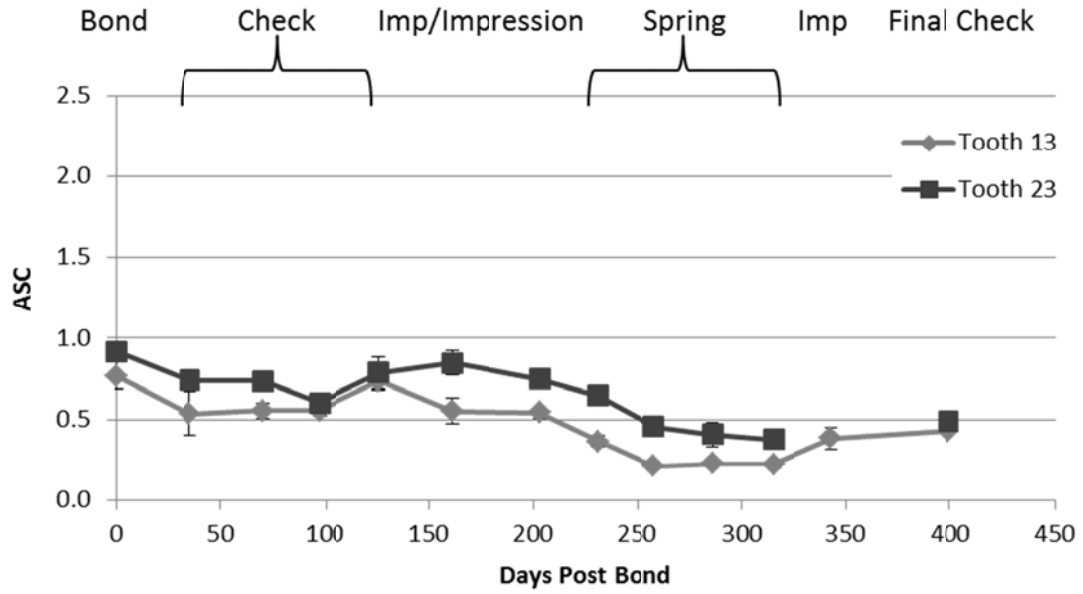


Figure 6.32: Longitudinal ASC measurements for Patient 2

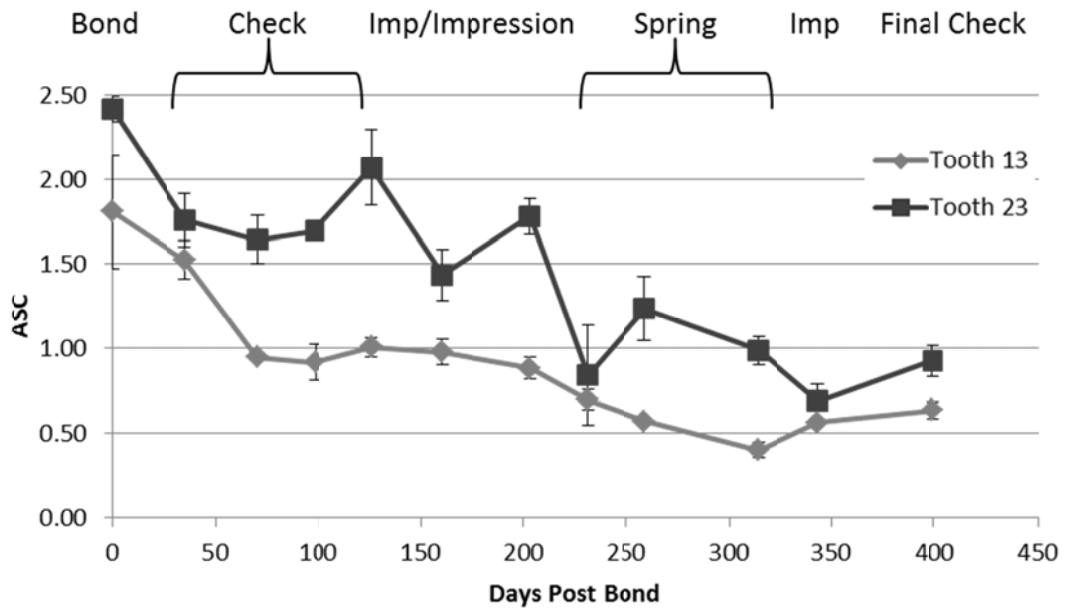


Figure 6.33: Longitudinal ASC measurements for Patient 3

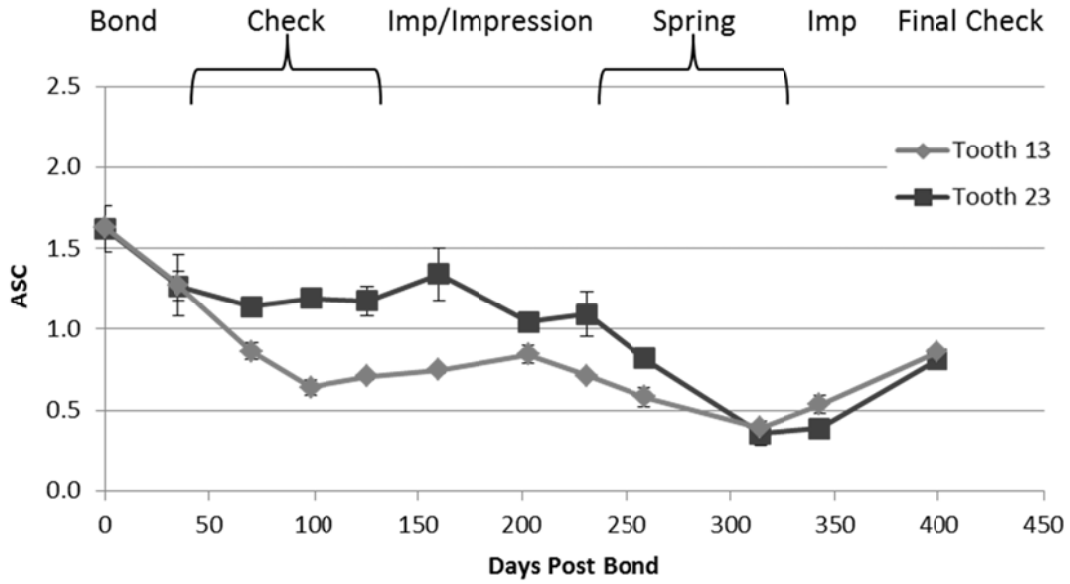


Figure 6.34: Longitudinal ASC measurements for Patient 4

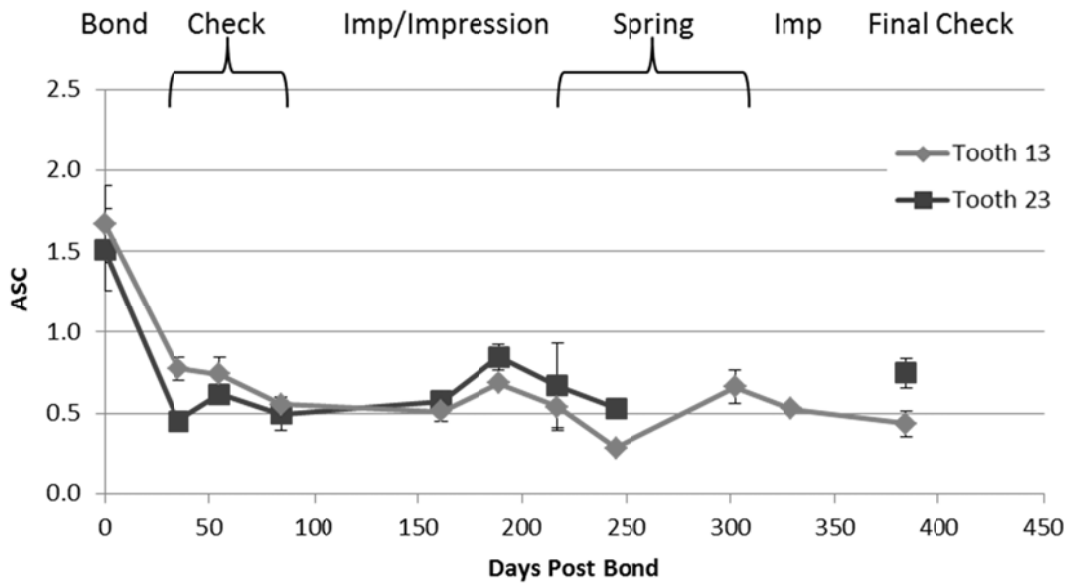


Figure 6.35: Longitudinal ASC measurements for Patient 5

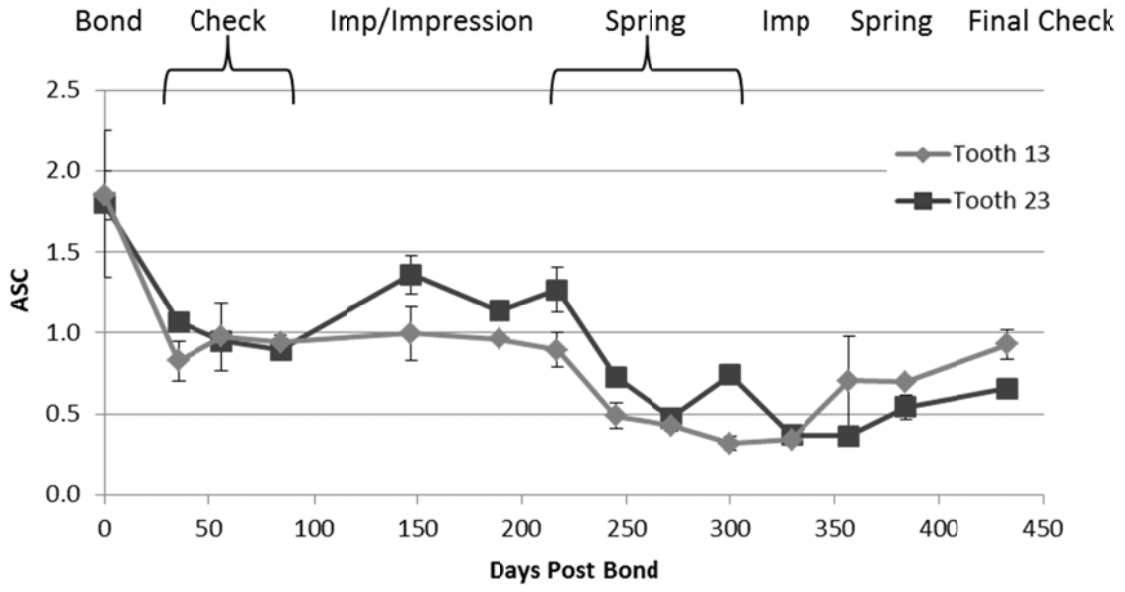


Figure 6.36: Longitudinal ASC measurements for Patient 6

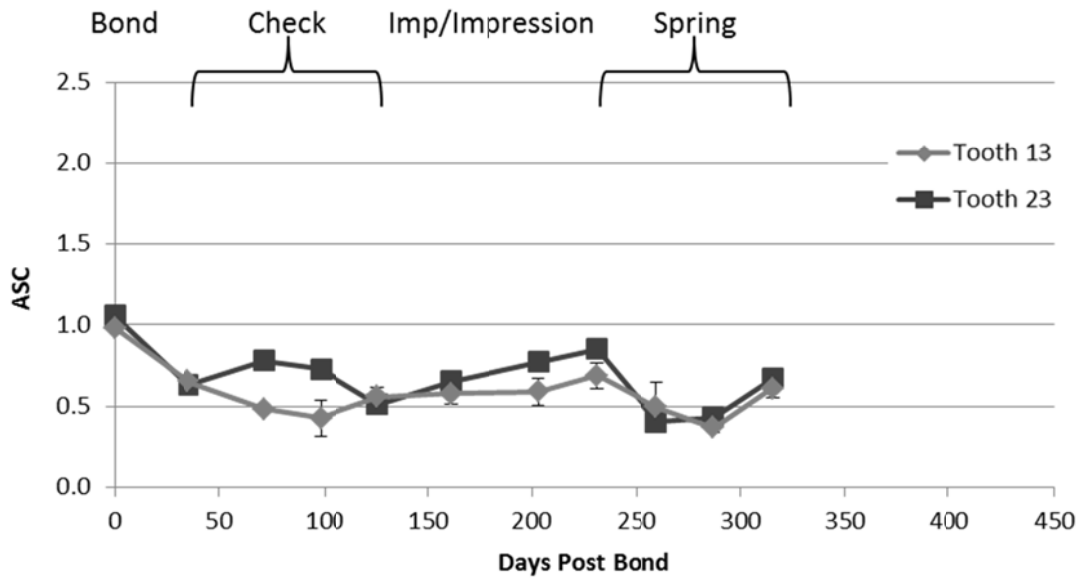


Figure 6.37: Longitudinal ASC measurements for Patient 7

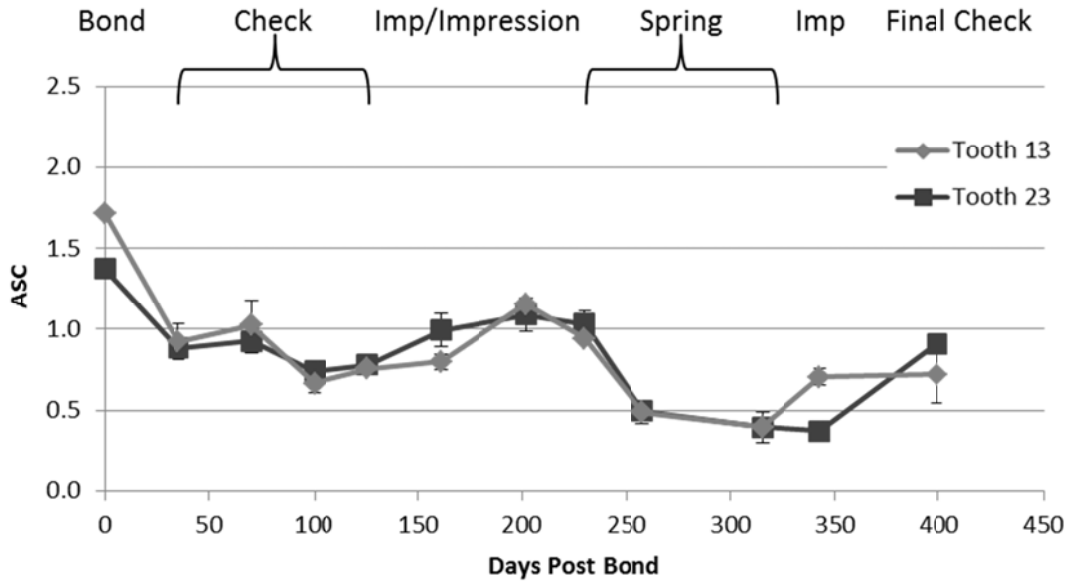


Figure 6.38: Longitudinal ASC measurements for Patient 8

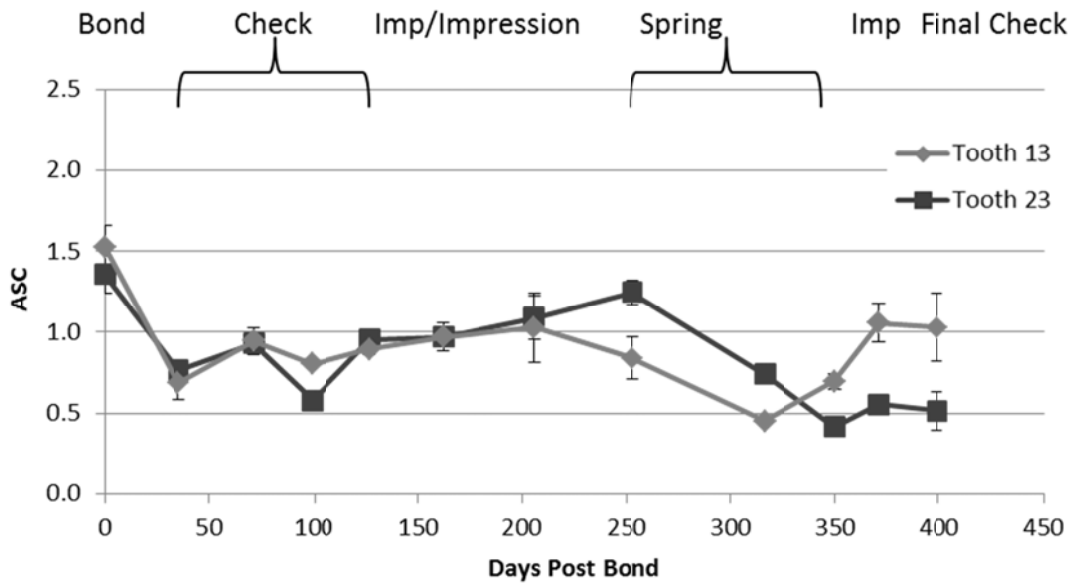


Figure 6.39: Longitudinal ASC measurements for Patient 9

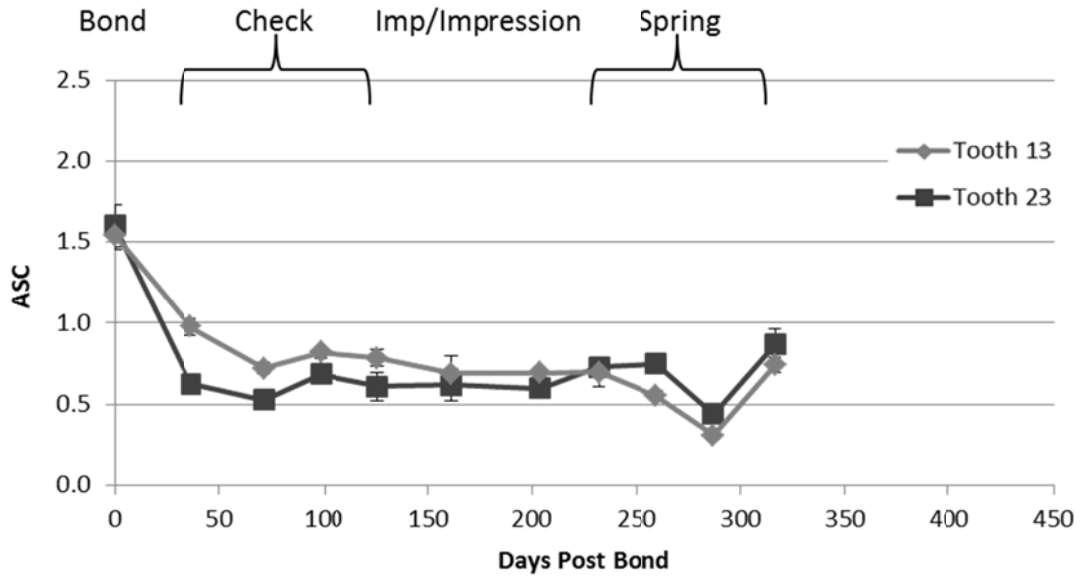


Figure 6.40: Longitudinal ASC measurements for Patient 10

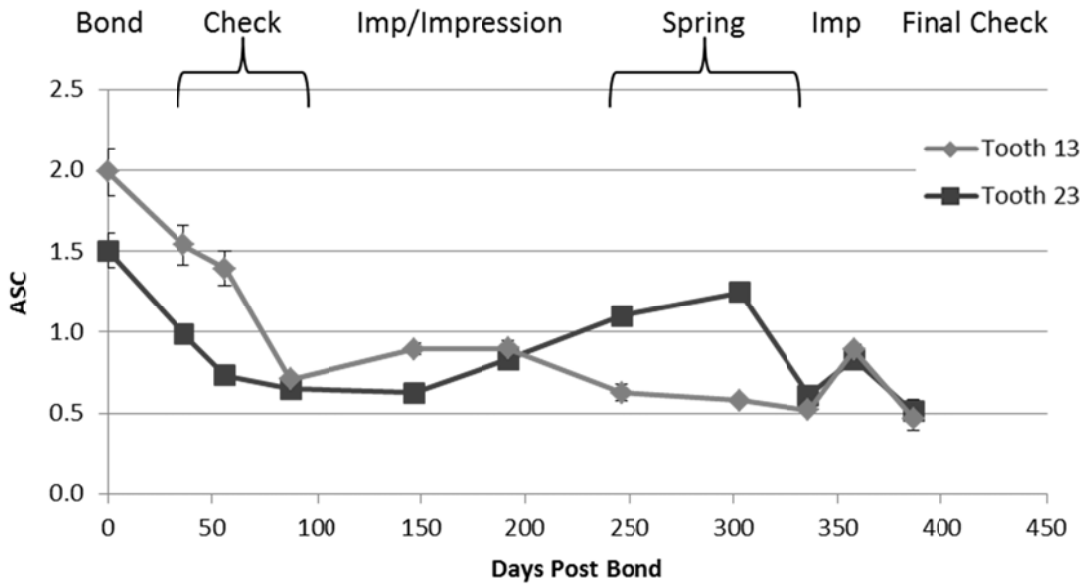


Figure 6.41: Longitudinal ASC measurements for Patient 11

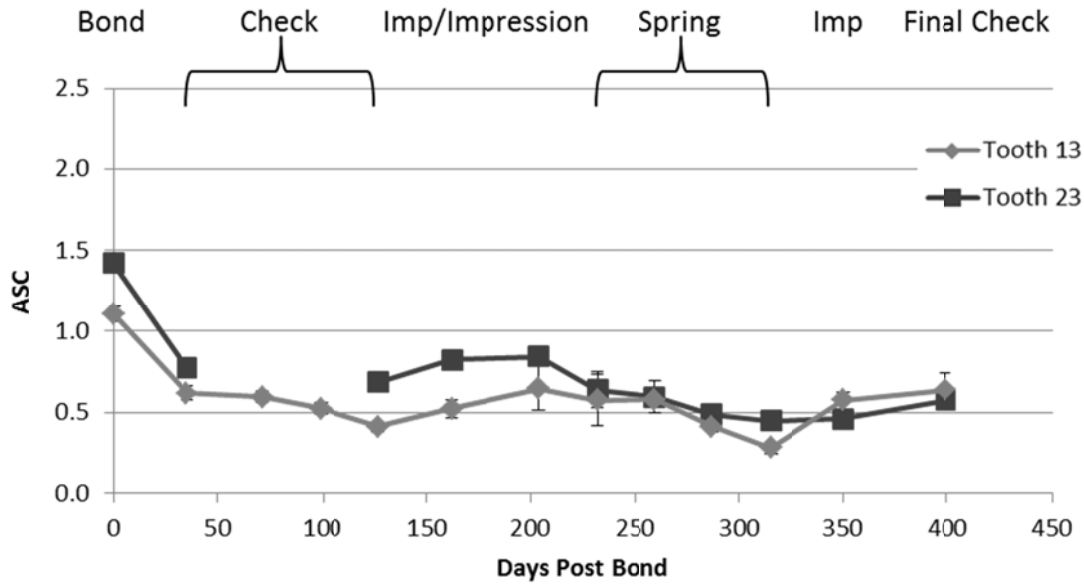
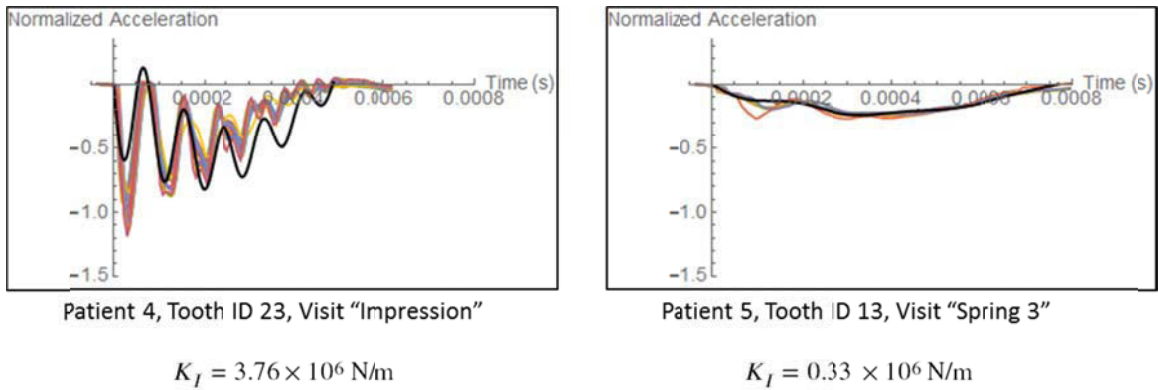


Figure 6.42: Longitudinal ASC measurements for Patient 12

All patients showed some decrease in the PDL stiffness (as measured by the ASC value) during the course of orthodontic treatment. The reduction in stiffness was  $72.2 \pm 6.7\%$  (average  $\pm$  SD) over all the teeth examined. All patients showed a substantial reduction in stiffness following the initial visit (during the alignment and leveling phase). Many patients showed a slight recovery in PDL stiffness following the alignment and leveling phase which was then followed by a second decrease in stiffness during the retraction phase. Some recovery was again observed for most patients at the final check-up; however, none of the patients had the PDL stiffness return to the pre-treatment value by the end of the study period. On average, the ASC value at the final visit was  $47.2 \pm 12.1\%$  of the value at the initial visit.

The impact stiffness was found to vary by approximately one order of magnitude over all measurements with all patients. The average impact stiffness was  $K_I = 1.87 \times 10^6 \pm 0.70 \times 10^6$  N/m (average  $\pm$  SD) with a range of  $0.33 \times 10^6 - 3.76 \times 10^6$  N/m. Figure 6.43 shows the datasets with the highest and lowest predicted impact stiffness values, which demonstrates the range of acceleration response shapes that was seen across the clinical data.



**Figure 6.43: Examples of patient measurements with the highest predicted impact stiffness (left) and the lowest predicted impact stiffness (right)**

The damping ratio of the higher frequency component was estimated from the curve fit approximation of the measured acceleration for all patient data. The damping ratio was found to be  $0.118 \pm 0.067$  with a range of  $0.040 - 0.917$ . There was one dataset that had an unusually high damping ratio (0.917) which is shown in Figure 6.44. Removing this outlier from the clinical dataset results in an average damping ratio of  $0.115 \pm 0.048$  and a range of  $0.040 - 0.422$ . It was found that the teeth had a significantly higher damping ratio than the BAHA clinical data (which was  $0.039 \pm 0.017$ ) based on a *t*-test with  $p = 1.4 \times 10^{-20}$ .

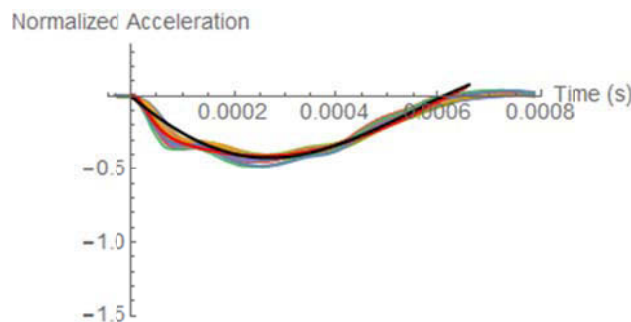
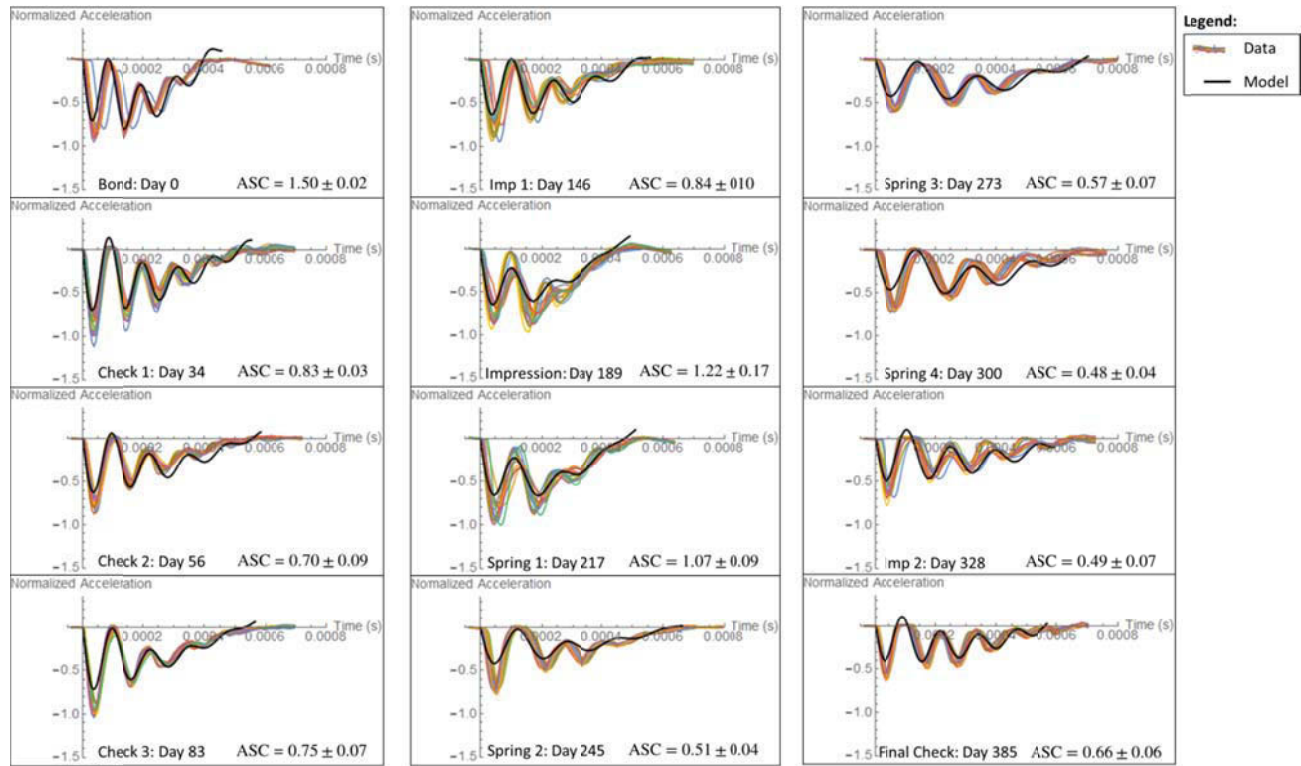


**Figure 6.44: Example of patient data with unusually high damping ratio (0.917). Colored lines are the measured acceleration, red line is the curve fit approximation of the data, and black line is the model prediction.**

### 6.6.2. Optimized CT Geometry

Figure 6.45 shows the measured accelerometer data and resulting model prediction for each visit for one example patient (Patient 1; tooth ID 13). The model prediction is obtained using the

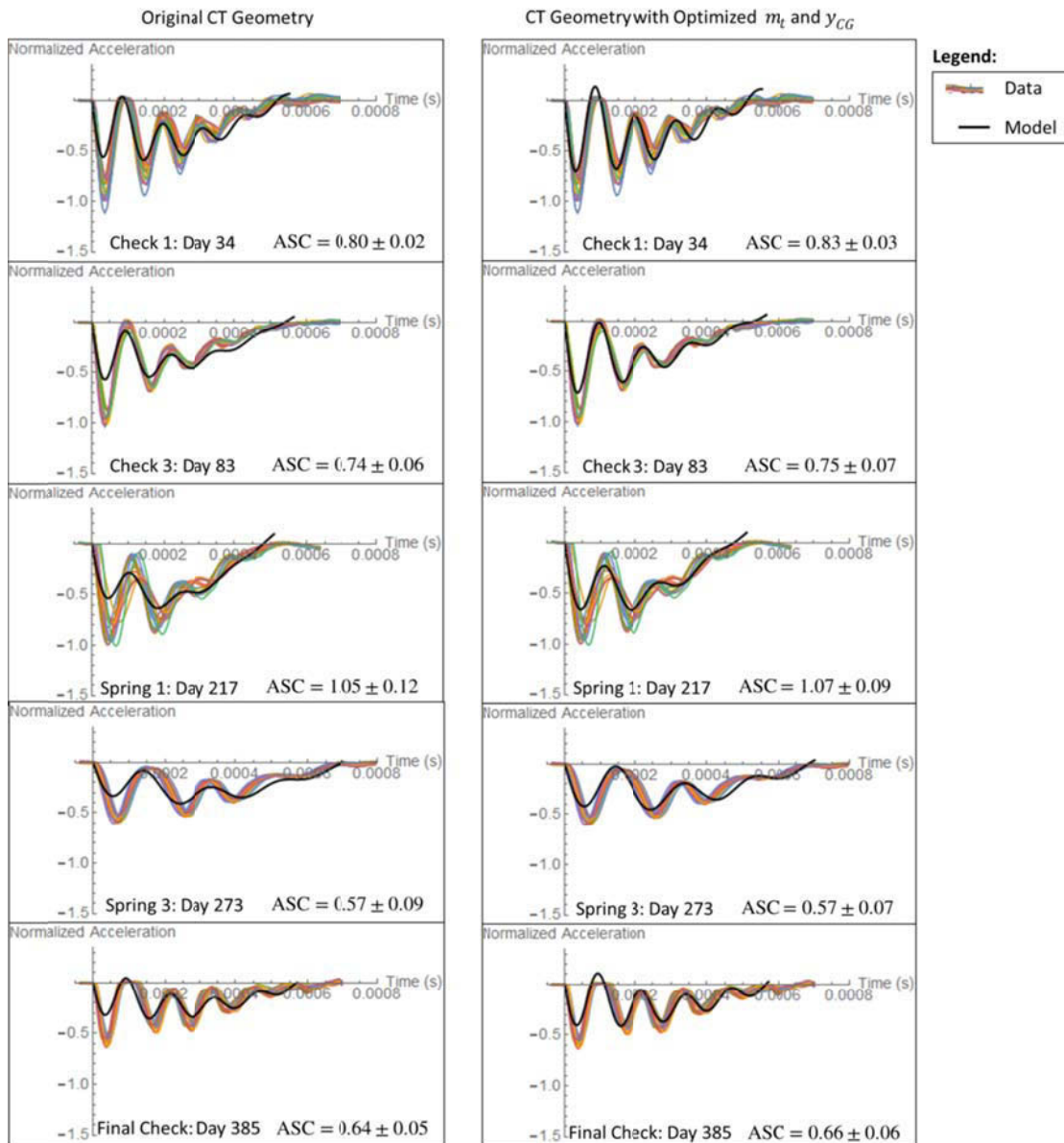
optimized CT geometry and it can be seen from the figure that there is a good fit between the model and the measured data for each case. The figures show one example from each visit (visit day is reported on the figure). The example datasets are the same as those shown in Figure 6.30, with the difference here being the model prediction. The ASC values are also shown on the figures and are reported as the average  $\pm$  SD for repeated measures at each visit.



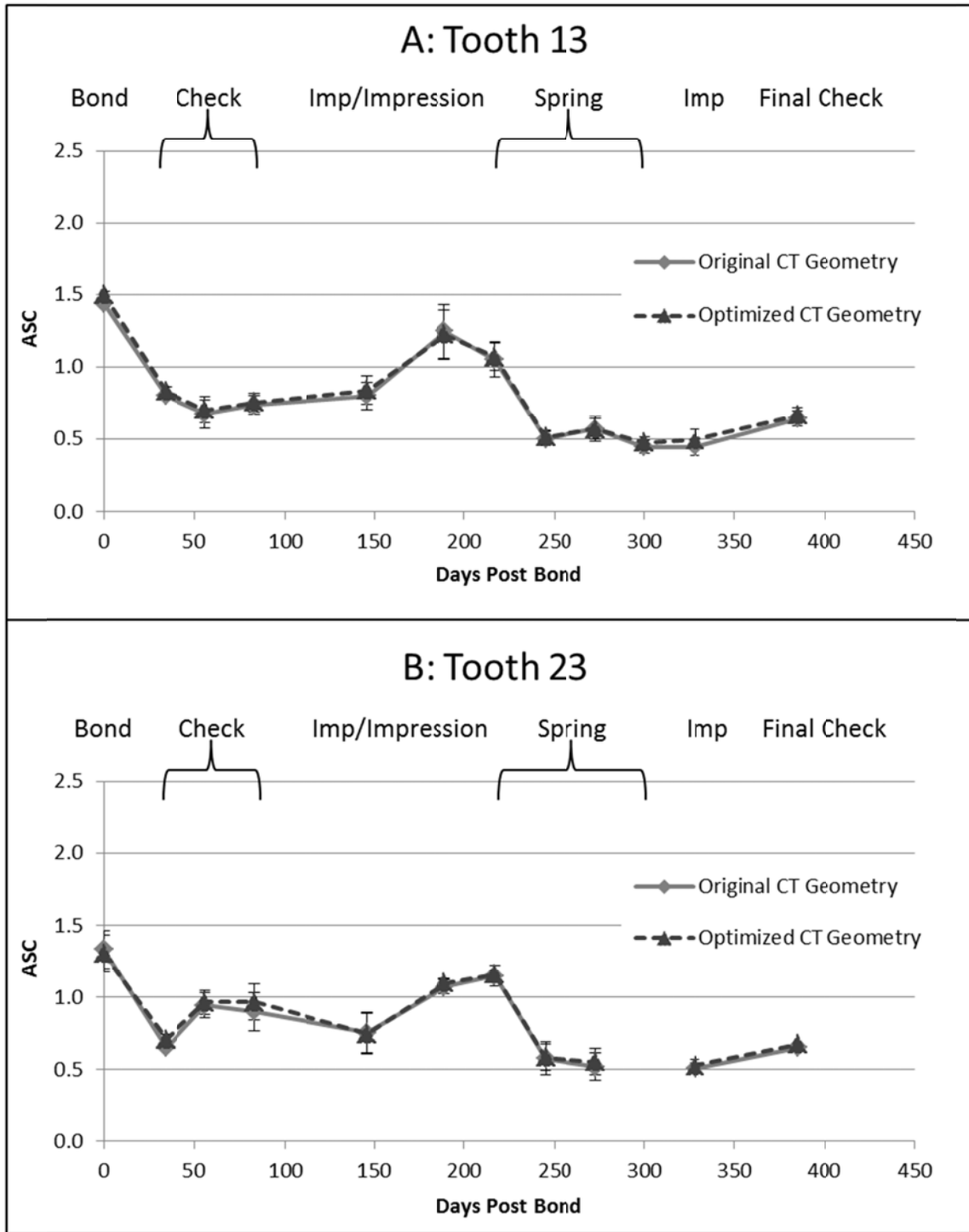
**Figure 6.45: Measured accelerometer data (colored lines) and model predicted response (black line) for Patient 1 (AS) tooth ID 13 using CT geometry with optimized mass and center of mass. Each plot shows an example of the data and model fit for each clinic visit (visit day indicated on each figure). The ASC values are average  $\pm$  SD for repeated measures on each day.**

Figure 6.46 shows a direct comparison between the model prediction with the original CT geometry (left column) and the CT geometry with optimized mass and center of mass values (right column) for several example datasets for Patient 1 (Tooth ID 13) over the course of treatment. It can be seen from the figure that the optimized CT geometry tends to show a better fit between the model prediction and the measured acceleration, particularly in matching the first cycle of the second mode frequency. It can also be seen from the figure that the adjusted geometry parameters result in only minor differences in the resulting ASC values. Figure 6.47

shows a direct comparison of the longitudinal changes in ASC value for an example patient (Patient 1) for both maxillary cuspid teeth again showing that there are only minor differences between the two methods. Over all visits with all patients, the difference in ASC between the original CT geometry model and the optimized geometry CT model was  $0.04 \pm 0.04$  (average  $\pm$  SD) or  $5.8 \pm 5.3\%$ .



**Figure 6.46:** Measured accelerometer data (colored lines) and model predicted response (black line) for sample data at several visits for Patient 1 (AS) tooth ID 13 comparing the model predicted acceleration response using the original CT geometry (left) and the CT geometry with optimized mass and center of mass (right). For each day (visit day indicated on the figure) the same dataset is shown with the two different model predictions. The ASC values are average  $\pm$  SD for repeated measures on each day.



**Figure 6.47: Comparison of longitudinal ASC measurements using the original CT geometry and the optimized CT geometry for Patient 1. A: Right maxillary cuspid (Tooth ID 13). B: Left maxillary cuspid (Tooth ID 23). Reported values are the average of repeated measurements and error bars show one standard deviation.**

### 6.6.3. Approximate Geometry

Figure 6.48 shows the measured accelerometer data and resulting model prediction for each visit for one example patient (Patient 1; tooth ID 13). The model prediction is obtained using the approximate geometry and it can be seen from the figure that there is a good fit between the model and the measured data for each case. The figures show one example from each visit (visit day is reported on the figure). The example datasets are the same as those shown in Figure 6.30 and Figure 6.45 above, with the difference here being the model prediction. The ASC values are also shown on the figures and are reported as the average  $\pm$  SD for repeated measures at each visit.

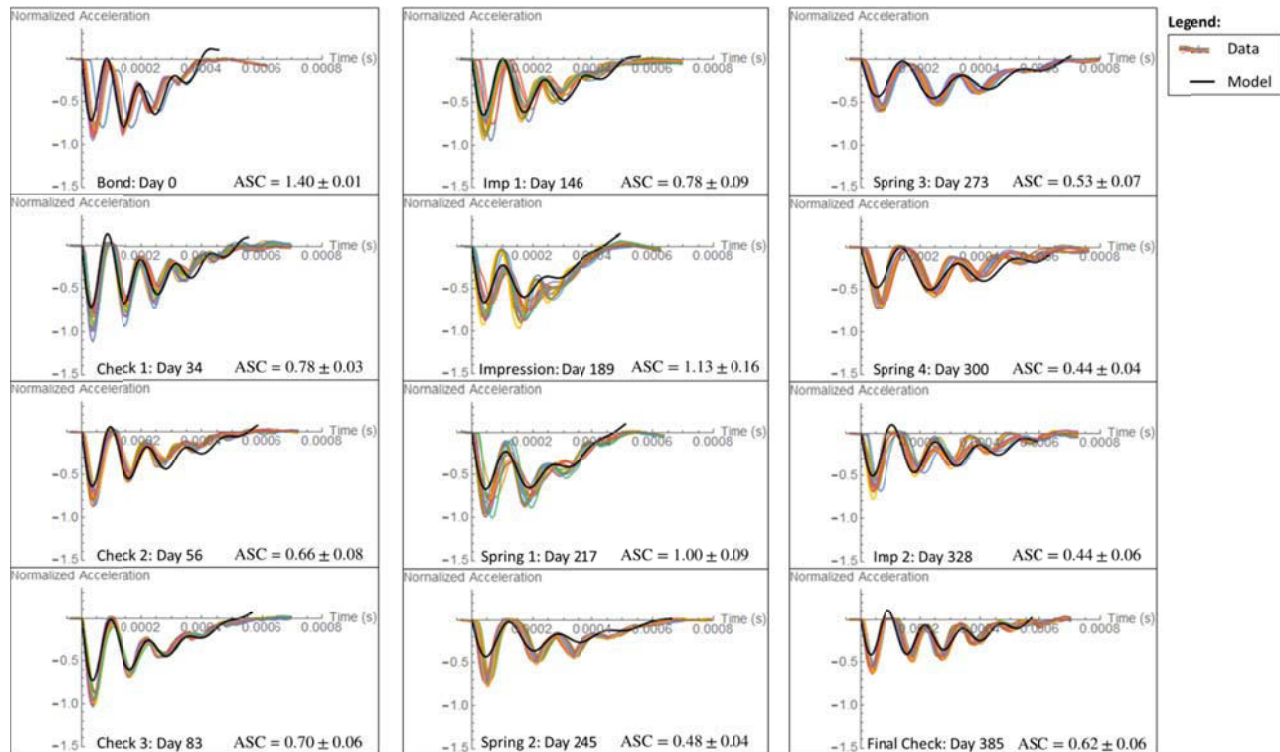


**Figure 6.48: Measured accelerometer data (colored lines) and model predicted response (black line) for Patient 1 tooth ID 13 using approximate geometry. Each plot shows an example of the data and model fit for each clinic visit (visit day indicated on each figure). The ASC values are average  $\pm$  SD for repeated measures on each day.**

The pattern of longitudinal changes during the course of treatment for individual patients using the approximate geometry model was found to be generally the same as both the original CT and optimized CT geometry models. However, there were some differences noted in the absolute

ASC values with the approximate geometry model compared to the CT geometry. An example of a direct comparison between the longitudinal ASC values for one patient (Patient 1) is shown in Figure 6.49. From the figure, it can be seen that there is a slight offset in the ASC values between the two models.

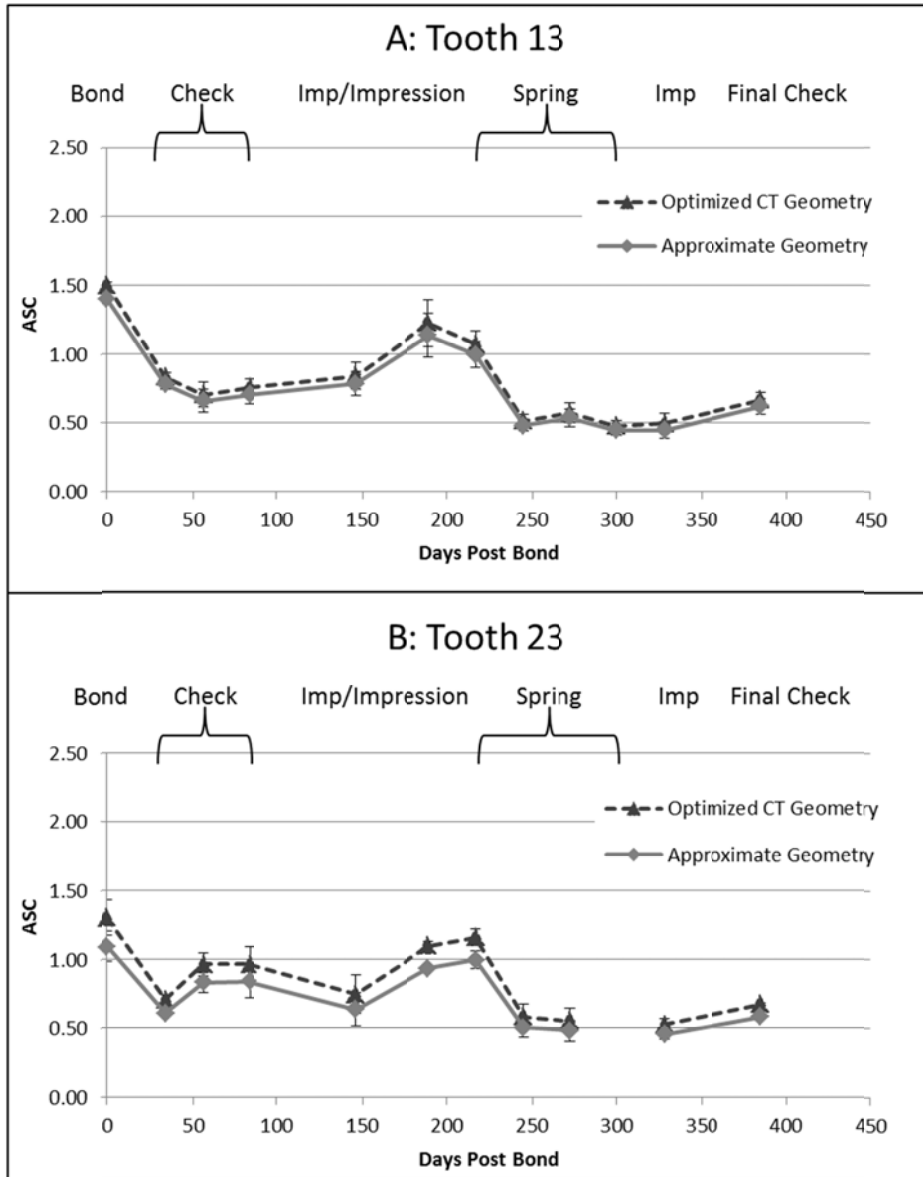
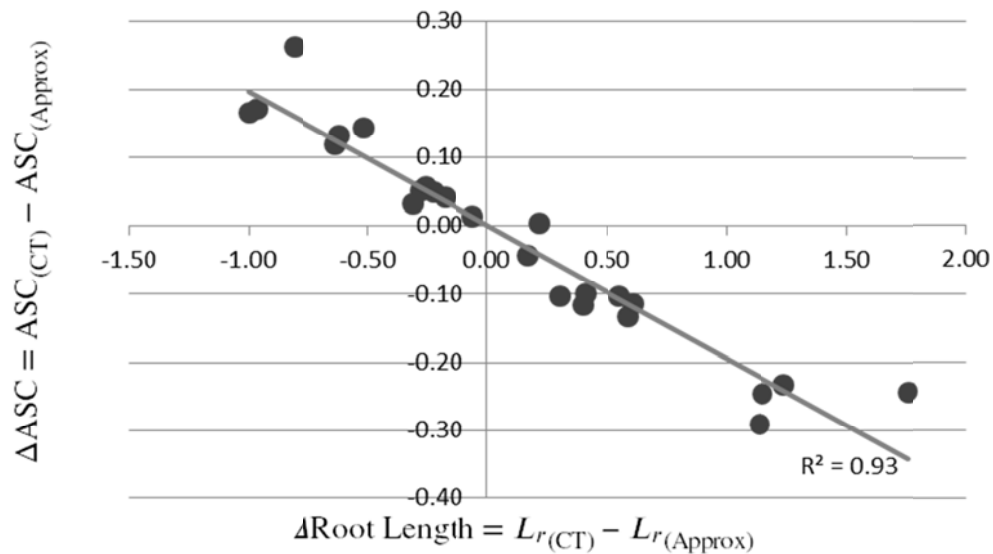


Figure 6.49: Comparison of longitudinal ASC measurements using the optimized CT geometry and the approximate geometry for Patient 1. A: Right maxillary cuspid (Tooth ID 13). B: Left maxillary cuspid (Tooth ID 23). Reported values are the average of repeated measurements and error bars show one standard deviation.

The offset in the absolute ASC values can be attributed to a difference in the root area. The root length was a parameter that was calculated based on the approximate geometry model and the area of the root contributes to the effective interface stiffness and in turn contributes to the ASC value. Figure 6.50 shows a plot of the difference in ASC value between the optimized CT geometry and the approximate geometry ( $ASC_{(CT)} - ASC_{(Approx)}$ ) as a function of the difference in root length ( $L_{r(CT)} - L_{r(Approx)}$ ). The reported values are the average difference over the course of treatment for each tooth. From the figure it is clear that there is a linear relationship between these parameters ( $R^2 = 0.93$ ) with an increase in root length resulting in a decrease in ASC value.



**Figure 6.50: Change in ASC value between the optimized CT geometry and the approximate geometry ( $ASC_{(CT)} - ASC_{(Approx)}$ ) as a function of the change in root length ( $L_{r(CT)} - L_{r(Approx)}$ ). Reported data is the average change for a particular tooth.**

#### 6.6.4. Comparison with Literature

Estimates of tooth stiffness (or mobility) have been reported in the literature. For example, Mühlemann (1954) and Laster et al. (1975) measured tooth displacement under an applied static load. Assuming a linear force-displacement curve (supported by the initial tooth mobility curve reported by Mühlemann, 1954), the effective tooth stiffness can be calculated as  $k = F/d$ . Using the force and displacement values reported in these papers, the effective tooth stiffness can be

estimated between  $6.54 \times 10^3 - 6.40 \times 10^4$  N/m. In another study, Nakago et al. (1994) evaluated the effective tooth stiffness using a mechanical impedance measuring device (MIMD) for the periodontal tissue. This device provides a dynamic test to estimate the periodontal tissue stiffness. Over the course of four weeks of orthodontic treatment, the stiffness of four maxillary canine teeth from two patients were reported between  $1.2 \times 10^5 - 4.1 \times 10^5$  N/m. The stiffness using the dynamic testing methods is approximately one order of magnitude higher than that using the static testing methods. This can be attributed to the viscoelastic behaviour of the PDL. Under rapid (dynamic) loading the fluid in the tissue does not have time to escape and the viscoelastic effects are not observed, thus the stiffness of the tissue appears to be higher compared to the static loading case.

In the present study, the effective stiffness at the interface using the two density CT model (averaged over all measurements with all patients) is  $3.25 \times 10^6 \pm 1.49 \times 10^6$  N/m. The use of the analytical model allows us to isolate the interface properties, thus this value represents the effective stiffness of the tooth if a load was applied through the center of resistance. Conversely, the experimental procedure reported in the literature represents the effective stiffness of the tooth with a force applied near the top of the tooth and the deflection measured at the same location. The difference between these two scenarios is shown in Figure 6.51.

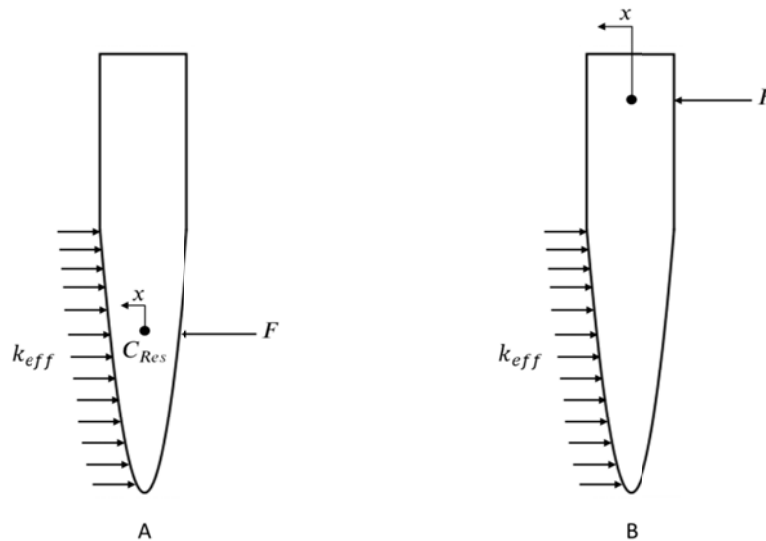


**Figure 6.51: Illustration of the difference between the effective stiffness at the tooth interface (A) and the effective stiffness of the entire tooth system with a force applied near the top of the crown (B)**

To compare the stiffness values determined in the present study with those reported in the literature, we can use our analytical model to determine the effective tooth stiffness with a load applied near the top of the tooth. Consider a horizontal force applied on the tooth with the force and displacement defined by the following:

$$[K] \begin{Bmatrix} x \\ x \\ \theta \end{Bmatrix} = \begin{Bmatrix} 0 \\ F \\ 0 \end{Bmatrix}$$

The effective stiffness of the system is defined as the force  $F$  resulting from a unit displacement  $x$ . The stiffness matrix can be developed for example for a tooth with  $L_r = 13.03$  mm,  $L_c = 10.28$  mm, and  $R_0 = 3.84$  mm. We can assume a striking height of  $L_o = 6$  mm. Additionally, we can assume an interface stiffness per unit area  $k = 2.91 \times 10^{10}$  N/m<sup>3</sup> corresponding to an effective stiffness at the interface equal to the average value over all the patient data ( $3.25 \times 10^6$  N/m). Solving the above equation with these parameters, we find that the effective tooth stiffness is  $3.61 \times 10^5$  N/m which is within the range of values reported by Nakago et al. (1994).

## 6.7. Summary

This chapter presented the ASIST application for natural teeth. This is the first application of the combined experimental technique and analytical model used to estimate the PDL characteristics. An analytical model for a single-rooted tooth system was developed and evaluated using clinical data from 24 maxillary cuspid teeth from 12 orthodontic patients. A parametric sensitivity analysis was presented, evaluating the effect of internal stiffness and geometric parameters on the analytical model response.

The analysis of the clinical data allowed comparisons of several methods for estimating the mass and geometry parameters of individual teeth including measurements from CT scans and a simplified approximate geometry model. Both methods were able to provide a good match between the model predicted response and the measured acceleration. Additionally, the clinical study presented here provided some insight into the changes in PDL stiffness during orthodontic alignment and cuspid retraction. Using the ASC value as the outcome measure, all patients

showed a substantial decrease in PDL stiffness during treatment. The PDL showed some recovery in stiffness at the end of the study (approximately 1 year); however, it did not reach its pre-treatment stiffness value in any of the cases. Orthodontic tooth movement is associated with remodeling in the dental and periodontal tissues including changes at the cellular, molecular, and tissue levels (Dolce et al., 2002; Krishnan and Davidovitch, 2006; Zainal Ariffin et al., 2011). Although it was difficult to find reports of longitudinal changes in the mechanical properties of the PDL within the literature, the biological changes reported during orthodontic tooth movement seem to support the reduction in PDL stiffness and ASC value that was observed in this study. Additionally, tooth mobility has been shown to increase during orthodontic treatment (mean treatment duration of 21.5 months) and decrease following a retention phase (mean duration of 27.9 months) as measured by the Periotest® (Tanaka et al., 2005). The reduction in PDL stiffness and ASC during treatment in this study is consistent with the increase in tooth mobility reported in the literature. The ASIST technique for natural teeth has the potential to provide valuable insight into the behavior of the PDL and tooth root interface as well as tooth stability across a range of clinical situations.

# Chapter 7: Summary and Conclusions

## 7.1. Summary

This research presents the development of a noninvasive system for evaluation of the interface integrity for both percutaneous implants and natural teeth. The developed system is termed the Advanced System for Implant Stability Testing (ASIST). The ASIST combines experimental acceleration measurements from an impact with the system of interest with an analytical model of the system to estimate the stiffness characteristics at the interface. The inclusion of the analytical model aids in the interpretation of the acceleration measurement and provides an improved understanding of the physical system.

This research builds upon previous work for percutaneous implants combining the experimental acceleration measurement with an analytical model of the system. This work presents several significant improvements over previous approaches. First was the development of a new electronic system for acceleration measurement which provides a cleaner acceleration signal that more accurately reflects the system response. To apply the ASIST technique in a clinical setting, appropriate analytical models were developed to include the two commercial BAHA systems that are commonly used across the bone anchored hearing community. A numerical analysis was presented to provide a robust method for estimating interface properties by matching the acceleration response from the analytical model with the measured acceleration through an optimization procedure. An alternative damping model using viscous damping was implemented to better reflect the physiological conditions, which may be particularly important for failing implants.

The ASIST was developed for the Oticon Medical Ponto and the Cochlear Baha® Connect implant-abutment systems and evaluated through *in vitro* laboratory testing with a variety of implant and abutment sizes. The ASIST is able to isolate the interface properties and provide a stability measure that is essentially independent of the attached components. In addition, it was shown that the system is able to detect differences in interface properties by evaluating a range of installations with the same type of implants.

The ASIST acceleration measurement is carried out with a handpiece which makes it a versatile tool for clinical use; however, it was important to understand how variations in handpiece position can influence the resulting ASC measure. This was evaluated through *in vitro* laboratory testing with controlled variations in handpiece position and through an intra-tester and inter-tester reliability analysis. It was shown that both intra-tester and inter-tester variations were low with an ICC of 0.941 and SEM of 1.52 ASC (6.5% of the average) for intra-tester reliability and an ICC of 0.964 and SEM of 2.90 ASC (12% of the average) for inter-tester reliability. The ICC values indicate excellent reliability for both intra- and inter-tester reliability (Hallgren, 2012).

There are currently available commercial devices that have been used for interface stability measurement for many years. For example, the Osstell™ system is widely used for BAHA implants; however it is known to suffer from several limitations. We presented a comparison of the ASIST and the Osstell™ ISQ system through an *in vitro* laboratory evaluation with BAHA implants. The ASIST was found to provide significant advantages over the Osstell™ in terms of the ability to isolate interface properties independent of attached components as well as sensitivity to changes in interface stiffness properties. The Osstell™ ISQ was shown to be more sensitive to changes in system components such as variations in abutment length than actual changes in interface properties, while the ASIST was found to be more sensitive to interface changes and essentially independent of the system components.

This research also presented a clinical evaluation of the ASIST for BAHA patients through a collaboration with iRSM. It was found that the ASIST shows potential to detect differences in interface stability between surgeons or surgical techniques and between various implant designs; however, additional larger studies are required to confirm these findings. Longitudinal changes in implant stability were evaluated for BAHA patients within the first year following surgery. The ease of use and ability to isolate the properties of the bone-implant interface will allow the ASIST to be a valuable clinical tool, enabling clinicians to quickly and noninvasively evaluate the status of bone anchored implants throughout their entire life.

Finally, this research presented the development of the ASIST technique for natural teeth. The development and evaluation was presented using longitudinal clinical data from maxillary cuspid retraction for adolescents during orthodontic treatment. A three degree of freedom analytical

model was presented for a single-rooted tooth system. Several geometric approximations were presented and compared. The first was based on mass and geometry parameters estimated from CT scans of individual teeth while the second was a completely approximated model based solely on the length and radius of the tooth. The model prediction of the acceleration was found to provide a good match with the measured acceleration suggesting that the ASIST technique can be applicable to natural teeth. A longitudinal evaluation was presented showing changes in PDL stiffness properties throughout orthodontic alignment and cuspid retraction. Similar patterns of longitudinal changes were observed across patients with all patients showing reductions in PDL stiffness during treatment and many patients showing some degree of recovery near the end of treatment (approximately 1 year). The PDL stiffness parameters at the end of treatment did not return to pre-treatment levels for any of the patients during the time of the study. This work presented a significant contribution to the experimental-analytical modeling approach for natural teeth and shows promise for future research in this area. The ASIST for natural teeth can provide a valuable clinical tool for assessment of tooth stability properties and PDL stiffness in a variety of clinical situations such as dental trauma, orthodontics, and periodontology.

## 7.2. Conclusions

- The ASIST technique was developed for commercial bone anchored hearing aid systems including the Oticon Medical Ponto and the Cochlear Baha® Connect systems.
- The ASIST was shown to have significant advantages over commercially available systems such as the Osstell™ ISQ for evaluation of BAHA implant stability.
- The inclusion of the analytical model in the interpretation allows the ASIST Stability Coefficient (ASC value) to be essentially independent of attached components such as abutment length. The ASIST was found to be sensitive to changes in interface properties.
- The ASIST has shown promising results with an *in vivo* longitudinal clinical evaluation with BAHA patients. Differences in initial stability values were identified between surgeons and between implant types.
- Implant stability measurements were found to vary substantially across patients.
- Patients with relatively low initial stability were found to have a similar trend of longitudinal changes with minimal variations or gradual increases in ASC over time. The

remaining patients were found to have varied patterns of longitudinal changes with increases and decreases over time.

- The ASIST procedure was developed for natural teeth and was found to show promise for future work with this application.
- The stiffness of the PDL was found to be approximately two orders of magnitude less than the bone-implant interface of BAHA systems.
- Longitudinal changes in PDL stiffness were evaluated with clinical data for patients undergoing orthodontic alignment and cuspid retraction. The ASIST was able to detect substantial changes in PDL stiffness over time. Longitudinal changes were similar between two maxillary cuspid teeth within individual patients as well as between patients.

### **7.3. Limitations**

The work presented has several limitations that could be addressed in future applications of the ASIST method. The analytical model assumes that the interface is both uniform over the area and represented by a linear force-displacement relationship. Physiologically, the interface may vary along the length or over the interface area for a variety of reasons. A non-uniform interface model was investigated in this work for BAHA implant systems showing minimal effects on the system response; however, these effects may be more important for different implant systems or for both implants and natural tooth systems with compromised or variable interface integrity. Additionally, the interface relationship of both bone anchored implant systems and natural teeth may not be linear (i.e. constant  $k$ ). In this work, we found a good match between the measured acceleration and the analytical model for both BAHA systems and teeth suggesting that the analytical model is a good approximation of the physiological situation; however, situations with compromised interface integrity were not investigated. For implants with poor osseointegration or a fibrous tissue interface or for teeth with very low stability, a non-linear interface may more accurately reflect the physiology. These assumptions should be investigated for varying levels of interface integrity.

In the experimental work for BAHA systems, the preparation of the interface was not strictly controlled resulting in varying interfaces for similar installations and we do not have an

alternative measure of the actual interface properties with which to compare the ASIST (or Osstell™) measure. Additionally, a clamp was used to fix the implant installation to the platform, which may not provide a consistent and rigid connection.

The BAHA clinical study had several limitations including missing data due to a poor RF connection between the ASIST unit and the computer with an early version of the ASIST and differences in the data collection position between the surgical and post-operative measurements, which may have resulted in additional variability in the measure. Additionally, the sample size was limited in terms of the ability to account for multiple confounding variables through multiple regression analysis. It should also be noted that one of the primary functions of the ASIST is to detect compromised or failing implants; however, such interfaces were not investigated in this work. Implants with lower interface stability were evaluated in the laboratory setting, but these implants were still close to the range observed in the clinical study. The implants for all patients seen in the clinical BAHA study did not show any signs of failure. While this is a very good clinical result with obvious benefits to both the patients and the clinicians, it did not allow for evaluation of implants at risk of failure.

Finally, there were several limitations associated with the application to natural teeth, most notably the use of data from a previous study that was collected with an older variation of the ASIST device (the Osseometer). The data had to be transformed before use in order to remove the zero overshoot in the acceleration response. Additionally, the initial data collection did not have real-time feedback of the quality of the signal and we only had limited information regarding the data collection procedure in terms of the striking location and striking conditions. Some longitudinal changes in PDL stiffness were noted for all patients; however, with the limited data we do not have a sense of the variability in the measure thus making it difficult to assess the statistical or clinical significance of the stiffness changes that were noted. An evaluation of the repeatability of the measure for tooth systems would allow a power calculation to estimate an appropriate sample size for future clinical studies.

## **7.4. Future Considerations**

### **7.4.1. Further Expansion for BAHA Systems**

This work should be extended to provide robust and accurate models for the full range of clinically available BAHA implant-abutment systems. An extensive analysis was presented for the Oticon Medical Ponto system; however, further laboratory testing should be done with the Cochlear Baha® Connect system. Following this, the ASIST can be extended to a multi-center clinical study to provide further evaluation of the technique from a variety of clinicians and clinical protocols from other centers. Such a study would help to build the pool of clinical data which is critical to provide more concrete answers to important clinical questions such as an appropriate timeline for implant loading and thresholds for implant failure.

### **7.4.2. Evaluation of Implant Designs**

New implant designs and methods of improving or promoting osseointegration are often tested through experimental animal studies where the level of osseointegration is evaluated through destructive testing such as removal torque (Johansson et al., 2015). A laboratory evaluation should be conducted to understand the correlation between the ASC measure and the removal torque for percutaneous implants. This would first provide an understanding of how the ASIST measurement relates to a standard measure of the level of osseointegration. If a positive correlation exists this would allow future studies to evaluate different implant designs noninvasively instead of using destructive methods.

### **7.4.3. Application to Other Percutaneous Implant Systems**

This study focused on the development and evaluation of the ASIST for BAHA implant systems; however, percutaneous implants are used in many other applications including individual dental implants, full or partial dental arches, facial prosthetics and craniofacial reconstruction, and the attachment of prosthetic limbs. The methods presented here can be expanded to these other applications to understand healing patterns, identify patterns associated with failure, and provide ongoing stability evaluation in a wide variety of applications. For each application, an

appropriate analytical model must be developed along with laboratory testing and evaluation to develop a robust measure of interface integrity.

#### **7.4.4. Further Investigations with Natural Teeth**

The research presented here was the first application of the ASIST methodology for natural teeth; thus there are a variety of potential areas for future research in this area. In this work, the development and evaluation of the method was presented using a set of clinical data that had been previously collected. Future work should include a controlled laboratory study with a variety of teeth (both natural teeth and manufactured teeth where the dimensions and geometry can be controlled). Various materials can be tested to simulate the PDL. For example, a combination of silicone and gasket sealant can be developed with different ratios to control the material stiffness of a simulated PDL (George et al., 2015; Xia and Chen, 2013) to evaluate sensitivity to varying interface properties. Additionally, the precision of experimental testing should be investigated with natural teeth to understand the influence of handpiece positioning and to develop an appropriate protocol for testing with this application. An understanding of the intra-tester and inter-tester reliability would be beneficial.

Further investigation of the analytical model assumptions should be explored. For example different distributions of stiffness at the root interface could be investigated as well as different damping models. Additionally, a more robust treatment of the impact stiffness should be investigated. Controlled experimental studies with consistent striking conditions would help to develop appropriate assumptions for this parameter. The analytical modeling assumptions presented in this research showed promising results for the data examined with a good match between the model and the measured data. These assumptions provided a good baseline for the method; however, they may not be the best representation of the physiological situation and an investigation of other options would be beneficial. Further, the research presented here only focused on single-rooted teeth and the data investigated was only for maxillary cuspids. Future studies should expand the analytical model and experimental methods to include other single-rooted teeth as well as multiple-rooted teeth.

Finally, there is a lot of potential for further clinical studies in the dental area to evaluate various applications of orthodontic treatment, root resorption, treatments aimed at improving the root condition, dental trauma, and periodontal disease.

## References

- Akagawa, Y., Hashimoto, M., Kondo, N., Satomi, K., Tsuru, H. (1986). Initial bone-implant interfaces of submergible and supremargible endosseous single-crystal sapphire implants. *Journal of Prosthetic Dentistry*, 55(1):96-100.
- Akagawa, Y., Ichikawa, Y., Nikai, H., Tsuru, H. (1993). Interface histology of unloaded and early loaded partially stabilized zirconia endosseous implant in initial bone healing. *Journal of Prosthetic Dentistry*, 69(6):599-604.
- Albrektsson, T., Brånemark, P.I., Hansson, H.A., Lindström, J. (1981). Osseointegrated Titanium Implants: Requirements for ensuring a long-lasting, direct bone-to-implant anchorage in man. *Acta Orthopaedica Scandinavica*, 52:155-170.
- Aparicio, C., Lang, N.P., and Rangert, B. (2006). Validity and clinical significance of biomechanical testing of implant/bone interfaces. *Clinical Oral Implants Research*. 17(Suppl 2): 2-7.
- Atsumi, M., Park, S.H., and Wang, H.L. (2007). Methods used to assess implant stability: Current status. *International Journal of Oral & Maxillofacial Implants*, 22(5): 743-754.
- Beer, F.P., Johnston, E.R., Dewolf, J.T., Mazurek, D.F. (2012). *Mechanics of Materials*, 6<sup>th</sup> Ed. McGraw Hill, New York, NY, USA.
- Brånemark, PI. (1983). Osseointegration and its experimental background. *Journal of Prosthetic Dentistry*, 50(3): 399-410.
- Brånemark, PI., Zarb, G.A., and Albrektsson, T. (1985). *Tissue-Integrated Prostheses: Osseointegration in Clinical Dentistry*. Quintessence Publishing Company Inc. Chicago, IL, USA.
- Brunski, J.B. (1991). Influence of biomechanical factors at the bone-biomaterial interface. In: Davies, E.J. (Editor). *The Bone-Biomaterial Interface*, University of Toronto Press, Toronto, Canada, 391-405.
- Brunski, J.B. (1992). Biomechanical factors affecting the bone-dental implant interface. *Clinical Materials*, 10(3):153-201.
- Brunski, J.B. (1993). Avoid pitfalls of overloading and micromotion of intraosseous implants. *Dental Implantology Update* 4(10):77-81.

- Brunski, J.B., Moccia, A.F., Pollack, S.R., Korostoff, E., Trachtenberg, D.I. (1979). The influence of functional use of endosseous dental implants on the tissue-implant interface. I. Histological aspects. *Journal of Dental Research*, 58(10): 1953-1969.
- Cameron, H., Pilliar, R.M., Macnab, I. (1973). The effect of movement on the bonding of porous metal to bone. *Journal of Biomedical Materials Research*, 7(4):301-311.
- Carvalho, L. Moreira, R.A.S., Simões, J.A. (2006). Application of a vibration measuring technique to evaluate the dynamic stiffness of porcine periodontal ligament. *Technology and Health Care*, 14: 457-465.
- Castellini, P., Scalise, L., Tomasini, E.P. (1998). Teeth mobility measurement: A laser vibrometry approach. *Journal of Clinical Laser Medicine & Surgery*, 16(5): 269-272.
- Cehreli, M.C., Karasoy, D., Akca, K., Eckert, S.E. (2009). Meta-analysis of methods used to assess implant stability. *International Journal of Oral & Maxillofacial Implants*, 24(6): 1015-1032.
- Chopra, A.K. (2001). *Dynamics of Structures: Theory and Applications to Earthquake Engineering, 2<sup>nd</sup> Ed.* Prentice Hall, Upper Saddle River, New Jersey, USA.
- Cowin, S.C. (Editor). (2001). *Bone Mechanics Handbook, 2<sup>nd</sup> Ed.* CRC Press, Boca Raton, Florida, USA.
- Crockett, J.C., Roger, M.J., Coxon, F.P., Hocking, L.J., Helfrich, M.H. (2011). Bone remodelling at a glance. *Journal of Cell Science*, 124(7): 991-998.
- Davies, J.E. (2003). Understanding peri-implant endosseous healing. *Journal of Dental Education*, 67(8): 932-949.
- Den Hartog, J.P. (1985). *Mechanical Vibrations*, Dover Publications Inc. New York, NY, USA.
- Deporter, D.A., Watson, P.A., Pilliar, R.M., Chipmani, M.L., Valiquette, N. (1990). A histological comparison in the dog of porous-coated vs. threaded dental implants. *Journal of Dental Research*, 69(5):1138-1145.
- Dolce, C., Malone, J.S., Wheeler, T.T. (2002). Current concepts in the biology of orthodontic tooth movement. *Seminars in Orthodontics*, 8(1): 6-12.
- Ducheyne, P., De Meester, P., Aernoudt, E., Martens, M., Mulier, J.C. (1977). Influence of a functional dynamic loading on bone ingrowth into surface pores of orthopedic implants. *Journal of Biomedical Materials Research*, 11(6):811-838.

Dun, C., de Wolf, M., Hol, M., Wigren, S., Eeg-Olofsson, M., Green, K., Karlsmo, A., Flynn, M., Stalfors, J., Rothera, M., Mylanus, E., Cremers, C. (2011). Stability, Survival, and Tolerability of a Novel Baha Implant System: Six-Month Data from a Multicenter Clinical Investigation. *Otology & Neurotology*, 32(6): 1001-1007.

Dun, C., Faber, H., de Wolf, M., Mylanus, E., Cremers, C., Hol, M. (2012). Assessment of More Than 1,000 Implanted Percutaneous Bone Conduction Devices: Skin Reactions and Implant Survival. *Otology & Neurotology*, 33(2): 192-198.

Ellingsen, J.E., and Lyngstadaas, S.P. (2003). *Bio-Implant Interface: Improving Biomaterials and Tissue Reactions*. CRC Press, Boca Raton, Florida, USA.

Faber, H., Dun, C., Nelissen, R., Mylanus, E., Cremers, C., Hol, M. (2012). Bone-anchored hearing implant loading at 3 weeks: Stability and tolerability after 6 months. *Otology & Neurotology*, 34: 104-110.

Faulkner, G., Wolfaardt, J.F., and Chan, A. (1999). Measuring abutment/implant joint integrity with the Periotest instrument. *International Journal of Oral & Maxillofacial Implants*. 14(5): 681-688.

Fill, T.S., Carey, J.P., Toogood, R.W., Major, P.W. (2011). Experimentally determined mechanical properties of, and models for, the periodontal ligament: Critical review of current literature. *Journal of Dental Biomechanics*, 2011: 312980-1-10.

Foghsgaard, S., Caye-Thomasen, P. (2014). A new wide-diameter bone-anchored hearing implant – Prospective 1-year data on complications, implant stability, and survival. *Otology & Neurotology*, 35: 1238-1241.

Fontaine, N., Hemar, P., Schultz, P., Charpiot, A., Debry, C. (2014). BAHA implant: Implantation technique and complications. *European Annals of Otorhinolaryngology, Head and Neck diseases*, 131(1): 69-74.

George, M.G., Romanyk, D.L., George, A., Li, Y., Heo, G., Major, P.W., Carey, J.P. (2015). Comparison of third-order torque simulation with and without a periodontal ligament simulant. *American Journal of Orthodontics and Dentofacial Orthopedics*, 148(3): 431-439.

Giannitsios, D.K. (2001). Dynamic modeling of the Periotest® method. M.Sc. Thesis, University of Alberta, Edmonton, Canada.

Goellner, M., Berthold, C., Holst, S., Wichmann, M., Schmitt, J. (2012). Correlations between photogrammetric measurements of tooth mobility and the Periotest method. *Acta Odontologica Scandinavica*, 70: 27-35.

Goellner, M., Schmitt, J., Holst, S., Petschelt, A., Wichmann, M., Berthold, C. (2013). Correlations between tooth mobility and the Periotest method in periodontally involved teeth. *Quintessence International*, 44(4): 307-316.

Gray, H. (1918). *Anatomy of the Human Body*. URL: <http://www.bartleby.com/107/>

- Hagr, A. (2007). BAHA: Bone-Anchored Hearing Aid. *International Journal of Health Sciences*, 1(2): 265-276.
- Hallgren, K.A. (2012). Computing Inter-Rater Reliability for Observational Data: An Overview and Tutorial. *Tutorials in Quantitative Methods for Psychology*, 8(1): 23 – 34.
- Hashimoto, M., Akagawa, Y., Nikai, H., Tsuru, H. (1988). Single-crystal sapphire endosseous dental implant loaded with functional stress – clinical and histological evaluation of peri-implant tissues. *Journal of Oral Rehabilitation*, 15(1): 65-76.
- Hayashi, M., Kobayashi, C., Ogata, H., Yamaoka, M., Ogiso, B. (2010). A no-contact vibration device for measuring implant stability. *Clinical Oral Implants Research*, 21(9): 931-936.
- Hobkirk, J.A. and Wiskott, H.W.A. (2006). Biomechanical aspects of oral implants: Consensus report of working group 1. *Clinical Oral Implants Research*, 17(Suppl 2): 52-54.
- Hougaard, D.D., Jonhede, S., Holmberg, M., Foghsgaard, S. (2015). Towards direct loading: Ponto, new healing cap and early loading. *5<sup>th</sup> International Congress on Bone Conduction Hearing and Related Technologies*, Fairmont Chateau Lake Louise, Canada, May 20-23, 2015.
- House, J.W., Kutz, J.W. (2007). Bone-anchored hearing aids: Incidence and management of postoperative complications. *Otology & Neurotology*, 28(2): 213-217.
- Hurst, S.J. (2002). Investigation of Periotest® and Osstell® instruments for measuring craniofacial implant integrity. M.Sc. Thesis, University of Alberta, Edmonton, Canada.
- Johansson, C., Albrektsson, T. (1987). Integration of screw implants in the rabbit: A 1-yr follow-up of removal torque of titanium implants. *International Journal of Oral & Maxillofacial Implants*, 2(2): 69-75.
- Johansson, M.L., Omar, O., Palmquist, A., Simonsson, H., Emanuelsson, L., Norlindh, B., Thomsen, P., (2015). Site-specific laser modification promotes higher osseointegration of titanium implants. *OSSEO 2015 5<sup>th</sup> International Congress on Bone Conduction Hearing and Related Technologies*, Fairmont Chateau Lake Louise, Canada, May 20-23, 2015.
- Jönsson, A., Malmgren, O., Levander, E. (2007). Long-term follow-up of tooth mobility in maxillary incisors with orthodontically induced apical root resorption. *European Journal of Orthodontics*, 29: 482-487.
- Kamal, F., Lou, E., Faulkner, G., Westover, L. (2015). ASIST – A bluetooth real-time implant/bone interface stability measurement device. *OSSEO 2015 5<sup>th</sup> International Congress on Bone Conduction Hearing and Related Technologies*, Fairmont Chateau Lake Louise, Canada, May 20-23, 2015.
- Krishnan, V., Davidovitch, Z. (2006). Cellular, molecular, and tissue-level reactions to orthodontic force. *American Journal of Orthodontics and Dentofacial Orthopedics*, 129(4): 469.e1-32.

- Lagravère, M.O., Fang, Y., Carey, J., Toogood, R.W., Packota, G.V., Major, P.W. (2006). Density conversion factor determined using a cone-beam computed tomography unit NewTom QR-DVT 9000. *Dentomaxillofacial Radiology*, 35: 407-409.
- Laster, L., Laudenschlager, K.W., and Stoller, N.H. (1975). An evaluation of clinical tooth mobility measurements. *Journal of Periodontology*, 46(10): 603-607.
- Lukas, D. and Schulte, W. (1990). Periotest – A dynamic procedure for the diagnosis of the human periodontium. *Clinical Physics and Physiological Measurement*, 11(1): 65-75.
- Lum, L.B., Beirne, O.R., Curtis, D.A. (1991). Histological evaluation of hydroxylapatite coated versus uncoated titanium blade implants in delayed and immediately loaded applications. *International Journal of Oral & Maxillofacial Implants*, 6(4): 456-462.
- Marcotte, M.R. (1990). *Biomechanics in Orthodontics*. B.C. Decker, Inc. Toronto ON, Canada.
- Marsella, P., Scorpecci, A., D'Eredità, R., Della Volpe, A., Malerba, P. (2012). Stability of Osseointegrated Bone Conduction Systems in Children: A Pilot Study. *Otology & Neurotology*, 33(5): 797-803.
- McLarnon, C.M., Johnson, I., Davison, T., Hill, J., Henderson, B., Leese, D., Marley, S. (2012). Evidence for early loading of osseointegrated implants for bone conduction at 4 weeks. *Otology & Neurotology*, 33(9): 1578-1582.
- Meredith, N. (1997). On the clinical measurement of implant stability and osseointegration. Ph.D. Thesis, Göteborg University, Sweden.
- Meredith, N., Alleyne, D., Cawley, P. (1996). Quantitative determination of the stability of the implant-tissue interface using resonance frequency analysis. *Clinical Oral Implants Research* 7(3): 261-267.
- Mo, A., (2009). The impact technique for monitoring intraoral implant stability. M.Sc. Thesis, University of Alberta, Edmonton, Canada.
- Mühlemann, H.R. (1954). Tooth Mobility: The Measuring Method. Initial and Secondary Tooth Mobility. *Journal of Periodontology*, 25(1): 22-29.
- Mühlemann, H.R. (1960). 10 years of tooth-mobility measurements. *Journal of Periodontology*, 38(6): Suppl: 686-713.
- Mühlemann, H.R. (1967). Tooth mobility: A review of clinical aspects and research findings. *Journal of Periodontology*, 31: 110-122.
- Nakago, T., Mitani, S., Hijjiya, H., Hattori, T., and Nakagawa, Y. (1994). Determination of the tooth mobility change during the orthodontic tooth movement studied by means of PERIOTEST and MIMD (the mechanical impedance measuring device for the periodontal tissue). *American Journal of Orthodontics and Dentofacial Orthopedics*, 105(1): 92-96.

- Nelissen, R.C., den Besten, C.A., Mylanus, E.A., Hol, M.K. (2016). Stability, survival, and tolerability of a 4.5 mm-wide bone-anchored hearing implant: 6-month data from a randomized controlled clinical trial. *European Archives of Otorhinolaryngology*, 273(1): 105-111.
- Nelissen, R.C., Stalfors, J., de Wolf, M., Flynn, M.C., Wigren, S., Eeg-Olofsson, M., Green, K., Rothera, M.P., Mylanus, E.A., Hol, M.K. (2014). Long-term stability, survival, and tolerability of a novel osseointegrated implant for bone conduction hearing: 3-year data from a multicenter, randomized, controlled, clinical investigation. *Otology & Neurotology*, 35(8): 1486-1491.
- Nelissen, R.C., Wigren, S., Flynn, M.C., Meijer, G.J., Mylanus, E.A., Hol, M.K. (2015). Application and interpretation of resonance frequency analysis in auditory osseointegrated implants: A review of literature and establishment of practical recommendations. *Otology & Neurotology*, 36(9): 1518-1524.
- Nishihira, M., Yamamoto, K., Sato, Y., Ishikawa, H., Natali, A.N. (2003). Mechanics of periodontal ligament. In Natali, A.N. (Ed.), *Dental Biomechanics*. Taylor & Francis, New York, NY, USA.
- Nordin, M., Frankel, V.H. (2001). *Basic Biomechanics of the Musculoskeletal System*, 3<sup>rd</sup> Ed. Lippincott Williams & Wilkins, Baltimore, Maryland, USA.
- Noyes, D.H., Solt, C.W. (1973). Measurement of mechanical mobility of human incisors with sinusoidal forces. *Journal of Biomechanics*, 6(5): 439-442.
- Persson, R., Svensson, A. (1980). Assessment of tooth mobility using small loads. *Journal of Clinical Periodontology*, 7(4): 259-275.
- Pilliar, R.M. (1991). Quantitative evaluation of the effect of movement at a porous coated implant-bone interface. In: Davies, E.J. (Editor). *The Bone-Biomaterial Interface*, University of Toronto Press, Toronto, Canada, 380-387.
- Provatidis, C.G. (2001). An analytical model for stress analysis of a tooth in translation. *International Journal of Engineering Science*, 39: 1361-1381.
- Reinfeldt, S., Håkansson, B., Taghavi, H., Eeg-Olofsson, M. (2015). New developments in bone-conduction hearing implants: a review. *Medical Devices: Evidence and Research*, 8: 79-93.
- Romanyk, D.L., Melenka, G.W., Carey, J.P. (2013). Modeling stress-relaxation behavior of the periodontal ligament during the initial phase of orthodontic treatment. *Journal of Biomechanical Engineering*, 135(9): 091007-1-8.
- Schatzker, J., Horne, J.G., Sumner-Smith, G. (1975). The effect of movement on the holding power of screws in bone. *Clinical Orthopaedics and Related Research*, 111:257-262.
- Sennerby, L., Meredith, N. (2008). Implant stability measurements using resonance frequency analysis: biological and biomechanical aspects and clinical implications. *Periodontology 2000*, 47: 51-66.

- Shultz, S.J., Nguyen, A., Windley, T.C., Kulas, A.S., Botic, T.L., Beynon, B.D. (2006). Intratester and intertester reliability of clinical measures of lower extremity anatomic characteristics: Implications for multicenter studies. *Clinical Journal of Sport Medicine* , 16(2): 155 – 161.
- Sundén, S., Gröndahl, K., Gröndahl, H-G. (1995). Accuracy and precision in the radiographic diagnosis of clinical instability in Brånemark dental implants. *Clinical Oral Implants Research*, 6(4): 220-226.
- Swain, R. (2006). The development and modeling of an impact test to determine the bone-implant interface properties of osseointegrated implants. Ph.D. Thesis, University of Alberta, Edmonton, Canada.
- Swain, R., Faulkner, G., Raboud, D., Wolfaardt, J. (2008a). A dynamic analytical model for impact evaluation of percutaneous implants. *Journal of Biomechanical Engineering* , 130(5): 051013-1-13.
- Swain, R., Faulkner, G., Raboud, D., Wolfaardt, J. (2008b). An improved impact technique for monitoring percutaneous implant integrity. *International Journal of Oral and Maxillofacial Implants*, 23(2): 263-269.
- Szmukler-Moncler, S., Salama, H., Reingewirtz, Y., Dubruille, J.H. (1998). Timing of loading and effect of micromotion on bone-dental implant interface: Review of experimental literature. *Journal of Biomedical Materials Research*, 43(2):192-203.
- Taghavi, H. (2014). The Bone Conduction Implant (BCI): Preclinical Studies, Technical Design and a Clinical Evaluation. Ph.D. Thesis, Chalmers University of Technology, Gothenburg, Sweden.
- Tanaka, E., Ueki, K., Kikuzaki, M., Yamada, E., Takeuchi, M., Dalla-Bona, D., Tanne, K. (2005). Longitudinal measurements of tooth mobility during orthodontic treatment using a Periotest. *Angle Orthodontist*, 75(1): 101-105.
- Tjellström, A., Granström, G. (1994). Long-term follow up with the bone-anchored hearing aid: A review of the first 100 patients between 1977 and 1985. *Ear, Nose, & Throat Journal* , 73(2): 112-114.
- Tjellström, A., Rosenhall, U., Lindström, J., Hallen, O., Albrektsson, T., and Brånemark, PI. (1983). Five-year experience with skin-penetrating bone-anchored implants in the temporal bone. *Acta oto-laryngologica*, 95(5-6): 568-575.
- Toms, S.R., Dakin, G.J., Lemons, J.E., Eberhardt, A.W. (2002). Quasi-linear viscoelastic behavior of the human periodontal ligament. *Journal of Biomechanics*, 35(10): 1411-1415.
- Türp, J.C., Alt, K.W. (1995). Designating teeth: The advantages of the FDI's two-digit system. *Quintessence International*, 26(7): 501-504.

- Uthoff, H.K. (1973). Mechanical factors influencing the holding power of screws in compact bone. *The Journal of Bone and Joint Surgery. British Volume*, 55(3):633-639.
- van der Pouw, C.T.M., Johansson, C.B., Mylanus, E.A.M., Albrektsson, T., Cremers, C.W.R.J. (1998). Removal of titanium implants from the temporal bone: Histological findings. *The American Journal of Otology*, 19(1): 46-51.
- Wang, Y., Zhang, Y., Miron, R.J. (2016). Health, Maintenance, and Recovery of Soft Tissues around Implants. *Clinical Implant Dentistry and Related Research*, 18(3): 618-634.
- Wazen, J.J., Gupta, R., Ghossaini, S., Spitzer, J., Farrugia, M., Tjellström, A. (2007). Osseointegration timing for Baha system loading. *The Laryngoscope*, 117(5):794-796.
- Wolfram Language & System Documentation Center. *Principal Axis Method*. <http://reference.wolfram.com/language/tutorial/UnconstrainedOptimizationPrincipalAxisMethod.html>
- Xia, Z., Chen, J. (2013). Biomechanical validation of an artificial tooth-periodontal ligament-bone complex for in vitro orthodontic load measurement. *Angle Orthodontist*, 83(3): 410-417.
- Yamane, M., Yamaoka, M., Hayashi, M., Furutoyo, I., Komori, N., Ogiso, B. (2008). Measuring tooth mobility with a no-contact vibration device. *Journal of Periodontal Research*, 43(1): 84-89.
- Zainal Ariffin, S.H., Yamamoto, Z., Zainol Abidin, I.Z., Megat Abdul Wahab, R., Zainal Ariffin, Z. (2011). Cellular and molecular changes in orthodontic tooth movement. *The Scientific World Journal*, 11: 1788-1803.

# Appendix A: Analytical Model Parameters for BAHA Implant-Abutment Systems

## A.1 Derivation of the Mass Matrix

The inertia influence coefficients  $m_{ij}$  are defined as the force that must be applied at coordinate  $i$  to produce a unit acceleration at coordinate  $j$ , while maintaining zero acceleration at all other coordinates.

For example, the first column of the mass matrix can be determined by applying a unit acceleration at coordinate  $x_1$  with zero acceleration at the other coordinates, and examining the free body diagrams (FBD) and mass-acceleration diagrams (MAD) of the system components.

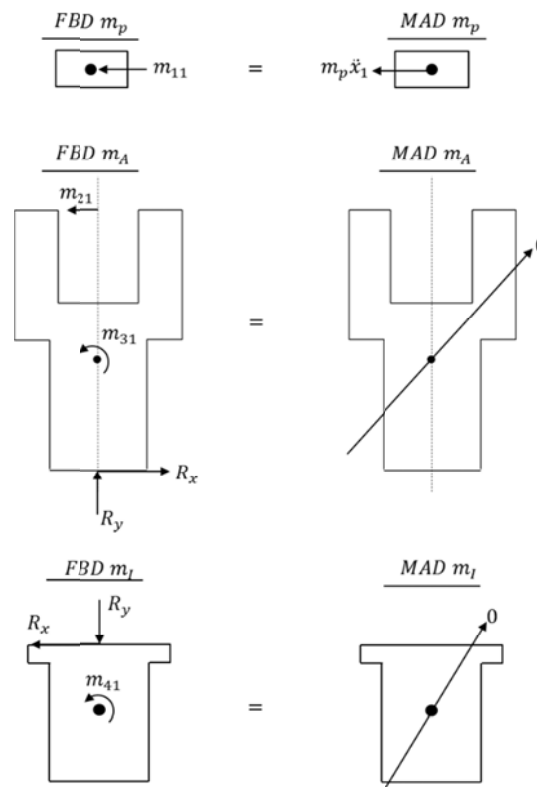


Figure A.1: Free body diagrams for the system components with a unit acceleration applied:  $\ddot{x}_1 = 1$

From the FBD's in Figure A.1 we can write the following equations (calling the connection between the implant and the abutment point C):

Mass:  $\sum F_x = ma_x \rightarrow m_{11} = m_p$

Implant:  $\sum F_x = 0 \rightarrow R_x = 0$   
 $\sum M_c = 0 \rightarrow m_{41} = 0$

Abutment:  $\sum F_x = 0 \rightarrow m_{21} = 0$   
 $\sum M_c = 0 \rightarrow m_{31} = 0$

The second column of the mass matrix can be determined by applying a unit acceleration at coordinate  $x_2$  with zero acceleration at the other coordinates.

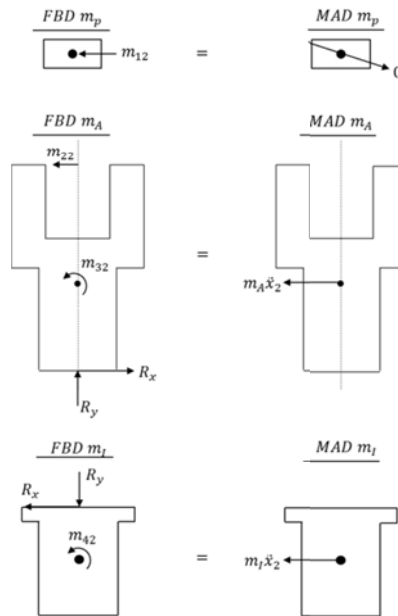


Figure A.2: Free body diagrams for the system components with a unit acceleration applied:  $\ddot{x}_2 = 1$

Mass:  $\sum F_x = 0 \rightarrow m_{12} = 0$

Implant:  $\sum F_x = ma_x \rightarrow R_x = m_I$

$$\left(\sum M_c\right)_{FBD} = \left(\sum M_c\right)_{MAD} \rightarrow m_{42} = -m_I(L_I - \bar{y}_I)$$

Abutment:  $\sum F_x = ma_x \rightarrow m_{22} = m_I + m_A$

$$\left(\sum M_c\right)_{FBD} = \left(\sum M_c\right)_{MAD} \rightarrow m_{32} = m_A \bar{y}_A - (m_I + m_A)h$$

The third column of the mass matrix can be determined by applying a unit acceleration at coordinate  $\theta_1$  with zero acceleration at the other coordinates.

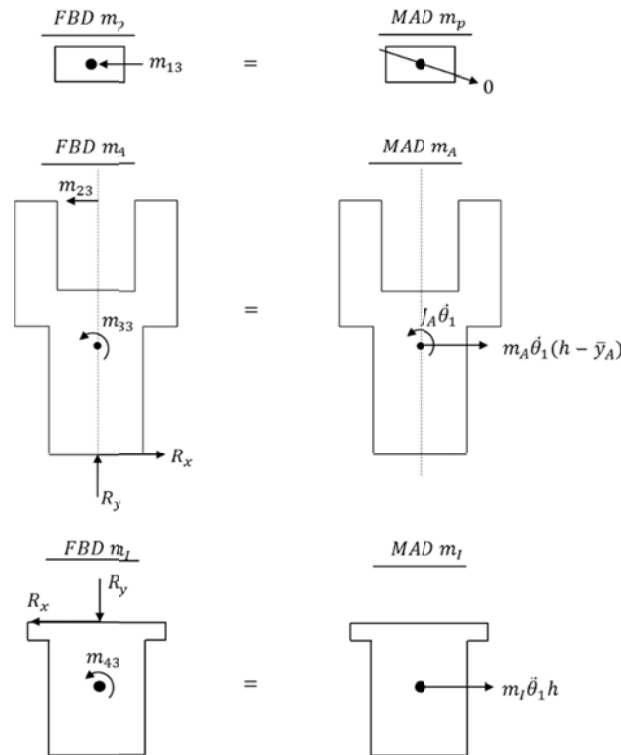


Figure A.3: Free body diagrams for the system components with a unit acceleration applied:  $\ddot{\theta}_1 = 1$

Mass:  $\sum F_x = 0 \rightarrow m_{13} = 0$

Implant:  $\sum F_x = ma_x \rightarrow R_x = -m_I h$

$$\left(\sum M_c\right)_{FBD} = \left(\sum M_c\right)_{MAD} \rightarrow m_{43} = m_I h(L_I - \bar{y}_I)$$

Abutment:  $\sum F_x = ma_x \rightarrow m_{23} = m_A \bar{y}_A - (m_I + m_A)h$

$$\left(\sum M_c\right)_{FBD} = \left(\sum M_c\right)_{MAD} \rightarrow m_{33} = J_A + m_A(h - \bar{y}_A)^2 + m_I h^2$$

The fourth column of the mass matrix can be determined by applying a unit acceleration at coordinate  $\theta_2$  with zero acceleration at the other coordinates.

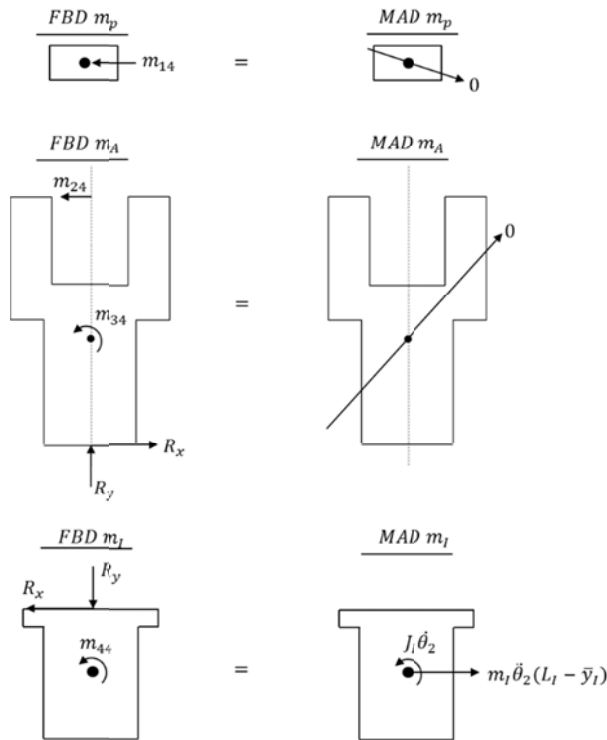


Figure A.4: Free body diagrams for the system components with a unit acceleration applied:  $\ddot{\theta}_2 = 1$

$$\text{Mass: } \sum F_x = 0 \rightarrow m_{14} = 0$$

$$\text{Implant: } \sum F_x = ma_x \rightarrow R_x = -m_I(L_I - y_I)$$

$$\left(\sum M_c\right)_{FBD} = \left(\sum M_c\right)_{MAD} \rightarrow m_{44} = J_I + m_I(L_I - \bar{y}_I)^2$$

$$\text{Abutment: } \sum F_x = ma_x \rightarrow m_{24} = -m_I(L_I - \bar{y}_I)$$

$$\left(\sum M_c\right)_{FBD} = \left(\sum M_c\right)_{MAD} \rightarrow m_{34} = m_I h(L_I - \bar{y}_I)$$

The matrix  $[M]$  is given by the following:

$$[M] = \begin{bmatrix} m_p & 0 & 0 & 0 \\ 0 & m_I + m_A & m_A \bar{y}_A - (m_I + m_A)h & -m_I(L_I - \bar{y}_I) \\ 0 & m_A \bar{y}_A - (m_I + m_A)h & J_A + m_A(h - \bar{y}_A)^2 + m_I h^2 & m_I h(L_I - \bar{y}_I) \\ 0 & -m_I(L_I - \bar{y}_I) & m_I h(L_I - \bar{y}_I) & J_I + m_I(L_I - \bar{y}_I)^2 \end{bmatrix}$$

Where:

$L_I$  = length of the implant

$\bar{y}_A$  = distance from the bottom of the abutment to the center of mass

$\bar{y}_I$  = distance from the bottom of the implant to the center of mass

$h$  = distance from the bottom of the abutment to the striking location

## A.2 Derivation of the Stiffness Matrix:

The interface stiffness is represented as a stiffness per unit area covering the threaded portion of the implant. Consider an implant with threaded length  $l_i$  as shown in Figure A.5. Consider a slice through the diameter of the implant of thickness  $dl$  at a distance  $l$  from the top of the implant flange.

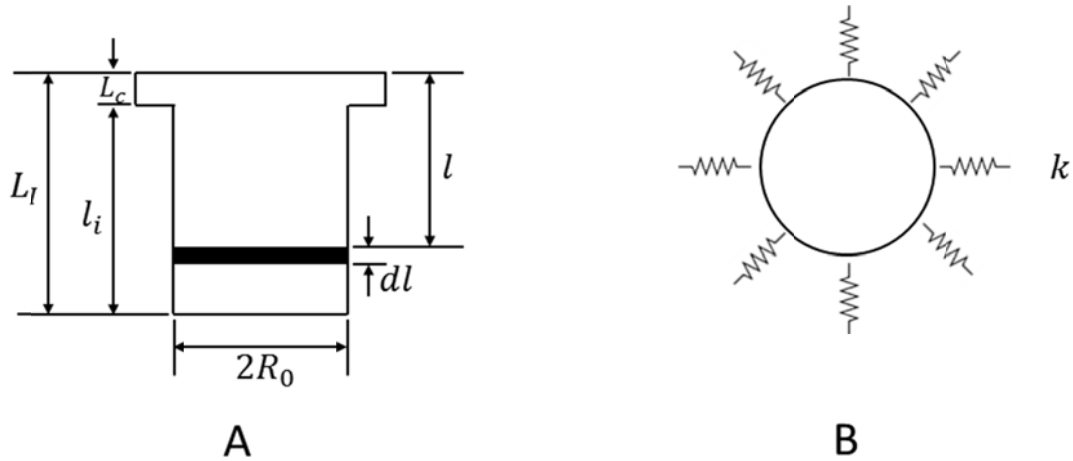


Figure A.5: BAHA implant schematic. A: Front view cross-section. B: Top view.

The effective stiffness of such a slice can be determined by applying a unit horizontal displacement  $x = 1$ . The force on an element of the slice at an angle  $\theta$  from the direction of the applied displacement is equal to  $dF = kx \cos \theta R_0 d\theta dl = k \cos \theta R_0 d\theta dl$ .

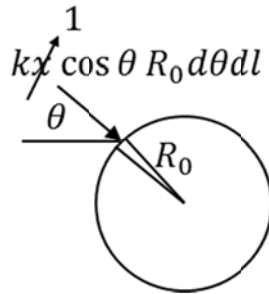


Figure A.6: Cross-section of an implant (top view) showing the force on an element of the slice at an angle  $\theta$  from the direction of the applied displacement

The effective stiffness for each slice can be determined by integrating the elemental force over the diameter of the implant. Thus  $k_{eff}$  in the following equation is a stiffness per unit length applied over the threaded portion of the implant.

$$k_{eff} = 2 \int_{-\frac{\pi}{2}}^{\frac{\pi}{2}} k \cos \theta R_0 d\theta dl = 4kR_0 dl$$

The stiffness matrix  $[K]$  for the 4-DOF system can now be determined using the method of influence coefficients. The stiffness coefficients  $k_{ij}$  are defined as the force that must be applied at coordinate  $i$  to produce a unit deflection at coordinate  $j$ , while maintaining zero deflection at all other coordinates.

The first column in the stiffness matrix can be determined by applying a unit displacement to  $x_1$  with zero displacement at the other coordinates, and examining the FBD's of the system components.

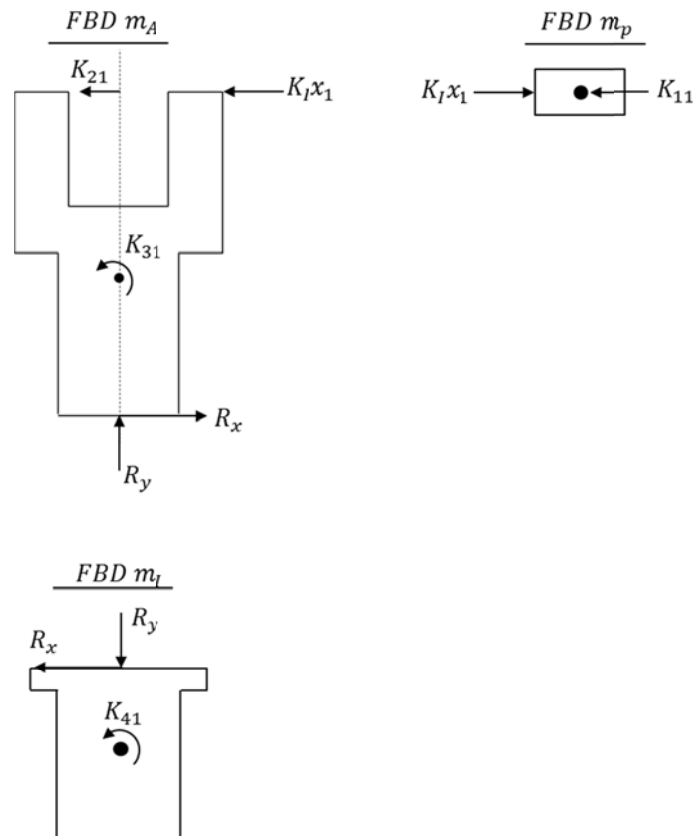


Figure A.7: Free body diagrams for the system components with a unit displacement applied at  $x_1$

Mass:  $\sum F_x = 0 \rightarrow K_{11} = K_I$

Implant:  $\sum F_x = 0 \rightarrow R_x = 0$

$\sum M_c = 0 \rightarrow K_{41} = 0$

Abutment:  $\sum F_x = 0 \rightarrow K_{21} = -K_I$

$\sum M_c = 0 \rightarrow K_{31} = 0$

The second column in the stiffness matrix can be determined by applying a unit displacement to  $x_2$  with zero displacement at the other coordinates.

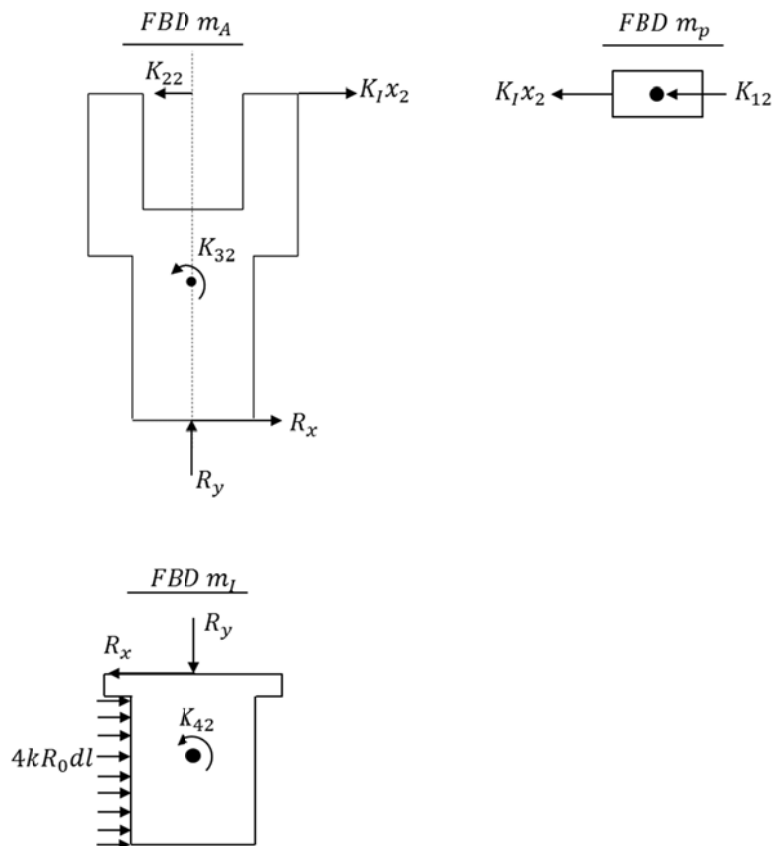


Figure A.8: Free body diagrams for the system components with a unit displacement applied at  $x_2$

Mass:  $\sum F_x = 0 \rightarrow K_{12} = -K_I$

Implant:  $\sum F_x = 0 \rightarrow -R_x + \int_{L_c}^{L_I} 4kR_0 dl = 0 \rightarrow R_x = 4kR_0(L_I - L_c)$

$$\sum M_c = 0 \rightarrow K_{42} + \int_{L_c}^{L_I} 4kR_0 l dl = 0 \rightarrow K_{42} = -2kR_0(L_I^2 - L_c^2)$$

Abutment:  $\sum F_x = 0 \rightarrow K_{22} = K_I + 4kR_0(L_I - L_c)$

$$\sum M_c = 0 \rightarrow K_{32} = -4kR_0(L_I - L_c)h$$

The third column in the stiffness matrix can be determined by applying a unit rotation to  $\theta_1$  with zero displacement at the other coordinates.

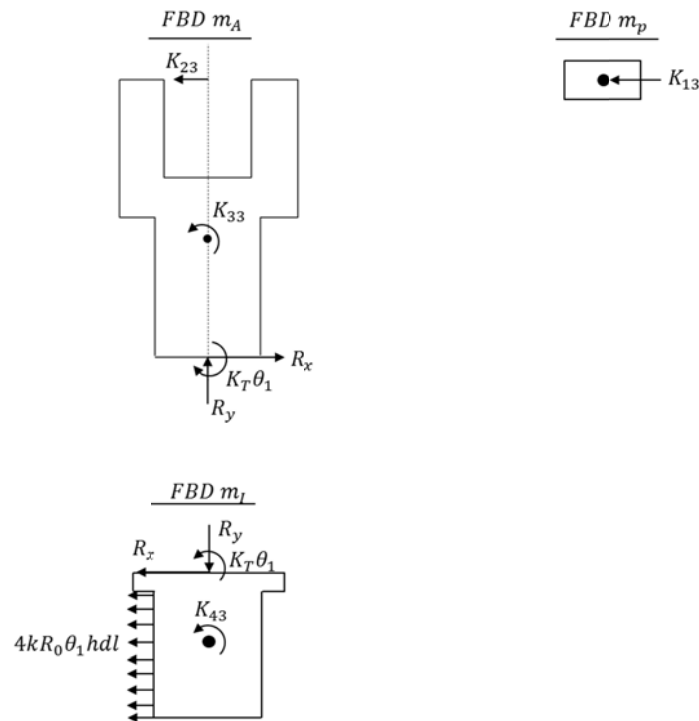


Figure A.9: Free body diagrams for the system components with a unit displacement applied at  $\theta_1$

Mass:  $\sum F_x = 0 \rightarrow K_{13} = 0$

Implant:  $\sum F_x = 0 \rightarrow -R_x - \int_{L_c}^{L_I} 4kR_0h dl = 0 \rightarrow R_x = -4kR_0(L_I - L_c)h$

$\sum M_c = 0 \rightarrow K_{43} + K_T - \int_{L_c}^{L_I} 4kR_0h l dl = 0 \rightarrow K_{43} = -K_T + 2kR_0(L_I^2 - L_c^2)h$

Abutment:  $\sum F_x = 0 \rightarrow K_{23} = -4kR_0(L_I - L_c)h$

$\sum M_c = 0 \rightarrow K_{33} = K_T + 4kR_0(L_I - L_c)h^2$

The fourth column in the stiffness matrix can be determined by applying a unit rotation to  $\theta_2$  with zero displacement at the other coordinates.

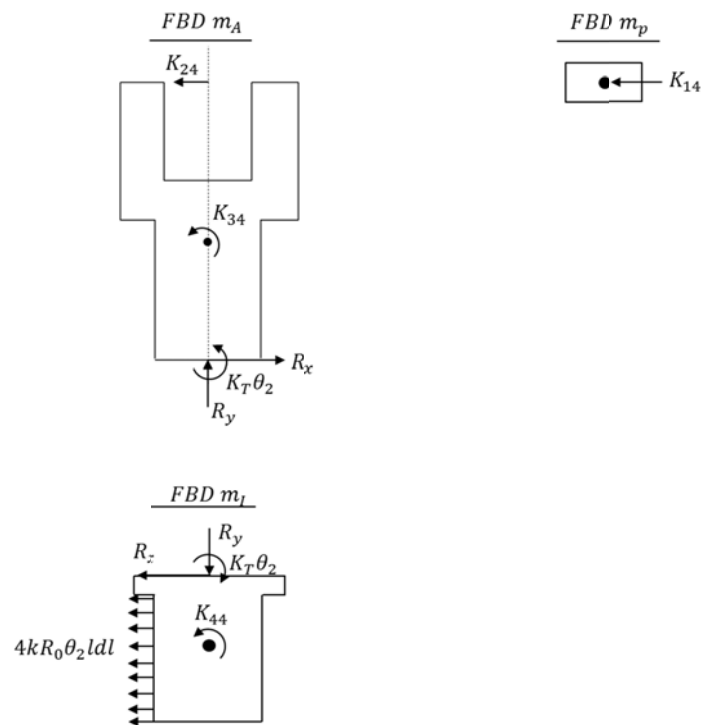


Figure A.10: Free body diagrams for the system components with a unit displacement applied at  $\theta_2$

$$\text{Mass: } \sum F_x = 0 \rightarrow K_{14} = 0$$

$$\text{Implant: } \sum F_x = 0 \rightarrow -R_x - \int_{L_c}^{L_I} 4kR_0 l dl = 0 \rightarrow R_x = -2kR_0(L_I^2 - L_c^2)$$

$$\sum M_c = 0 \rightarrow K_{44} - K_T - \int_{L_c}^{L_I} 4kR_0 l^2 dl = 0 \rightarrow K_{44} = K_T + \frac{4}{3}kR_0(L_I^3 - L_c^3)$$

$$\text{Abutment: } \sum F_x = 0 \rightarrow K_{24} = -2kR_0(L_I^2 - L_c^2)$$

$$\sum M_c = 0 \rightarrow K_{34} = -K_T + 2kR_0(L_I^2 - L_c^2)h$$

The stiffness matrix  $[K]$  is given by the following:

$$[K] = \begin{bmatrix} K_I & -K_I & 0 & 0 \\ -K_I & K_I + 4kR_0(L_I - L_C) & -4kR_0(L_I - L_C)h & -2kR_0(L_I^2 - L_C^2) \\ 0 & -4kR_0(L_I - L_C)h & K_T + 4kR_0(L_I - L_C)h^2 & -K_T + 2kR_0(L_I^2 - L_C^2)h \\ 0 & -2kR_0(L_I^2 - L_C^2) & -K_T + 2kR_0(L_I^2 - L_C^2)h & K_T + \frac{4}{3}kR_0(L_I^3 - L_C^3) \end{bmatrix}$$

Where  $L_C$  is the portion of the implant that extends above the bone surface (i.e. the distributed stiffness at the bone-implant interface  $k$  only acts along the length  $L_I - L_C$ ) and  $R_0$  is the radius of the implant.

### A.3 Approximation of the Torsional Stiffness $K_T$

The assumptions for the torsional stiffness coefficient  $K_T$  are based on the work of Swain (2006; 2008a). Let us assume that the abutment is fixed at its connection to the implant. Let us also assume that there is an applied load  $P$  at the impact site, a distance  $L$  from the fixed support (Figure A.11).

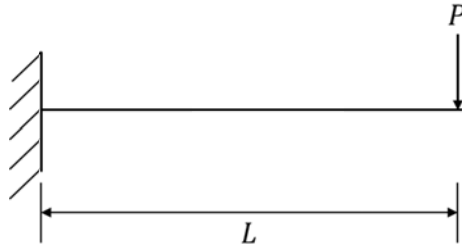


Figure A.11: Abutment acting as a cantilever beam with an applied load  $P$

If we assume that the abutment behaves as a cantilever beam, the deflection at the free end is given by the following (Figure A.12):

$$\Delta = \frac{PL^3}{3EI}$$

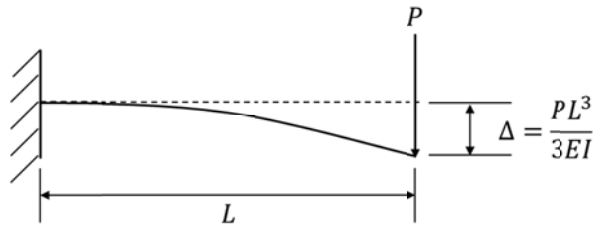


Figure A.12: Deflection of a cantilever beam

Now, if we instead assume that the abutment behaves as a rigid beam with a torsional spring  $K_T$  at the support, the deflection at the free end is given by (Figure A.13):

$$\Delta = L\theta = L \left( \frac{PL}{K_T} \right)$$

Where  $\theta$  is the angle of rotation of the beam. Note for a torsional spring, we have  $K_T\theta = PL$  where  $PL$  is the applied moment.

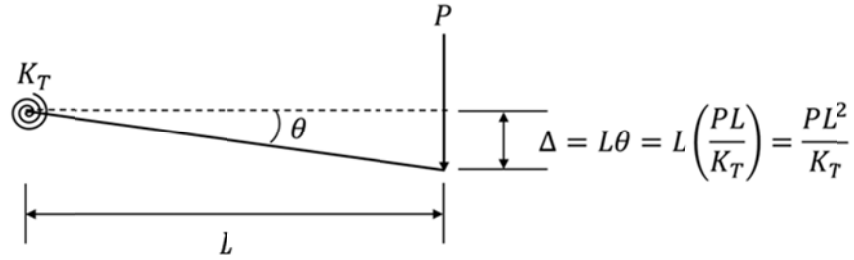


Figure A.13: Abutment acting as a rigid beam with a torsional spring

The deflection is the same in both of these cases, thus we can determine the following relation for the torsional spring coefficient:

$$\frac{PL^3}{3EI} = \frac{PL^2}{K_T} \Rightarrow K_T = \frac{3EI}{L}$$

With this derivation, we assume that the abutment is rigidly fixed at the connection to the implant. Thus this expression for  $K_T$  should be a maximum value. However, the connection is simply a screw connection which is not rigidly fixed. To account for this, we can include a factor in the definition of  $K_T$  suggesting that the actual value is some fraction of this theoretical maximum.

$$K_T = \alpha \left( \frac{3EI}{L} \right)$$

It is clear that the torsional spring coefficient is related to the Young's modulus of the abutment material ( $E$ ), the second moment of area of the cross-section ( $I$ ), and the distance from the connection to the site of impact ( $L$ ), which is effectively the length of the abutment. To determine the maximum value for each abutment, these values had to be approximated. The nominal length of each abutment was used ( $L = 6, 9, 12, 14$  mm) and the Young's modulus of titanium ( $E = 110$  GPa). The second moment of area of the cross-section was calculated based on the approximate geometry of the abutment. Since the cross-section of the abutment varies along its length, we cannot simply use the expression above to determine the deflection of the cantilever beam in bending. To account for the varying cross-section (and thus the varying

second moment of area), we can use the following procedure. Consider the beam shown in Figure A.14 approximating the geometry of the abutment.

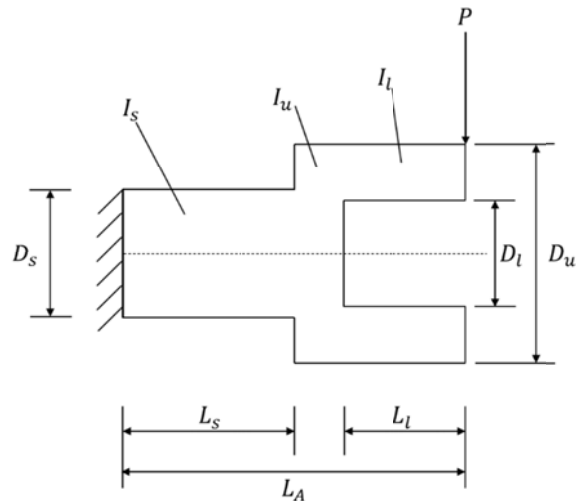


Figure A.14: Approximate geometry of the abutment

The second moment of area for each section is given by:

$$I_s = \frac{\pi}{64} D_s^4$$

$$I_u = \frac{\pi}{64} D_u^4$$

$$I_s = \frac{\pi}{64} (D_u^4 - D_l^4)$$

The strain energy for a beam under bending is given by:

$$dU = \frac{M^2}{2EI} dx$$

Where  $M$  is the bending moment as a function of the distance from the fixed end  $x$ . For the loading considered:

$$M = -P(L_A - x) \Rightarrow M^2 = P^2(L_A - x)^2$$

We can integrate this expression over the length of the abutment to get the total strain energy of the beam:

$$U = \int_0^{L_s} \frac{P^2(L_A - x)^2}{2EI_s} dx + \int_{L_s}^{L_A-L_l} \frac{P^2(L_A - x)^2}{2EI_u} dx + \int_{L_A-L_l}^{L_A} \frac{P^2(L_A - x)^2}{2EI_l} dx$$

Once the strain energy is known, the deflection of the free end of the beam (where the load  $P$  is applied) can be determined from Castigliano's method (Beer et al., 2012):

$$\Delta = \frac{\partial U}{\partial P}$$

Finally, the maximum  $K_T$  for each abutment is given by the expression:

$$K_{T(max)} = \frac{PL_A^2}{\Delta}$$

**Table A.1: Maximum  $K_T$  values for Oticon Abutments**

Abutment Length (mm)	Maximum $K_T$ (Nm)
6 mm	2183
9 mm	1191
12 mm	856
14 mm	725

Again, the actual torsional spring coefficient used in the model is some fraction of this maximum value for each abutment.

$$K_T = \alpha K_{T(max)}$$

# **Appendix B: Parametric Sensitivity of the Analytical Model for BAHA Implant-Abutment Systems**

## **B.1 Modal Analysis**

A program was implemented in Mathematica (Wolfram Mathematica 10, Champaign, IL, USA) to determine the natural frequencies and mode shapes of the implant-abutment system. The natural frequencies and mode shapes are dependent on the system parameters, so the analysis was completed for two different levels of interface stiffness for each implant-abutment combination ( $k = 2 \times 10^{12}$  N/m<sup>3</sup>; ASC between 11 – 18 and  $k = 5 \times 10^{12}$  N/m<sup>3</sup>; ASC between 28 – 45 ). The mode shapes for the long/narrow Oticon Medical implant (M50128) with each of the abutments (6 mm, 9 mm, 12 mm, 14 mm) and both high and low interface stiffness values are shown in Figures B.1 – B.4 for illustration. The grey dashed lines represent the initial position of the system, while the solid black lines represent the normalized mode shape. The solid dots represent the location of the center of mass of the impact rod, the center line of the abutment at the height of the strike, the implant-abutment connection, and the bottom of the implant. The patterns of the mode shapes are the same in all cases.

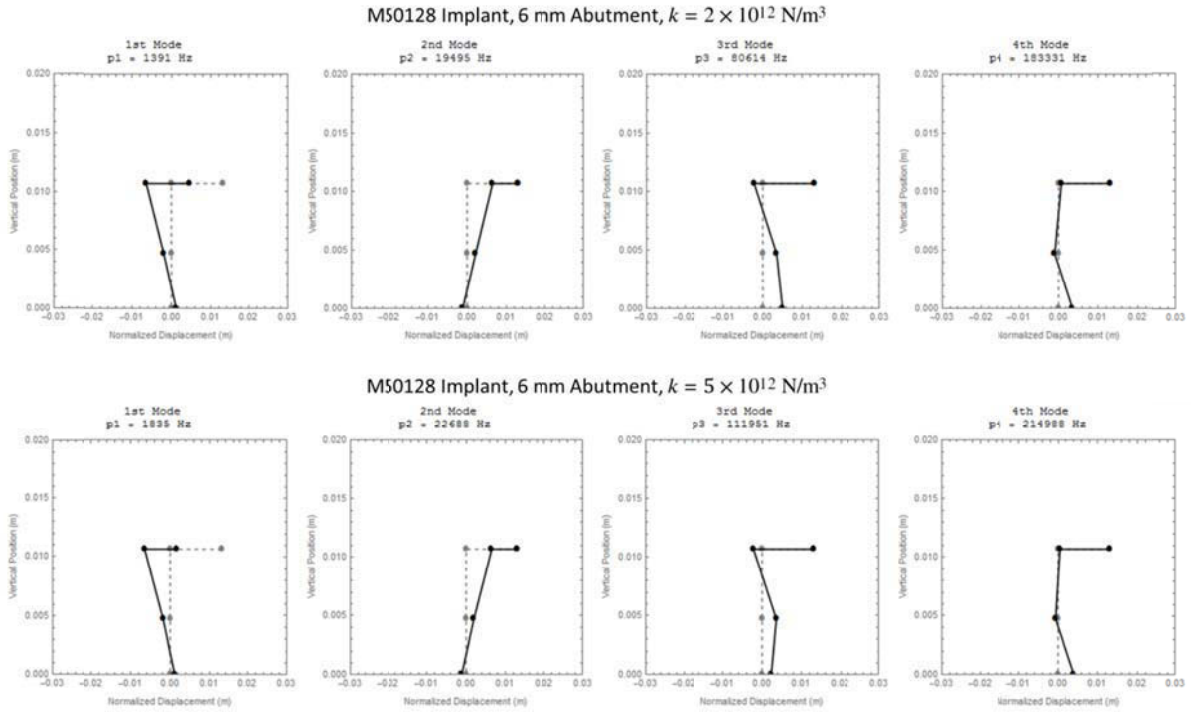


**Figure B.1: Mode shapes for long/narrow implant (M50128) with 6 mm abutment. Top:  $k = 2 \times 10^{12} \text{ N/m}^3$ ; Bottom:  $k = 5 \times 10^{12} \text{ N/m}^3$**

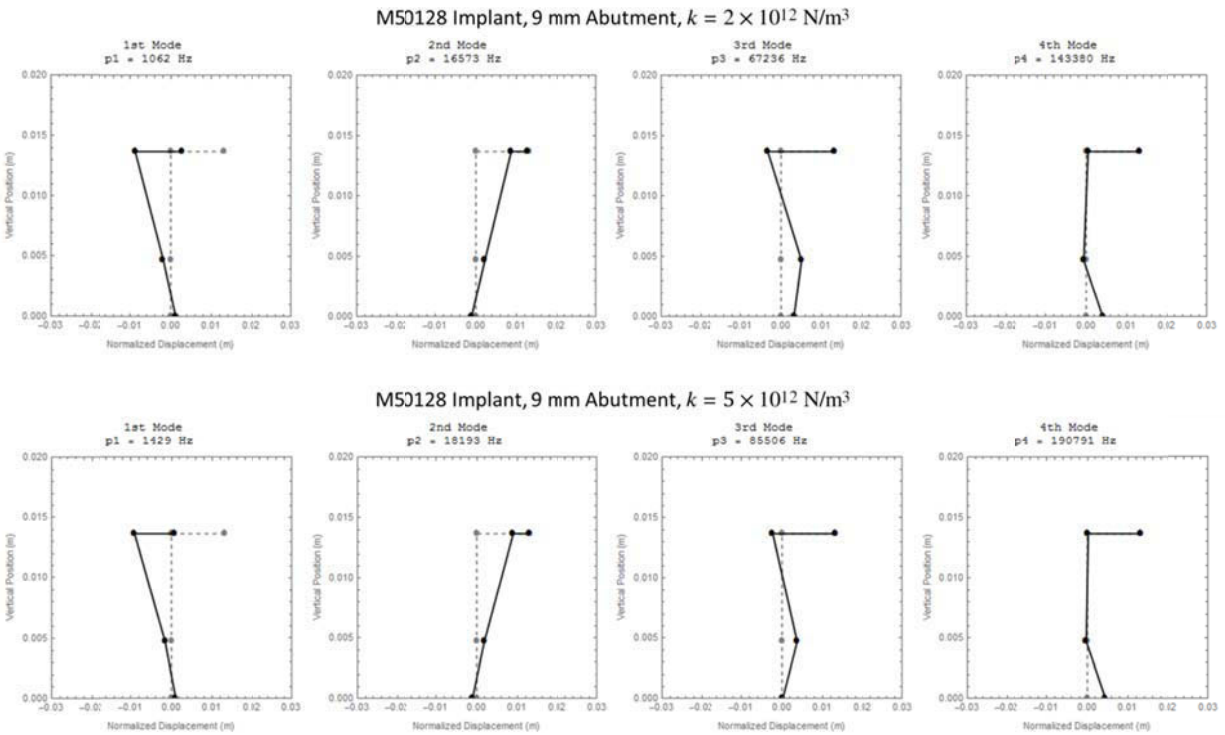


**Figure B.2: Mode shapes for long/narrow implant (M50128) with 9 mm abutment. Top:  $k = 2 \times 10^{12} \text{ N/m}^3$ ; Bottom:  $k = 5 \times 10^{12} \text{ N/m}^3$**

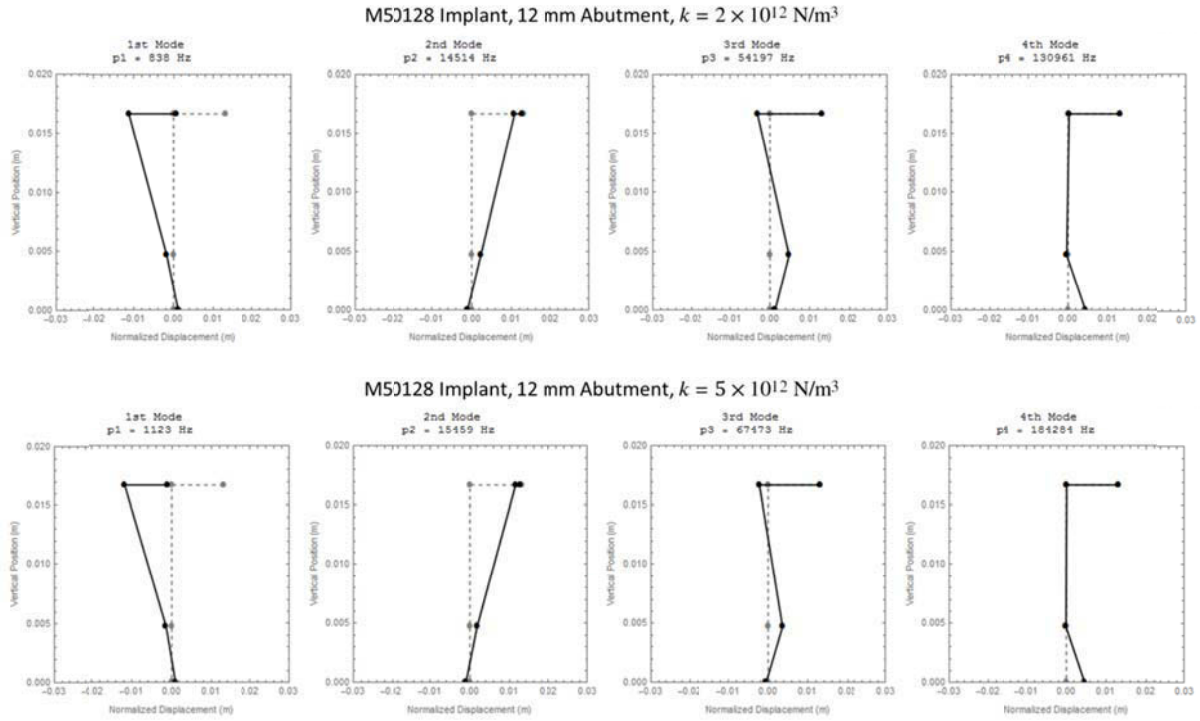


**Figure B.3: Mode shapes for long/narrow implant (M50128) with 12 mm abutment. Top:  $k = 2 \times 10^{12} \text{ N/m}^3$ ; Bottom:  $k = 5 \times 10^{12} \text{ N/m}^3$**

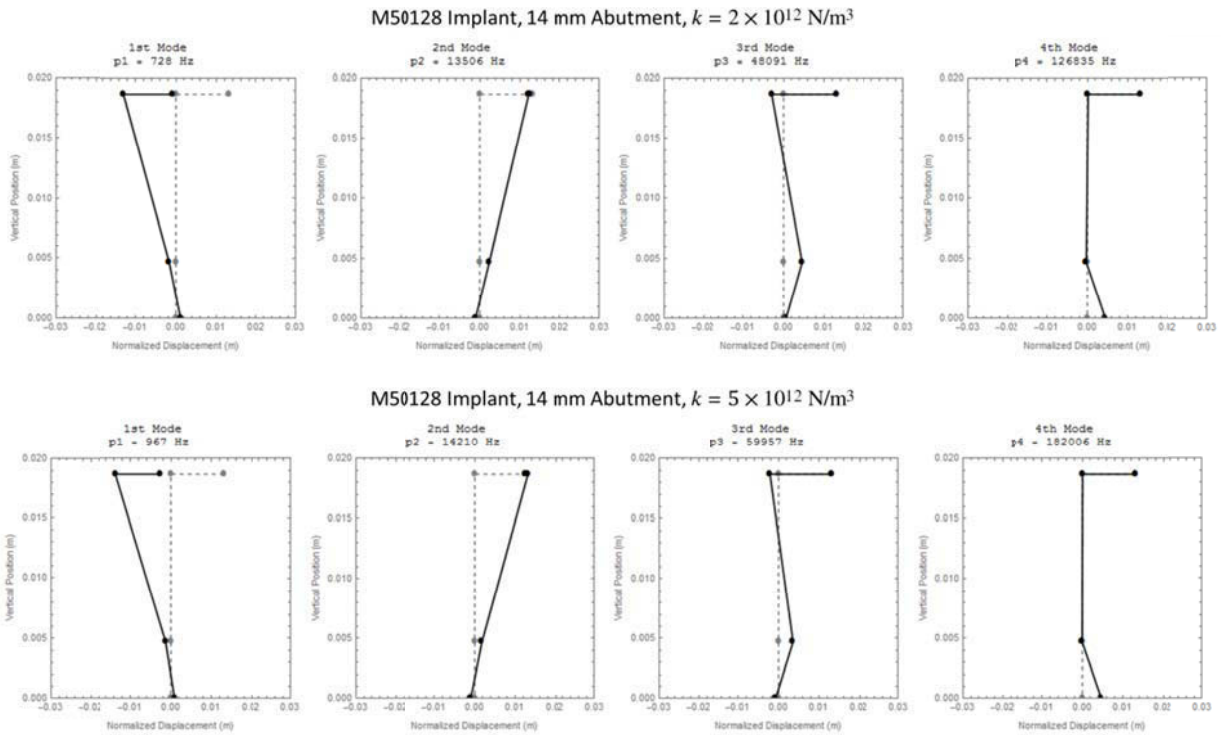


**Figure B.4: Mode shapes for long/narrow implant (M50128) with 14 mm abutment. Top:  $k = 2 \times 10^{12} \text{ N/m}^3$ ; Bottom:  $k = 5 \times 10^{12} \text{ N/m}^3$**

The four natural frequencies of the system were calculated for each implant-abutment combination at the two levels of interface stiffness. The first mode frequency ranged from 530 Hz – 1915 Hz for the systems analyzed. On average, the second mode frequency is 16 times larger than the first mode (range: 12 – 25 times), the third mode frequency is 69 times larger than the first mode (range: 53 – 90 times), and the fourth mode frequency is 165 times larger than the first mode (range: 96 – 262). In general, the ratio of a higher mode frequency to the first mode frequency for a given implant interface condition increases with increasing abutment length.

As expected, when increasing from a softer interface ( $k = 2 \times 10^{12} \text{ N/m}^3$ ) to a stiffer interface ( $k = 5 \times 10^{12} \text{ N/m}^3$ ), all of the natural frequencies increase. For the given change in interface stiffness (150% increase), the average increase in first mode frequency is 42% for the shorter 3 mm implants (range: 39 – 44%) and 32% for the longer 4 mm implants (range: 29 – 35%).

For each implant interface condition, the natural frequencies decrease as the abutment length is increased, as expected. It can be seen from Figure B.5, that there is an approximately quadratic relationship between the first mode frequency and the abutment length ( $p_1$  decreases as a function of  $L_A^2$ ). The  $R^2$  correlation values are essentially equal to 1.0 in each case and are displayed on the chart with the polynomial equations.

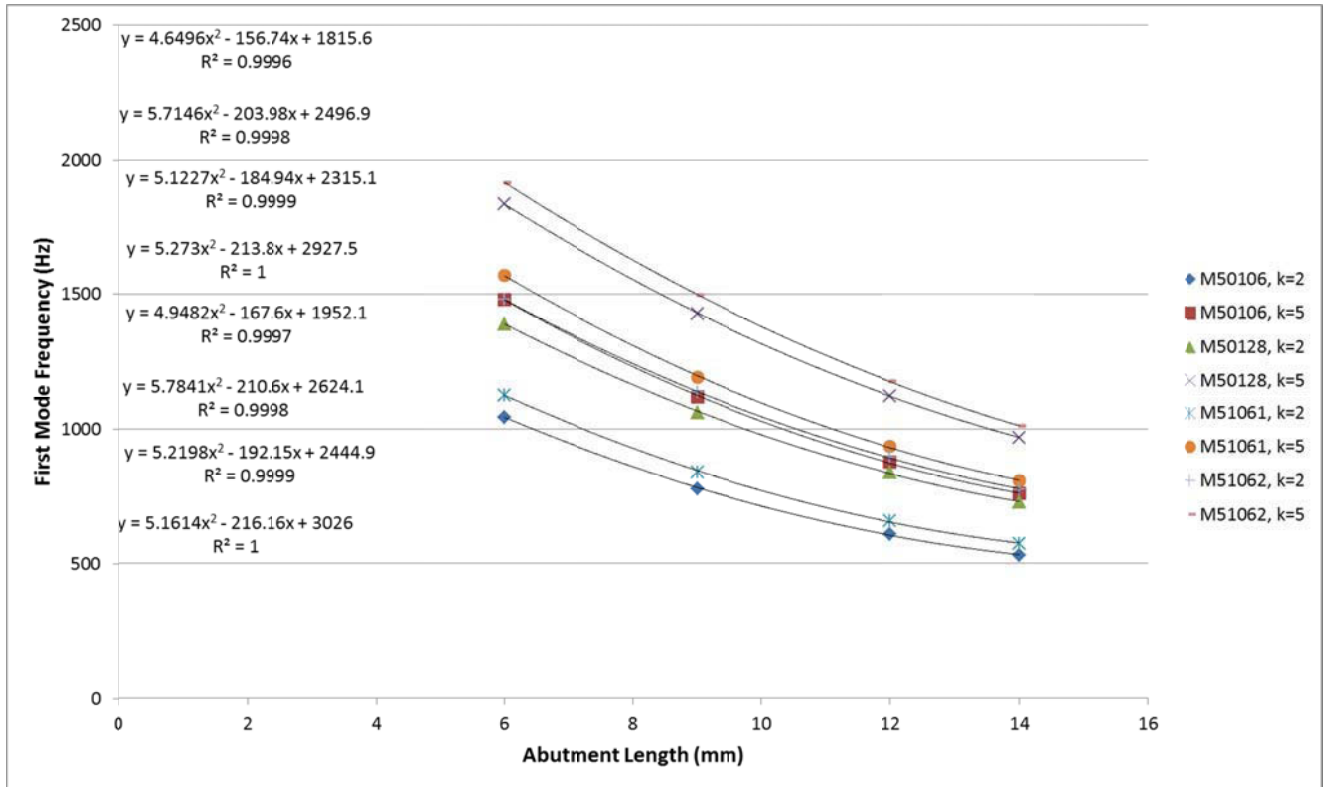


Figure B.5: Relationship between first mode frequency ( $p_1$ ) and abutment length for different Oticon implant sizes at two interfaces stiffness level ( $k = 2 \times 10^{12} \text{ N/m}^3$  and  $k = 5 \times 10^{12} \text{ N/m}^3$ ). Quadratic curve fits are shown with  $R^2$  values for each case.

## B.2 Analytical Model Frequency Response versus Stiffness Parameters

The important stiffness parameters in the analytical model are the impact stiffness ( $K_I$ ) and the torsional stiffness ( $K_T$ ) while the primary variables of interest are the interface stiffness ( $k$ ) and the related ASC value. Using the analytical model, the relationship between the stiffness parameters and the first and second mode frequency components is examined following a similar procedure to the work of Swain (2006). The first and second mode frequencies are readily visible in the measured acceleration response, while the higher (third and fourth) modes are not visible. Thus the analysis here will only focus on the visible first and second modes as these are the modes that can affect the fit between the model prediction of the acceleration and the measured acceleration response. This analysis can provide an understanding of the effect of the internal

stiffness parameters on the theoretical acceleration response, which will aid in interpreting the measured acceleration signals. Additionally, this analysis will provide an understanding of the sensitivity of the ASIST measure to errors in the estimated parameters such as  $K_I$  and  $K_T$ .

The relationship between the first mode frequency  $p_1$ , the second mode frequency  $p_2$ , the ratio  $p_2/p_1$  and the interface stiffness  $k$  can be seen in Figure B.6 for each type of Oticon Medical implant. Each subfigure shows the relationship for each abutment length (6 mm, 9 mm, 12 mm, 14 mm). It can be seen that the first mode frequency varies sharply with changing interface stiffness for the low stiffness values and starts to plateau for larger stiffness values.

As expected, the interface stiffness is sensitive to changes in the first mode frequency. In the higher stiffness range, where the curves become flatter, small errors in the frequency measurement can result in large changes in the calculated interface stiffness. These errors should not be clinically important because implants in the high stiffness range would be considered stable. In the lower frequency range, smaller changes in stiffness would result in considerable changes in the first mode frequency and would thus be detected by the ASIST measurement.

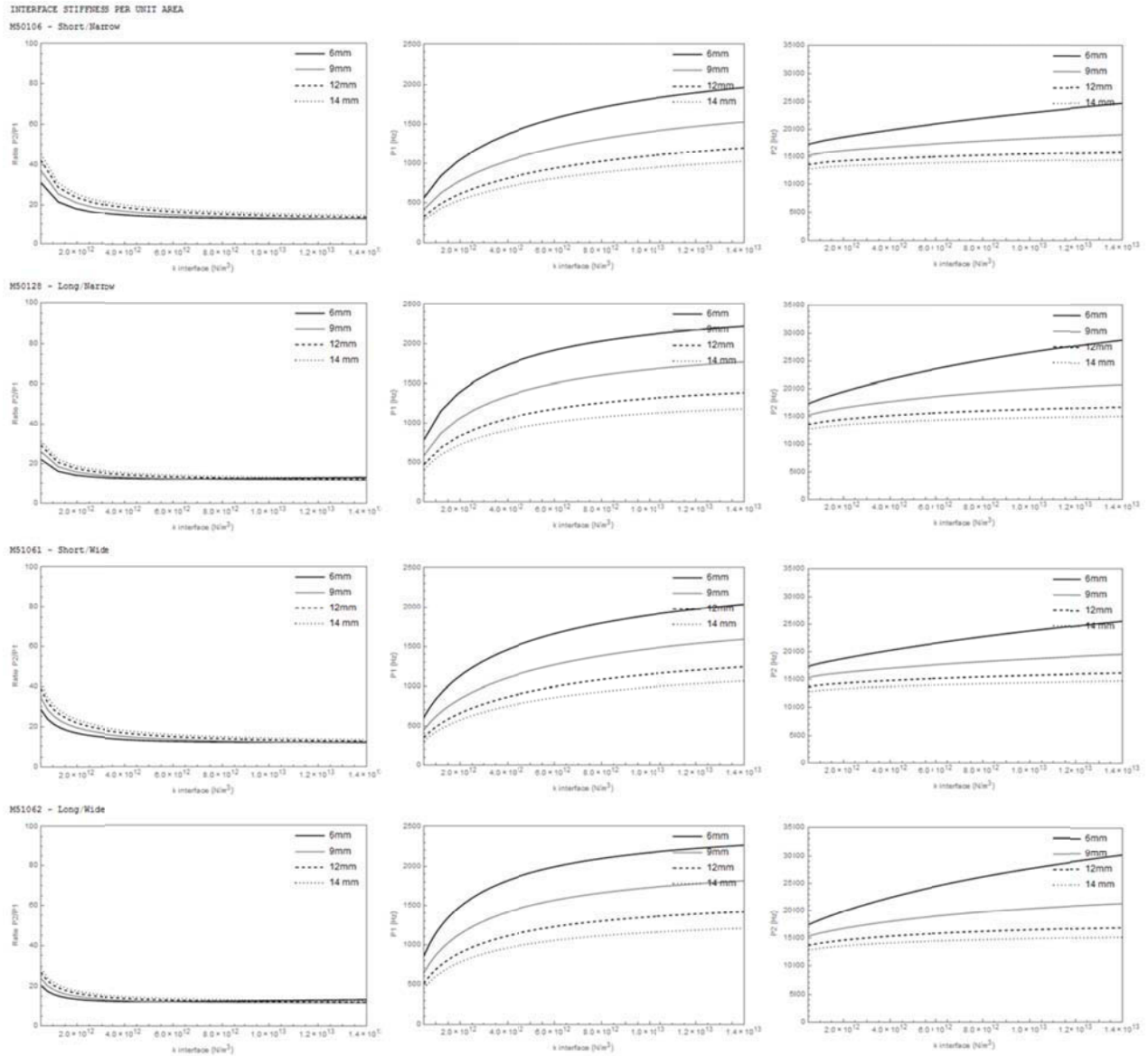


**Figure B.6: Relationship between the ratio  $p_2/p_1$ ,  $p_1$ , and  $p_2$  and the interface stiffness per unit area  $k$  for each type of Oticon Medical implant. The different curves on each plot show the relationship for each abutment length.**

Consider for example a long/narrow implant (M50128) with a 9 mm abutment with an interface stiffness (per unit area) in the lower range of  $2 \times 10^{12}$  N/m<sup>3</sup> and a corresponding first mode frequency of 1062 Hz. A unit increase in interface stiffness ( $k = 3 \times 10^{12}$  N/m<sup>3</sup>) results in a first mode frequency of 1225 Hz, which is an increase of 163 Hz or a 15% increase. Consider the same implant-abutment combination with an interface stiffness in the higher range of  $10 \times 10^{12}$  N/m<sup>3</sup> and a corresponding first mode frequency of 1672 Hz. In this case, a unit increase in

interface stiffness ( $k = 11 \times 10^{12} \text{ N/m}^3$ ) results in a first mode frequency of 1701 Hz, which is an increase of 29 Hz or a 2% increase. Alternatively, we can consider a doubling of the interface stiffness. For the lower stiffness range, doubling the interface stiffness from  $2 \times 10^{12} \text{ N/m}^3$  to  $4 \times 10^{12} \text{ N/m}^3$  results in an increase in the first mode frequency of 279 Hz (26% increase). While for the higher stiffness range, doubling the interface stiffness from  $10 \times 10^{12} \text{ N/m}^3$  to  $20 \times 10^{12} \text{ N/m}^3$  results in an increase in the first mode frequency of 179 Hz (11% increase). This further illustrates that the frequency response is most sensitive to interface stiffness at low stiffness values.

The second mode frequency is also shown to increase with the increasing interface stiffness; however, less of a plateau effect is present compared to the first mode frequency. In general, the second mode frequency is less sensitive to changes in the interface stiffness than the first mode frequency. It can also be noted that the second mode frequency is much less sensitive to changes in the interface stiffness for the longer abutments compared to the shorter abutments. For example, consider the long/narrow implant (M50128) with the 6 mm abutment compared to the 14 mm abutment. With the 6 mm abutment, a unit change in interface stiffness from  $2 \times 10^{12} \text{ N/m}^3$  to  $3 \times 10^{12} \text{ N/m}^3$  results in an increase in the second mode frequency of 1169 Hz (6% increase). The same change in interface stiffness with the 14 mm abutment results in an increase in the second mode frequency of 289 Hz (2.1% increase).

The same relationships are presented in Figure B.7 using the ASC measure. Consider again the long/narrow implant (M50128) with a 9 mm abutment in the lower stiffness range (ASC of 23 corresponding to an interface stiffness of  $3.07 \times 10^{12} \text{ N/m}^3$ ). A unit change in ASC from 23 to 24 results in an increase in first mode frequency of 17 Hz (from 1234 – 1251 Hz) or an increase of 1.4%. A doubling of ASC from 15 to 30 results in an increase in first mode frequency of 340 Hz (24% increase). In the high stiffness range (ASC of 75 corresponding to an interface stiffness of  $10 \times 10^{12} \text{ N/m}^3$ ), a unit change in ASC from 75 to 76 results in an increase in first mode frequency of 4 Hz (0.2% increase).

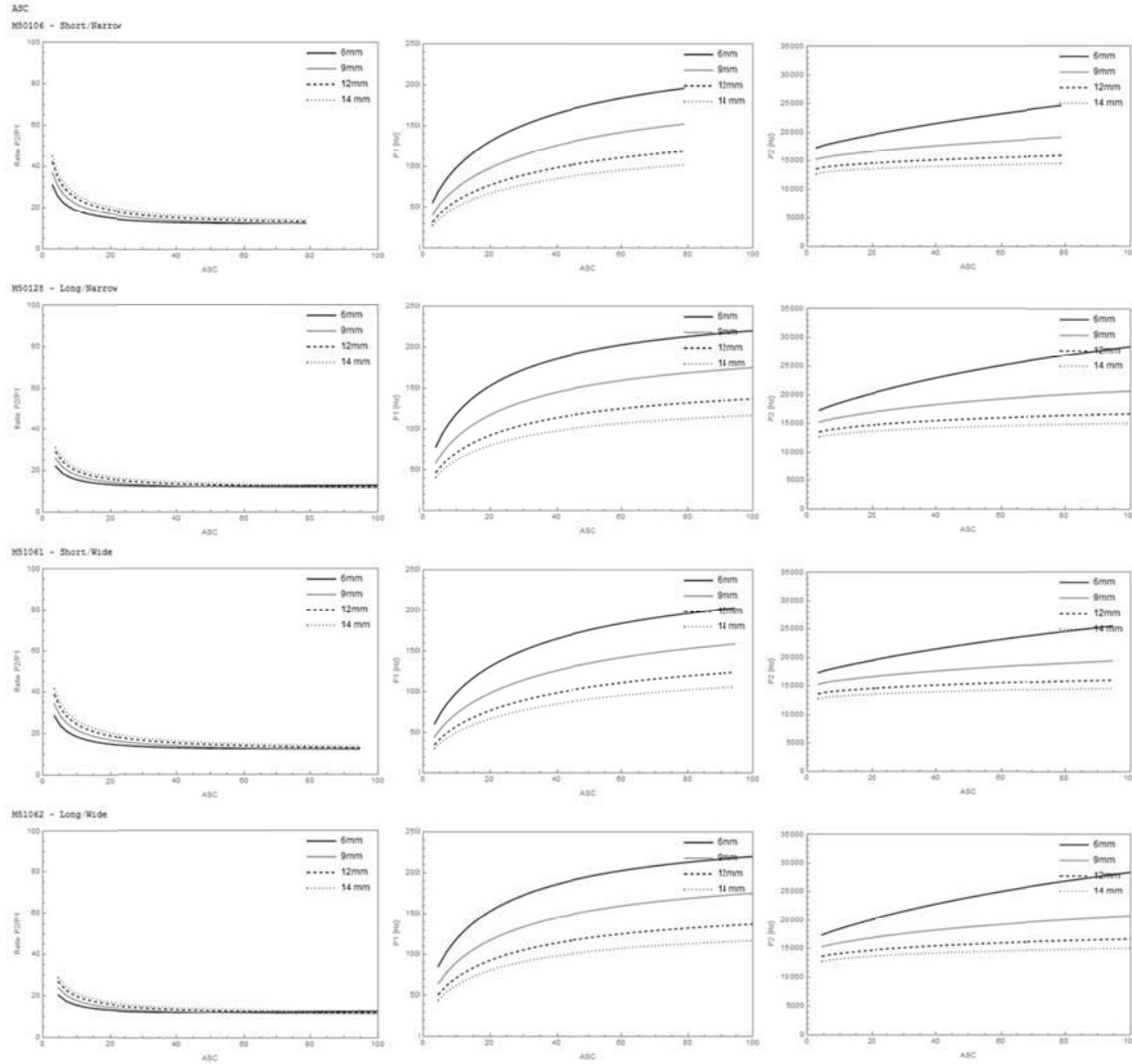


**Figure B.7: Relationship between the ratio  $p_2/p_1$ ,  $p_1$ , and  $p_2$  and the ASC value for each type of Oticon Medical implant. The different curves on each plot show the relationship for each abutment length.**

The relationship between the frequency components and the impact stiffness  $K_I$  is shown in Figure B.8 for the different Oticon Medical implant types and abutment sizes. The first mode frequency is relatively insensitive to changes in the impact stiffness, particularly for the longer abutments. For example, consider a long/narrow implant (M50128) with a 6 mm abutment. A unit change in impact stiffness from  $K_I = 2.9 \times 10^6$  N/m to  $3.9 \times 10^6$  N/m results in an increase in first mode frequency of 110 Hz (from 1835 – 1945 Hz) or a 6% increase. The same change in impact stiffness for a 14 mm abutment results in an increase in first mode frequency of only 15

Hz (from 967 – 982 Hz) or a 1.5% increase. The second mode frequency is more sensitive to changes in the impact stiffness and varies with an approximately linear relationship that is similar across abutment sizes. For the same changes in  $K_I$ , the second mode frequency showed an increase of 2112 Hz (9%) for the 6 mm abutment and 1970 Hz (14%) for the 14 mm abutment.

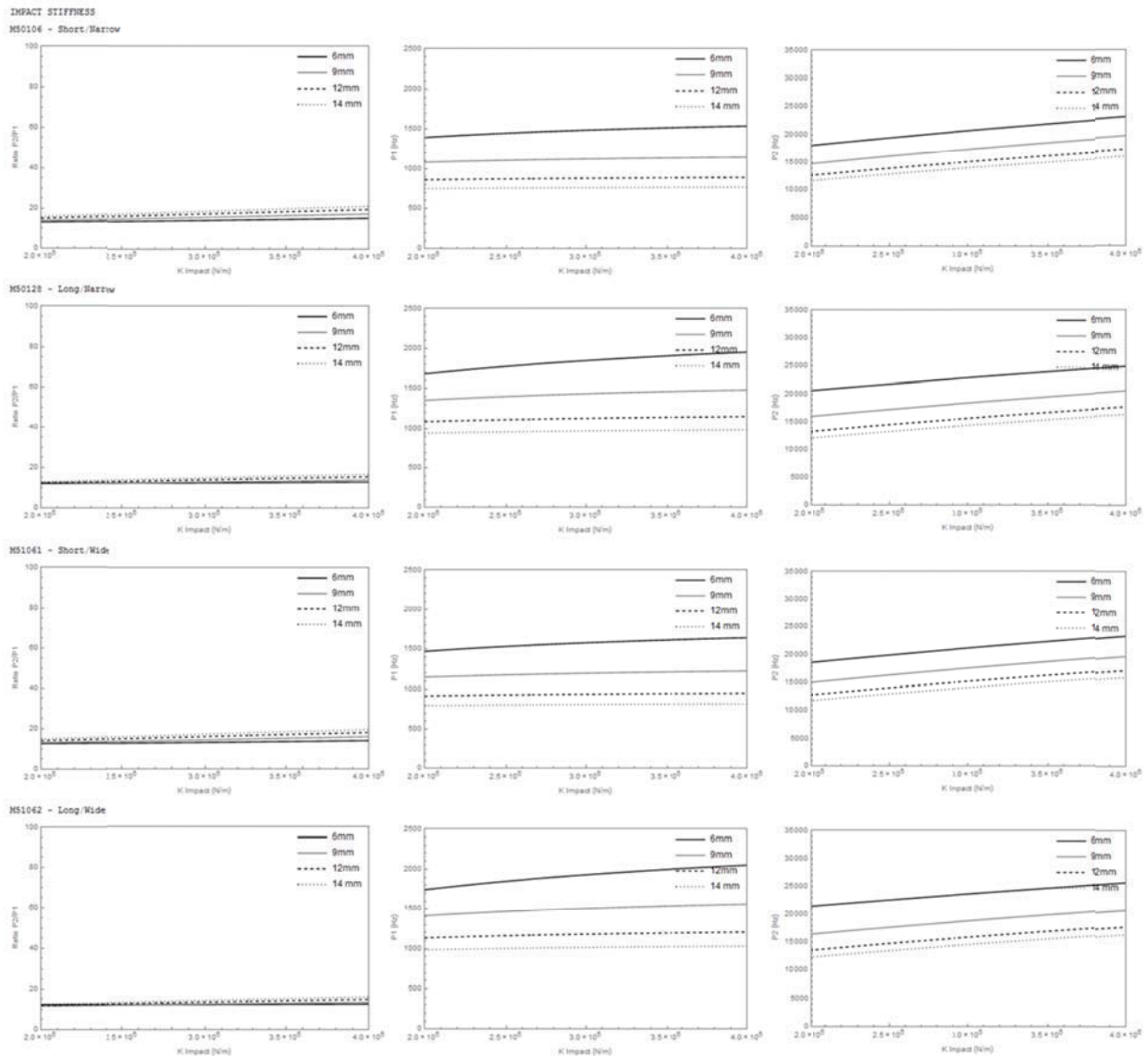


Figure B.8: Relationship between the ratio  $p_2/p_1$ ,  $p_1$ , and  $p_2$  and the impact stiffness  $K_I$  for each type of Oticon Medical implant. The different curves on each plot show the relationship for each abutment length.

The relationship between the frequency components and the torsional connection stiffness  $K_T$  is shown in Figure B.9 for the different Oticon Medical implant types and abutment sizes. The first mode frequency is sensitive to changes in the torsional stiffness parameter only in the low stiffness range. Beyond a threshold, both the first and second modes are virtually insensitive to changes in  $K_T$ . In such a situation, the implant/abutment is essentially responding as a rigid body. The sensitivity in the lower  $K_T$  range, suggests that the ASIST measure may be able to detect changes in the implant-abutment connection such as loosening of the abutment screw.

Consider a long/narrow implant (M50128) with a 9 mm abutment. For this implant-abutment combination, a 100 unit increase in the torsional stiffness from 300 to 400 Nm results in an increase in the first mode frequency of 39 Hz (3% increase) and an increase in the second mode frequency of 66 Hz (0.4% increase). In the lower torsional stiffness range, an increase in  $K_T$  from 100 – 200 Nm results in an increase in the first mode frequency of 159 Hz (13%) and an increase in the second mode frequency of 244 Hz (1.4%). In the higher torsional stiffness range approximately corresponding to a torsional stiffness coefficient of 0.5, and increase in  $K_T$  from 600 – 700 Nm results in an increase in the first mode frequency of 13 Hz (0.8%) and an increase in the second mode frequency of 23 Hz (0.1%). In each case the second mode frequency is proportionally less sensitive to changes in  $K_T$  than the first mode frequency.

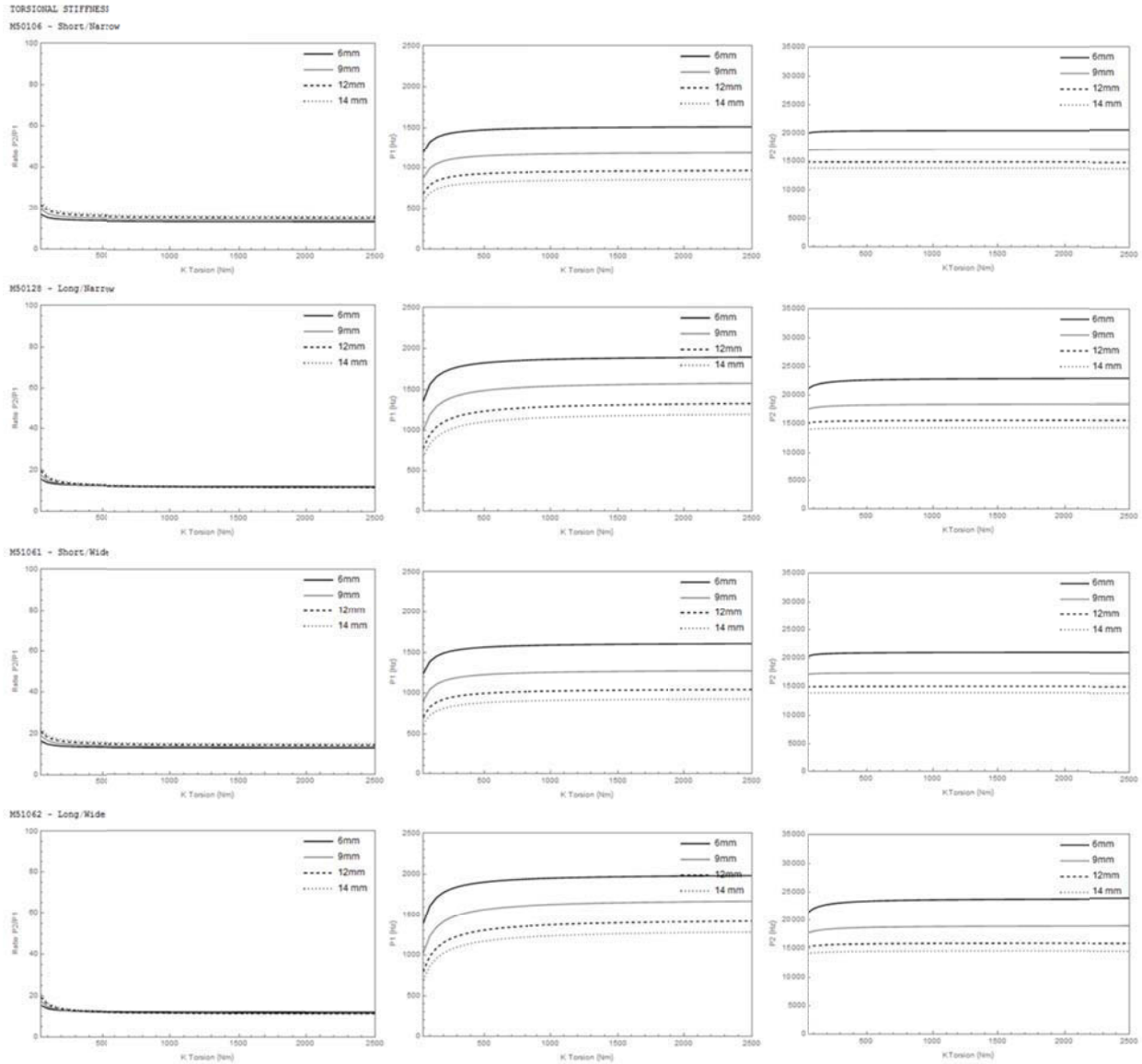


Figure B.9: Relationship between the ratio  $p_2/p_1$ ,  $p_1$ , and  $p_2$  and the torsional stiffness  $K_T$  for each type of Oticon Medical implant. The different curves on each plot show the relationship for each abutment length.

### B.3 Model Solution (ASC and Fit with Measured Data) with Stiffness Parameters $K_I$ and $K_T$

In the analytical model, we have made assumptions for the internal stiffness parameters, namely the impact stiffness ( $K_I$ ) and the torsional stiffness ( $K_T$ ). In this section, we will evaluate the sensitivity of the model solution to errors in these parameters. As  $K_I$  or  $K_T$  are varied, the

calculated interface stiffness and associated ASC value are determined along with the resulting  $R^2$  fit between the model predicted signal and the measured acceleration. For each analysis, a sample dataset is used in order to calculate the ASC and  $R^2$  values.

For a given set of data, the impact stiffness was varied from  $2 \times 10^6$  N/m to  $4 \times 10^6$  N/m. For each impact stiffness, the model was used to estimate the ASC value that resulted in a best fit match to the measured data and the associated  $R^2$  value. Similarly, the torsional stiffness coefficient was varied from 0.05 to 0.5 for a given set of data and the model was used to determine the ASC value and  $R^2$  fit at each variation.

Consider for example the long/narrow implant (M50128) with a 9 mm abutment. Figure B.10 shows the variation in ASC and  $R^2$  value with changing  $K_I$ . The two plots are overlaid with the scale for the ASC value (blue line) on the left of the figure and the scale for the  $R^2$  value (black line) on the right of the figure.

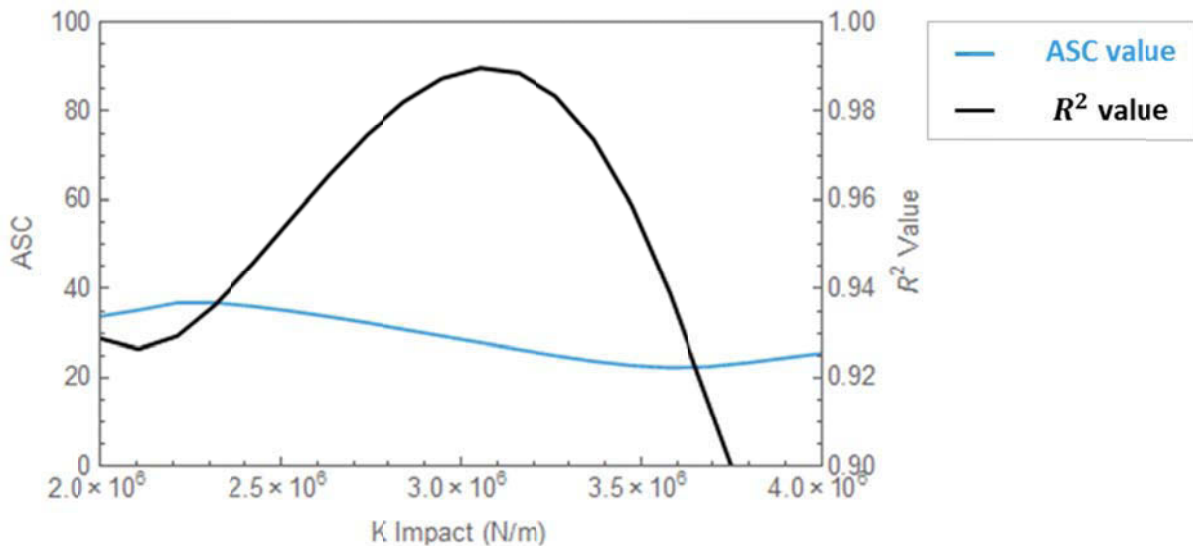


**Figure B.10: Variation in ASC value (blue line) and  $R^2$  fit (black line) with changes in impact stiffness ( $K_I$ ) for a long/narrow implant and 9 mm abutment**

As shown in the figure, there is some variation in the ASC value over the range of tested  $K_I$  and a clear peak in the fit between the measured signal and the model prediction as measured by the

$R^2$  value. Over the full range, the ASC values range from 22 – 37, with the ASC value corresponding to the best fit with the data of 27.9 at an impact stiffness of  $3.05 \times 10^6$  N/m. If we consider the region close to the best fit (i.e.  $R^2$  values above 0.98), the impact stiffness values vary from  $2.84 \times 10^6$  -  $3.26 \times 10^6$  N/m and the calculated ASC values vary from 25 – 31, which is a difference of 6 ASC values or 21% of the “best-fit” value. Figure B.11 show the variation in the shape of the signals as  $K_I$  is varied. The measured data is shown in the colored lines (the same for all subfigures) and the model predicted signal is shown in black. The subfigure that is highlighted with a red outline corresponds to the best match between the measured signal and the model response ( $K_I = 3.05 \times 10^6$  N/m, ASC = 27.9 for this sample dataset). It is clear from the figures that variations in the impact stiffness affect the second mode frequency of the model response, which can result in a poor fit between the measured data and model signal.

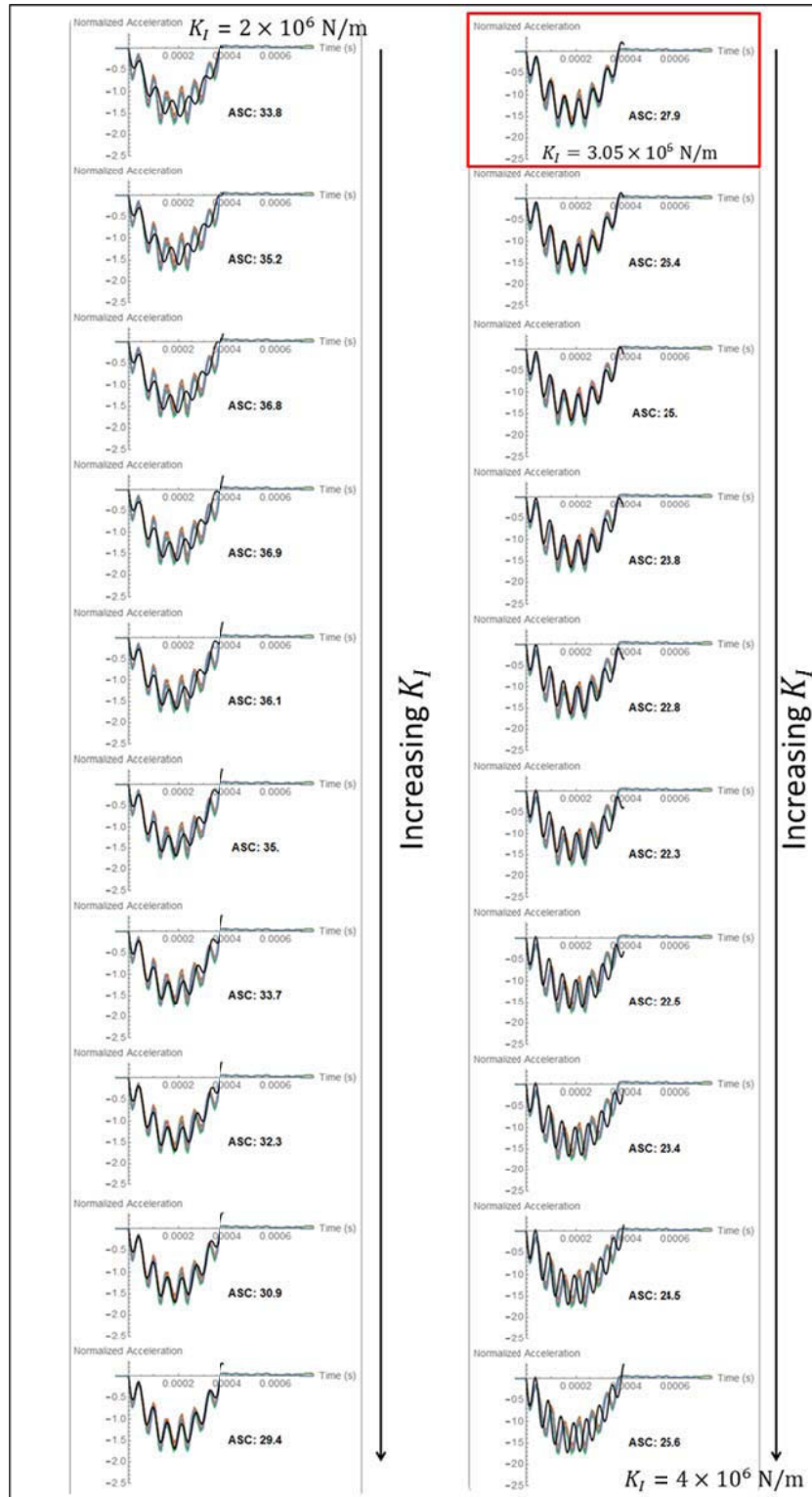


Figure B.11: Variation in the model fit (black line) with the measured acceleration (colored lines) with changing impact stiffness ( $K_I$ ) for an example dataset with a long/narrow implant and 9 mm abutment. The best match between the model and the measured data as measured by the  $R^2$  value is highlighted in red.

For the same sample dataset of a long/narrow implant (M50128) with a 9 mm abutment, the variation in ASC and  $R^2$  with changing torsional stiffness  $K_T$  are shown in Figure B.12. It can be seen that beyond a threshold of approximately 150 Nm, which corresponds to a torsional stiffness coefficient of 0.13 for a 9 mm abutment, there is only minor variation in both the ASC value and the  $R^2$  fit between the measured data and model prediction and the ASC value determined does not vary substantially. Unlike the impact stiffness curve shown previously, there is no clear peak in the  $R^2$  value curve with a steep drop on either side. In this case there is a steep drop at lower values of  $K_T$  but a very gradual decrease at higher values of  $K_T$ . At higher values of  $K_T$  the implant-abutment is essentially acting as a single rigid body.

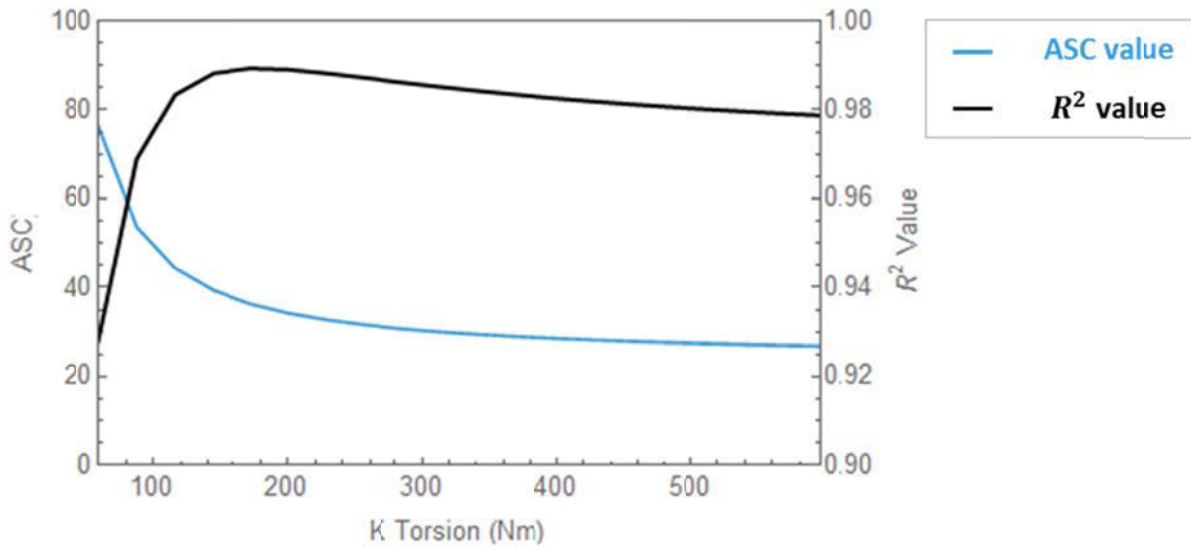


Figure B.12: Variation in ASC value (blue line) and  $R^2$  fit (black line) with changes in torsional stiffness ( $K_T$ ) for a long/narrow implant and 9 mm abutment

The variation in the shape of the signals as  $K_T$  is varied is shown in Figure B.13. The measured data is shown in the colored lines (the same for all subfigures) and the model predicted signal is shown in black. Most of the subfigures show a very good match between the measured data and the model response, with the exception of the two lowest  $K_T$  values as discussed above. As  $K_T$  is increased, the variation in the model response is primarily evident as an upward shift in the last cycle of the second mode frequency.

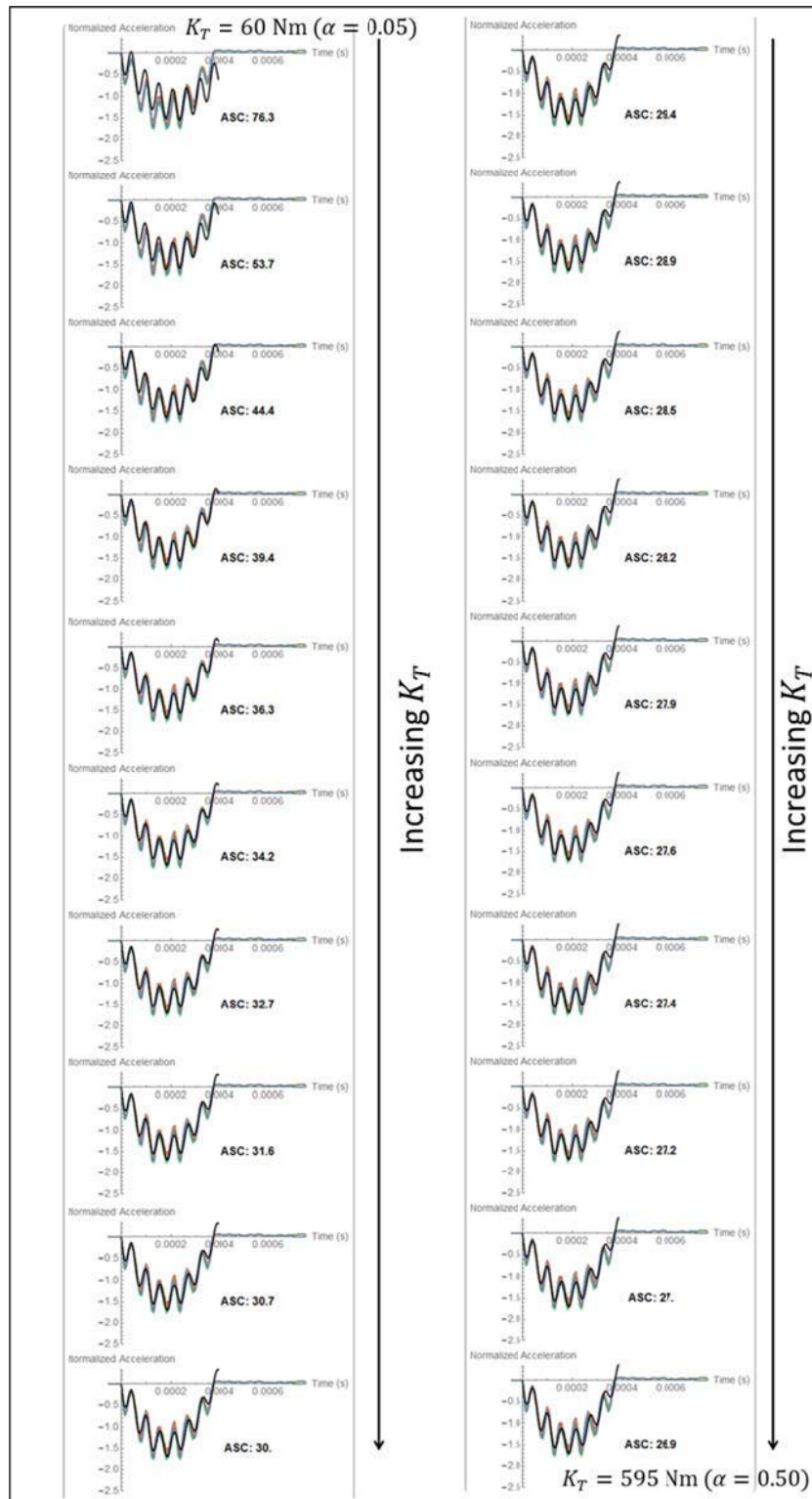
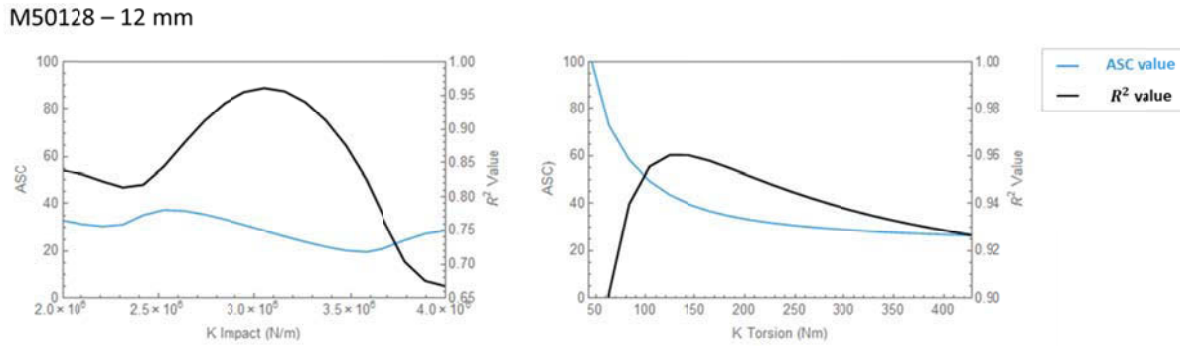


Figure B.13: Variation in the model fit (black line) with the measured acceleration (colored lines) with changing torsional stiffness ( $K_T$ ) for an example dataset with a long/narrow implant and 9 mm abutment

Similar patterns for the impact stiffness and torsional stiffness variation were observed for other implants with both the 9 mm and 12 mm abutments. For example, the results for the long/narrow implant (M50128) with the 12 mm abutment are shown in Figure B.14.



**Figure B.14: Variation in ASC value (blue line) and  $R^2$  fit (black line) with changes in impact stiffness (left) and torsional stiffness (right) for a long/narrow implant and 12 mm abutment**

For the shorter 6 mm abutment with the FRB-20 systems, the variation in the ASC value and the  $R^2$  fit is much smaller than the longer abutment cases. For the frequency range of stiffer implant systems (FRB-20) and 6 mm abutment, second mode frequency has a smaller contribution to the acceleration response. The correlation fit between the measured data and the model acceleration is significantly affected by the fit of the second mode. From the matching procedure, the first mode frequency (or contact time) should match relatively well between the measured and modeled response. This is because there is only half of one cycle of the first mode with a large amplitude compared to the second mode. Intuitively, in order to minimize the difference between the measured signal and the model response, the first mode of the response would have to line up relatively well. Thus, a relatively “poor fit” between the measured signal and the model response tends to appear as a mismatch in the second mode frequency. Since the second mode has less of a contribution in the higher frequency systems, there is much less variation in the correlation coefficient  $R^2$  despite actual changes in the second mode frequency. The results for the long/narrow implant (M50128) and the 6 mm abutment are shown in Figure B.15. It is clear that there is very little variation in the  $R^2$  value.

M50128 – 6 mm

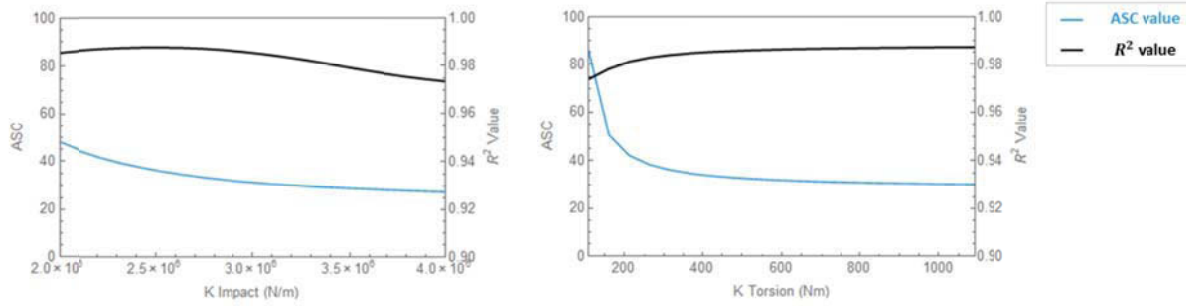
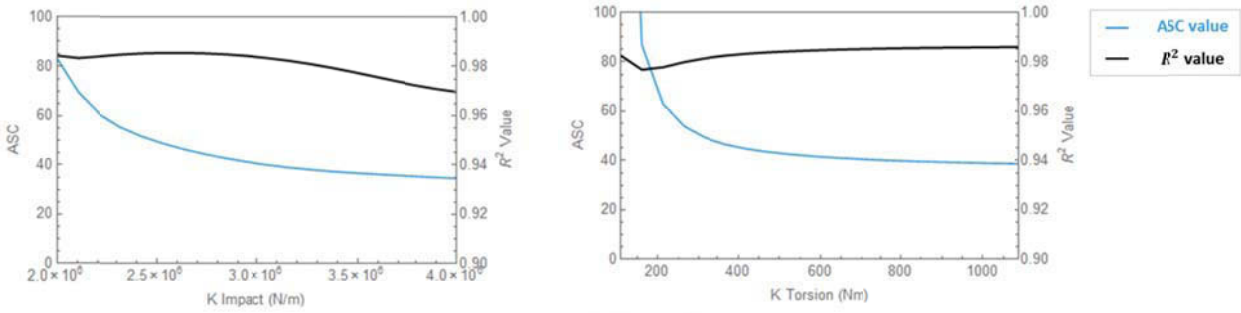


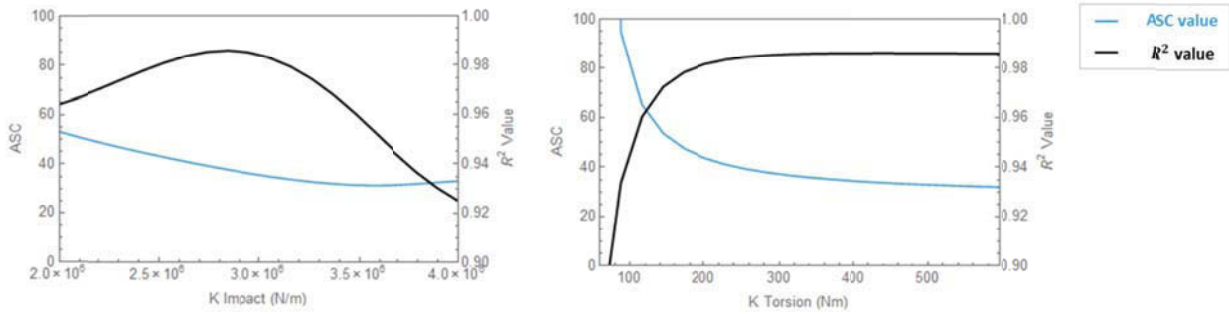
**Figure B.15: Variation in ASC value (blue line) and  $R^2$  fit (black line) with changes in impact stiffness (left) and torsional stiffness (right) for a long/narrow implant and 6 mm abutment**

Similar patterns were found for the other implant-abutment combinations. For example, the results for the long/wide implant (M51062) with each of the four abutment sizes are shown in Figure B.16.

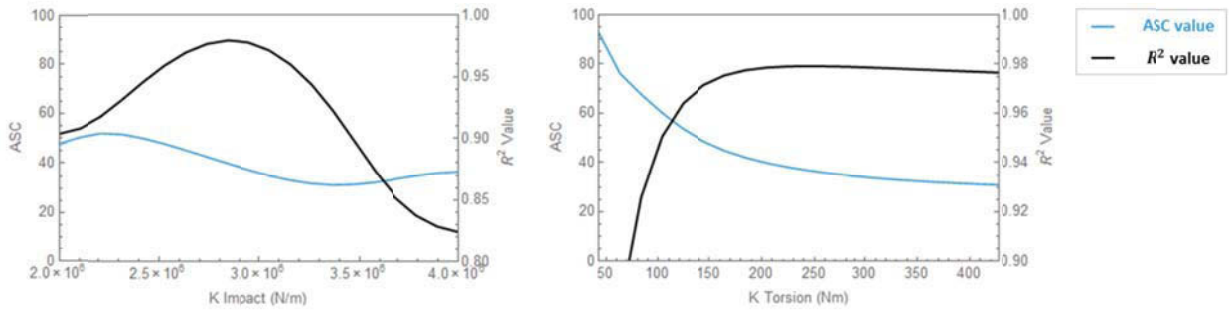
M51062 – 6 mm



M51062 – 9 mm



M51062 – 12 mm



M51062 – 14 mm

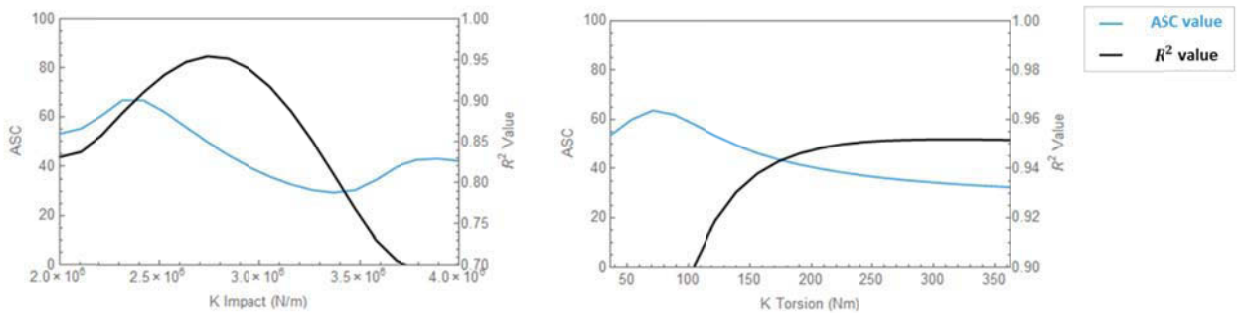


Figure B.16: Variation in ASC value (blue line) and  $R^2$  fit (black line) with changes in impact stiffness (left) and torsional stiffness (right) for a long/wide implant with various abutment sizes

## B.4 Analytical Model Frequency Response versus Geometric and Inertial Parameters

The important geometric and inertial parameters for the implants in the analytical model are the mass ( $m_I$ ), the length of the threaded portion ( $l_i$ ), the diameter ( $d_i = 2R_0$ ), the location of the center of mass ( $\bar{y}_I$ ), and the mass moment of inertia ( $J_I$ ). Similarly, the important geometric parameters for the abutments in the analytical model are the mass ( $m_A$ ), the length ( $L_A$ ), the location of the center of mass ( $\bar{y}_A$ ), and the mass moment of inertia ( $J_A$ ).  $l_i$ ,  $L_A$ ,  $m_I$ ,  $m_A$ , and  $d_i$  are straightforward to determine and are not subject to appreciable error.

Using the analytical model, the relationships between the geometric parameters and the first and second mode frequency components are examined following the same procedure as the stiffness parameters. This can provide an understanding of the effect of the various geometric parameters on the theoretical acceleration response. Additionally, this analysis will provide an understanding of the sensitivity of the ASIST measure to errors in the estimated parameters such as  $\bar{y}_I, \bar{y}_A, J_I$ , and  $J_A$ . For each parameter, the value was varied over the range of values used in the analytical model from 10% less than the lowest value to 10% greater than the highest value. All other values were kept fixed in the model. It should be noted that when the abutment mass was varied, the abutment mass moment of inertia was adjusted as a function of the mass based on the simplified geometric model shown in Figure 2.3. Similarly, when the abutment length was varied, the location of the abutment center of mass and the abutment moment of inertia were adjusted as a function of the length. An interface stiffness of  $k = 5 \times 10^{12}$  N/m<sup>3</sup> (corresponding to an ASC value of approximately 30 – 40) was used for all analyses.

The relationship between the first mode frequency  $p_1$ , the second mode frequency  $p_2$ , and the ratio  $p_2/p_1$ , and the implant geometric parameters can be seen in Figures B.17 – B.21 for the Oticon Medical implants. The different curves on each figure show the relationships for each abutment length (6 mm, 9 mm, 12 mm, 14 mm). The vertical gridlines in each of the figures show the actual sizes for the different Oticon Medical implants in the analytical model.

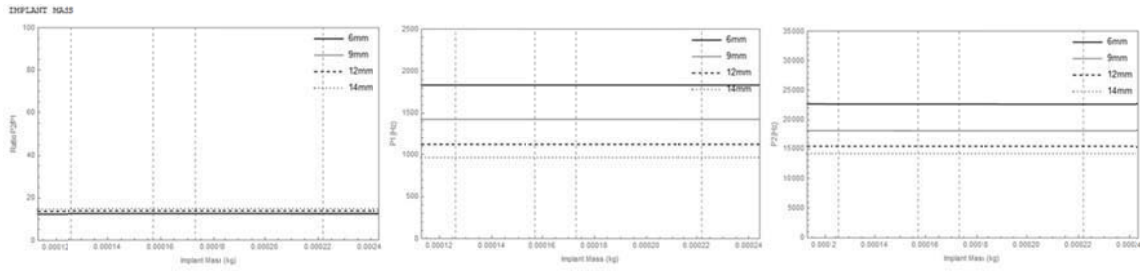


Figure B.17: Relationship between the first and second mode frequency components and the implant mass

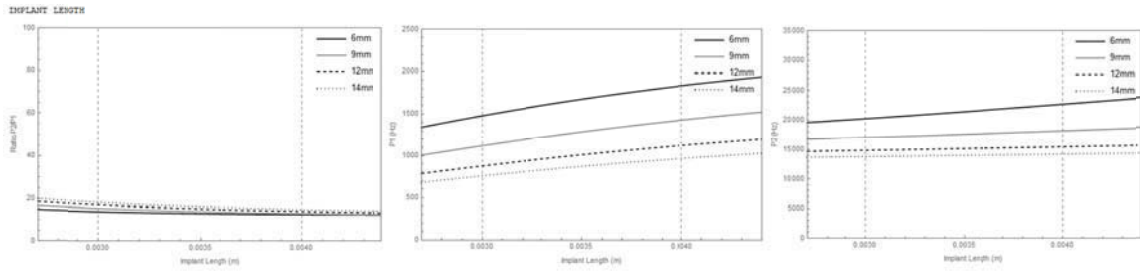


Figure B.18: Relationship between the first and second mode frequency components and the implant length

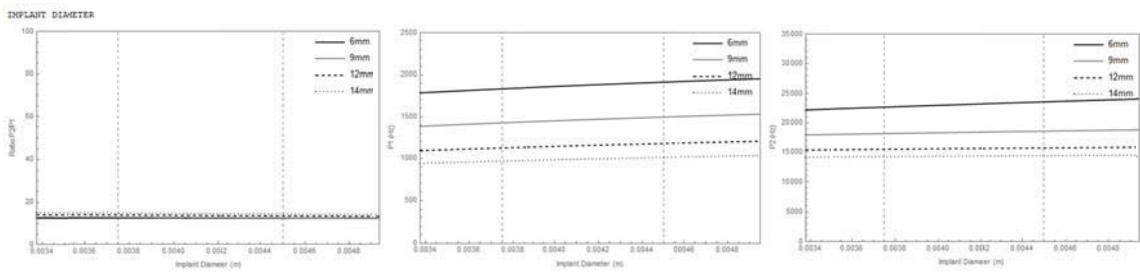


Figure B.19: Relationship between the first and second mode frequency components and the implant diameter

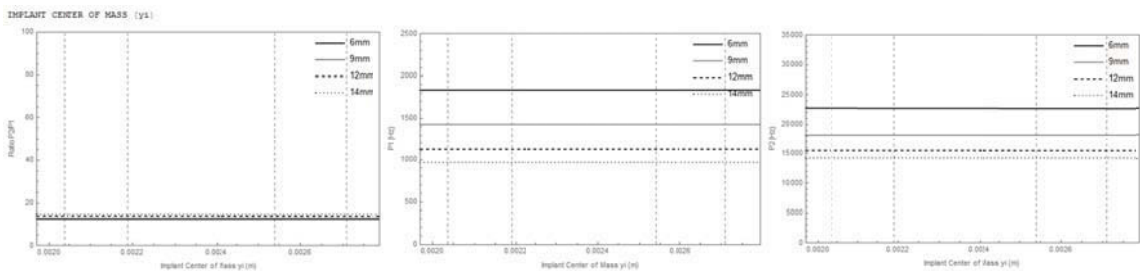
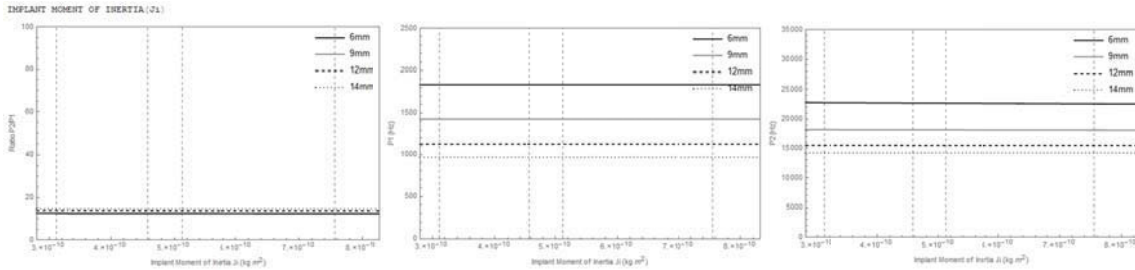


Figure B.20: Relationship between the first and second mode frequency components and the location of the implant center of mass



**Figure B.21: Relationship between the first and second mode frequency components and the implant mass moment of inertia**

Both the first and second mode frequency components of the model response were found to be virtually insensitive to changes in the implant mass, location of the center of mass, and mass moment of inertia. The center of mass and moment of inertia were estimated for the implants based on simplified geometry. Since the model is fairly insensitive to these parameters, errors in these estimates would not have a large impact on the overall model performance.

The model response is sensitive to changes in implant length and the relationship is nearly linear. The first mode frequency is relatively more sensitive than the second mode frequency. Consider for example an implant with a 9 mm abutment. A change in length from 3 mm to 4 mm (33% increase) results in a change in first mode frequency from 1120 – 1429 Hz, which is an increase of 309 Hz or a 28% increase. The same change in length results in an increase in second mode frequency from 17054 – 18193 Hz, which is an increase of 1139 Hz or a 7% increase. The model response was found to vary slightly with changing implant diameter and again the relationship is nearly linear. Consider again an implant with a 9 mm abutment. A change in diameter from 3.75 mm to 4.50 mm (20% increase) results in an increase of first mode frequency of 69 Hz (5% increase) and a change in second mode frequency of 417 Hz (2% increase).

The relationship between the ratio  $p_2/p_1$ , the first mode frequency  $p_1$ , and the second mode frequency  $p_2$  and the abutment geometric parameters can be seen in Figures B.22 – B.25 for the Oticon Medical implants. The different curves on each figure show the relationships for each implant type: M50106 (short/narrow), M50128 (long/narrow), M51061 (short/wide), M51062 (long/wide). The vertical gridlines in each of the figures show the actual sizes for the different Oticon Medical abutments in the analytical model.

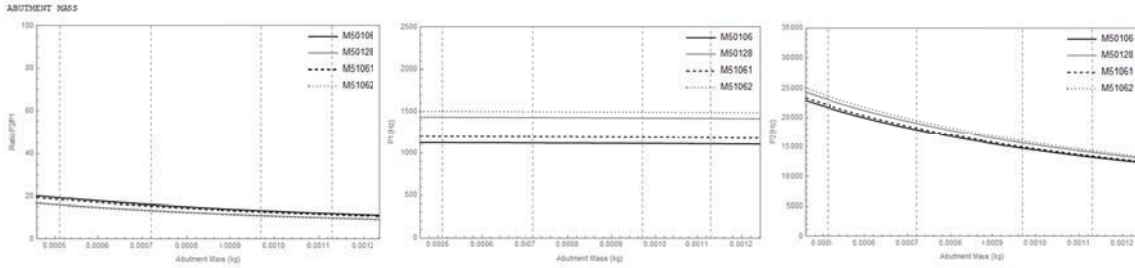


Figure B.22: Relationship between the first and second mode frequency components and the abutment mass

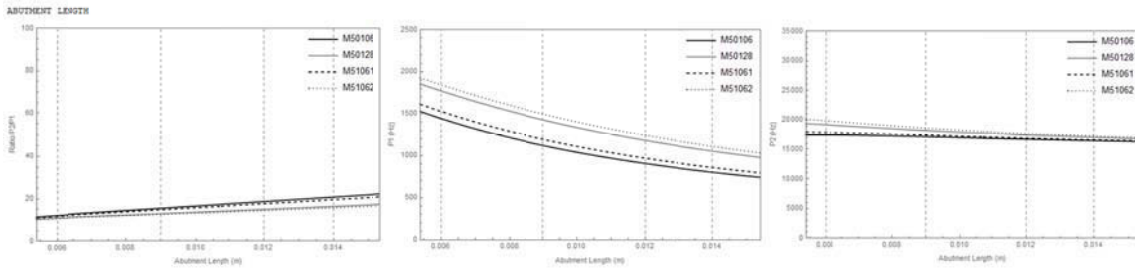


Figure B.23: Relationship between the first and second mode frequency components and the abutment length

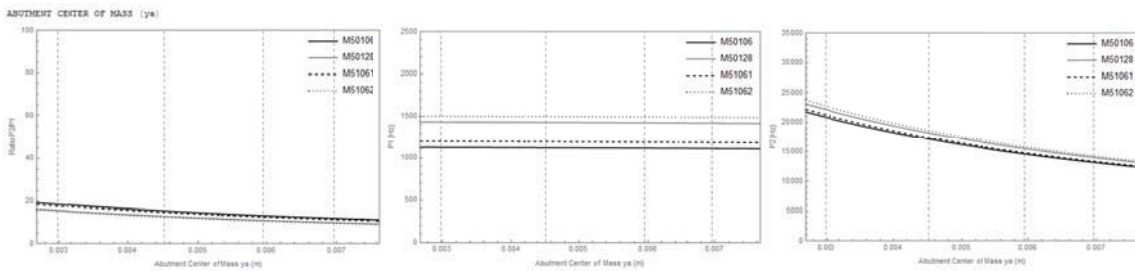


Figure B.24: Relationship between the first and second mode frequency components and the location of the abutment center of mass

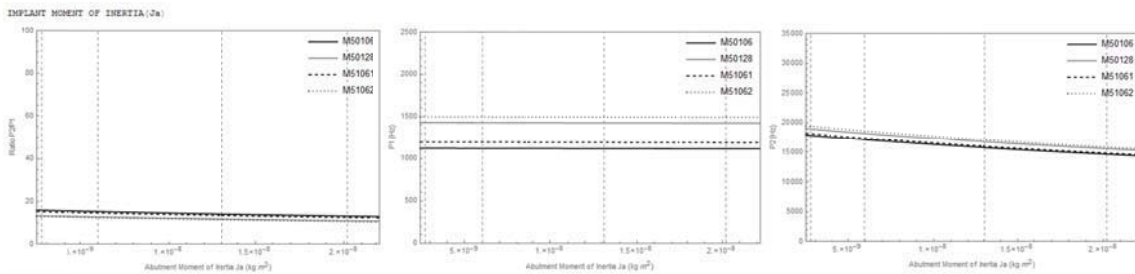


Figure B.25: Relationship between the first and second mode frequency components and the abutment mass moment of inertia

In general, the model response was found to be significantly more sensitive to the abutment geometric parameters compared to the implant parameters, particularly in the second mode frequency. The first mode frequency was found to be insensitive to changes in the abutment mass, while the second mode frequency decreases with increasing abutment mass showing a decreasing slope with increasing mass. Consider for example a long/narrow implant (M50128). Increasing the mass from 0.707g to 0.995g (approximately the change from a 9 mm to 12 mm abutment) which is a 41% increase in mass results in a decrease in first mode frequency of only 7 Hz (0.5% decrease). The same change in mass results in a decrease in second mode frequency of 3888 Hz (20% decrease). Similarly, the first mode frequency was found to be virtually insensitive to changes in the location of the center of mass and the moment of inertia, while the second mode frequency was more sensitive to these parameters. Consider again a long/narrow implant. An increase in the center of mass from 4.515 mm to 6.085 mm (approximately the change from a 9 mm to 12 mm abutment) results in a decrease in first mode frequency of 6 Hz (0.4% decrease). The same change in  $\bar{y}_A$  results in a decrease in second mode frequency of 2957 Hz (16% decrease). The model response was found to be only slightly sensitive to changes in the abutment moment of inertia. Again for the long/narrow implant, an increase in the mass moment of inertia from  $5.56 \times 10^{-9} \text{ kgm}^2$  to  $1.08 \times 10^{-8} \text{ kgm}^2$  (nearly double: 94% increase) results in a decrease in first mode frequency of 2 Hz (0.1% decrease) and a decrease in second mode frequency of 1090 Hz (6% decrease).

As expected, the first mode frequency was found to be sensitive to changes in the abutment length, while the second mode frequency was less sensitive. In both cases the frequency was found to decrease with increasing abutment length. For a long/narrow implant, an increase in abutment length from 9 mm to 12 mm (33% increase) results in a decrease in the first mode frequency of 249 Hz (18% decrease) and a decrease in the second mode frequency of 793 Hz (4% decrease). Other measurement methods such as the Periotest® and Osstell™ ISQ that rely on a correlation between the first mode frequency and the interface stiffness without consideration for the abutment length will produce different answers for the stability measurement for varying abutment lengths because of this sensitivity shown here. This is why it is important in the ASIST model to account for the abutment length in the analysis procedure.

## B.5 Model Solution (ASC and Fit with Measured Data) with Geometric Parameters $\bar{y}_A$ and $J_A$

In the analytical model, the location of the center of mass and mass moment of inertia of the implant and abutment were estimated based on assumed, simplified geometry. It was shown that the implant parameters including  $\bar{y}_I$  and  $J_I$  have very little effect on the model response, thus errors in these parameters should not have a large effect on the model performance. Conversely, the abutment parameters including  $\bar{y}_A$  and  $J_A$  were found to have more of an effect on the second mode frequency response of the analytical model (particularly  $\bar{y}_A$ ). In this section, we will evaluate the sensitivity of the model solution to errors in these abutment parameters. As  $\bar{y}_A$  or  $J_A$  are varied, the calculated interface stiffness and associated ASC value are determined along with the resulting  $R^2$  fit between the model predicted signal and the measured acceleration. For each analysis, a sample dataset is used in order to calculate the ASC and  $R^2$  values.

For a given set of data with a known implant and abutment, the location of the center of mass was varied  $\pm 30\%$  from the value used in the analytical model for the particular abutment in a total of 20 discrete steps. The model was used to determine the ASC value and  $R^2$  fit for each variation in  $\bar{y}_A$ . As before, an initial guess for the interface stiffness was chosen for the first analysis and each subsequent analysis used the previously calculated interface stiffness as the initial guess. Similarly, the mass moment of inertia was varied  $\pm 30\%$  from the value used in the analytical model for the particular abutment.

Consider for example the long/narrow implant (M50128) in FRB-20 with a 9 mm abutment. Figure B.26 shows the variation in ASC and  $R^2$  value with changing  $\bar{y}_A$ . The two plots are overlaid with the scale for the ASC value (blue line) on the left of the figure and the scale for the  $R^2$  value (black line) on the right of the figure.

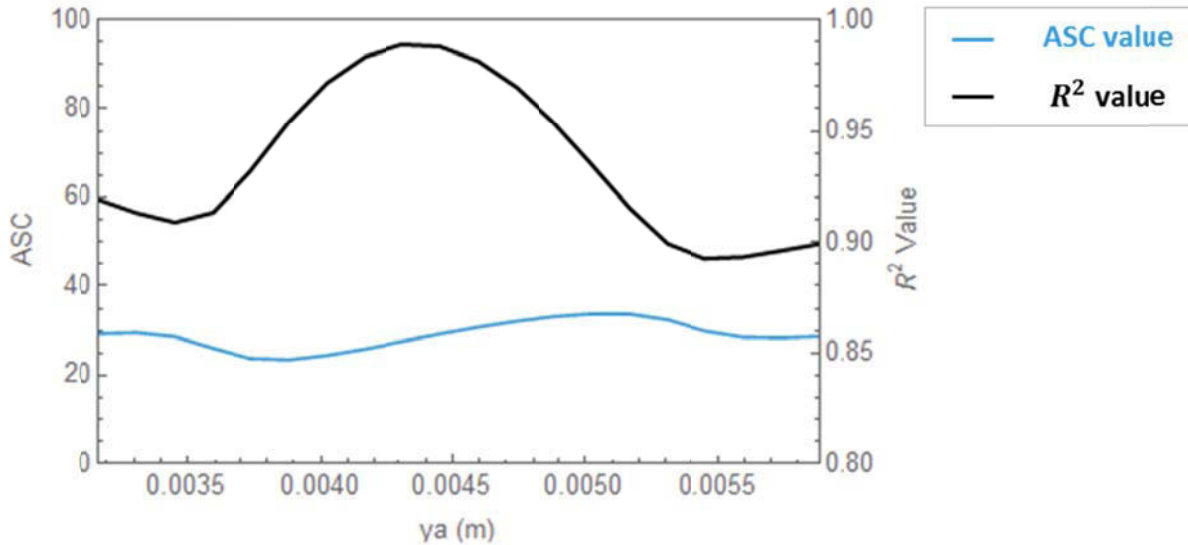


Figure B.26: Variation in ASC value (blue line) and  $R^2$  fit (black line) with changes in abutment center of mass ( $\bar{y}_A$ ) for a long/narrow implant and 9 mm abutment

As shown Figure B.26, there is some variation in the ASC value over the range of tested  $\bar{y}_A$  and a clear peak in the fit between the measured signal and the model prediction as measured by the  $R^2$  value. Over the full range, the ASC values range from 24 – 34, with the ASC value corresponding to the best fit with the data of 27.6 at a value of  $\bar{y}_A = 4.31$  mm. If we consider the region close to the best fit (i.e.  $R^2$  values above 0.98), the  $\bar{y}_A$  values vary from 4.166 – 4.594 mm and the calculated ASC values vary from 26 – 31, which is a difference of 5 ASC values or 18% of the “best-fit” value. Figure B.27 shows the variation in the shape of the signals as  $\bar{y}_A$  is varied. The measured data is shown in the colored lines (the same for all subfigures) and the model predicted signal is shown in black. The subfigure that is highlighted with a red outline corresponds to the best match between the measured signal and the model response ( $\bar{y}_A = 4.31$  mm, ASC = 27.6 for this sample dataset). It is clear from the figures that variations in the location of the abutment center of mass affect the second mode frequency of the model response, which can result in a poor fit between the measured data and model signal.

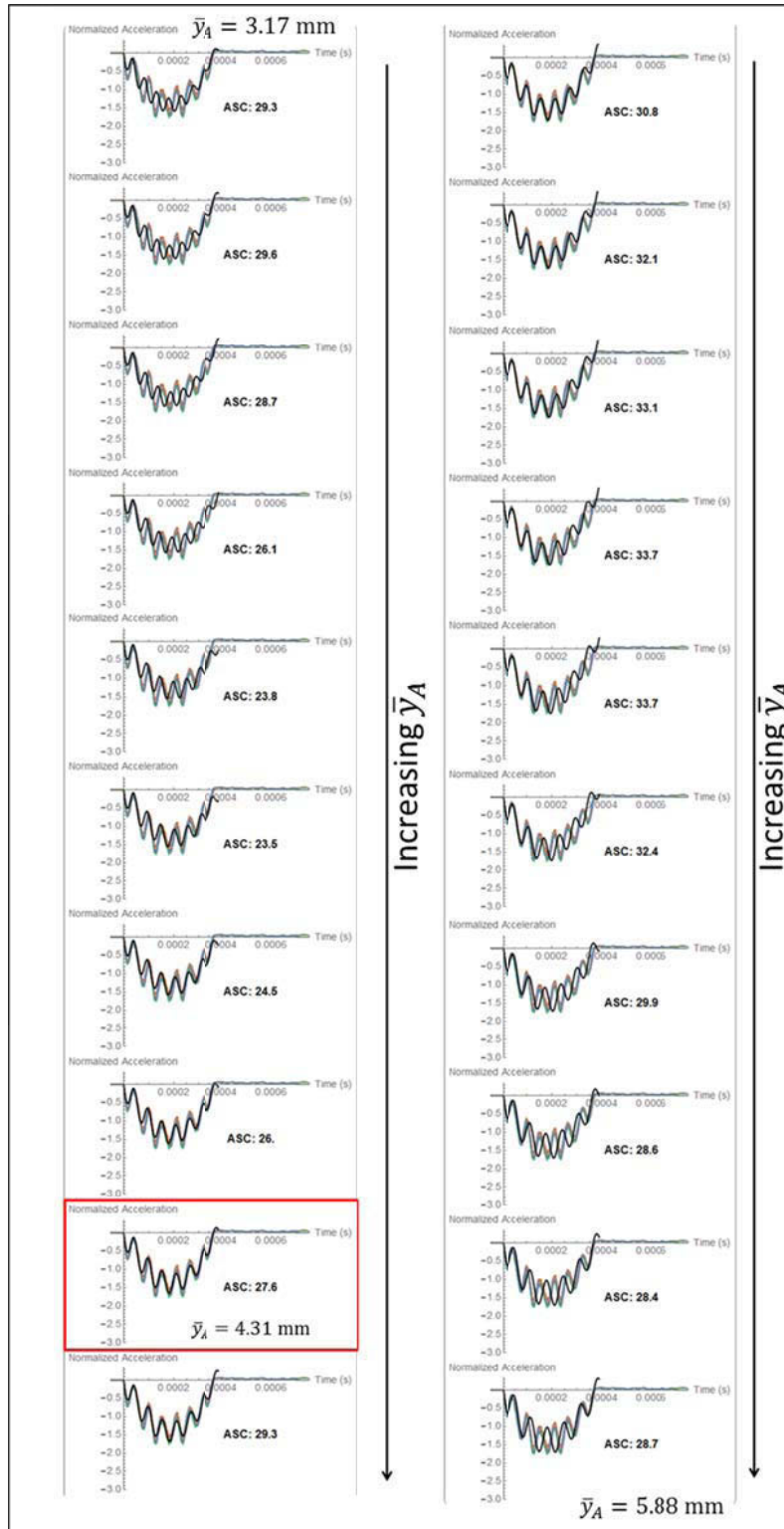
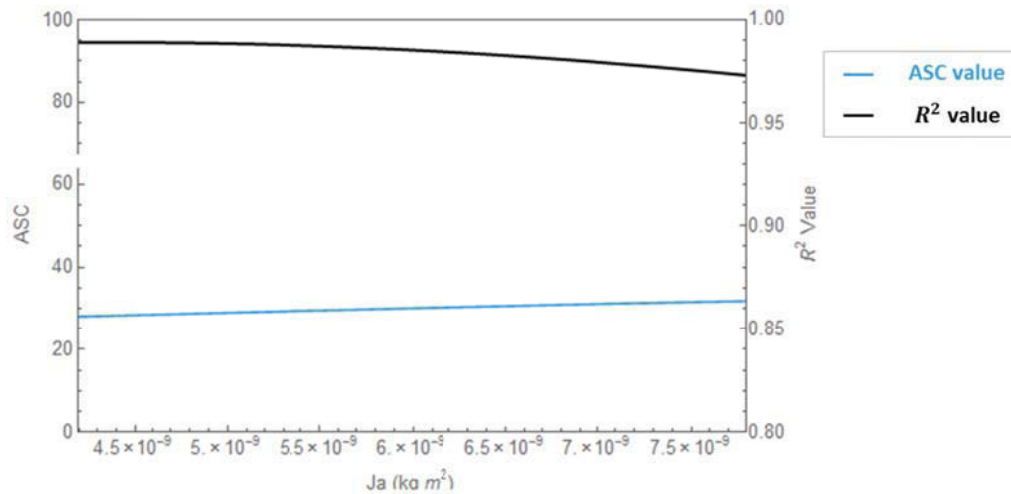


Figure B.27: Variation in the model fit (black line) with the measured acceleration (colored lines) with changing abutment center of mass ( $\bar{y}_A$ ) for an example dataset with a long/narrow implant and 9 mm abutment. The best match between the model and the measured data as measured by the  $R^2$  value is highlighted in red.

Again considering the long/narrow implant with a 9 mm abutment, the variation in ASC and  $R^2$  with changing  $J_A$  is shown in Figure B.28. It can be seen that there is very little variation in both the ASC value and the  $R^2$  fit with varying abutment moment of inertia. Over the full range tested, there is a change in ASC of 4 (13% change) and all  $R^2$  values are above 0.97 for this sample dataset.



**Figure B.28: Variation in ASC value (blue line) and  $R^2$  fit (black line) with changes in abutment mass moment of inertia ( $J_A$ ) for a long/narrow implant and 9 mm abutment**

The variation in the shape of the signals as  $J_A$  is varied is shown in Figure B.29. The measured data is shown in the colored lines (the same for all subfigures) and the model predicted signal is shown in black. It can be seen that most of the subfigures show a very good match between the measured data and the model response. As  $J_A$  is increased, the variation in the model response is primarily evident as an upward shift in the last cycle of the second mode frequency.

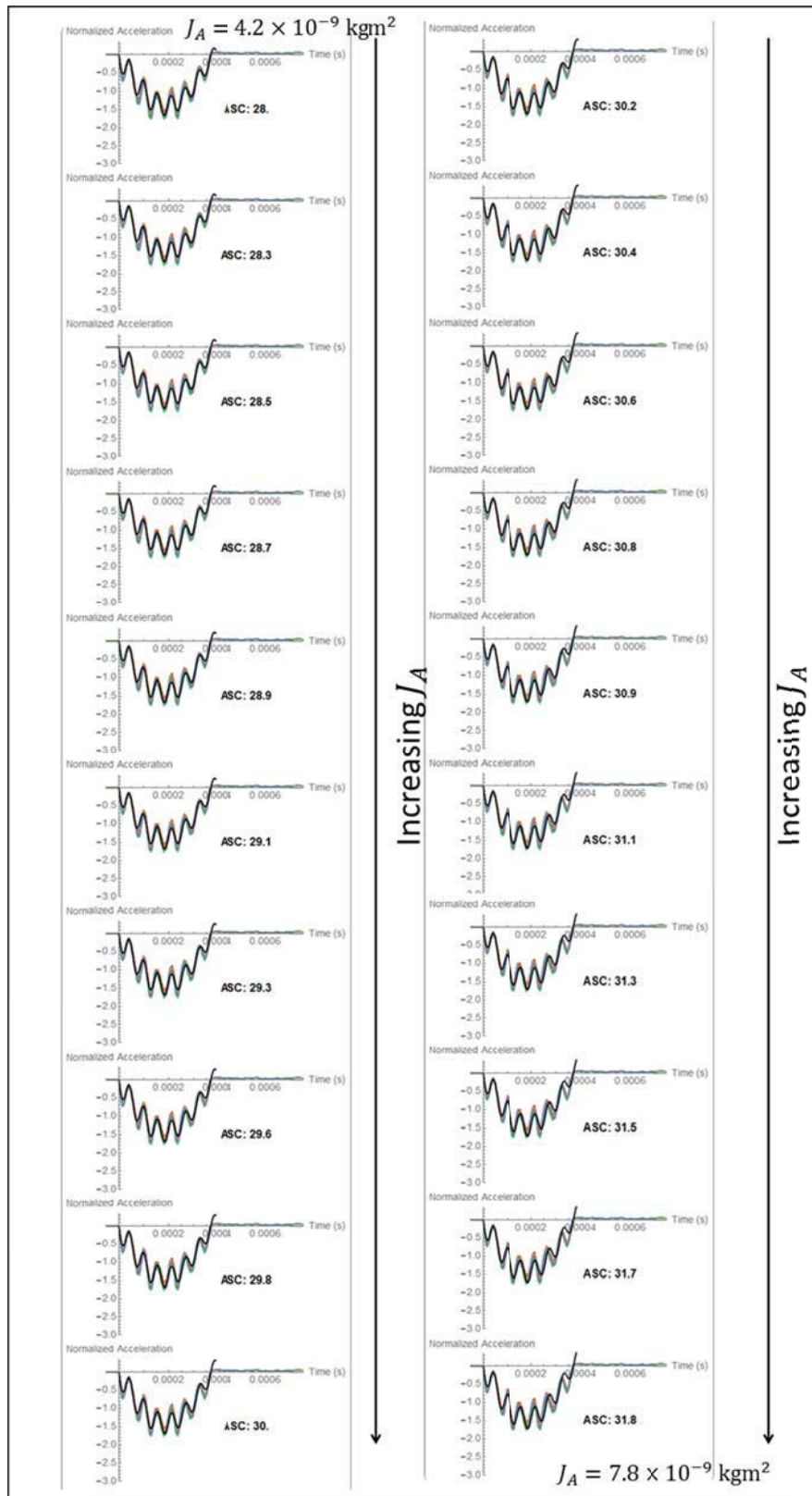
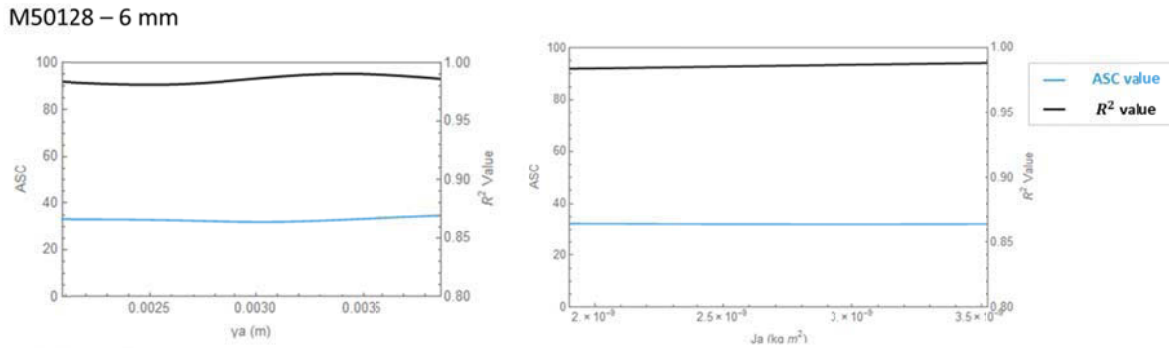


Figure B.29: Variation in the model fit (black line) with the measured acceleration (colored lines) with changing abutment mass moment of inertia ( $J_A$ ) for an example dataset with a long/narrow implant and 9 mm abutment

Similar to the stiffness sensitivity results, the shorter 6 mm abutments were found to have much less variation in the  $R^2$  fit, due to the smaller contribution of the second mode to the overall frequency response (Figure B.30). However, there is still a peak in the  $R^2$  fit curve and a clear variation in the second mode frequency with varying  $y_A$ . As with the 9 mm abutment, there is very little variation in both the ASC and  $R^2$  value due to changes in  $J_A$ .



**Figure B.30: Variation in ASC value (blue line) and  $R^2$  fit (black line) with changes in abutment center of mass (left) and abutment moment of inertia (right) for a long/narrow implant and 6 mm abutment**

With the 12 mm abutment, very similar patterns are observed as compared to the 9 mm abutment. In this case there is a larger variation in  $R^2$  due to the larger contribution of the second mode frequency for the longer abutments (Figure B.31).

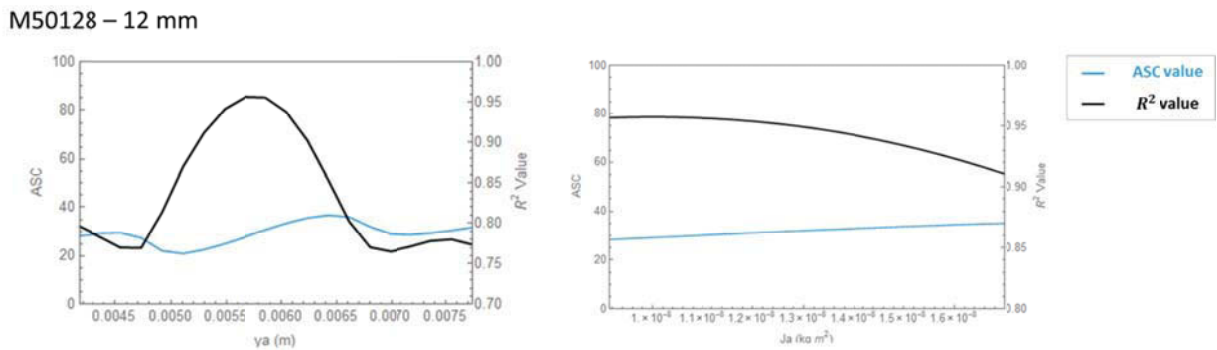
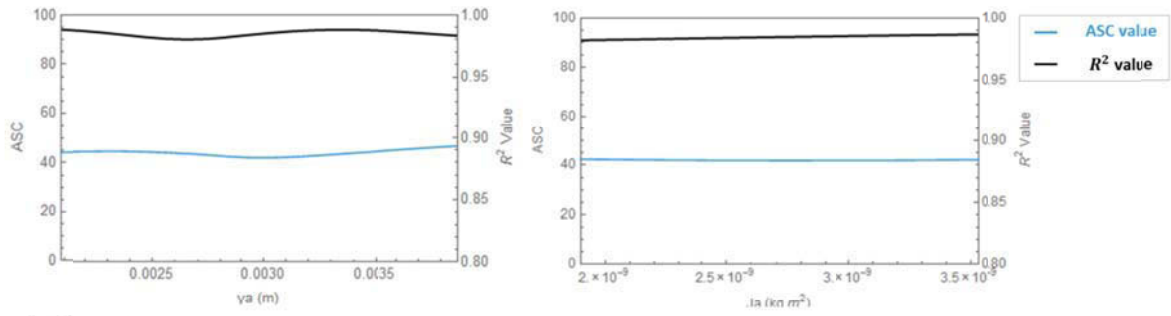


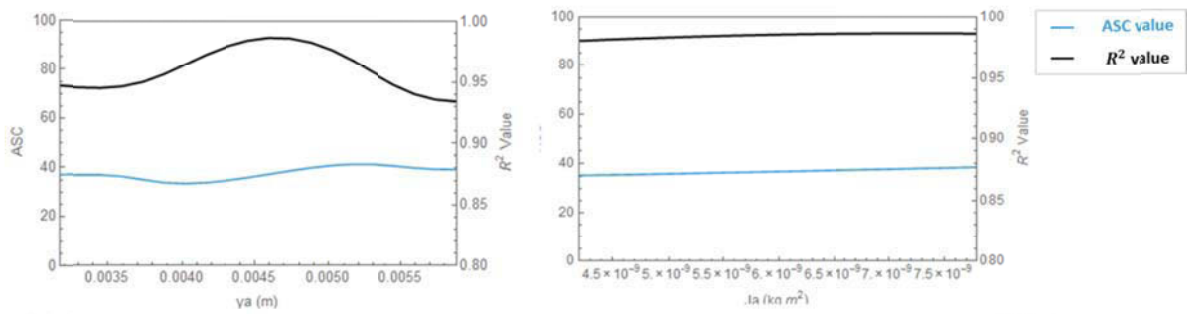
**Figure B.31: Variation in ASC value (blue line) and  $R^2$  fit (black line) with changes in abutment center of mass (left) and abutment moment of inertia (right) for a long/narrow implant and 12 mm abutment**

Similar patterns are observed for the other implant-abutment combinations. For example, the results for the long/wide implant (M51062) with the four different Oticon Medical abutment sizes are shown in Figure B.32.

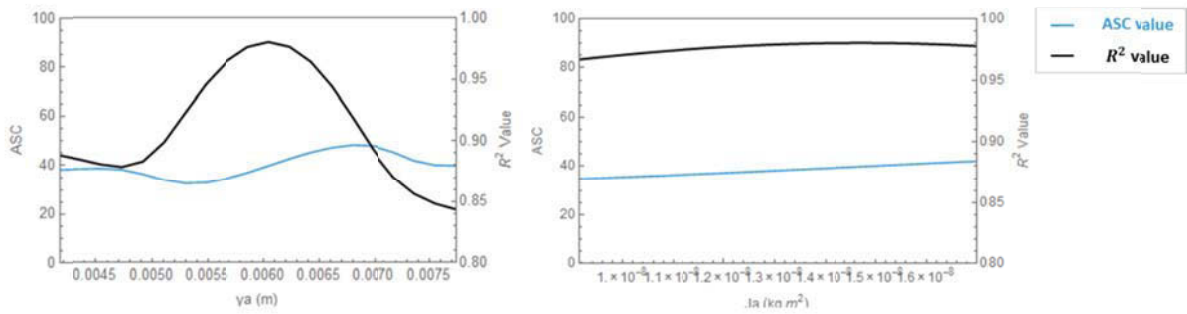
M51052 – 6 mm



M51052 – 9 mm



M51052 – 12 mm



M51052 – 14 mm

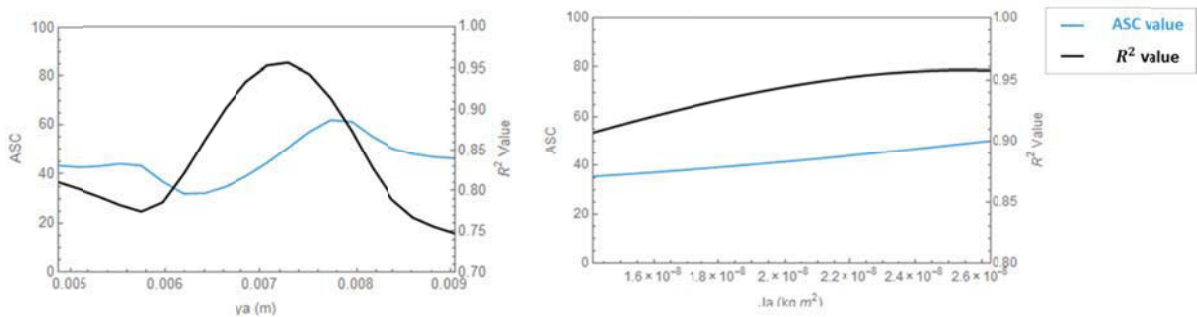


Figure B.32: Variation in ASC value (blue line) and  $R^2$  fit (black line) with changes in abutment center of mass (left) and abutment moment of inertia (right) for a long/wide implant and various abutment sizes

Since the model prediction and  $R^2$  fit are sensitive to the location of the center of mass of the abutment, which is an estimated parameter, this parameter was adjusted for each abutment to find an average value that produced a good fit with each implant type. The procedure for this adjustment is outlined in Section 3.1. Conversely, since the moment of inertia of the abutment was found to have minimal effect on the model outcome, the values estimated based on the simplified geometry were used as the final values in the model with no further adjustment.

## B.6 Damping Model

### Proportional Damping:

The damping assumption used in the previous work of Swain et al. (2006) was proportional damping which maintains the ability to uncouple the equations using modal analysis. This is a case of classical damping and in this case the damping matrix  $[C]$  is assumed to be proportional to the stiffness matrix  $[K]$ , so that  $[C] = \beta[K]$ . The mass matrix was not considered in the proportional damping assumption because the mass matrix is constant for a given implant-abutment configuration; thus the inclusion of the mass matrix would simply add a constant term to the damping expression. The constant  $\beta$  is related to the damping ratio of each mode  $\zeta_n$  and the natural frequency of each mode  $p_n$  by:

$$\beta = \frac{2\zeta_n}{p_n}$$

For the implant-abutment system, the damping ratio of the second mode of vibration is assumed (i.e.  $\zeta_2 = 0.03$ ), and the constant  $\beta$  is determined from the above relation. Subsequently, the damping ratios for the remaining vibration modes can be determined. With this assumption for the damping model, the damping ratio is directly proportional to the natural frequency for a particular mode, and thus the higher modes will be damped out faster than the lower modes.

For the case of proportional damping, modal analysis can be used to solve the equations of motion. The resulting displacement response is of the form:

$$\{x(t)\} = \sum_{n=1}^N \{\phi_n\} e^{-\zeta_n p_n t} \left[ q_n(0) \cos(\omega_{dn} t) + \frac{\dot{q}_n(0) + \zeta_n p_n q_n(0)}{\omega_{dn}} \sin(\omega_{dn} t) \right]$$

where:

$N$  is the number of degrees of freedom in the system (number of modes of vibration)

$\phi_n$  is the  $n^{th}$  mode shape

$\zeta_n$  is the damping ratio of the  $n^{th}$  mode

$p_n$  is the natural frequency of the  $n^{th}$  mode

$\omega_{dn} = \sqrt{1 - \zeta_n^2} p_n$  is the damped natural frequency of the  $n^{th}$  mode

$q_n(0)$  is the initial displacement of the  $n^{th}$  degree of freedom in modal coordinates

$\dot{q}_n(0)$  is the initial velocity of the  $n^{th}$  degree of freedom in modal coordinates

Of course it is also possible to solve the equations numerically using the same procedure that has been used in the ASIST technique for general viscous damping.

### General Viscous Damping:

In developing a model of the implant-abutment system, viscous damping can be included in much the same way as the spring stiffness. If a damper is included at the location of each spring ( $C_I, C_T, c$ ), then a damping matrix can be assembled using the same procedure of influence coefficients that was used for the stiffness matrix. We have assumed that the damping only occurs at the bone-implant interface with negligible damping in the rest of the system (i.e.  $C_I = C_T = 0$ ). The damping matrix  $[C]$  is thus given by:

$$[C] = \begin{bmatrix} 0 & 0 & 0 & 0 \\ 0 & 4cR_0(L_I - L_C) & -4cR_0(L_I - L_C)h & -2cR_0(L_I^2 - L_C^2) \\ 0 & -4cR_0(L_I - L_C)h & 4cR_0(L_I - L_C)h^2 & 2cR_0(L_I^2 - L_C^2)h \\ 0 & -2cR_0(L_I^2 - L_C^2) & 2cR_0(L_I^2 - L_C^2)h & \frac{4}{3}cR_0(L_I^3 - L_C^3) \end{bmatrix}$$

Where  $c$  is the viscous damping coefficient per unit area surrounding the implant.

When general viscous damping is used, modal analysis cannot be used to solve the equations of motion. In this case, the equations must be solved numerically for the known set of initial conditions.

## Damping Assumption Comparison

The two damping methods were implemented in Mathematica (both using the numerical solution procedure) and were evaluated on a subset of clinical data from 11 BAHA patients. The patient data is summarized in Table B.5.

**Table B.5: Patient demographics for data used in the damping assumption comparison**

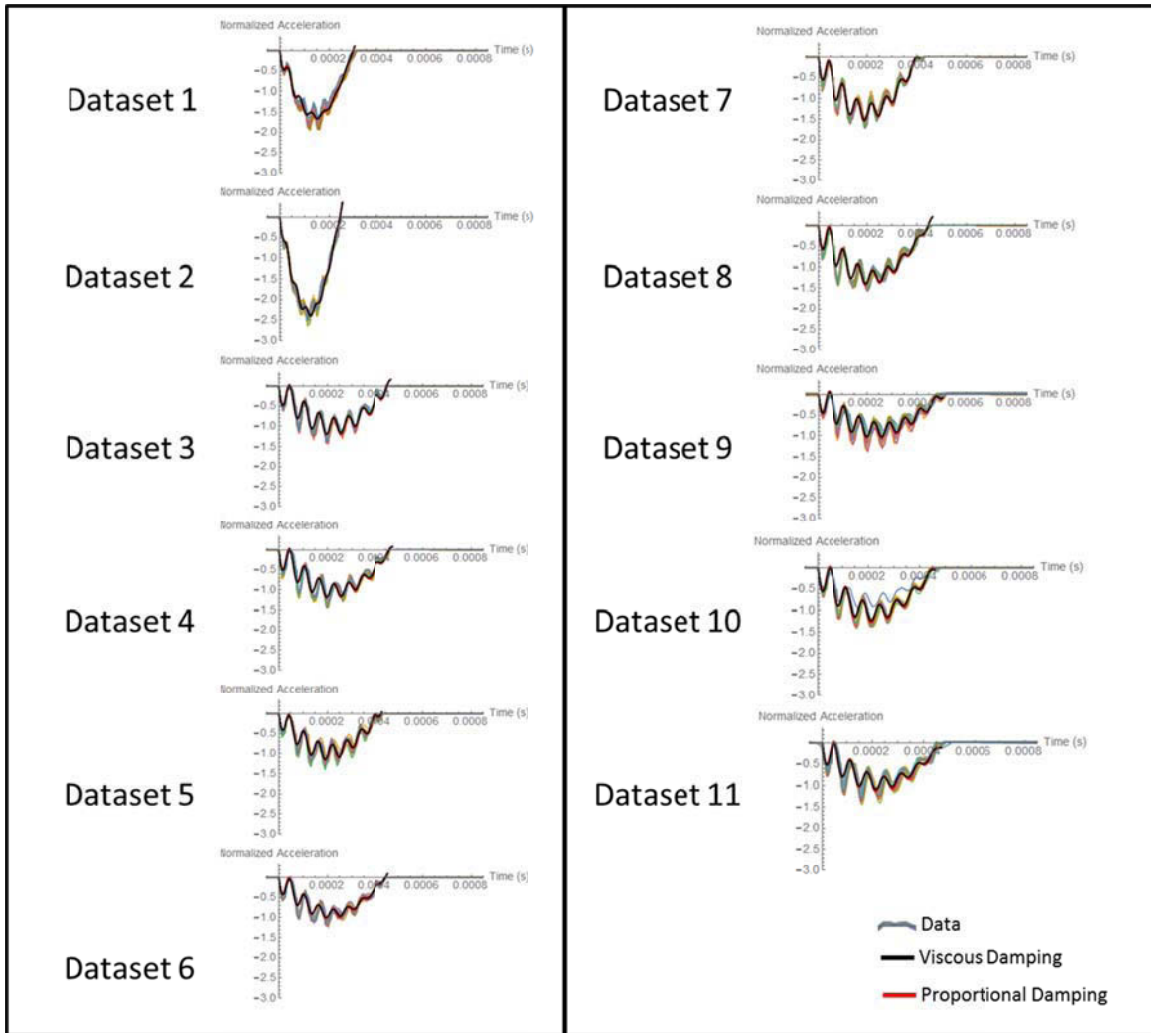
Dataset	Patient ID	Sex	Age at Surgery	Abutment Length	Visit
1	21	F	64	6 mm	1 Month
2	7	F	43	6 mm	6 Month
3	25	F	30	9 mm	3 Month
4	27	F	48	9 mm	3 Month
5	20	M	58	9 mm	3 Month
6	13	F	49	9 mm	3 Month
7	26	F	24	9 mm	2 Week
8	9	M	17	9 mm	3 Month
9	6	F	36	9 mm	6 Month
10	17	F	56	12 mm	1 Month
11	4	M	63	12 mm	6 Month

The ASIST procedure was used to estimate the interface stiffness and calculate the associated ASC value using both the proportional damping assumption and the general viscous damping assumption. The second mode damping ratio was extracted from the curve fit for each dataset and used in the analysis. It can be seen from Table B.6, that the damping ratio for the BAHA patients is generally very low with an average damping ratio of 0.034 (3.4%) and a range of 0.020 – 0.066 for this sample data. The ASC values and  $R^2$  values using both damping methods are also presented in Table B.6. It can be seen that there are very small differences in the results for the two procedures with a maximum difference in the ASC value of 2.2% and differences in the  $R^2$  value below 1%. With such a small damping content, we can see that the choice of damping assumption does not have a large impact on the ASC results.

**Table B.6: Comparison of ASC and  $R^2$  values using different damping assumptions for example datasets from clinical BAHA patients**

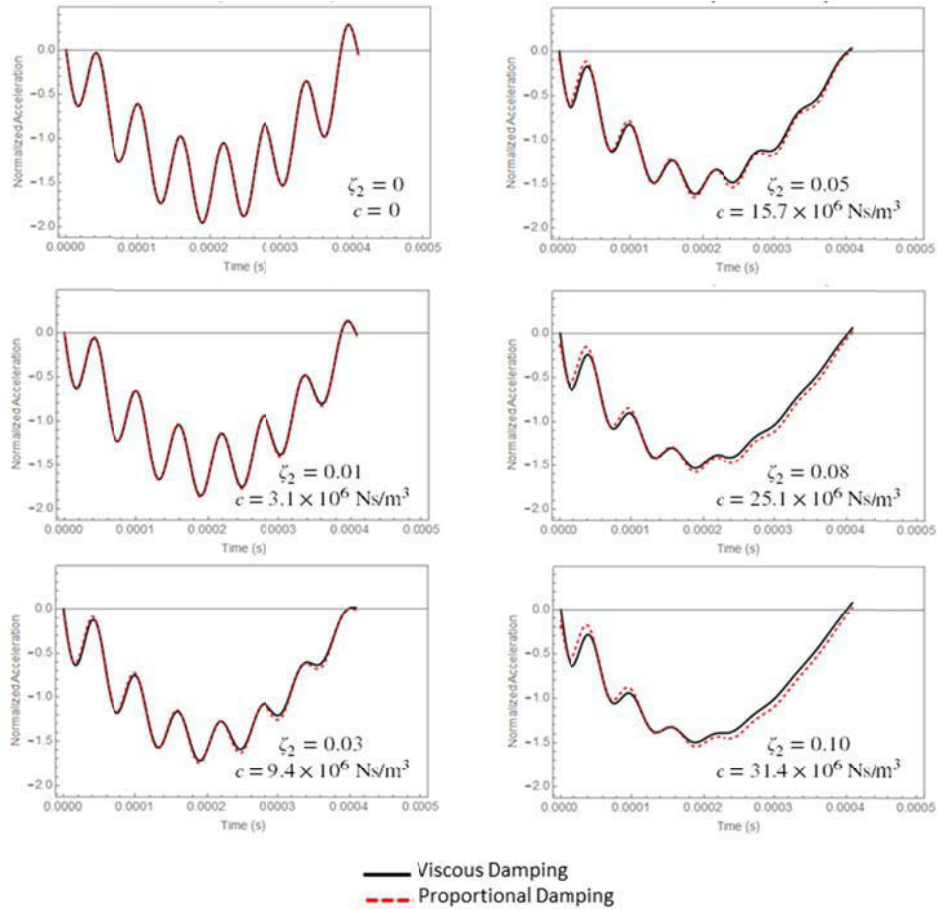
Dataset	Damping Ratio (Curve Fit)	ASC Viscous	ASC Proportional	% Diff ASC	$R^2$ Viscous	$R^2$ Proportional	% Diff $R^2$
1	0.066	27.2	27.4	0.84	0.99	0.99	0.11
2	0.026	67.7	67.6	0.12	0.99	0.99	0.01
3	0.023	15.8	15.8	0.32	0.98	0.97	0.33
4	0.033	14.8	14.9	1.05	0.97	0.96	0.57
5	0.020	21.0	21.1	0.27	0.98	0.98	0.09
6	0.044	16.9	17.2	1.70	0.98	0.97	0.42
7	0.027	22.2	22.3	0.66	0.99	0.98	0.24
8	0.039	17.1	17.3	1.37	0.97	0.96	0.74
9	0.027	12.5	12.6	0.84	0.97	0.96	0.42
10	0.033	31.6	32.2	2.03	0.98	0.98	0.20
11	0.038	27.8	28.5	2.21	0.96	0.95	0.32

Figure B.33 shows the data with the model response using viscous damping (shown in black) and using proportional damping (shown in red). It can be seen that there are very minor differences in the model response with the two damping assumptions for this sample data.



**Figure B.33: Comparison of model solution with viscous damping (black lines) and proportional damping (red lines) for BAHA patient datasets (shown in colored lines)**

The acceleration response can be determined for any combination of interface stiffness and damping ratio using both the viscous damping and proportional damping assumptions. Figure B.34 shows a comparison between the acceleration response for each damping model for a long/narrow Oticon implant (M50128) with a 9 mm abutment and an interface stiffness of  $k = 3 \times 10^{12} \text{ N/m}^3$  ( $ASC = 22.5$ ). The figure shows the comparison for damping ratios of  $\zeta_2 = 0, 0.01, 0.03, 0.05, 0.08, \text{ and } 0.10$ . The corresponding interface damping coefficient values ( $c$ ) are shown on the subfigures. At higher damping ratios, the difference in the acceleration response of the two models becomes slightly more evident as expected.



**Figure B.34: Comparison of viscous damping and proportional damping for various damping ratios. Second mode damping ratio ( $\zeta_2$ ) and interface damping coefficient ( $c$ ) values are shown on the figures.**

Using proportional damping it is possible to solve the model equations using both modal analysis and a numerical solution procedure. In the results presented above, the numerical solution procedure was used in order to maintain consistency with the viscous damping model. Figure B.35 shows a comparison of the two solution procedures for a long/narrow Oticon implant (M50128) with a 9 mm abutment. This example is for an interface stiffness of  $k = 3 \times 10^{12} \text{ N/m}^3$  (ASC = 22.5) and a second mode damping ratio of  $\zeta_2 = 0.05$ .

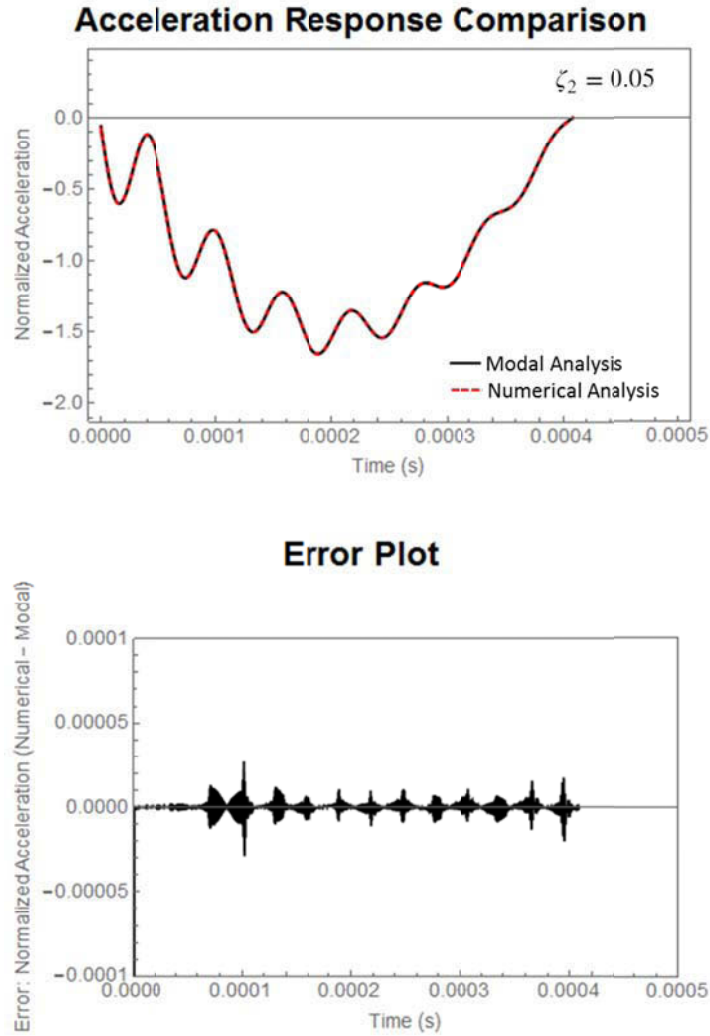


**Figure B.35: Comparison of the model solution using modal analysis and numerical analysis solution procedures. Top: Model results overlaid for  $\zeta_2 = 0.05$ ; Bottom: Error defined as the difference between the two solutions for this example.**

When the two acceleration response curves are plotted on the same figure, the lines are indistinguishable from each other. The second plot in Figure B.35 shows the difference between the two solutions for the duration of the strike (scale of normalized acceleration). The magnitude of the peak normalized acceleration for this example is approximately 1.7 while the error is below approximately 0.00003 or less than 0.002% of the peak normalized acceleration.

## B.7 Effective Interface Stiffness

In the analytical model, we consider the bone-implant interface to be a uniform stiffness distributed over the osseointegrated area of the implant. We can also consider the interface stiffness to be represented by an equivalent effective stiffness model. This will allow investigation of the effect of various interface stiffness distributions.

Considering a differential element through the implant of height  $dl$  and considering the component of the interface stiffness acting in the direction of the applied loading, the effective stiffness on the differential element was found to be:

$$K_{eff(dl)} = 4kR_0dl$$

Integrating over the length of the implant, the effective interface stiffness is:

$$K_{eff} = 4kR_0l_i$$

It is possible to instead consider the interface stiffness as a single effective stiffness  $K_{eff}$  acting at a height  $h_I$  and a torsional stiffness  $K_R$ . This would allow us to model a non-uniform interface by varying the parameter  $h_I$ . Note that  $h_I = l_i/2$  corresponds to the situation with a uniform interface over the length of the implant. Also note that the torsional stiffness  $K_R$  is required because the implant has a rotational degree of freedom  $\theta_2$ .

Consider a rod with a distributed stiffness  $k_f(y)$  in the horizontal plane with two degrees of freedom (Figure B.36-A):  $x$  is the horizontal displacement at the centroid of the distributed stiffness and  $\theta$  is the angle of rotation about the centroid of the distributed stiffness. In general, the distributed stiffness is a function of the height  $y$  measured from the bottom of the rod. This system can be represented by an equivalent effective stiffness  $K_{eff}$  acting at a height  $h_I$  and a rotational stiffness  $K_R$  at the height of  $h_I$  (Figure B.36-B).

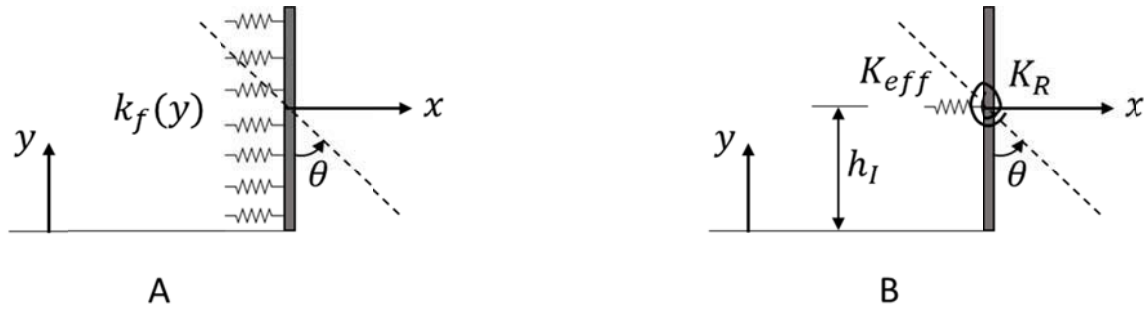


Figure B.36: Distributed stiffness model (left) and equivalent effective stiffness model (right)

For some deformation  $x = ay + b$ ;  $a, b \in \mathbb{R}$ , we can determine the equivalent system parameters ( $K_{eff}, h_I, K_R$ ) as functions of the distributed stiffness ( $k_f$ ) by comparing the force and moment in both cases.

For the distributed system:

$$F_1 = \int_L k_f(ay + b) dy$$

$$M_1 = \int_L k_f(ay + b)y dy$$

For the equivalent system (assuming small deformation  $\Rightarrow \theta = a$ ):

$$F_2 = K_{eff}(ah_I + b)$$

$$M_2 = K_{eff}(ah_I + b)h_I + K_R a$$

Now,  $F_1 = F_2$  and  $M_1 = M_2 \forall a, b \in \mathbb{R}$ . Thus, the equivalent system parameters can be determined for a given distribution by comparing the coefficients of  $a$  and  $b$ . This gives us three independent equations which can be solved for the equivalent system parameters.

For example, consider a uniform stiffness  $k_f(y) = k$ .

$$F_1 = \int_0^L k(ay + b) dy = k \left[ a \frac{y^2}{2} + by \right]_0^L = a \frac{kL^2}{2} + bkL$$

$$M_1 = \int_0^L k(ay + b)y dy = k \left[ a \frac{y^3}{3} + b \frac{y^2}{2} \right]_0^L = a \frac{kL^3}{3} + b \frac{kL^2}{2}$$

Equating the forces and moments:

$$F_1 = F_2 \Rightarrow a \frac{kL^2}{2} + bkL = K_{eff}(ah_I + b)$$

$$M_1 = M_2 \Rightarrow a \frac{kL^3}{3} + b \frac{kL^2}{2} = K_{eff}(ah_I + b)h_I + K_R a$$

Comparing coefficients:

$$\text{Force Equation } a: \quad \frac{kL^2}{2} = K_{eff}h_I \quad \Rightarrow \quad h_I = \frac{L}{2}$$

$$\text{Force Equation } b: \quad kL = K_{eff}$$

$$\text{Moment Equation } a: \quad \frac{kL^3}{3} = K_{eff}h_I^2 + K_R$$

$$\text{Substituting for } h_I \text{ and } K_{eff} \text{ gives: } \frac{kL^3}{3} = kL \left( \frac{L}{2} \right)^2 + K_R \quad \Rightarrow \quad K_R = \frac{kL^3}{12}$$

In the BAHA implant-abutment system, replacing the uniformly distributed interface stiffness with an equivalent system of  $K_{eff}$ ,  $h_I$ , and  $K_R$  results in the following stiffness matrix:

$$[K] = \begin{bmatrix} K_I & -K_I & 0 & 0 \\ -K_I & K_I + K_{eff} & -K_{eff}h & -K_{eff}(L_I - h_I) \\ 0 & -K_{eff}h & K_T + K_{eff}h^2 & -K_T + K_{eff}h(L_I - h_I) \\ 0 & -K_{eff}(L_I - h_I) & -K_T + K_{eff}h(L_I - h_I) & K_T + K_{eff}(L_I - h_I)^2 + K_R \end{bmatrix}$$

$K_{eff}$ ,  $h_I$ , and  $K_R$  are dependent on the specific distribution  $k_f(y)$ .

We can evaluate the effect of the distribution on the acceleration response of the model by varying  $h_I$  while keeping the total effective stiffness  $K_{eff}$  constant. This can be done by defining the interface stiffness as a piecewise distribution with a uniform distribution over a portion of the implant interface and zero stiffness elsewhere along the interface (Figure B.37). Figure B.37 also shows the equivalent system representation. The proportion of the interface covered by the distributed stiffness can be varied in order to vary the height  $h_I$ . In each case, the magnitude of the distributed stiffness can be adjusted to maintain an equal  $K_{eff}$ . Additionally, in each case an associated  $K_R$  must be calculated.

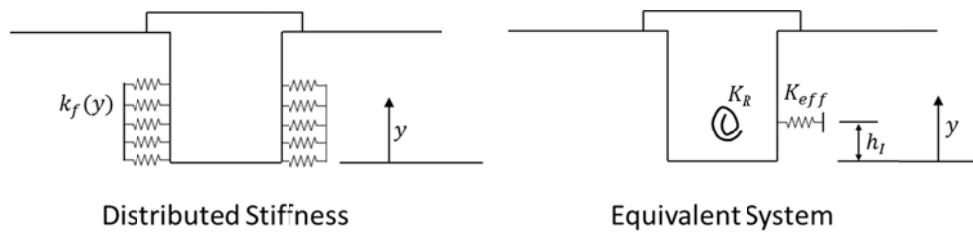
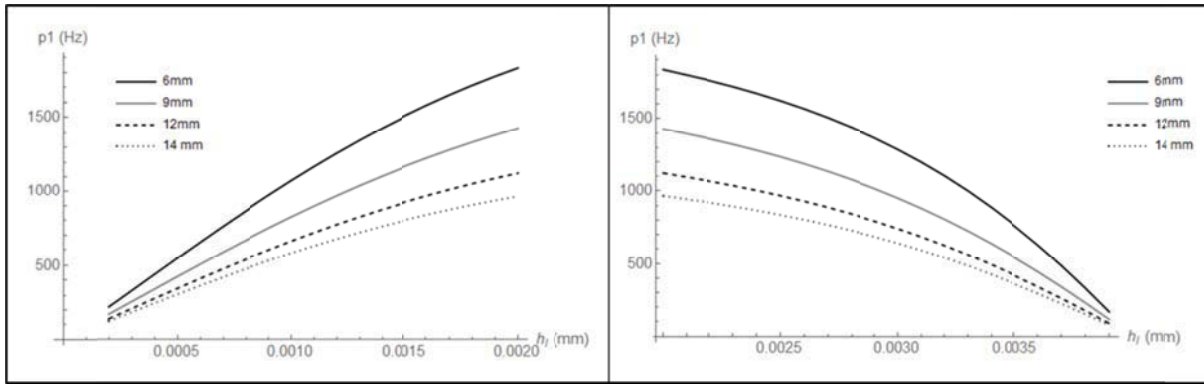


Figure B.37: Distributed stiffness implant model (left) and equivalent effective stiffness implant model (right)

For a long/narrow implant (M50128) and each Oticon abutment length, the effect on the first mode frequency of the acceleration response was determined for varying height  $h_I$ . The stiffness was distributed such that the effective stiffness remained constant providing an ASC of 37.5 ( $K_{eff} = 1.5 \times 10^8$  N/m). The proportion of the interface covered by the uniform stiffness was varied from 10% to 100% increasing the stiffness from the bottom of the implant ( $y = 0$ ) resulting in a range of  $h_I$  from 0.2 – 2.0 mm. The analytical model was used to determine the acceleration response for each distribution. Subsequently, the proportion of the interface was decreased from 100% to 10% reducing the stiffness towards the top of the implant resulting in a range of  $h_I$  from 2.0 – 3.9 mm. Figure B.38 shows the first mode frequency as a function of the height  $h_I$  for each of the abutment lengths. It can be seen that the shorter abutments are more sensitive to changes in  $h_I$  than the longer abutments.



**Figure B.38: Variation in first mode frequency with changing height of effective stiffness ( $h_I$ ) for a long/narrow implant and various abutment lengths. Left: increasing the stiffness from the bottom of the implant. Right: reducing the stiffness towards the top of the implant.**

We can examine the effect of a linear distribution of the interface stiffness on both the height of the effective stiffness  $h_I$  and the resulting acceleration response. For example, two extreme scenarios are shown in Figure B.39. Scenario (a) has the stiffness concentrated at the top of the implant and decreasing linearly towards the bottom of the implant. This may occur if the top threads of the implant are engaged in strong cortical bone and the bottom threads are not required to provide additional support. Scenario (b) has the stiffness concentrated at the bottom of the implant and decreasing linearly towards the top. This situation could occur if the bone has started to resorb near the top of the bone surface and the connection of the implant begins to rely primarily on the bottom threads.

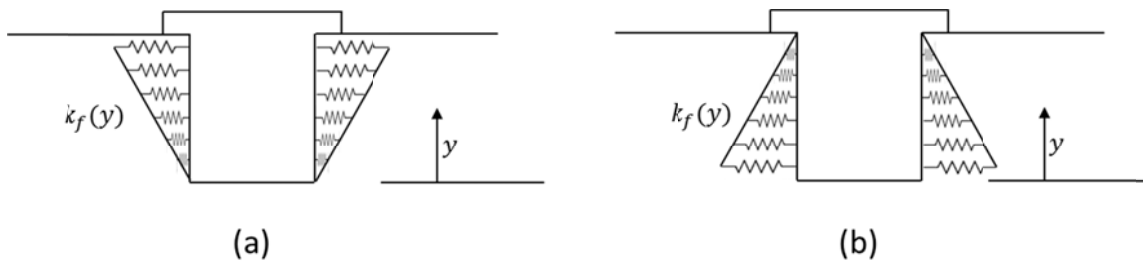


**Figure B.39: Examples of linear interface distributions**

For a 4 mm implant, the location of the effective stiffness for these extreme scenarios is 2.67 mm from the bottom for (a) and 1.33 mm from the bottom for (b) (and  $h_I = 2$  mm from the bottom

for the uniform interface case). This is a difference of  $\pm 0.67$  mm or a total difference of 1.33 mm. The difference in the acceleration response for the three scenarios (uniform interface, upper triangular linear distribution, and lower triangular linear distribution) is shown in Figure B.40 for the long/narrow implant (M50128) and four different abutment sizes. The difference between the first mode frequency for the uniform interface and the upper triangular linear interface ranges from 6 – 8%. The difference between the first mode frequency for the uniform interface and the lower triangular linear interface ranges from 13 – 14%. The difference between first mode frequency for the upper and lower triangular interface cases ranges from 5 – 9% and the difference is higher for the shorter 6 mm abutment and lower for the longer 14 mm abutment.

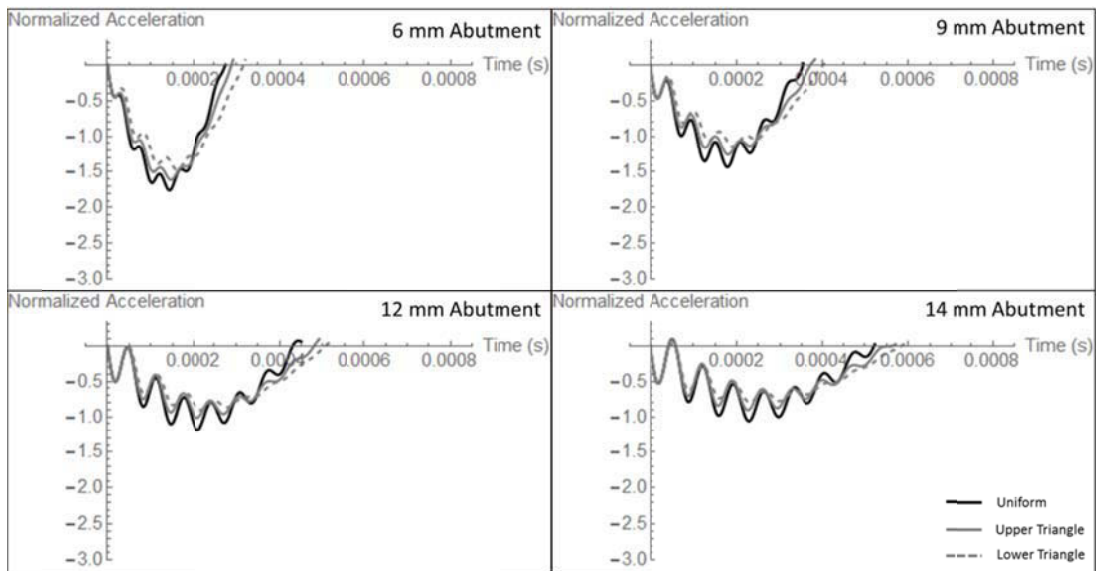


**Figure B.40: Acceleration response for a long/narrow implant and four different abutment lengths using three different interface distributions: uniform, upper triangular linear, and lower triangular linear.**

# Appendix C: Details of the Numerical Analysis

## C.1 Curve Fit Initial Guess

The curve fit procedure provides a single analytical description representing the average of the measured acceleration data. This is done using the Mathematica function `NonlinearModelFit[]`, which uses nonlinear regression to find the best fit parameters for the specified model to match the given data. The procedure requires an initial guess for each of the model parameters. In this section, we evaluate the performance of the curve fitting procedure for variations in the initial guess for each of the parameters.

The curve fit model is a 2-DOF response with unknown model parameters  $A, p_1, p_2, \zeta_2, \phi_1, \phi_2$ . For this analysis, nine sample datasets were used from the three Oticon Medical long/narrow implant specimens (M50128: FRB-20(1), FRB-20(2), PLA) with each of the three abutment lengths (6 mm, 9 mm, 12 mm). The model was used to determine the ASC value for each dataset with variations in the initial guess for each of the curve fit parameters. The outcome measures were the resulting best fit parameters from the curve fit procedure and the ASC value. The range of ASC values for these datasets was approximately 13 – 68.

The initial guess for the amplitude parameter  $A$  is  $A_0 = 1$ . Variations in the initial guess from  $10^{-8}$  to  $10^8$  were investigated. Values for the best fit  $A$  value ranged from  $1.69 \times 10^{-8}$  to  $3.23 \times 10^{-8}$ . The average difference in  $A$  due to variations in the initial guess was  $8.18 \times 10^{-18}$  ( $2.76 \times 10^{-8}$  %) and the average difference in ASC was 0.003 (0.009%).

The initial guess,  $p_{10}$  for the first mode frequency  $p_1$  is determined from the average contact time for each strike in a dataset. The average contact time is determined in order to specify an appropriate cutoff time for the measured data since many values of zero voltage are recorded beyond the end of the actual strike event. Using this value gives a reasonable approximation to the first mode frequency. The initial guess for the first mode frequency  $p_{10}$  was varied  $\pm 40\%$  from the model value. Values for the best fit  $p_1$  ranged from 4864 to 12477 rad/s. In general there was a very small difference in the best fit  $p_1$  value due to variations in the initial guess. There was one case (M50128 FRB-20(1) – 6 mm) where a variation in the initial guess produced

a different model fit with a 1.3% change in the resulting first mode frequency and a 6.5% change in ASC. This case represents a situation with a high frequency and very little amplitude contribution from the second mode. Some numerical instability caused a slightly different model solution to be found. However, this was only 1 case out of the 153 cases that were examined. With the exception of this case, the average difference in  $p_1$  due to variations in the initial guess was  $1.06 \times 10^{-6}$  rad/s ( $1.86 \times 10^{-8}$  %) and the average difference in ASC was 0.003 (0.009%).

The initial guess for the second mode frequency  $p_2$  is 10 times the initial guess for the first mode frequency. From the data examined for BAHA implant-abutment systems, the second mode frequency was found to be approximately one order of magnitude larger than the first mode frequency. The initial guess for the second mode frequency  $p_{20}$  was varied between  $\pm 10\%$  to  $\pm 40\%$  for each dataset. The best fit values for  $p_2$  ranged from 90854 to 180073 rad/s. For some datasets, varying the initial guess by a large margin caused the curve fit procedure to be unable to find a solution. In these cases, the range was shortened to either  $\pm 20\%$  or  $\pm 10\%$ . With the cases tested, there were several instances where no solution was found from the curve fit procedure. Again there was one case with the M50128 FRB-20(1) – 6mm implant-abutment sample where a slightly different result was found resulting in a 34% difference in the best fit  $p_2$  and a 6.5% difference in the ASC value. With the exception of this case, the average difference in  $p_2$  was  $1.63 \times 10^{-5}$  rad/s ( $1.40 \times 10^{-8}$  %) and the average difference in ASC was 0.003 (0.008%).

The initial guess for the second mode damping ratio  $\zeta_2$  is  $\zeta_{20} = 0$ . Variations in the initial guess from 0 to 0.1 were investigated. The best fit values for  $\zeta_2$  ranged from 0.006 to 0.058. There were a few cases where no solution was found and there was one case with the M50128 FRB-20(1) – 9 mm implant-abutment sample where a slightly different model was found resulting in a difference in damping ratio of 0.037 and a difference in ASC of 3.1%. With the exception of this case, the average difference in damping ratio with variations in the initial guess was  $1.16 \times 10^{-10}$  ( $1.10 \times 10^{-6}$  %) and the average difference in ASC was 0.003 (0.010%).

The initial guess for both phase angles  $\phi_1$  and  $\phi_2$  were set to 0.1 rad. Variations in the initial guess for these parameters was varied from 0 to 1.6 rad. Best fit values for  $\phi_1$  typically ranged between 0.056 and 0.27 rad while best fit values for  $\phi_2$  were more varied and typically ranged between -3.54 and 2.68. There were several cases where no solution could be found. For

example, with the initial guess for the phase angles equal to zero, no solution could be found from the curve fit procedure. Additionally, with large values for the initial guess (i.e. larger than 1.2 rad) the curve fit procedure produced a solution with a negative amplitude causing the subsequent model optimization to fail to find an appropriate solution. In some cases, essentially the same model was found; however, the produced phase angle was offset by a factor of a multiple of  $\pi$  or  $2\pi$ . The average difference in ASC for all cases tested was 0.003 (0.008%).

For the datasets examined, it was found that varying the initial guess in the curve fit procedure results in negligible differences in the calculated best fit parameters with differences in the resulting ASC values less than 0.01% on average. Varying the initial guess can sometimes cause the curve fit procedure to fail to find a solution; however, when a solution is found, it is typically able to find a unique solution within a very small numerical error.

## C.2 Curve Fit Time Cutoff

When the data is recorded for the impact event as described in Section 2.1 some data is collected following the end of the strike, thus the actual end of the strike must be identified. To do this, each individual strike is filtered using a moving average filter and the absolute difference between consecutive data points is determined for each of the filtered strikes. Starting from the end of the data and working towards  $t = 0$ , the end of each strike is estimated as the time when the absolute difference between the voltage recorded for consecutive data points exceeds a given tolerance. This tolerance was set to 0.01 as this value was found to provide a good estimate of the end of the strike for the full range of data. The end of the impact event is then taken as the average of the time estimated for each strike. For example, the dashed line in Figure C.1 shows the end of the impact event for this set of data.

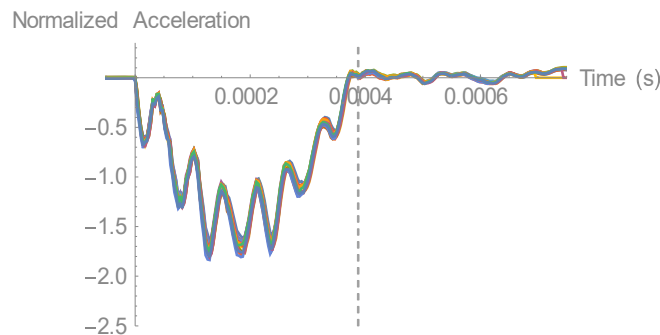
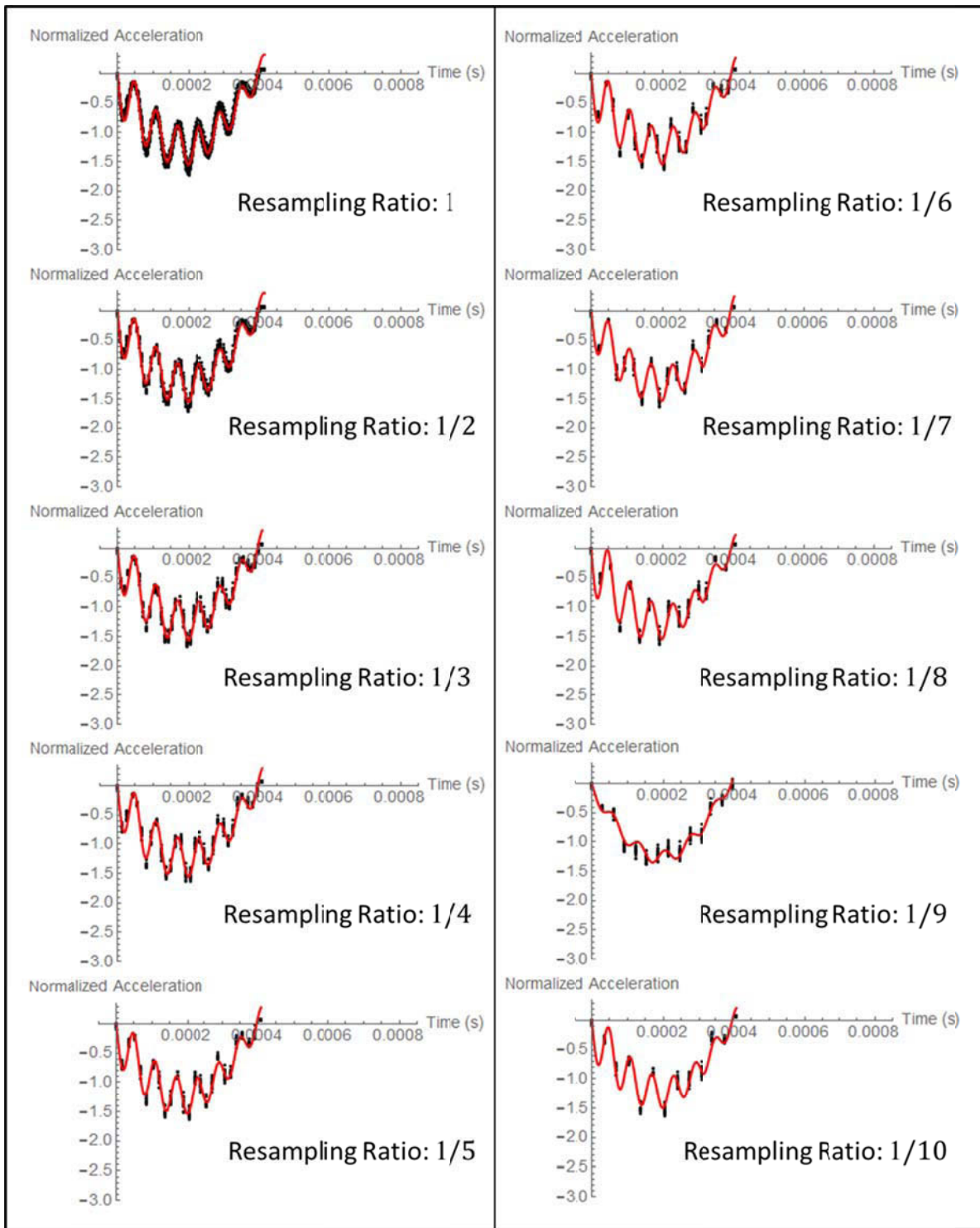


Figure C.1: Acceleration data for 16 strikes. The dashed line shows the end of the strike.

The cutoff time identifies the range of data that is used for the curve fit procedure. Only the data points that fall between  $t = 0$  and the cutoff time are included. The sensitivity of the curve fit procedure and resulting model prediction to changes in the data cutoff time were investigated. The same nine datasets described in the previous section were used for this analysis. The cutoff time was varied  $\pm 5\%$  from the calculated value (in 1% increments) and the change in the best fit first mode frequency ( $p_1$ ) from the curve fit and the ASC from the model were evaluated. In several cases where the cutoff time was increased, the curve fit procedure failed to find a solution (10/99 cases). For the remaining cases, the average difference in first mode frequency from the curve fit was 65.6 rad/s (0.82 %) and the average difference in ASC was 0.88 (1.97 %).

### **C.3 Data Resampling**

The curve fit procedure is based on the measured accelerometer data which is recorded with a sampling frequency of 294 kHz. We investigated the behavior of the curve fit solution when the measured acceleration data was uniformly reduced by  $1/n$  where  $n$  took integer values from 1-10. This analysis can provide some understanding about the effect of a lower sampling frequency on the results. The same nine datasets described in the previous sections were used for this analysis. An example of the reduced datasets and the resulting curve fit models are shown in Figure C.2 for one implant-abutment combination (M50128 FRB-20(2) – 12 mm). The curve fit procedure failed to find a solution in 15/90 cases (7 of those cases were with the same dataset M50128 FRB-20(2) – 6 mm abutment greater than 1/3 reduction in data).



**Figure C.2: Reduced datasets (black dots) and curve fit models (red lines) for an example implant-abutment combination M50128 FRB-20(2) – 12 mm abutment.**

With a reduction in the data of 1/2, the average change in first mode frequency from the curve fit was 12.3 rad/s (0.15%) and the average change in ASC was 0.25 (0.53%). With a reduction in the data of 1/5, the average change in first mode frequency from the curve fit was 26.8 rad/s (0.38%) and the average change in ASC was 0.40 (0.92%). With a reduction in the data of 1/10, the average change in first mode frequency from the curve fit was 85.6 rad/s (1.08%) and the average change in ASC was 1.10 (2.94%). For all of the datasets examined, the average change in first mode frequency from the curve fit was 70.3 rad/s (0.94%) and the average change in ASC was 0.85 (2.0%). A lower sampling frequency in the acceleration measurement would reduce the time required to transfer the data to the computer and would slightly reduce the computation time from the model. This analysis suggests that the sampling frequency of the ASIST measurement may be reduced without substantially affecting the ASC value.

## C.4 Individual Strikes

Each impact event with the ASIST handpiece consists of 16 individual strikes. The ASIST modeling procedure uses the data from all 16 strikes to provide a single average estimate of the ASC. It is also possible to use the modeling procedure to calculate an ASC value for each individual strike. An average estimate of the interface stability can then be determined by calculating the average ASC over the 16 strikes. The difference in these two solution procedures was investigated for one sample dataset of each of the 9 implant-abutment combinations described in the previous sections: the Oticon Medical long/narrow implant specimens (M50128: FRB-20(1), FRB-20(2), PLA) and each of the three abutment lengths (6 mm, 9 mm, 12 mm).

The results of this analysis is shown in Table C.1. For the datasets analyzed the average difference in average ASC between the two procedures was 0.07 (0.20%). Analyzing each strike individually provides an indication of the variability between the 16 strikes. The maximum and minimum ASC values for each dataset are shown in Table C.1. On average, the standard deviation of the 16 measurements was found to be 1.1 with a maximum standard deviation of 3.6 (M50128 FRB-20(2) – 6 mm dataset with average ASC = 63.90).

Table C.1: ASC Values Using All Data and Average ASC Values for Individual Strikes

	ASC (All Data)	Average ASC (Individual Strikes)	Min ASC (Individual Strikes)	Max ASC (Individual Strikes)	Diff ASC	% Diff ASC
<b>M50128 FRB-20(1) - 6 mm</b>	32.10	32.21	30.77	35.08	0.11	0.35
<b>M50128 FRB-20(1) - 9 mm</b>	30.07	30.10	28.87	31.45	0.02	0.08
<b>M50128 FRB-20(1) - 12 mm</b>	32.00	32.14	30.68	33.51	0.14	0.43
<b>M50128 FRB-20(2) - 6 mm</b>	63.88	63.90	60.65	66.85	0.01	0.02
<b>M50128 FRB-20(2) - 9 mm</b>	57.83	57.83	55.53	60.54	0.01	0.01
<b>M50128 FRB-20(2) - 12 mm</b>	68.87	69.17	63.73	78.15	0.30	0.44
<b>M50128 PLA - 6 mm</b>	16.81	16.82	16.38	17.27	0.01	0.06
<b>M50128 PLA - 9 mm</b>	16.54	16.58	16.23	16.88	0.04	0.23
<b>M50128 PLA - 12 mm</b>	13.17	13.19	12.54	13.79	0.02	0.19
<b>Average</b>					<b>0.07</b>	<b>0.20</b>
<b>SD</b>					<b>0.10</b>	<b>0.17</b>

## C.5 Interface Stiffness Initial Guess

The optimization procedure to match the model response to the measured acceleration from the impact (Section 2.3.3.) requires an initial guess for the solution and finds a local minimum for the specified objective function. The effect of the initial guess for the interface stiffness per unit area ( $k$ ) was investigated for the nine sample datasets described above. The interface stiffness values for these datasets ranged from  $1.75 \times 10^{12} - 9.19 \times 10^{12} \text{ N/m}^3$ . For each dataset, the initial guess for  $k$  was varied from  $1 \times 10^{12} - 10 \times 10^{12} \text{ N/m}^3$  and the model was used to determine the ASC value.

For each dataset, the curve fit for each case was the same, with the only difference being the initial guess for the matching optimization procedure. The matching procedure was unable to find a solution in 13/90 cases. For the remaining cases, the average difference in ASC was 0.005 (0.014%). For the datasets examined it was found that varying the initial guess for the interface stiffness can sometimes cause the matching procedure to fail to find a solution; however, when a solution is found, it is a unique solution within a small numerical error.

## C.6 Matching: Numerical Optimization

The matching procedure outlined in Section 2.3.3. minimizes the Euclidean norm between the model predicted acceleration and the curve fit approximation of the measured acceleration signal and the ASC is determined from the interface stiffness ( $k$ ) that minimizes this objective function. The choice of this objective function assumes that the curve fit procedure provides a good approximation to the measured acceleration data from the 16 strikes. It is possible instead to use an objective function representing the error between the model predicted acceleration and the original data from the measured signal. Thus, an alternative objective function is:

$$\epsilon_0 = \sqrt{\sum_i (f_i - f_{d_i})^2}$$

where:  $f_i$  is the model predicted acceleration of the impact rod (normalized) at the  $i^{th}$  time point

$f_{d_i}$  is the measured acceleration signal at the  $i^{th}$  time point

$\epsilon_0$  is a measure of the distance between the two functions over the entire strike

It should be noted that the use of the original data in the objective function does not eliminate the need for the curve fit procedure in the ASIST modeling technique. The curve fit approximation of the data is still used to estimate the amplitude of the measured acceleration signal (to calculate the normalized acceleration) and to estimate the damping content of the measured acceleration signal.

Five sample datasets for each of the implant-abutment combinations described in the previous sections were used for this analysis the: Oticon Medical long/narrow implant specimens (M50128: FRB-20(1), FRB-20(2), PLA) and each of the three abutment lengths (6 mm, 9 mm, 12 mm).

Table C.2 shows the average ASC values (average of 5 measurements) for each implant-abutment sample using both objective functions. For each implant-abutment sample, the average difference in ASC between the two procedures and the average percent difference in ASC between the two procedures are also shown. For the datasets investigated, it was found that there

was minimal difference in the calculated ASC value between the two minimization procedures. Considering all of the measurements, the average difference in ASC between the two procedures was 0.45 (1.09%).

**Table C.2: ASC values using curve fit for minimization (ASC (CF) – average of 5 measurements), ASC values using original data for minimization (ASC (OD) – average of 5 measurements), Average difference in ASC values between the two procedures, and Average percent difference in ASC values between the two procedures.**

	<b>ASC (CF) (Average)</b>	<b>ASC (OD) (Average)</b>	<b>Diff ASC (Average)</b>	<b>% Diff ASC (Average)</b>
<b>M50128 FRB-20(1) - 6 mm</b>	31.15	31.08	0.08	0.26
<b>M50128 FRB-20(1) - 9 mm</b>	30.10	30.24	0.14	0.45
<b>M50128 FRB-20(1) - 12 mm</b>	29.00	29.17	0.18	0.61
<b>M50128 FRB-20(2) - 6 mm</b>	64.44	62.06	2.38	3.69
<b>M50128 FRB-20(2) - 9 mm</b>	58.47	58.33	0.14	0.24
<b>M50128 FRB-20(2) - 12 mm</b>	69.09	68.49	0.59	0.86
<b>M50128 PLA - 6 mm</b>	16.62	16.64	0.02	0.13
<b>M50128 PLA - 9 mm</b>	16.75	17.05	0.30	1.80
<b>M50128 PLA - 12 mm</b>	13.44	13.20	0.24	1.81
<b>Average</b>			<b>0.45</b>	<b>1.09</b>
<b>SD</b>			<b>0.74</b>	<b>1.17</b>

The minimization procedure uses the Euclidean or  $L^2$  norm as the objective function to be minimized. This is a commonly used measure that is often used in regression analysis, curve fitting, and measuring lengths of vectors or distances between points. However, it is possible to choose other norms for the minimization procedure.

With a different choice of norm, the minimization procedure is not guaranteed to produce the same result. This can be illustrated with a simple example. Consider a point (0,1) on the plane  $(x_1, x_2)$  and suppose we want to determine a point on the line  $x_1 = x_2$  that minimizes the distance (norm induced metric) between the given point and the line (Figure C.3).

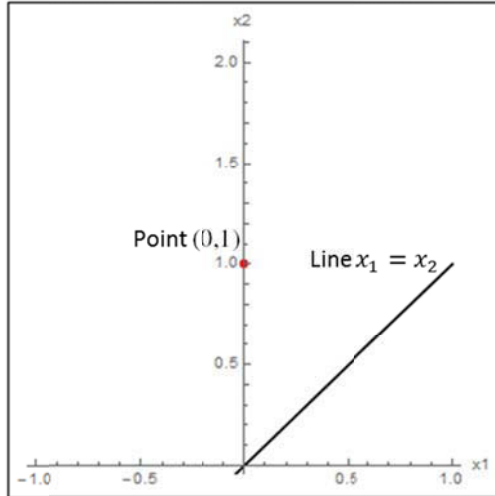


Figure C.3: Point  $(0, 1)$  and line  $x_1 = x_2$

We can consider for example three different norm functions for this minimization, namely the Euclidean ( $L^2$ ) norm which uses the square root of the sum of the squares, the  $L^1$  norm which uses the sum of the absolute values, and the  $L^\infty$  norm which uses the maximum of the absolute values. Figure C.4 shows the points that minimize these different norms and the resulting minimum norm values. The dashed lines show the path to help visualize the norm in each case. It can be noted that the  $L^1$  norm does not produce a unique solution and many points along the line can be found that have the same distance to the given point. The figure shows one point for illustration.

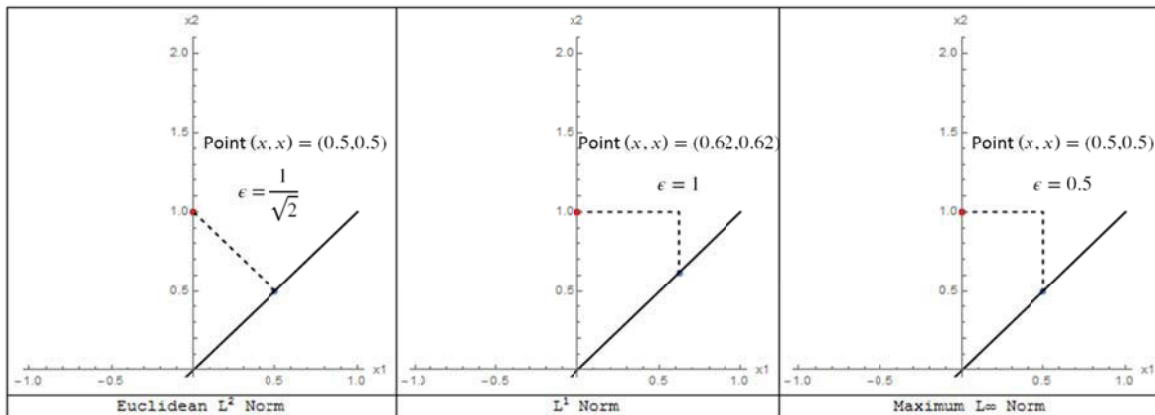


Figure C.4: Point  $(x, x)$  that minimizes the distance between  $(0, 1)$  and the line  $x_1 = x_2$  using the  $L^2$  norm,  $L^1$  norm, and  $L^\infty$  norm

Using the ASIST modeling procedure, we investigated the  $L^1$  norm and compared the results to the original results with the  $L^2$  norm. The objective function in the case of the  $L^1$  norm is:

$$\epsilon_1 = \sum_i |f_i - f_{c_i}|$$

where:  $f_i$  is the model predicted acceleration of the impact rod (normalized) at the  $i^{th}$  time point

$f_{c_i}$  is the curve fit approximation of the measured acceleration signal at the  $i^{th}$  time point

$\epsilon_1$  is a measure of the distance between the two functions over the entire strike

Table C.3 shows the average ASC values (average of 5 measurements) for each implant-abutment combination using both the Euclidean ( $L^2$ ) norm and the absolute value ( $L^1$ ) norm. For each implant-abutment sample, the average difference in ASC between the two procedures and the average percent difference in ASC between the two procedures are also shown. Considering all of the measurements, the average change in ASC with the two different norms was 0.43 (1.08%). Thus, for the datasets investigated, it was found that there was minimal difference in the calculated ASC value for the two choices of norm in the objective function.

**Table C.3: ASC values using Euclidean or  $L^2$  norm (average of 5 measurements), ASC values using  $L^1$  norm (average of 5 measurements), Average difference in ASC values between the two procedures, and Average percent difference in ASC values between the two procedures.**

	ASC ( $L^2$ ) (Average)	ASC ( $L^1$ ) (Average)	Diff ASC (Average)	% Diff ASC (Average)
<b>M50128 FRB-20(1) - 6 mm</b>	31.15	30.49	0.66	2.11
<b>M50128 FRB-20(1) - 9 mm</b>	30.10	30.41	0.31	1.01
<b>M50128 FRB-20(1) - 12 mm</b>	29.00	29.27	0.29	0.98
<b>M50128 FRB-20(2) - 6 mm</b>	64.44	66.19	1.75	2.71
<b>M50128 FRB-20(2) - 9 mm</b>	58.47	58.17	0.30	0.52
<b>M50128 FRB-20(2) - 12 mm</b>	69.09	69.31	0.23	0.33
<b>M50128 PLA - 6 mm</b>	16.62	16.59	0.03	0.16
<b>M50128 PLA - 9 mm</b>	16.75	16.85	0.10	0.60
<b>M50128 PLA - 12 mm</b>	13.44	13.27	0.17	1.29
<b>Average</b>			<b>0.43</b>	<b>1.08</b>
<b>SD</b>			<b>0.55</b>	<b>0.95</b>

# Appendix D: Derivation of the Mass and Stiffness Matrices for Tooth Model

## D.1 Mass Matrix

The inertia influence coefficients  $m_{ij}$  are defined as the force that must be applied at coordinate  $i$  to produce a unit acceleration at coordinate  $j$ , while maintaining zero acceleration at all other coordinates.

The first column of the mass matrix can be determined by applying a unit acceleration at coordinate  $x_1$  with zero acceleration at the other coordinates and examining the FBD's and MAD's of the system components.

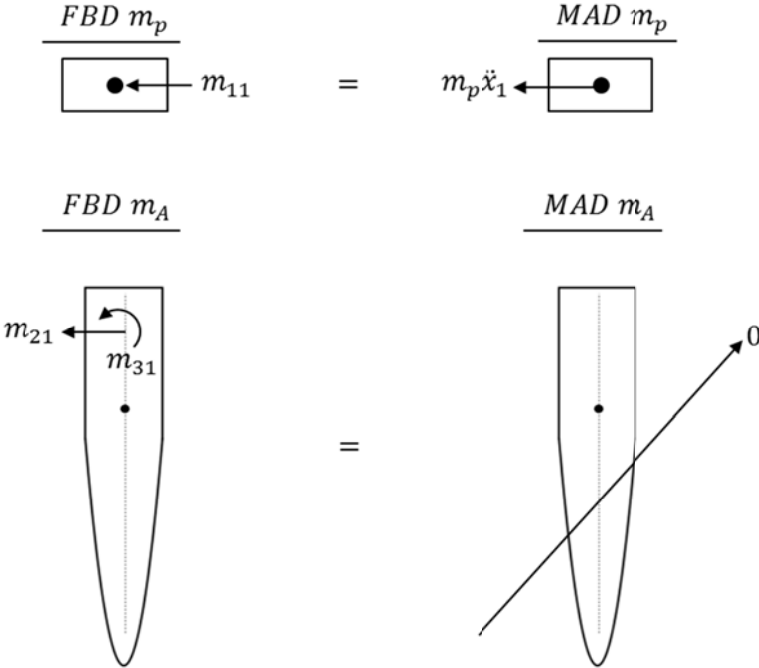


Figure D.1: Free body diagrams for the system components with a unit acceleration applied:  $\ddot{x}_1 = 1$

From the FBD's in Figure D.1 we can write the following equations:

$$\text{Mass: } \sum F_x = ma_x \rightarrow m_{11} = m_p$$

$$\text{Tooth: } \sum F_x = 0 \rightarrow m_{21} = 0$$

$$\sum M_c = 0 \rightarrow m_{31} = 0$$

The second column of the mass matrix can be determined by applying a unit acceleration at coordinate  $x_2$  with zero acceleration at the other coordinates.

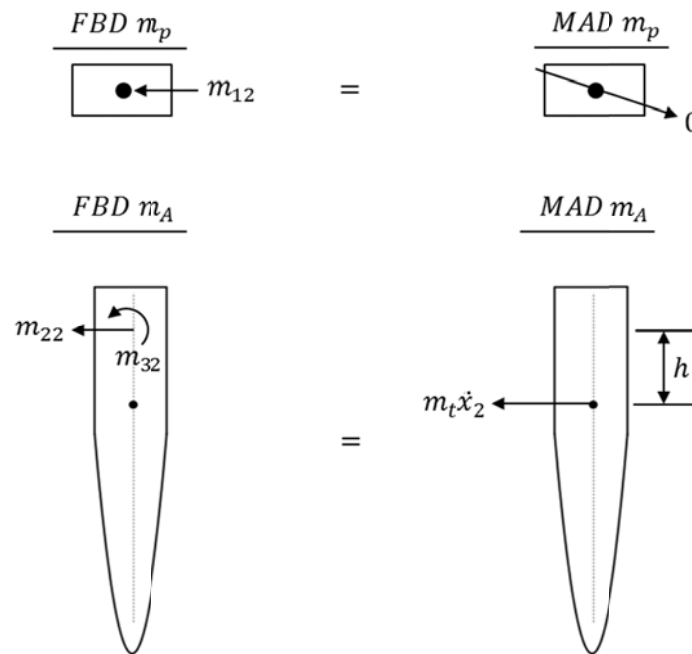


Figure D.2: Free body diagrams for the system components with a unit acceleration applied:  $\ddot{x}_2 = 1$

From the FBD's in Figure D.2 we can write the following equations:

$$\text{Mass: } \sum F_x = 0 \rightarrow m_{12} = 0$$

$$\text{Tooth: } \sum F_x = ma_x \rightarrow m_{22} = m_t$$

$$\left(\sum M_c\right)_{FBD} = \left(\sum M_c\right)_{MAD} \rightarrow m_{32} = -m_t h$$

The third column of the mass matrix can be determined by applying a unit acceleration at coordinate  $\theta$  with zero acceleration at the other coordinates.

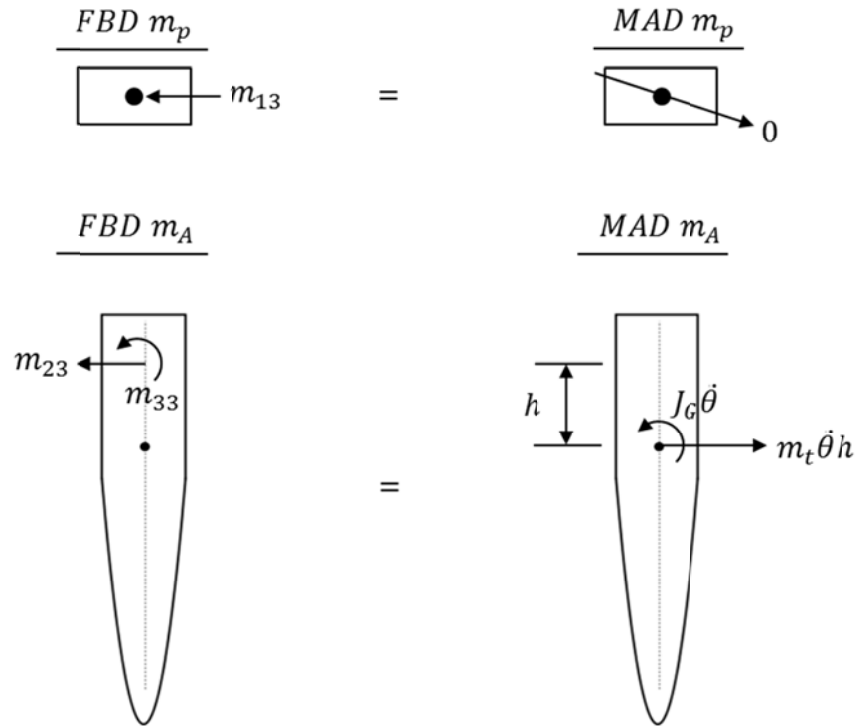


Figure D.3: Free body diagrams for the system components with a unit acceleration applied:  $\ddot{\theta} = 1$

From the FBD's in Figure D.3 we can write the following equations:

$$\text{Mass: } \sum F_x = 0 \rightarrow m_{13} = 0$$

$$\text{Tooth: } \sum F_x = ma_x \rightarrow m_{23} = -m_t h$$

$$\left( \sum M_c \right)_{FBD} = \left( \sum M_c \right)_{MAD} \rightarrow m_{33} = J_G + m_t h^2$$

The mass matrix  $[M]$  is given by:

$$[M] = \begin{bmatrix} m_p & 0 & 0 \\ 0 & m_t & -m_t h \\ 0 & -m_t h & J_G + m_t h^2 \end{bmatrix}$$

## D.2 Stiffness Matrix:

The interface stiffness is represented as a stiffness per unit area covering the tooth root and oriented perpendicular to the tooth surface. Consider a slice through the tooth root of thickness  $dy$  at a distance  $y$  from the bottom of the tooth as shown in Figure D.4. The effective stiffness on such a slice can be determined by applying a unit horizontal displacement  $x = 1$ . The component of the force in the horizontal plane is  $dF_H = dF \cos \alpha$  and the elongation of one of the springs is  $\Delta l = x \cos \alpha = \cos \alpha$ . So, the horizontal component of the force is  $dF_H = dF \cos \alpha = (k \cos \alpha) \cos \alpha = k \cos^2 \alpha$ . Now, considering the components of the force in the horizontal plane, the force on an element of the slice at an angle  $\theta$  from the direction of the applied displacement is equal to  $k \cos^2 \alpha \cos \theta r d\theta dy$ , where  $r$  is the radius of the root at the location of the slice.

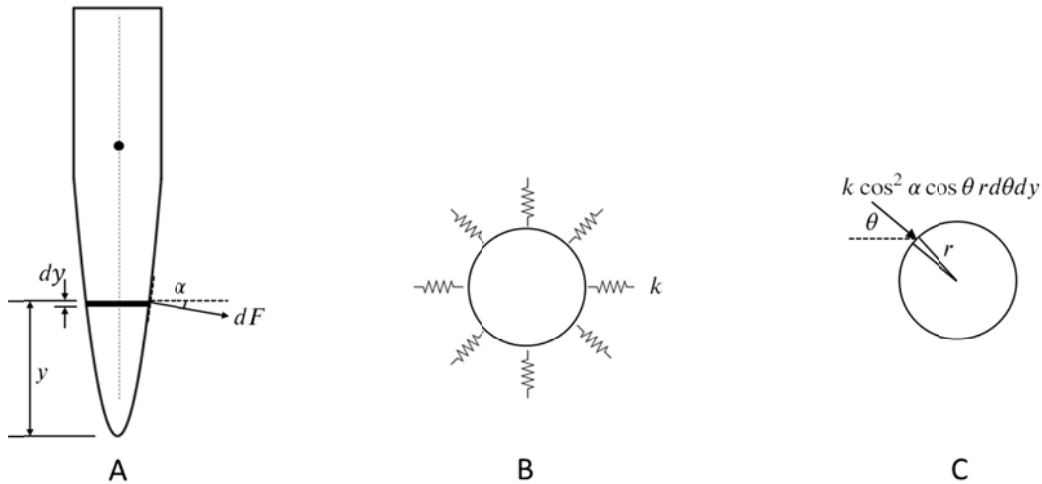


Figure D.4: Tooth schematic. A: Front view cross-section. B: Top view. C: Top view showing the effective stiffness

The effective stiffness for each slice can be determined by integrating the elemental force over the diameter of the tooth root. Thus  $k_{eff}$  in the following equation is a stiffness per unit length applied over the threaded portion of the implant.

$$k_{eff} = 2 \int_{-\frac{\pi}{2}}^{\frac{\pi}{2}} k \cos^2 \alpha \cos \theta r d\theta dy = 4kr \cos^2 \alpha dy$$

Note that  $\alpha$  and  $r$  vary along the length of the tooth root according to the assumed shape.

The stiffness matrix  $[K]$  for the 4-DOF system can now be determined using the method of influence coefficients. The stiffness coefficients  $k_{ij}$  are defined as the force that must be applied at coordinate  $i$  to produce a unit deflection at coordinate  $j$ , while maintaining zero deflection at all other coordinates.

The first column of the stiffness matrix can be determined by applying a unit displacement at  $x_1$  with zero displacement at the other coordinates and examining the FBD's of the system components.

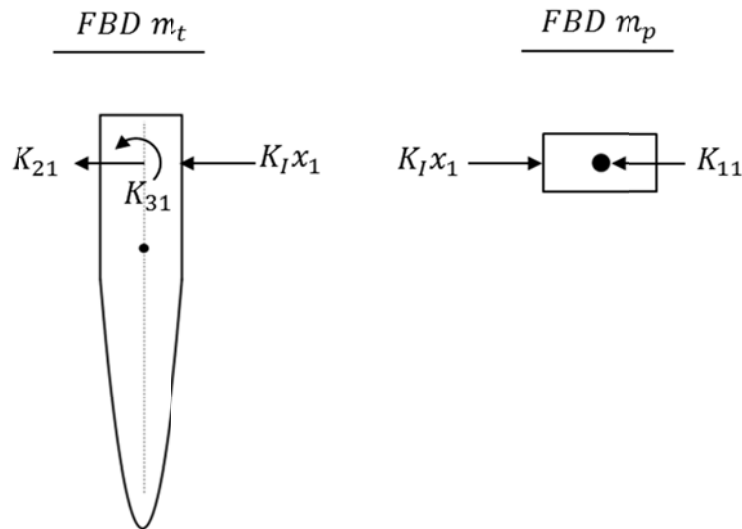


Figure D.5: Free body diagrams for the system components with a unit displacement applied:  $x_1 = 1$

From the FBD's in Figure D.5 we can write the following equations:

$$\text{Mass: } \sum F_x = 0 \rightarrow K_{11} = K_I$$

$$\text{Tooth: } \sum F_x = 0 \rightarrow K_{21} = -K_I$$

$$\sum M_c = 0 \rightarrow K_{31} = 0$$

The second column of the stiffness matrix can be determined by applying a unit displacement at coordinate  $x_2$  with zero displacement at the other coordinates.

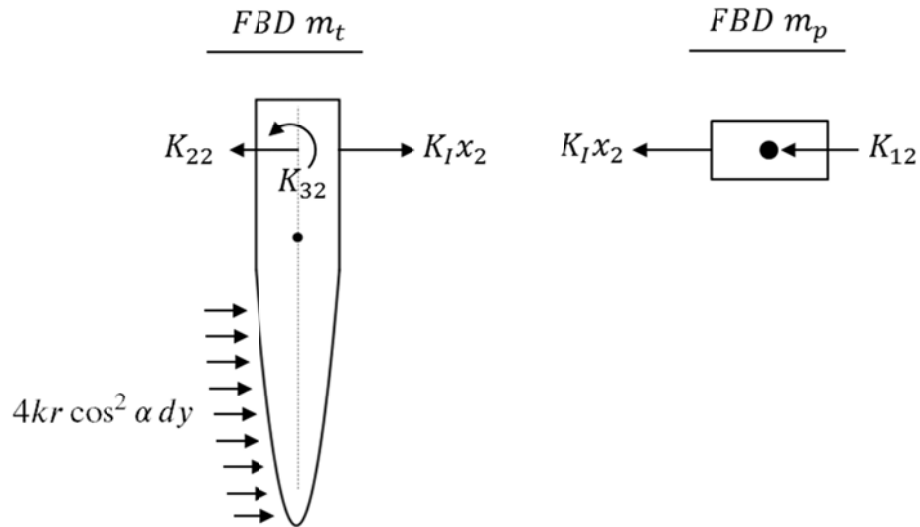


Figure D.6: Free body diagrams for the system components with a unit displacement applied:  $x_2 = 1$

From the FBD's in Figure D.6 we can write the following equations:

$$\text{Mass: } \sum F_x = 0 \rightarrow K_{12} = -K_I$$

$$\text{Tooth: } \sum F_x = 0 \rightarrow K_{22} = K_I + 4 \int_0^{L_r} kr \cos^2 \alpha dy$$

$$\sum M_c = 0 \rightarrow K_{32} = -4 \int_0^{L_r} kr \cos^2 \alpha (L - L_o - y) dy$$

The third column of the stiffness matrix can be determined by applying a unit rotation at coordinate  $\theta$  with zero displacement at the other coordinates.

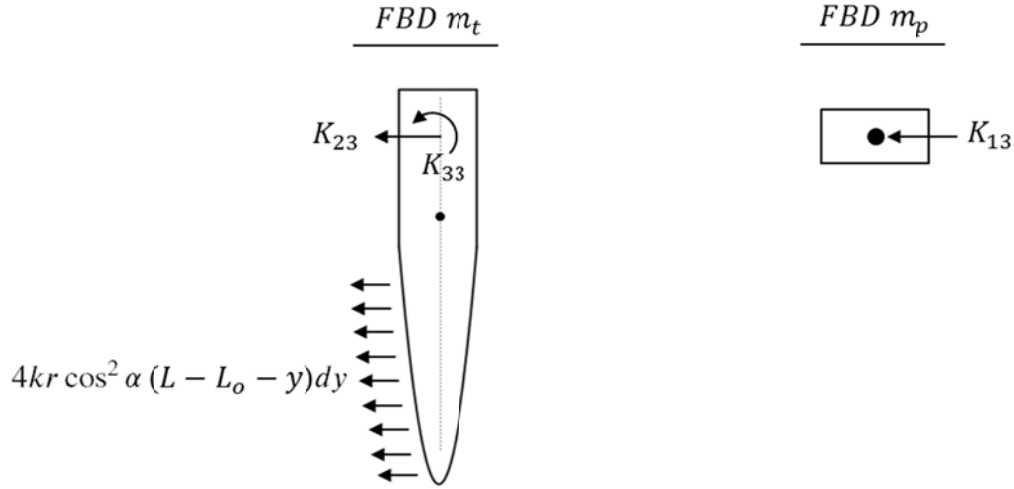


Figure D.7: Free body diagrams for the system components with a unit displacement applied:  $\theta = 1$

From the FBD's in Figure D.7 we can write the following equations:

$$\text{Mass: } \sum F_x = 0 \rightarrow K_{13} = 0$$

$$\text{Tooth: } \sum F_x = 0 \rightarrow K_{23} = -4 \int_0^{L_r} kr \cos^2 \alpha (L - L_o - y) dy$$

$$\sum M_c = 0 \rightarrow K_{33} = 4 \int_0^{L_r} kr \cos^2 \alpha (L - L_o - y)^2 dy$$

The stiffness matrix  $[K]$  is given by:

$$[K] = \begin{bmatrix} K_I & -K_I & 0 \\ -K_I & K_I + 4 \int_0^{L_r} kr \cos^2 \alpha dy & -4 \int_0^{L_r} kr \cos^2 \alpha (L - L_o - y) dy \\ 0 & -4 \int_0^{L_r} kr \cos^2 \alpha (L - L_o - y) dy & 4 \int_0^{L_r} kr \cos^2 \alpha (L - L_o - y)^2 dy \end{bmatrix}$$

Where:

$k$  is the stiffness per unit area surrounding the tooth root

$r$  is the radius of the tooth root as a function of the height  $y$

$\alpha$  is the angle between a line perpendicular to the tooth root and the horizontal as a function of the height  $y$

$L_r$  is the total length of the tooth root

$L$  is the total length of the tooth

$L_o$  is the distance from the top of the tooth (tip) to the location of the strike